Instrumentation for Thermal Noise Spectroscopy

Richard Pedurand

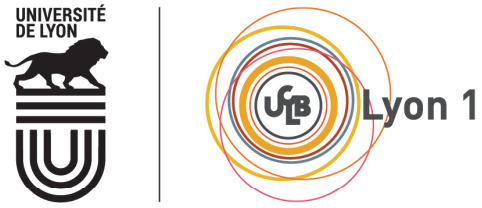

N° d'ordre NNT : 2019LYSE1356

THÈSE DE DOCTORAT DE L'UNIVERSITÉ DE LYON
opérée au sein de
l'Université Claude Bernard Lyon 1

École Doctorale ED52
Physique et Astrophysique

Spécialité de doctorat : Physique
Discipline : Instrumentation

Soutenue publiquement le 19/12/2019, par :
Richard PEDURAND

Instrumentation for Thermal Noise Spectroscopy

Devant le jury composé de :

Pillonet Anne, Professeure, ILM	Présidente
Proksch Roger, Directeur R&D, Oxford Instrument Asylum Reasearch	Rapporteur
Pinto Innocenzo, Professeur, Università di Sannio a Benevento	Rapporteur
Galliou Serge, Professeur, ENS2M	Examinateur
Piednoir Agnès, Ingénieure de recherche CNRS, ILM	Examinatrice
Bellon Ludovic, Chargé de Recherche CNRS, ENS de Lyon	Directeur de thèse
Cagnoli Gianpietro, Professeur, ILM	co-Directeur de thèse, Invité
Granata Massimo, Ingénieur de recherche CNRS, LMA	Invité

à la mémoire de Laurent Balzarini
06/08/1970 – 10/08/2018

Université Claude Bernard – LYON 1

Président de l'Université	**M. Frédéric FLEURY**
Président du Conseil Académique	M. Hamda BEN HADID
Vice-Président du Conseil d'Administration	M. Didier REVEL
Vice-Président du Conseil des Etudes et de la Vie Universitaire	M. Philippe CHEVALLIER
Vice-Président de la Commission de Recherche	M. Jean-François MORNEX
Directeur Général des Services	M. Damien VERHAEGHE

Composantes santé

Faculté de Médecine Lyon-Est – Claude Bernard	Doyen : M. Gilles RODE
Faculté de Médecine et Maïeutique Lyon Sud Charles Mérieux	Doyenne : Mme Carole BURILLON
UFR d'Odontologie	Doyenne : Mme Dominique SEUX
Institut des Sciences Pharmaceutiques et Biologiques	Directrice : Mme Christine VINCIGUERRA
Institut des Sciences et Techniques de la Réadaptation	Directeur : M. Xavier PERROT
Département de Formation et Centre de Recherche en Biologie Humaine	Directrice : Mme Anne-Marie SCHOTT

Composantes et Département de Sciences et Technologie

UFR Biosciences	Directrice : Mme Kathrin GIESELER
Département Génie Electrique et des Procédés (GEP)	Directrice : Mme Rosaria FERRIGNO
Département Informatique	Directeur : M. Behzad SHARIAT
Département Mécanique	Directeur M. Marc BUFFAT
UFR - Faculté des Sciences	Administrateur provisoire : M. Bruno ANDRIOLETTI
UFR (STAPS)	Directeur : M. Yannick VANPOULLE
Observatoire de Lyon	Directrice : Mme Isabelle DANIEL
Ecole Polytechnique Universitaire Lyon 1	Directeur : Emmanuel PERRIN
Ecole Supérieure de Chimie, Physique, Electronique (CPE Lyon)	Directeur : Gérard PIGNAULT
Institut Universitaire de Technologie de Lyon 1	Directeur : M. Christophe VITON
Institut de Science Financière et d'Assurances	Directeur : M. Nicolas LEBOISNE
ESPE	Administrateur Provisoire : M. Pierre CHAREYRON

Résumé de la thèse

La résolution des interféromètres gravitationnelles est limitée par le mouvement Brownien - ou bruit thermique - de leur miroir dans la partie centrale de leur bande de détection. La répartition en fréquence de ce bruit thermique est dictée par les mécanismes de dissipation d'énergie mécanique à l'origine de cette vibration, en accord avec le théorème fluctuation-dissipation. Cette dissipation provient principalement des revêtements optiques déposées sur les miroirs pour leur donner leur réflectivité. Dans le but de réduire ce bruit thermique, une nouvelle génération de détecteur d'ondes gravitationnelles employant des miroirs refroidis à température cryogénique a été proposé. Le développement de nouveaux matériaux optique en couche mince à faible dissipation mécanique, opérant à la fois à température ambiante et température cryogénique, demande donc de nouveaux outils expérimentaux. L'objet principal de cette thèse est la construction d'un nouvel instrument, le CryoQPDI, qui consiste en l'association d'un interféromètre haute résolution et d'un cryostat basé sur un refroidisseur pulse tube. Il est capable de mesurer directement le mouvement Brownien d'un microlevier entre 300 K et 7 K. En combinant des mesures effectuées sur un microlevier avant et après le dépôt d'une couche mince, il est possible de caractériser la dissipation mécanique interne de cette couche mince.

Mots clef : fluctuations thermiques, dissipation mécanique, interféromètre, théorème fluctuation-dissipation, couche mince, micro-levier, mesure cryogénique, viscoélasticité

Thesis abstract

The resolution limit of gravitational wave interferometers is set by their mirrors' Brownian motion – or thermal noise - in the central part of their detection band. This thermal noise frequency distribution is given by the mechanical energy dissipation mechanisms it originates from, in agreement with the fluctuation-dissipation theorem. This dissipation mainly derives from the optical coatings deposited on the mirrors to give them their reflectivity. To reduce this thermal noise, a new generation of gravitational wave detectors employing mirrors cooled to cryogenic temperature has been suggested. The development of new optical thin-film materials with low mechanical dissipation, operating at both room and cryogenic temperatures, therefore requires new experimental tools. The main object of this thesis is the construction of a new instrument, the CryoQPDI, which is an association between a high-resolution interferometer and a cryostat based on a pulse tube cooler. It can directly measure the Brownian motion of a microcantilever between 300 K and 7 K. By combining measurements made on a microcantilever before and after the deposition of a thin film, it is possible to characterize the internal mechanical dissipation of this thin film.

Keywords: thermal fluctuations, mechanical dissipation, interferometer, fluctuation-dissipation theorem, thin film, micro-cantilever, cryogenic measurement, viscoelasticity

Résumé substantiel

La détection directe des ondes gravitationnelles émises lors de la coalescence de deux trous noirs a été réalisée pour la première fois le 14 septembre 2015. Cette première détection, depuis suivie par beaucoup d'autres, marqua le début d'une nouvelle ère pour l'astronomie et l'astrophysique. Là où nous avions d'abord appris à regarder notre univers, il est désormais devenu possible de l'entendre, ceci après plusieurs décennies de progrès scientifiques et technologiques. En effet, les ondes gravitationnelles observables sont d'une amplitude extrêmement faible, et leur détection n'est aujourd'hui possible que suite au développement d'une nouvelle classe d'interféromètres laser extrêmement sensibles, les interféromètres gravitationnels.

Les interféromètres gravitationnels sont des interféromètres de Michelson qui se distinguent entre autres par des bras de plusieurs kilomètres et par l'emploi d'une cavité Fabry-Pérot dans chaque bras. Plusieurs interféromètres gravitationnels sont aujourd'hui opérationnels, en particulier les détecteurs jumeaux Advanced LIGO aux États-Unis, le détecteur européen Advanced Virgo et le détecteur KAGRA dont les dernières phases de développement s'achèvent au Japon. Bien que de multiples ondes gravitationnelles aient pu être observées, la technologie de ces détecteurs continue à faire l'objet d'une recherche constante pour améliorer leur sensibilité. Il s'agit d'augmenter la fréquence des détections et d'écouter une plus large portion de l'Univers.

Les interféromètres gravitationnels font appel à des composants optiques qui se distinguent par leur grande taille et leurs qualités exceptionnelles. En particulier, leurs miroirs sont des miroirs de Bragg formés par le dépôt d'un empilement de couches minces transparentes sur un substrat de verre. Ces couches minces sont formées d'oxydes amorphes déposés par pulvérisation par faisceau d'ions (*Ion Beam Sputtering*, IBS). Les deux matériaux utilisés actuellement sont la silice SiO_2 et le pentoxyde de tantale Ti :Ta_2O_5.

Une des principales limites à la sensibilité des interféromètres gravitationnels est le bruit thermique provoqué par le mouvement Brownien de leurs miroirs dans la partie centrale de leurs bandes de détections. En accord avec le théorème fluctuation-dissipation, la distribution en fréquence de ce bruit thermique est dictée par les mécanismes de dissipation d'énergie mécanique opérant au sein des matériaux qui composent ces miroirs. Cette dissipation est plus particulièrement localisée dans le revêtement optique des miroirs, qui est donc la principale origine de leur bruit thermique. Une des pistes proposées pour réduire ce bruit est la construction d'interféromètres gravitationnels employant des miroirs refroidis à température cryogénique. Le projet KAGRA est le premier à implémenter cette stratégie.

Pour mieux comprendre et réduire le bruit thermique des miroirs des interféromètres gravitationnels, il est donc nécessaire de pouvoir caractériser la dissipation mécanique

des matériaux optiques en couches minces qui composent le revêtement de ces miroirs, ceci à la fois à température ambiante et à température cryogénique. Ce manuscrit de thèse décrit le développement d'un nouvel instrument de laboratoire qui répond à cette problématique.

Cet instrument est appelé CryoQPDI, pour "Quadrature Phase Differential Interferometry on Cryocooled microresonators". Il est le fruit d'une collaboration entre le Laboratoire des Matériaux Avancés (LMA), qui est responsable des revêtements optiques sur tout les grands composants employés dans les interféromètres gravitationnels, et le laboratoire de physique de l'ENS de Lyon (LPENSL), où a été développé le concept de QPDI (*Quadrature Phase Differential Interferometer*). Le QPDI est un interféromètre homodyne haute résolution combinant un schéma de mesure différentiel et une détection en quadrature. Le CryoQPDI implémente cet interféromètre pour la mesure directe des vibrations thermiques d'un microlevier refroidi dans un cryostat. Les microleviers utilisés sont semblables à ceux employés en microscopie à force atomique (AFM), et leurs dimensions microscopiques leur confèrent une très faible raideur qui les rend particulièrement susceptibles au bruit thermique. La dissipation d'une couche mince peut être extraite en comparant les résultats obtenus avant et après son dépôt sur un microlevier. Le CryoQPDI permet de réaliser ces mesures entre 300 K et 7 K, et sur une bande passante de 1 MHz.

La mesure directe du bruit thermique d'un microlevier est une originalité en comparaison des méthodes de mesures employées précédemment dans ce domaine, par rapport auquelles elle offre une combinaison d'avantages uniques : la petite taille des microleviers permet de les refroidir très facilement, les rendant particulièrement appropriés aux mesures à températures cryogéniques. La forme d'un spectre de vibration thermique fourni des renseignements supplémentaires sur le mécanisme dissipatif à l'oeuvre dans l'échantillon. Les microleviers n'ont pas besoin de montrer une grande réflectivité, ce qui permet de caractériser à la fois des revêtements monocouches et multicouches. Il est également pas nécessaire d'exciter leurs modes de vibration, ce qui permet de les mesurer simultanément, rendant cette méthode particulièrement rapide. Enfin, les revêtements étudiés sont d'une épaisseur comparable à celle des microleviers, ce qui permet d'extraire plus facilement leur dissipation.

Mesurer le bruit thermique d'un microlevier avec une résolution élevée n'est possible qu'avec une attention particulière au bruit interne et externe de l'instrument. Le développement du CryoQPDI détaillé dans ce manuscrit est donc une quête permanente pour un très faible bruit de mesure. Dans ce sens, le schéma optique de l'interféromètre a reçu trois modifications principales :

- Nous avons développé un système optique formé de lentilles mobiles nommé le *scanning objective*. Il permet à la fois de focaliser le faisceau laser de l'interféromètre malgré une longue distance de travail et de le positionner sur l'échantillon suivant

trois axes (translation latérale et focus). Pour garantir une faible taille du spot laser, le *scanning objective* a été construit avec l'assistance d'un logiciel de lancé de rayon et à partir d'une sélection de lentilles disponibles commercialement pour compenser son aberration sphérique.

- Nous avons découvert qu'une forme d'astigmatisme du premier ordre introduit par la lame biréfringente utilisée comme séparatrice de l'interféromètre était à l'origine de sa plus importante perte de contraste. Ce problème a été corrigé en utilisant une lame de Semel Savart, qui est une combinaison de quatre lames biréfringentes respectant un rapport d'épaisseurs qui permet de compenser cette aberration.
- Nous avons introduit une vision par caméra dans l'interféromètre, qui simplifie considérablement les étapes d'alignements et de calibration. Le CryoQPDI reste ainsi pratique d'utilisation.

Le design des quatre photodétecteurs de l'interféromètre a également été revisité. Nous avons découvert un excès de bruit à haute fréquences et nous l'avons relié au modèle d'amplificateur opérationnel employé dans le premier étage d'amplification transimpédance. Le choix d'un autre amplificateur opérationnel nous a permis d'atteindre une détection limitée par le shot noise sur toute la bande passante de l'instrument.

Pour permettre l'étude de la dissipation de couche mince, nous avons également dû développer l'ensemble du protocole expérimental associé. Lors de la phase de dépôt, la faible raideur des leviers les rend particulièrement sensibles aux contraintes internes des couches déposées. Nous avons développé un dispositif mécanique appelé le RVDS, pour *Recto Verso Deposition System*, qui permet de retourner les microleviers à l'intérieur d'un bâti de dépôt par IBS. Le dépôt alterné du revêtement optique sur chacune des deux faces du microlevier permet de compenser les contraintes et d'obtenir des échantillons exploitables.

Comme preuve de concept, nous avons étudié les dissipations internes d'un microlevier en silicium recouvert d'une couche de pentoxyde de tantale (non dopé) entre 10 K et 150 K. L'angle de perte de la couche présente un maximum mou autour des 50 K, avec une valeur et une position qui dépendent du mode de vibration observé. Les maxima de l'angle de perte correspondant suivent une faible dépendance en fréquence, et la température correspondant à ces maximas obéit à une loi d'Arrhenius avec une énergie d'activation de 53 meV. Le facteur de dilution, correspondant à la part de dissipation attribué à la couche seule, était de 0.5, permettant d'ignorer l'angle de perte du substrat.

Remerciements

Je tiens à adresser mes premiers remerciements à Ludovic Bellon, sans qui ce travail n'aurait sûrement jamais abouti. Je te remercie pour la confiance infaillible que tu m'as accordée malgré tout, ta bienveillance chaleureuse, tes encouragements et ta très, très grande patience. Je le redis, pour moi tu es le meilleur directeur de thèse que l'on peut trouver.

Je remercie Renée Pignard et Gianpietro Cagnoli de m'avoir offert l'opportunité d'effectuer un stage puis une thèse au sein du LMA.

Je remercie également Thierry Dauxois de m'avoir permis de travailler au laboratoire de physique de l'ENS de Lyon. Je remercie le LABEX Institut Lyonnais des Origines (ANR-10-LABX-0066) de l'Université de Lyon pour son soutien financier dans le cadre du programme "Investissements d'Avenir" (ANR-11-IDEX-0007) de l'État français géré par l'Agence Nationale de la Recherche (ANR). Je remercie également la Fédération de Recherche André Marie Ampère (FRAMA) et la Mission pour l'Interdisciplinarité du CNRS pour leur aide financière.

Je remercie Anne Pillonet, Roger Proksch, Innocenzo Pinto, Agnès Piednoir et Massimo Granata d'avoir accepté de faire partie de mon jury de thèse. Je remercie en particulier Roger Proksch et Innocenzo Pinto pour leurs remarques et leurs conseils en tant que rapporteur. Merci tout spécialement à Massimo Granata qui, en plus d'être un très bon ami et collègue, a entrepris de corriger les fautes de mon manuscrit, une tâche rendue particulièrement ingrate par la grande densité surfacique de ces fautes et l'épaisseur déraisonnable de ce document.

C'est avec beaucoup d'enthousiasme que je remercie Ghaouti Hansali pour toute son aide et pour tout le temps qu'il a bien voulu passer avec moi à démonter, remonter, ajuster, tester, et encore démonter notre "manip", ceci malgré son grand âge. Tu m'as aidé à voir les choses sous un autre angle, à (un peu) lâcher prise et à me focaliser sur l'essentiel. Crois-moi, tu m'as aidé bien plus que tu ne le penses.

Merci au “chef” Vincent Dolique, pour m’avoir si bien encadré lorsque que je débutais au LMA comme stagiaire, et pour m’avoir si bien encouragé ensuite. Et le tout avec une très grande élégance s’il vous plaît.

Je remercie David Hofman pour son aide épique lors de la conception du *scanning objective*. Sans ta maîtrise de Zemax et ta force tranquille, je n’aurai pas été très loin dans ce projet.

J’adresse des remerciements très spéciaux à Danièle Forest pour m’avoir accordé cette aide très précieuse dans ma vie personnelle.

Je remercie les membres de la Plateforme Technique d’Enseignement et de Recherche (PTER) de l’Ecole National d’Ingénieurs de Saint-Etienne (ENISE), en particulier Christophe Claudin, Florian Dumont, Patrick Polly et Hervé Seux, qui ont proposé de réaliser gratuitement un ensemble de pièces vitales pour le fonctionnement de mon instrument. Vous ne le savez peut-être pas, mais en faisant cela vous avez beaucoup aidé notre projet à un moment où il en avait très besoin. Je n’en reviens toujours pas.

Pour leur aide, leurs conseils, pour les nombreuses réunions et discussions, pour les moments de rigolade au coin café, et parce qu’ils contribuent ou ont contribué à faire du LMA ce laboratoire si particulier, je remercie aussi Jérôme, Benoit, Bernard, Bertrand, Eleonore, Laurent P, Lorenzo, Christophe, Matthieu et Julien.

Je remercie Nathalie et Justine du LMA ainsi que Camille, Fatiha, Laure, Laurence et Nadine de l’ENS pour leur travail de soutiens capital au secrétariat et pour m’avoir aidé à traiter mes très nombreuses commandes au travers du brouillard de Gestlab.

Merci à Caroline, Audrey et Antoine pour leur soutien, leur encouragement et pour avoir partagé leur temps et leur vie avec moi et avec simplicité. Ce sont des gens comme vous qui font du labo de physique de l’ENS un endroit ou il fait si bon travailler.

Je remercie la providence de m’avoir fait rencontrer un physicien aussi brillant, talentueux et magnifique que Basile Pottier. Tu as été et tu restes une vraie source d’inspiration.

Merci à Jérôme, Clément, Geraldinne, Timothée, Hélène, Charles-Edouard, Valentin, Lucas, Yeraldine, Cristobal, Ignacio, Marcelo, Lavi, et tous ceux avec qui, de près ou de loin, j’ai partagé ma vie pendant toutes ces années.

Merci à Laura et Pauline d’avoir partagé ces moments de force et de robustesse stakhanovistes lors de la joyeuse rédaction de nos thèses. Merci notamment pour les plantes, le chocolat et les câlins de la Mezza.

Je remercie très chaleureusement Alex Amato et Alex Fontana de m’avoir accordé leur amitié suite à leur immigration. Je vous remercie d’avoir partagé avec moi le plénum,

beaucoup de bière, Bassano del Grappa et Ventimiglia, une importante quantité de curry, Catan, et la liste est encore très longue. Pourvu que notre amitié dure encore longtemps.

Je remercie très sincèrement Mickaël Bourgoin qui a accepté de me recruter en post-doc, pour ensuite me laisser consacrer plusieurs mois de ce postdoc pour finir mon manuscrit. Sans toi non plus, je ne sais vraiment pas comment j'aurai pu faire pour terminer cette thèse.

Je remercie toute ma famille et tous mes amis pour leur amour et leur soutien. Je remercie en particulier mon frère Alexandre Pedurand parce qu'il me donne un si fier exemple.

Ma Paola ma Pioupiou ma chérie, merci pour ton soutien, ta patience et ta douceur, merci pour tous ces weekends passés à travailler ensemble. Merci de m'aimer malgré tout et malgré moi.

Merci à tous ceux mentionnés ici et à tous les autres d'avoir partagé votre lumière avec moi pendant toutes ces années de doctorat.

C'est avec beaucoup d'émotion que j'adresse mes derniers remerciements à Laurent Balzarini. C'est en grande partie à tes côtés que j'ai découvert le monde fascinant de la mécanique de précision, le tour, la fraiseuse, l'odeur de l'huile de coupe et la satisfaction que peut donner une pièce de métal usiné au centième de millimètre. Merci de m'avoir laissé t'accompagner à l'atelier quand j'avais besoin de parler et de m'échapper. Merci pour ces cigarettes que nous avons partagées ensemble en parlant du quotidien et de la vie. Tu es partie trop tôt. Je te dédie ce manuscrit. Puisque nous partagions certains traits de caractère, j'espère que tu ne m'en voudras pas.

Contents

List of Figures

List of Tables

1 General introduction

1.1 Gravitational waves

Albert Einstein's theory of general relativity explains that the phenomenon of gravitation is caused by the curvature of spacetime generated by the distribution of masses and energies in the universe.
If a charged particle is accelerated, it can emit energy in the form of an electromagnetic wave. In 1916 [35, 36] , Einstein observed that in a similar way, the linearized equations of general relativity predict that the spacetime curvature caused by an accelerated massive object can propagate like a transversal wave at the speed of light. These oscillations of the fabric of spacetime are called gravitational waves.

On its way, a gravitational wave causes a quadrupole deformation of the distance between massive particles only subject to gravitation (figure 1.1) . The amplitude of this deformation is quantified by the strain $h = \Delta l/l$, defined as the variation in distance Δl between two particles in free fall separated by the distance l.

One important characteristic of gravitational waves is their extremely weak amplitude, making them impossible to detect at the laboratory scale. The only detectable gravitational waves are emitted during extreme astronomical events involving very massive objects submitted to very strong accelerations. The main expected sources of gravitational waves are the coalescence of a binary system of black holes (figure 1.2), neutron stars, or a black hole with a neutron star, the rapid rotation of a Pulsar, or the explosion of a supernovae. Still, the typical amplitude of gravitational wave expected from these event is less than $h \approx 10^{-21}$, making their detection extremely challenging: one must be able to measure a length variation comparable to the size of an atom relative to the Sun-Earth distance.

During the past century, astronomy and astrophysics have been revolutionized by the developpement of new instruments able to detect high energy particles and electromagnetic radiations outside of the visible spectrum. These developpements led to important discoveries for our understanding of the Universe, among which the Big Bang, the existance of black holes, pulsars, quasars and the expansion of the Universe itself. In the same vein, gravitational waves astronomy offers a mean to listen the Universe in a way that has never been possible before.

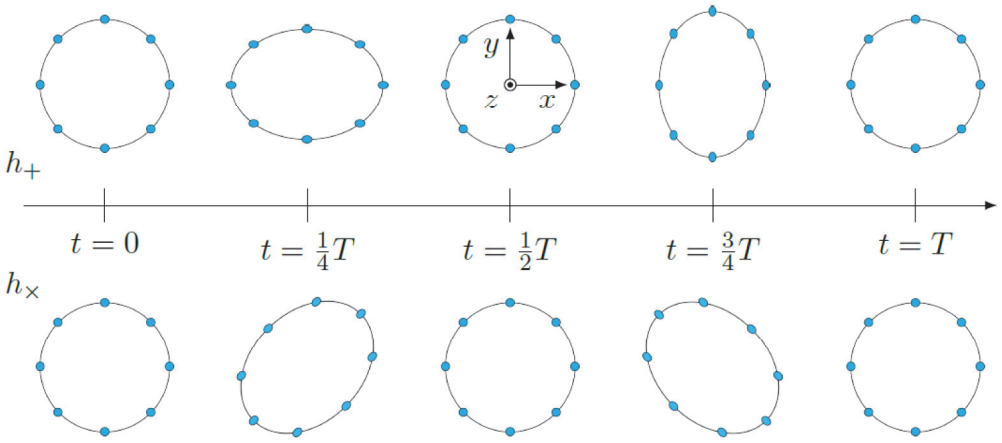

Figure 1.1 Effect of a gravitational wave on a ring of free-falling massive particles. The wave is travelling along an axis perpendicular to the ring plane. The two possible polarizations + and × are represented with the same amplitude for one oscillation period T. They only differ by a rotation of $45°$.

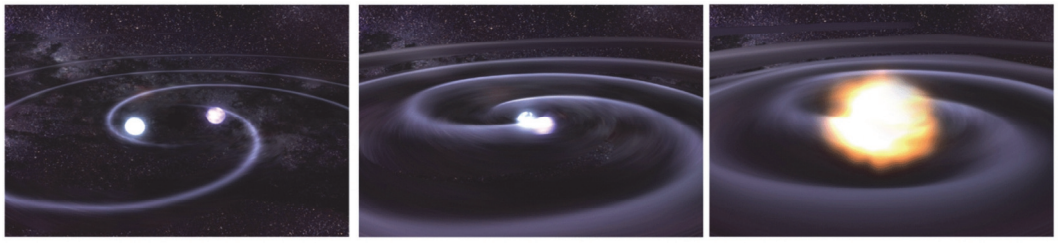

Figure 1.2 Artist view of a binary black hole merger [27]. Spacetime is disturbed by the inspiral motion of two black holes rotating around each other. The system loses energy by gravitational wave radiation until the two black holes collide and merge to form a single black hole (the coalescence). Only the last few seconds of the coalescence event emits measurable gravitational waves, where the two black holes weighting several sun masses are the closest and are accelerated near the speed of light.

The first strong evidence of the existence of gravitational waves was provided by Hulse and Taylor [123]. They studied the binary pulsar system PSR1913+16 and observed a quadratic decay of the system's orbital period compatible with a loss of energy by gravitational wave radiation. They were awarded the Nobel Prize in Physics in 1993 for this discovery.

1.2 Gravitational wave detectors

Given the nature of gravitational waves, a laser Michelson interferometer with perpendicular arms appeared as particularly suitable for their detection, which is the basis of the laser interferometer gravitational wave detectors. To obtain a detectable signal, these instruments have kilometer long arms (figure 1.3), whose effective length is further increased by the use of Fabry-Perot cavities (figure 1.4). The deformation of

Figure 1.3 Second generation gravitational wave detectors [27, 25]. At the time of writing, the detector presented here are the only ones to have acheived detection. On the left: Advanced VIRGO, Cascina, Italy. On the middle and on the right: Advanced LIGO twin interferometers, located at Hanford, Washington (middle) and Livingston, Louisiana (right).

space time caused by a gravitational wave induces a small differential displacement of the interferometer mirror's, which is detected by interferometry.

The enormous challenge of building gravitational wave detectors was faced by large scientifics collaborations, and covers an history of more than 30 years. The Virgo collaboration [27] started as a conjoint effort between France and Italy and was then extended to several European countries. It is named after the Virgo cluster, a collection of 1500 galaxies in the Virgo constellation. This collaboration completed and has operated the Virgo interferometer since 2003 (figure 1.3). It is located at Cascina, Italy and has 3 km arms.

The LIGO collaboration [25] (Laser Interferometer Gravitational-Wave Observatory) constructed two twin detectors with 4 km arms in the USA. They are located at Hanford, Washington and Livingston, Louisiana, and have been operated since 2005.

Beside these three large gravitational wave detectors, the GEO600 project, located in Hannover, Germany, with 600 m arms, is the fourth detector to belong to the first generation of ground based detectors. Neither of these first attempts acheived detection, but they demonstrated the feasibility of a kilometer scale interferometer.

A tenfold improvement of sensitivity, corresponding to a $\sim 10^3$ increase of the probed Universe volume and of the detection rates, motivated the developpement of a second generation of detector: Advanced Virgo (aVirgo), Advanced LIGO (aLIGO) and the KAGRA project (Kamioka Gravitational Wave Detector), located in Kamioka, Japan, with 3 km arms. Both the aVirgo and aLIGO detectors are currently operational, and the KAGRA interferometer construction was completed in october 2019, with a beginning of observations expected before the end of 2019.

The first direct detection of a gravitational wave was accomplished by both of the aLIGO detectors the 14th of september 2015, almost 100 years after Einstein prediction.

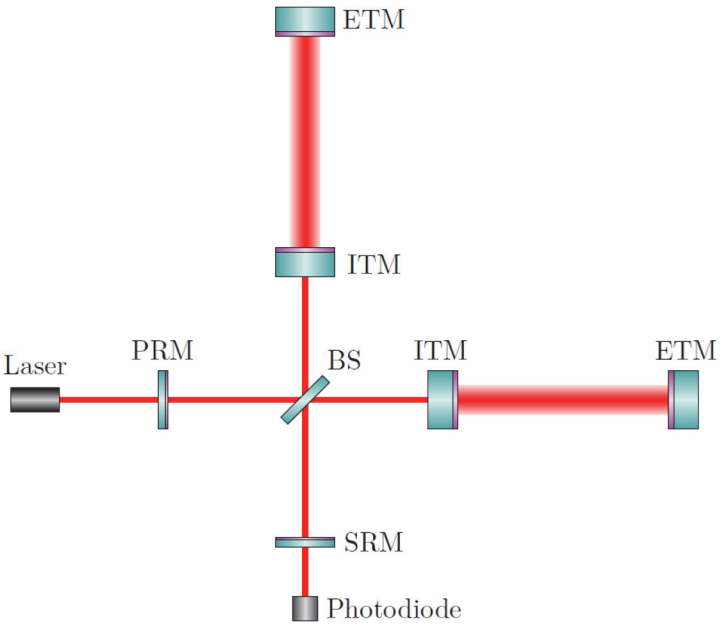

Figure 1.4 Simplified optical schematic of a gravitational wave detector [27, 26]. The basic optical arrangement is the one of a Michelson interferometer, with a laser, a beam splitter (BS), two end mirrors (end test-mass, ETM) and a photodiode. Inserting the two input test-masses (ITM) creates a Fabry-Perot cavity in each arm. To further increase the interferometer sensitivity, two additional mirrors are used to implement power recycling (PRM) and signal recycling (SRM).

This was also the first direct observation of a binary black hole merger. The detected signal is shown in figure 1.5. This first major achievement has then since been followed by several detections performed by both aVirgo and aLIGO. The events detected before the end of 2018 are listed in reference [24]. The 2017 Nobel prize in physics was attributed to Rainer Weiss, Barry C. Barish and Kip S. Thorne for their pioneering contribution to the development of the gravitational wave detectors leading to this first detection.

A global network A single gravitational wave detector allows the observation of a gravitational wave signal but does not permit a localization of the source. Similarly to the relation between earthquakes and seismometers, at least three detectors are required for a precise localization of the source. This is important for the observation of the electromagnetic counterpart of a gravitational wave signal, which is the principle of multi-messenger astrophysic. The first exemple of such a multi-messenger observation is the GW170817 event [7], which was made possible by a triple detection from the aVirgo and aLIGO detectors. The current global gravitational wave detector network is displayed in figure 1.6.

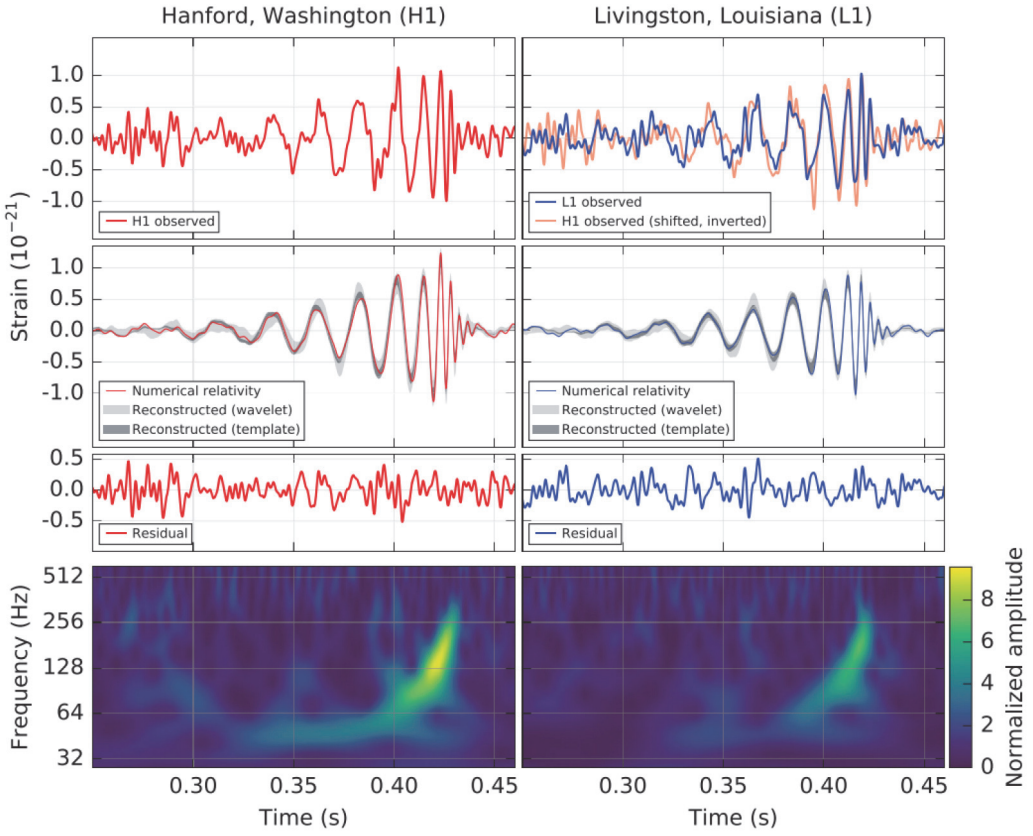

Figure 1.5 The first ever detected gravitational wave event, named GW150914, was observed simultaneously by the two LIGO detectors [1]. Left panel: LIGO Hanford (H1) data. Right panel: LIGO Livingston (L1) data. First row: GW150914 signal. Second row: a numerical relativity waveform is compared to a reconstructed signal. Third row: residual. Bottom row: time frequency representation of the strain data, showing the increase of frequency of the signal over time.
This event was identified as the coalescence of two black holes with a mass of 36 and 29 solar mass respectively, occuring 410 megaparsec from Earth.

1.3 Gravitational wave detectors' sensitivity: the coating thermal noise problem

Detector sensitivity The ability of a gravitational wave interferometer to detect an event is limited by several noise sources. An exemple is given in figure 1.7 by the advanced Virgo design sensitivity curve [26].

Detecting the very weak signal of a gravitational wave supposes that all the possible effects which can result in a displacement of the interferometer's mirror have been greatly attenuated. Two examples of such noise sources are ground vibrations or a finite gas pressure around the mirrors and inside the arms. In aVirgo, the ground vibrations are mitigated by suspending all the main interferometer's optics using so called superattenuators (figure 1.8). To reduce the effect of gas particles, all the interferometer main components are placed at a vacuum of 10^{-9} mbar, including

Figure 1.6 Current ground based gravitational wave detector world map [106]. The GEO 600 interferometer never achieved detection with its 600 m arms, but served as an important test center for new gravitational wave detector technologies and is still operational. The KAGRA interferometer construction was acheived at the beginning of october 2019. It is the first advanced detector to employ cryocooled mirrors, and also has the particularity of being located underground. LIGO-India is a new detector project to be built in India [100]. Two other future gravitational wave detector projects not shown on this map are the LIGO cosmic explorer project [37] and the Einstein telescope project [99]. At last, the LISA project [9] is worth mentioning, as it will be the first space-born gravitational wave observatory.

the full path of the laser beam in each arms (figure 1.8). This makes the interiors of gravitational wave detectors one of the largest pumped volumes on Earth.

Mirrors for gravitational wave detectors Mainly because of the very long arm length of a gravitational wave interferometer and of the very large laser power involved, the mirrors of a gravitational wave detectors do not only need to be relatively large, but they also require the ultimate optical quality to reduce the effects of absorption and scattering.

An aVirgo end test-mass (ETM) is represented in figure 1.9. The mirror needs to have a large diameter to accomodate a large laser spot size and reduce the effect of diffraction, but also very thick to increase its mass and rigidity, to reduce in particular the effect of the laser radiation pressure. The mirrors for aLIGO and aVirgo are made of fused silica, and undergo a multilayer interference coating to increase their reflectivity. The relevant properties of an ETM are listed in table 1.1. The coatings are made using the ion beam sputtering deposition technique, which is know to provides the amorphous optical coatings with the highest optical quality.

Coating thermal noise In the frequency range where the aVirgo interferometer is the most sensitive, between 40 Hz and 300 Hz, the most limiting noise source is the coating Brownian noise, or coating thermal noise (CTN). This noise arise from

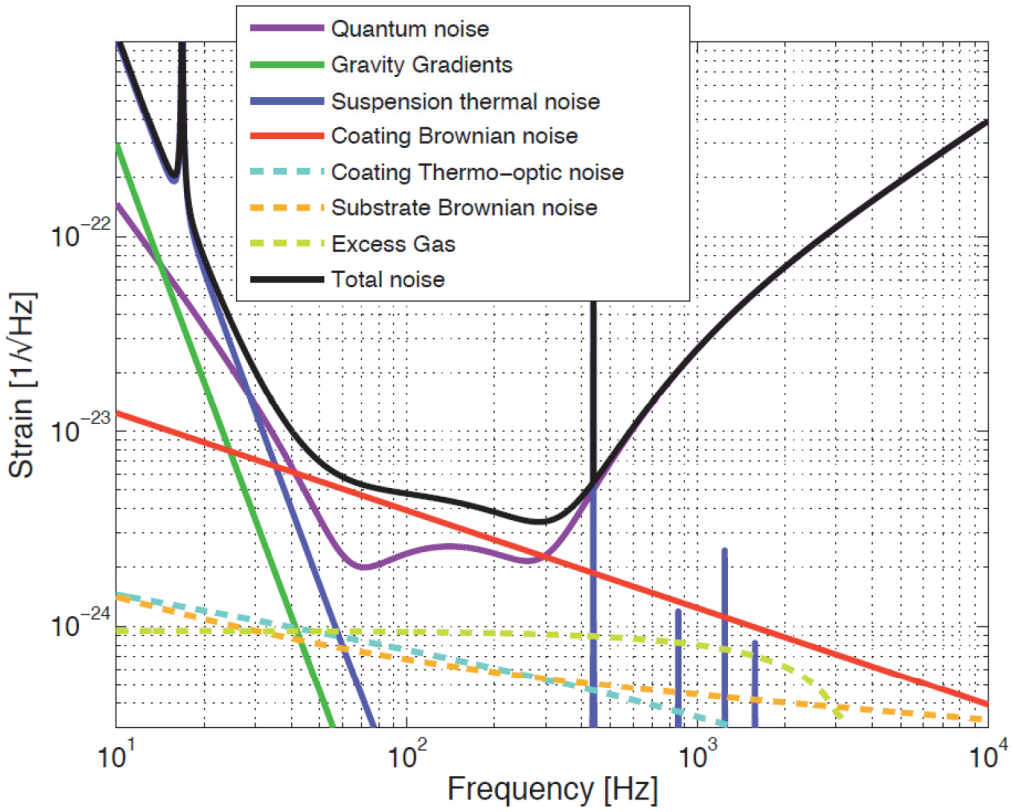

Figure 1.7 Advanced Virgo design sensitivity curve [26]. Each noise source is represented by a color curve giving its spectral density in equivalent gravitational wave amplitude (strain h). Any event producing a signal below the black curve (total noise) will not be detected. Between 40 Hz and 300 Hz, where the detector is the most sensitive, the most limiting noise source is the coating brownian noise.

fluctuations of the interferometer mirrors' surfaces under thermal agitation. Its power spectrum density can be computed with the following relation [52]:

$$S_{\mathrm{CTN}} \propto \frac{k_{\mathrm{B}} T t_{\mathrm{c}}}{w^2 f} \frac{1-\sigma^2}{Y} \phi \tag{1.1}$$

where w is the laser beam size on the mirror, k_{B} the Boltzmann constant,t_{c} the total coating thickness, σ its Poisson ratio, Y its Young's modulus, T its temperature, and where ϕ the loss angle (or loss tangent) of the coating material.

The loss angle ϕ of a material is an intensive quantity quantifying the internal friction within this material, thus translating its tendency to dissipate mechanical energy. This dissipation is related to the mirror fluctuations via the fluctuation dissipation theorem [18]. A higher value of ϕ implies a higher mechanical dissipation within the coating and a larger amount of coating thermal noise. Table 1.1 also lists the loss angles of the material used to make a mirror: even if the coating represents only a very small portion of the mirror, the loss angles of the coating materials are several order of magnitude larger than the substrates one, so that the coating Brownian noise largely

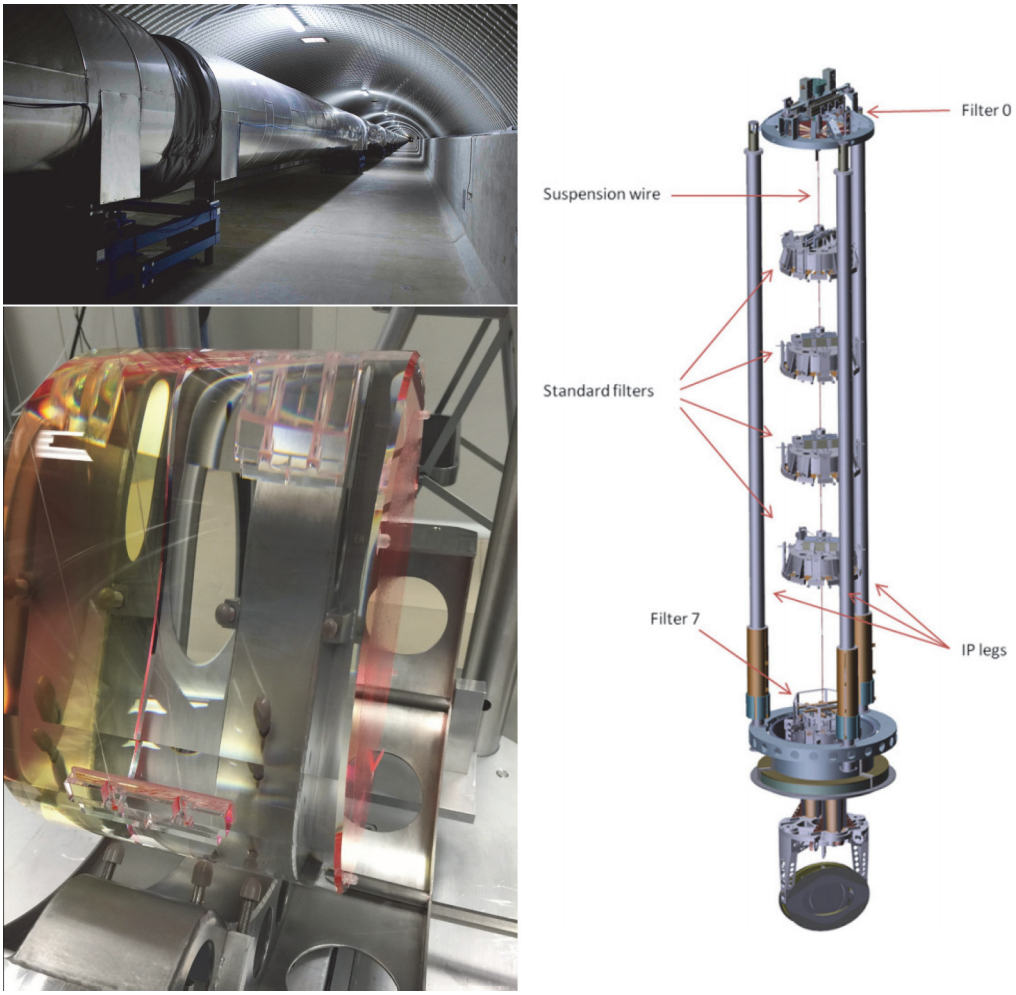

Figure 1.8 Illustration of Advanced VIRGO construction [27]. On the top left: vacuum tube of one of the interferometer arms. Bottom left: suspension of a mirror. Notice the two very thin glass wires suspensions attached to the mirror side. They are employed to reduce the suspension thermal noise. Right: the superattenuator is a multistage mechanical filter intended for an agressive attenuation of the ground vibration.

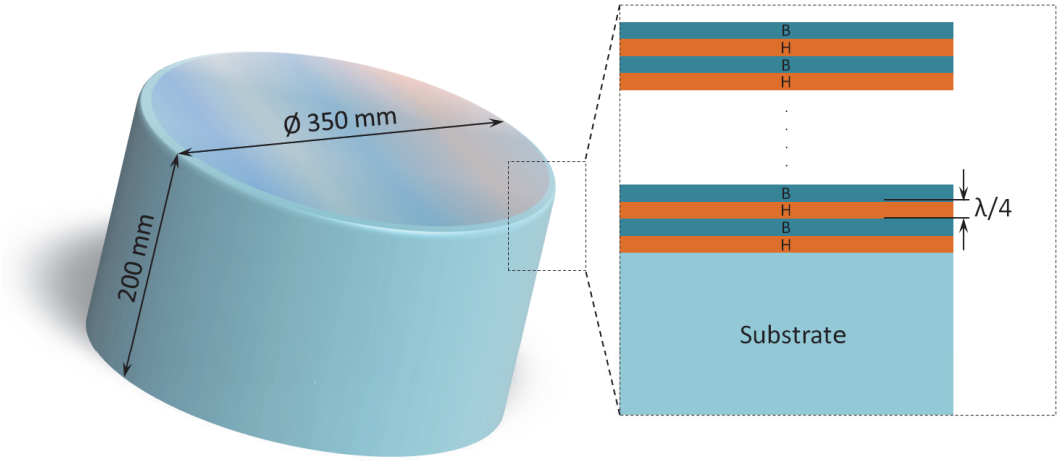

Figure 1.9 Schematic of an Advanced Virgo end test-mass (ETM) mirror. The reflectivity of the glass substrate is increased to almost 100 % by the deposition of a multilayer Bragg optical interference coating. The coating is grown as an alternating stack of thin films made from two transparent materials having a low (B) and a high (H) refractive index. The optical thickness of each film is adjusted to roughly[1] a quarter of the interferometer laser wavelength of 1064 nm, so that the many reflections occuring at each interface interfer constructively.

dominates the substrate brownian noise[2] in figure 1.7. This observation generalizes to all the gravitational wave interferometers.

Accordingly, a intense research effort have been devoted in the past years to find and optimize coating materials showing both good optical and mechanical properties for gravitational wave detector mirrors. Due to its relatively higher loss angle, this effort have been focused on the tantala Ta_2O_5 and has led to the developpement of the titanium doping of this material ($Ti:Ta_2O_5$,[38]).

As seen from equation 1.1, another possibility is to reduce the mirrors' temperature. In this direction, the KAGRA interferometer is the first project to employ test-masses cooled down to 20 K, and the use of cryocooled mirror is also considered in future gravitational wave detectors project like the Einstein telescope [99]. This demands a detailed knowledge of the mirror's coating material properties in this temperature range. In particular, a degradation of the coating loss angle may counteract the improvement obtained by lowering temperature.

To further increase the sensitivity of gravitational wave detectors and observe an even larger part of the Universe, a better understanding of the dissipation in amorphous optical thin films is needed both at room and cryogenic temperature, which in turn requires new experimental tools.

[1] The high reflectivity coating on these mirrors is actually not a standard Bragg stack, but was rather optimized to obtain a relatively smaller ratio of $Ti:Ta_2O_5$ [119].

[2] Considering the large difference in thickness between a mirror's coating and substrate, this result may seem counterintuitive: see [52] for more details.

Table 1.1 Properties of an aVirgo ETM measured at the interferometer working wavelength of 1064 nm [48].

	substrate	coating H, n=2.065	coating B, n=1.449
material	suprasil 312	Ti:Ta_2O_5	SiO_2
loss angle	1×10^{-8}	2.4×10^{-4}	2.3×10^{-5}

Fabry-Perot cavity		coating	
∅ beam	58 mm	# layers	38
transmission	1 ppm	thickness	5.9 μm
finesse	443	absorption	0.2 ppm
losses	<75 ppm	diffusion	4 ppm
		roughness RMS	0.1 nm
mirror		planarity RMS	0.5 nm
mass	40 kg	loss angle	2.3×10^{-4}

1.4 The thesis

The work done during this PhD thesis took place within a collaboration between the *Laboratoire des Matériaux Avancés* (LMA) and the *Laboratoire de Physique de l'Ecole Normale Supérieure de Lyon* (LPENSL), both located in lyon, France. The LMA is responsible for the coating and characterization of all the gravitational wave interferometers' large optics. The loss angles measurements at LMA and in other laboratories engaged in the research for low mechanical loss material are mainly based on the ringdown measurement method, the most notable being GeNS [22]. Another noteworthy measurement method is well represented by the MIT CTN [49], where the thermal noise of a macroscopic mirror is measured using a high finess optical cavity. In contrast, in a previous conjoint work between the LMA and the LPENSL [68], it was demonstrated that the Brownian motion of an IBS coated μcantilever can be measured directly and used to assess the coating loss angle with a relative convenience and without a strong constrain on the sample reflectivity. These direct thermal noise measurement where performed using the high resolution quadrature phase differential interferometer (QPDI) developped by Bellon and coworkers [13].

The main object of this thesis is the construction of a new instrument, the CryoQPDI. CryoQPDI stand for "Quadrature Phase Differential Interferometry on Cryocooled microresonators". The instrument consists in the association of a pulse tube[1] based cryostat and of an interferometer based on the QPDI concept. It can directly measure the Brownian motion of a microcantilever between 300 K and 7 K. By combining measurements made on a microcantilever before and after the deposition of a thin film, it is possible to characterize the internal mechanical dissipation of this coating. This instrument is intented to eventually contribute to the optimisation of optical

[1] A pulse tube is a kind of cryo refrigerator. Additional information is available in chapter 4 , including references.

coatings of future gravitational wave detectors, aiming at minimizing the limitations due to thermal noise.

1.5 Thesis outline

- **Chapter 2** provides a general description of the quadrature phase differential interferometer. A calculation of the interferometer ideal response is first performed using the Jones calculus. The non ideal response of a real interferometer is then taken into account via the Heydemann correction. Details are provided on the realization of this correction procedure.
- **Chapter 3** introduces the theoretical tools used to interpret the interferometer signal. The dynamic of vibration of a μcantilever is first described by the Euler-Bernouilli model. The equipartition theorem is then invoked to link the magnitude of the μcantilever brownian motion to its rigidity. Lastly, the Fluctuation Dissipation Theorem is employed to predict the repartition of the μcantilever thermal noise in frequency based on a dissipation model.
- **Chapter 4** gives an overview of the system and discuss the basics of the instrument operation. This operation is based on a strategy to avoid an excessive distortion of the interferometer signal by external vibration.
- **Chapter 5** describes the optical design of the interferometer. The complete optical scheme of the interferometer is provided. This design was conducted with two main goals: improve on the existing level of sensitivity achieved with quadrature interferometry and adress the problematics of interfacing an interferometer with a cryostat. Accordingly, this chapter is mainly focused on the design of two opticals assemblies: the scanning objective which is used to position the laser spot on the sample and provides a long working distance, and the Semel-Savart plate which is the interferometer beam splitter and provides a significant improvement in contrast. Some detail on the intrument imaging system and on the design of the cryogenic sample holder are also provided.
- **Chapter 6** is concerned with the design of the CryoQPDI signal chain. After a theoretical description of the photodiode transimpedance amplifier principle, a design strategy is devised to obtain a low electronic noise with such an amplifier. This strategy and circuit simulation are used to construct the interferometer's photodetectors. The selection of a data acquisition card is exposed based on an account of the analog to digital converters quantization noise. The signal chain noise level is tested, and an excess of high frequency noise issue is discussed. A comparison is made between the CryoQPDI signal chain noise and the electronic noise of the reference QPDI system.

- **Chapter 7** is dedicated to the coating of μcantilevers via ion beam sputtering. After a review of the IBS deposition method, the problematic of the cantilever deformation under the coating internal stress is discussed. The design of a system intended to answer this problematics is then presented.
- **Chapter 8** presents the results of a cryogenic measurement performed on a tantala coated μcantilever. This results are a proof of concept for the CryoQPDI.
- At last, **chapter 9** is the general conclusion of the thesis.

2 Quadrature Phase Differential Interferometry

In this chapter, a general description of the Quadrature Phase Differential Interferometer (QPDI) optical scheme and operating principle is provided.
The QPDI is a kind of homodyne laser interferometer optimized for the measurement of a µcantilever deflection with very high resolution (down to ~1 fm/$\sqrt{\text{Hz}}$) and low environmental susceptibility [93]. This setup is based on differential interferometry [104] (figure 2.1): two parallel beams are focused on the cantilever, the first being reflected on the cantilever base ($\boldsymbol{E}_{\text{ref}}$) , the second at its free end ($\boldsymbol{E}_{\text{prob}}$). The optical path difference between those two beams is then directly proportional to the deflection of the cantilever, and the corresponding phase shift can be precisely calibrated to the laser wavelength. The two beams are produced by a birefringent beam splitter, latter called "birefringent element" BE (figure 2.1) in this chapter, namely a beam splitter exploiting the double refraction phenomenon occuring inside a birefringent material. Using a birefringent beam splitter allows for a small spatial separation between the two beams, compatible with the short lengths of µcantilevers. As the beams are also produced with orthogonal polarizations, analysis of their interferences is performed with a four detectors quadrature detection scheme for a complete determination of the cantilever's deflection [13].
The chapter is organized as follow: the Jones calculus is briefly introduced, before being used to describe the transformation occuring to the laser beam on its path inside an ideal Quadrature Phase Differential Interferometer. The mathematical relation between the deformation of the cantilever and the signals measured by the QPDI's four photodetectors is thus established in the ideal case. The processing of these signals is then described, along with a correction method accounting for the imperfections of a real interferometer. The advantages provided by the QPDI scheme are discussed throughout the chapter, and are then summarized in the conclusion.

2.1 Operating principle

2.1.1 Jones calculus

The Jones calculus [44] is a matrix formalism that allows for a compact mathematical treatement of polarized light and its transformations by polarizing optical components.

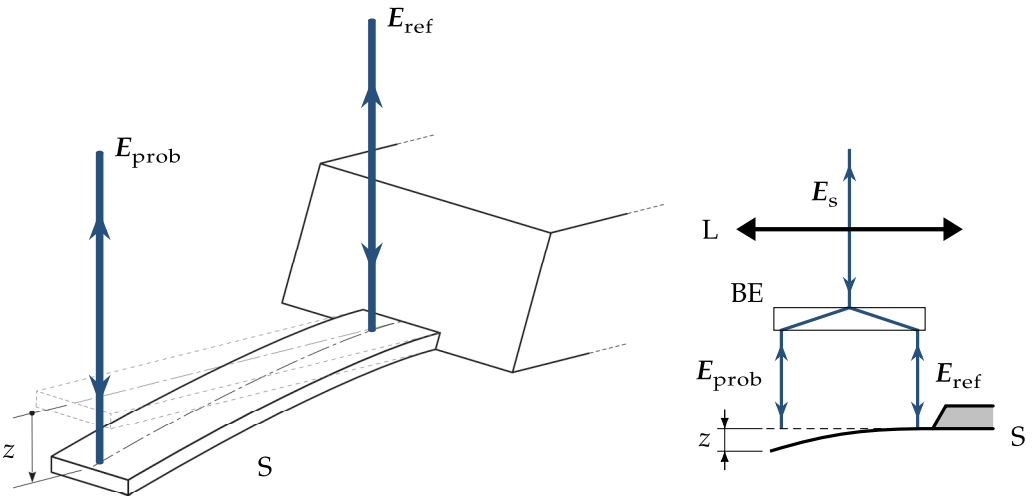

Figure 2.1 Differential interferometry principle. On the left: two parallel laser beams are focused on the μcantilever sample S. The reference one is reflected by the static base (electric field E_{ref}) and the sensing one by the free end of the cantilever (E_{prob}). A deflection z of the cantilever increases the optical path difference by $\delta L = 2z$, and this information is accessed through the interferences between the two beams. E_{ref} and E_{prob} are equivalents to the two arms of a conventional Michelson interferometer. On the right: the two beams are produced by a birefringent element BE. The birefringent element allows for a spatial separation of only a few hundred microns between the beams, compatible with the length of typical μcantilevers. The input laser beam E_s is also focused by a lens L. After separation, the two converging beams thus produce two spots which are made much smaller than the cantilever width.

It is well suited for problems involving both polarization and interference phenomena, where superposition of the light electric field must be considered, as long as the light under consideration can be assumed monochromatic, coherent and completely polarized. It is therefore appropriate for the description of a polarization interferometer employing a single mode laser source, like the QPDI.

A light beam propagating along the z direction is represented by the electric field component $\boldsymbol{E}$ of a plane and uniform electromagnetic wave, given by

$$\boldsymbol{E} = \boldsymbol{E}_x \boldsymbol{x} + \boldsymbol{E}_y \boldsymbol{y} \tag{2.1}$$

with

$$\begin{aligned} \boldsymbol{E}_x &= E_{0x} \cos(\omega t - kz + \delta_x) \\ \boldsymbol{E}_y &= E_{0y} \cos(\omega t - kz + \delta_y) \end{aligned} \tag{2.2}$$

where $\boldsymbol{E}_x$ and $\boldsymbol{E}_y$ are the field components along $\boldsymbol{x}$ and $\boldsymbol{y}$, E_{0x} and E_{0y} are the field amplitudes, k is the light wavenumber, ω the light angular frequency, and where δ_x and δ_y are the phases. The electric field $\boldsymbol{E}$ can be seen as the real part of a complex wave:

$$\boldsymbol{E} = \Re\left\{\boldsymbol{E}_0 \mathrm{e}^{i(\omega t - kz)}\right\} \tag{2.3}$$

where $\Re\{\ \}$ denotes the real part, and where $\boldsymbol{E}_0$, the Jones vector associated with $\boldsymbol{E}$, is given by

$$\boldsymbol{E}_0 = \begin{pmatrix} E_x \\ E_y \end{pmatrix} = \begin{pmatrix} E_{0x} e^{i\delta_x} \\ E_{0y} e^{i\delta_y} \end{pmatrix} \equiv \begin{pmatrix} E_{0x} \\ E_{0y} e^{i(\delta_y - \delta_x)} \end{pmatrix} \tag{2.4}$$

Notice that with the phase convention used here, a decrease in phase indicates retardation. In particular, $\delta_y - \delta_x < 0$ means that E_y is retarded relative to E_x.
Up to a multiplicative factor, the beam intensity[1] I of the beam $\boldsymbol{E}$ is given by:

$$I = \left(\boldsymbol{E}^\dagger \cdot \boldsymbol{E}\right) = \left(E_x {E_x}^* + E_y {E_y}^*\right) \tag{2.5}$$

where $\cdot$, $(\ )^*$ and $(\ )^\dagger$ indicate scalar product, complex conjugation and complex transposition respectively.
The Jones vector $\boldsymbol{E}_0$ represents the amplitude and phase of the electric field $\boldsymbol{E}$, and therefore contains all the information about the state of polarization of the associated light beam. From equation 2.5, it can be seen that knowledge of the Jones vectors is also sufficient for intensity calculations.
The change of polarization occuring to a beam passing through a linear optical element is represented by the following matrix operation:

$$\boldsymbol{E}_1 = \boldsymbol{J}\boldsymbol{E}_0 \tag{2.6}$$

where $\boldsymbol{E}_0$ is the state of the input beam, $\boldsymbol{E}_1$ the state of the output beam, and where $\boldsymbol{J}$ is the Jones matrix of the optical element considered. $\boldsymbol{J}$ is a 2×2 matrix as:

$$\boldsymbol{J} = \begin{pmatrix} J_{xx} & J_{xy} \\ J_{yx} & J_{yy} \end{pmatrix} \tag{2.7}$$

where the matrix elements J_{ij} are generally complex, and depend only of the optical component considered.
The optical scheme of the QPDI is given in the diagram of figure 2.2. The diagram is divided in three areas: in the input area, the polarization state of the laser beam entering the interferometer is appropriatly tuned, and the beam is directed to the sensing area where the cantilever deflection is detected. The beam then propagates to the analysis area where the interferometer signals are recorded.
The Jones matrix of a given component depend both on its nature and on its angular orientation relative to the beam axis of propagation. In the Jones formalism, the coordinate system used to locate this orientation "follows" a light beam along its optical path. In figure 2.2, the Jones coordinate system is drawn for the laser beam entering the interferometer (on the right of the input area). The z axis is always oriented along the beam direction of propagation, while the x axis always points out of the page (in the vertical direction), so only the y and z axis are reoriented with

[1] Here the term "intensity" is synonymous to"irradiance"

Table 2.1 Jones matrices of the ideal optical components of interest for the QPDI.

Optical component	Symbol	Jones matrix
vertical linear polarizer	$\boldsymbol{P}_x$	$\begin{pmatrix} 1 & 0 \\ 0 & 0 \end{pmatrix}$
horizontal linear polarizer	$\boldsymbol{P}_y$	$\begin{pmatrix} 0 & 0 \\ 0 & 1 \end{pmatrix}$
linear polarizer at 45°	$\boldsymbol{P}_{x+y}$	$\frac{1}{2}\begin{pmatrix} 1 & 1 \\ 1 & 1 \end{pmatrix}$
linear polarizer at -45°	$\boldsymbol{P}_{x-y}$	$\frac{1}{2}\begin{pmatrix} 1 & -1 \\ -1 & 1 \end{pmatrix}$
quarter wave plate, fast axis at 45°	$\boldsymbol{W}^q_{x+y}$	$\frac{1}{2}\begin{pmatrix} 1-i & 1+i \\ 1+i & 1-i \end{pmatrix}$
mirror	$\boldsymbol{M}$	$\begin{pmatrix} 1 & 0 \\ 0 & -1 \end{pmatrix}$

changes of the beam path. The Jones matrices relevant for the forthcoming analysis are listed in table 2.1.

2.1.2 Interferometer: input area

The collimated laser beam entering the interferometer is linearly polarized by a polarizer $\mathrm{P_{lin}}$, and its polarization is oriented along the $\boldsymbol{x}$ direction by a half wave plate $\frac{\lambda}{2}$, producing the input beam $\boldsymbol{E}_{\mathrm{in}}$. The incoming light is then partly reflected toward the interferometer sensing area by a nonpolarizing beam splitter $\mathrm{BS_s}$, resulting in the beam $\boldsymbol{E}_{\mathrm{s}}$.

The input beam is given by:

$$\boldsymbol{E}_{in} = E_{in}\begin{pmatrix} 1 \\ 0 \end{pmatrix} \tag{2.8}$$

and the beam entering the sensing area is given by

$$\boldsymbol{E}_{s} = E_{s}\begin{pmatrix} 1 \\ 0 \end{pmatrix} \tag{2.9}$$

E_s and E_{in} are related by

$$E_s = rE_{in} \tag{2.10}$$

where r is the reflection coefficient of $\mathrm{BS_s}$ $(0 < r < 1)$.

2.1.3 Interferometer: sensing area

The beam $\boldsymbol{E}_{\mathrm{s}}$ is focused by a lens L and split in two parallel beams with orthogonal polarizations $\boldsymbol{E}_{\mathrm{ref}}$ and $\boldsymbol{E}_{\mathrm{prob}}$ by a birefringent element BE. The two beams are reflected

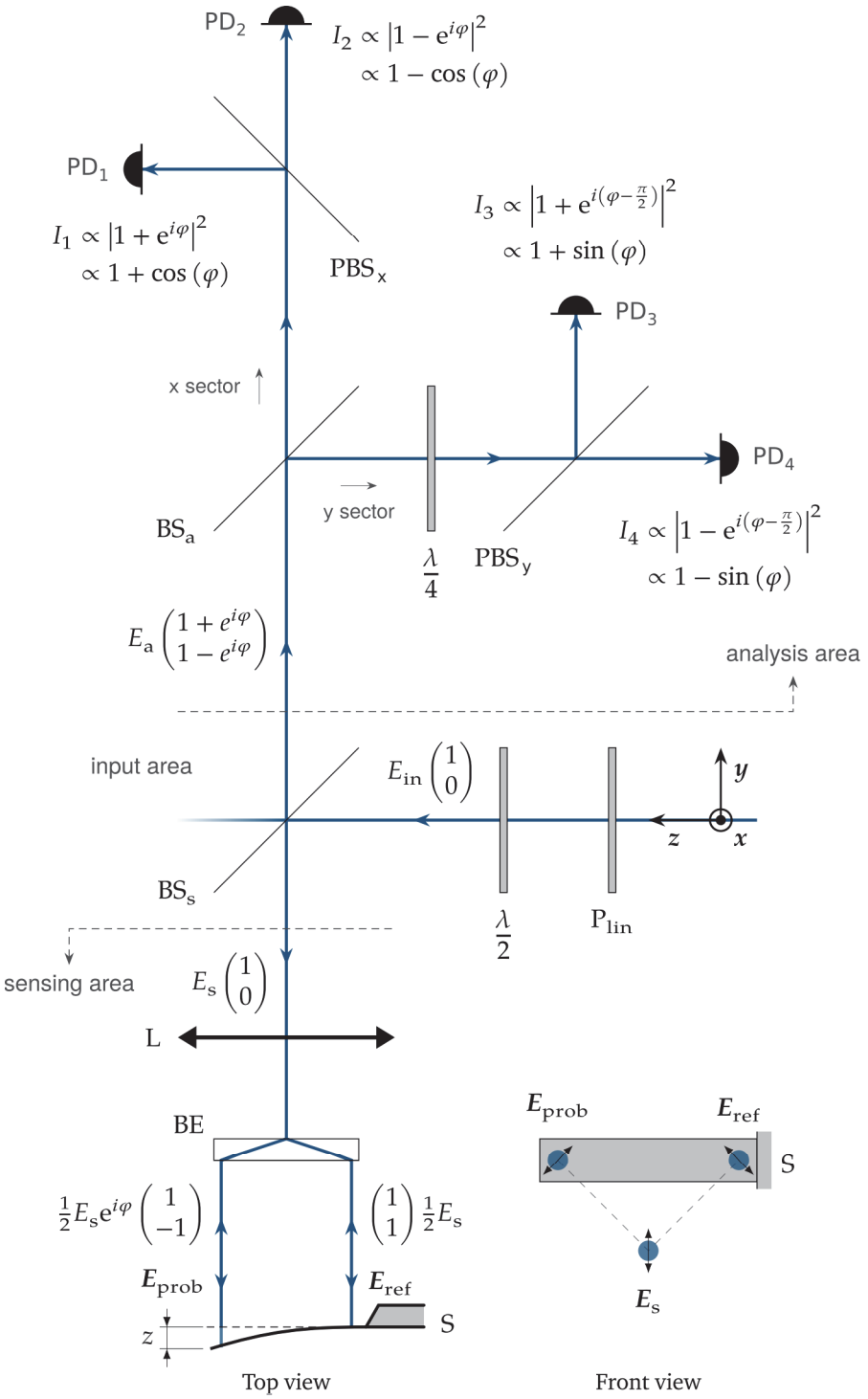

Figure 2.2 General diagram of an ideal Quadrature Phase Differential Interferometer (QPDI).The interferometer input port is in the middle right.

Symbol	Description	Symbol	Description
E_{in}	input beam	P_{lin}	linear polarizer
E_s	beam entering the sensing aera	$\lambda/2$	half wave plate
E_a	beam entering the analysis aera	$\lambda/4$	quarter wave plate
E_{ref}, E_{prob}	sensing beams (Michelson arms)	BE	birefringent element
L	lens (objective)	S	μcantilever sample
BS_s, BS_a	50:50 non-polarizing beam splitter	$PD_{1\to4}$	photodetectors
PBS_x, PBS_y	polarizing beam splitter	$I_{1\to4}$	quadrature signals

by the base and the free end of the μcantilever S, and upon reflection, $\boldsymbol{E}_{\mathrm{prob}}$ acquires an additional optical path difference δL proportional to the cantilever deflection z. After reflection, the two beams are merged back together by BE, and the merged beam is collimated by L before to reach the QPDI analysis area, after being partly transmitted by $\mathrm{BS_s}$.

The birefringent element BE is modeled as a polarizing beam splitter whose axes are oriented along $\boldsymbol{x}+\boldsymbol{y}$ and $\boldsymbol{x}-\boldsymbol{y}$, so that the polarization state in each arm just after BE is given by:

$$\begin{aligned} \boldsymbol{E}^i_{ref} &= \boldsymbol{P}_{x-y}\boldsymbol{E}_s = \frac{1}{2}E_s\begin{pmatrix}1\\-1\end{pmatrix} \\ \boldsymbol{E}^i_{prob} &= \boldsymbol{P}_{x+y}\boldsymbol{E}_s = \frac{1}{2}E_s\begin{pmatrix}1\\1\end{pmatrix} \end{aligned} \tag{2.11}$$

At the bottom right corner of figure 2.2 (front view), the double arrows represent the direction of polarization of each beam.
The optical path difference δL is twice the deflection z of the cantilever:

$$\delta L = 2z \tag{2.12}$$

The corresponding phase shift φ between the two beams is

$$\varphi = \frac{4\pi}{\lambda}z \tag{2.13}$$

After being reflected by the μcantilever, the beams thus become:

$$\begin{aligned} \boldsymbol{E}^r_{ref} &= \boldsymbol{M}\times\boldsymbol{E}^i_{ref} = \frac{1}{2}E_s\begin{pmatrix}1\\1\end{pmatrix} \\ \boldsymbol{E}^r_{prob} &= \boldsymbol{M}\times\boldsymbol{E}^r_{prob}\,\mathrm{e}^{i\varphi} = \frac{1}{2}E_s\mathrm{e}^{i\varphi}\begin{pmatrix}1\\-1\end{pmatrix} \end{aligned} \tag{2.14}$$

up to the Fresnel reflection coefficient of the μcantilever at normal incidence. The polarization state of the recombined beam is obtained by superimposing the fields of the two arms:

$$\boldsymbol{E}^r_{ref} + \boldsymbol{E}^r_{prob} = E_s\begin{pmatrix}1+\mathrm{e}^{i\varphi}\\1-\mathrm{e}^{i\varphi}\end{pmatrix} \tag{2.15}$$

After crossing $\mathrm{BS_s}$, the beam entering the analysis area is therefore given by:

$$\boldsymbol{E}_{\mathrm{a}} = E_{\mathrm{a}}\begin{pmatrix}1+\mathrm{e}^{i\varphi}\\1-\mathrm{e}^{i\varphi}\end{pmatrix} \tag{2.16}$$

E_{a} and E_{s} are related by

$$E_{\mathrm{a}} = tE_{\mathrm{s}} \tag{2.17}$$

where t is the transmission coefficient of BS_s ($0 < t < 1$).
At this point, it can be noted that as E_a results from the superposition of two beams having orthogonal polarizations, no interference can be recorded directly from it. The intensity I_a of E_a is found by an application of equation 2.5:

$$I_a = 2E_a^2 \tag{2.18}$$

which shows no dependance on φ. Here the phase shift caused by the cantilever deflection is encoded in the state of polarization of E_a, which is generally elliptical. To record interference, the beam E_a must be projected by at least a linear polarizer.

2.1.4 Interferometer: analysis area

The analysis area implements the quadrature phase detection technique mentioned before [13]. The purpose of this technique is to make four quadrature intensity signals available simultaneously, that is four intensity signals with an incremental phase shift of $\frac{\pi}{2}$. The advantages provided by this set of four signals will become clear in the next section.
The beam coming to the measurement area is split evenly in two sectors x and y by a nonpolarizing beam splitter BS_a. In each sector, the two polarization components of the beam are set to interfere after being projected by the polarizing beams splitters PBS_x and PBS_y, whose axes are oriented along the $\boldsymbol{x}$ and $\boldsymbol{y}$ directions. In the y sector, a quarter wave plate $\frac{\lambda}{4}$ oriented along $(\boldsymbol{x} + \boldsymbol{y})$ is used to add an additional delay of $\pi/2$ between the polarization components[1]. Eventually, the four quadrature signals I_1, I_2, I_3 and I_4 are recorded using four photodiodes based photodetectors PD_1 to PD_4.

The non-polarizing beam splitter BS_a contributes a factor of $\frac{1}{\sqrt{2}}$ to both the reflected and transmitted beams, corresponding to half the intensity of the $\boldsymbol{E}_a$ beam. The two fields produced in the x sector are then:

$$\begin{aligned} \boldsymbol{E}_1 &= \frac{1}{\sqrt{2}}\boldsymbol{P}_x \times \boldsymbol{E}_a = \frac{1}{\sqrt{2}}E_a \begin{pmatrix} 1 + e^{i\varphi} \\ 0 \end{pmatrix} \\ \boldsymbol{E}_2 &= \frac{1}{\sqrt{2}}\boldsymbol{P}_y \times \boldsymbol{E}_a = \frac{1}{\sqrt{2}}E_a \begin{pmatrix} 0 \\ 1 - e^{i\varphi} \end{pmatrix} \end{aligned} \tag{2.19}$$

[1] This is formally equivalent to adding a delay of $\pi/2$ to $\boldsymbol{E}_{ref}$, or a delay of $-\pi/2$ (phase lead) to $\boldsymbol{E}_{prob}$

and the two fields generated in the y sector computes as:

$$\begin{aligned} \boldsymbol{E}_3 &= \frac{1}{\sqrt{2}}\boldsymbol{P}_x \times \boldsymbol{W}^q_{x+y} \times \boldsymbol{E}_\mathrm{a} = \frac{1}{\sqrt{2}}E_\mathrm{a}\begin{pmatrix} 1+\mathrm{e}^{i\left(\varphi-\frac{\pi}{2}\right)} \\ 0 \end{pmatrix} \\ \boldsymbol{E}_4 &= \frac{1}{\sqrt{2}}\boldsymbol{P}_y \times \boldsymbol{W}^q_{x+y} \times \boldsymbol{E}_\mathrm{a} = \frac{1}{\sqrt{2}}E_\mathrm{a}\begin{pmatrix} 0 \\ 1-\mathrm{e}^{i\left(\varphi-\frac{\pi}{2}\right)} \end{pmatrix} \end{aligned} \tag{2.20}$$

By applying equation 2.5 to equations 2.19 and 2.20, the expression of the QPDI's four photodetectors signals are obtained as follow:

$$\begin{aligned} I_1 &= \frac{I_\mathrm{a}}{4}\left(1+\cos\left(\varphi\right)\right) & I_3 &= \frac{I_\mathrm{a}}{4}\left(1+\sin\left(\varphi\right)\right) \\ I_2 &= \frac{I_\mathrm{a}}{4}\left(1-\cos\left(\varphi\right)\right) & I_4 &= \frac{I_\mathrm{a}}{4}\left(1-\sin\left(\varphi\right)\right) \end{aligned} \tag{2.21}$$

From 2.21, the intensities I_1 to I_4 are found to form a set of four quadrature signals as defined before[1]. The crossed polarizations of the two interfering beam obtained by using a birefringent beam splitter allows for a direct implementation of this technique, since crossed polarizations is a key point of the processing made in the y sector (with the quarter wave plate).

2.2 Phase and deflection extraction, Heydemann correction

2.2.1 Ideal interferometer response

To retreive the phase φ, the contrast function of each sector is computed:

$$C_\mathrm{x} = \frac{I_1 - I_2}{I_1 + I_2} \qquad C_\mathrm{y} = \frac{I_3 - I_4}{I_3 + I_4} \tag{2.22}$$

In the ideal case (equation 2.21), the two constrast have the forms:

$$C_\mathrm{x} = \cos(\varphi) \qquad C_\mathrm{y} = \sin(\varphi) \tag{2.23}$$

From equation 2.23, it is convenient to define the following complex contrast:

$$C = C_\mathrm{x} + iC_\mathrm{y} = \cos\left(\varphi\right) + i\sin\left(\varphi\right) = \mathrm{e}^{i\varphi} \tag{2.24}$$

This formulation reveals one the advantages of the quadrature detection technique: it permits a complete determination of φ (modulo 2π). In a plot of C in the complex plane, a measurement will be located on the unit circle, with a polar angle equal to

[1] With an incremental phase shift of $\frac{\pi}{2}$ in the following order: $I_1 \rightarrow I_3 \rightarrow I_2 \rightarrow I_4$

the optical phase shift φ. In the context of a µcantilever thermal noise measurement, the observed phase can be separated into two parts:

$$\varphi = \varphi^w + \delta\varphi \tag{2.25}$$

Here φ^w represents a static or maybe slowly varying phase shift, corresponding to an intrinsic optical path difference between the two arms of the interferometer. It corresponds to the interferometer workpoint. $\delta\varphi$ represents small variations of the cantilever deflection around the workpoint coming from thermal agitation. Importantly, the system's sensitivity to $\delta\varphi$ does not depends on the value of φ^w:

$$\left|\frac{\partial C}{\partial z}\right| = \frac{4\pi}{\lambda} \tag{2.26}$$

As a consequence, no tuning of the workpoint must be done to maximize the interferometer's sensitivity, and the measurements are not affected by drifts of the workpoint due to environmental changes (e.g. temperature variation).

2.2.2 Real interferometer response: Heydemann correction

In an experimental realisation of the QPDI, the quadrature signals are affected by a set of unavoidable errors, related for example to residual misalignements of the system and the imperfection of real optical components. These errors can be accounted for by rewriting equations 2.21 as follow:

$$\begin{aligned} I_1 &= k\left(A_1 + B_1\cos\left(\varphi\right)\right) & I_3 &= k\left(A_3 + B_3\sin\left(\varphi+\psi\right)\right) \\ I_2 &= k\left(A_2 - B_2\cos\left(\varphi\right)\right) & I_4 &= k\left(A_4 - B_4\sin\left(\varphi+\psi\right)\right) \end{aligned} \tag{2.27}$$

where A_i is the signal mean value on the photodetector i, B_i is the signal modulation amplitude, $B_i \leqslant A_i$, ψ represents a deviation from perfect quadrature between sector x and sector y, and k is a common factor modeling the laser intensity fluctuations. For the contrast functions to take the ideal values of equation 2.23, the signals should exhibit perfect local contrast ($A_i = B_i$), perfect modulation balance inside each sector ($B_1 = B_2$, $B_3 = B_4$), and no deviation from a perfect $\frac{\pi}{2}$ quadrature ($\psi = 0$), which is not achievable in practice. The errors present in the quadrature signals are thus translated to a distortion of the interferometer response, that must be corrected to avoid an erroneous evaluation of the phase. By applying the contrast expressions of equation 2.23 to the nonideal signals of equation 2.27, one obtains:

$$\begin{aligned} C_\mathsf{x} &= \frac{A_1 - A_2 + (B_1 + B_2)\cos\left(\varphi\right)}{A_1 + A_2 + (B_1 - B_2)\cos\left(\varphi\right)} \\ C_\mathsf{y} &= \frac{A_3 - A_4 + (B_3 + B_4)\sin\left(\varphi+\psi\right)}{A_3 + A_4 + (B_3 - B_4)\sin\left(\varphi+\psi\right)} \end{aligned} \tag{2.28}$$

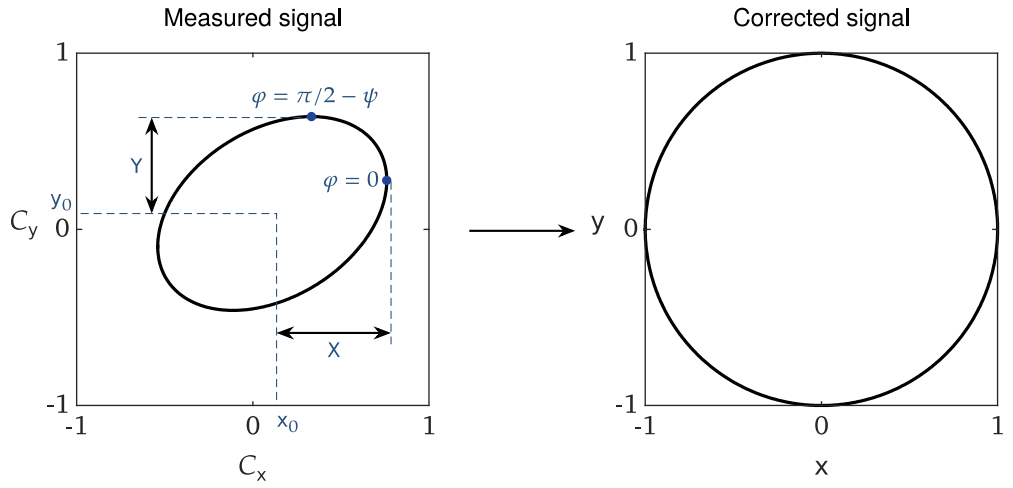

$$C_x + iC_y = \mathsf{X}\cos(\varphi) + \mathsf{x}_0 + i\,(\mathsf{Y}\sin(\varphi+\psi) + \mathsf{y}_0) \longrightarrow \mathsf{x} + i\mathsf{y} = \frac{C_x - \mathsf{x}_0}{\mathsf{X}} + i\frac{1}{\cos(\psi)}\left[\frac{C_y - \mathsf{y}_0}{\mathsf{Y}} - \frac{C_x - \mathsf{x}_0}{\mathsf{X}}\sin(\psi)\right]$$

Figure 2.3 Illustration of the contrast correction process expressed by equation 2.31 and 2.32 [92].

Remarkably, the laser noise factor k is factored out of the contrast expressions, meaning that the extracted phase φ is not affected by the laser intensity fluctuations.

In practice also, the modulation balance inside each sector holds to a good approximation. The distorded contrast functions can hence be modeled by:

$$\begin{aligned} C_x &= \mathsf{x}_0 + \mathsf{X}\cos(\varphi) \\ C_y &= \mathsf{y}_0 + \mathsf{Y}\sin(\varphi+\psi) \end{aligned} \tag{2.29}$$

with

$$\begin{aligned} \mathsf{x}_0 &= \frac{A_1 - A_2}{A_1 + A_2} \qquad \mathsf{X} = \frac{B_1 + B_2}{A_1 + A_2} = \frac{2B_1}{A_1 + A_2} \\ \mathsf{y}_0 &= \frac{A_3 - A_4}{A_3 + A_4} \qquad \mathsf{Y} = \frac{B_3 + B_4}{A_3 + A_4} = \frac{2B_3}{A_3 + A_4} \end{aligned} \tag{2.30}$$

x_0 and y_0 can be understood as the contrast offset in each sector, and X and Y as the contrast amplitudes, while ψ is still the quadrature mismatch introduced before. If these five parameters are known, equation 2.29 can be inverted to restore the interferometer response:

$$\begin{aligned} \mathsf{x} &= \cos(\varphi) = k_1 C_x + k_2 \\ \mathsf{y} &= \sin(\varphi) = k_3 C_x + k_4 C_y + k_5 \end{aligned} \tag{2.31}$$

with

$$k_1 = \frac{1}{\mathsf{X}} \qquad k_2 = -\frac{\mathsf{x}_0}{\mathsf{X}}$$
$$k_3 = -\frac{\tan(\psi)}{\mathsf{X}} \qquad k_4 = \frac{1}{\mathsf{Y}\cos(\psi)} \tag{2.32}$$
$$k_5 = \frac{\mathsf{x}_0 \tan(\psi)}{\mathsf{X}} - \frac{\mathsf{y}_0}{\mathsf{Y}\cos(\psi)}$$

One can then writes :

$$e^{i\varphi} = \cos(\varphi) + i\sin(\varphi) = \mathsf{x} + i\mathsf{y} \tag{2.33}$$

from which the optical phase φ is retrieved:

$$\varphi = \arg(\mathsf{x} + i\mathsf{y}) = \arctan\left(\frac{y}{x}\right) \tag{2.34}$$

The µcantilever displacement z can finally be computed using equation 2.13:

$$z = \frac{\lambda}{4\pi}\varphi \tag{2.35}$$

The contrast correction process expressed by equation 2.31 and 2.32 is a form of Heydemann correction [53]. It is illustrated in figure 2.3. The distorded contrast (equation 2.29) take the shape of an ellipse laying in the square tangent to the unit circle, as $-1 \leqslant C_\mathsf{x}, C_\mathsf{y} \leqslant 1$. The correction corresponds to a projection of this ellipse on the unit circle.

In practice, the QPDI Heydemann correction is implemented as an offline calibration procedure (figure 2.4):

- The cantilever is excited close to its first resonant frequency by a piezoelectric ceramic, with a deflection amplitude larger but close to half the laser wavelength. On a plot of the experimental contrast, the dataset then take the form of a closed ellipse, which is curve fitted with equation 2.31 to extract the 5 ellipse correction parameters.
- At this point, the system response is optimized by tuning the angular position of the interferometer's half wave and quarter wave plates. The contrast is thus settled closer to its ideal unit circle shape. By setting the interferometer input polarization, a rotation of the half wave plate affect the amplitude balance between $\boldsymbol{E}_{\text{ref}}$ and $\boldsymbol{E}_{\text{prob}}$, which translates into changes of the overall size of the contrast pattern. A rotation of the quarter wave plate directly impact the phase quadrature value between the x and y sectors, and in turn affects the contrast ellipticity.

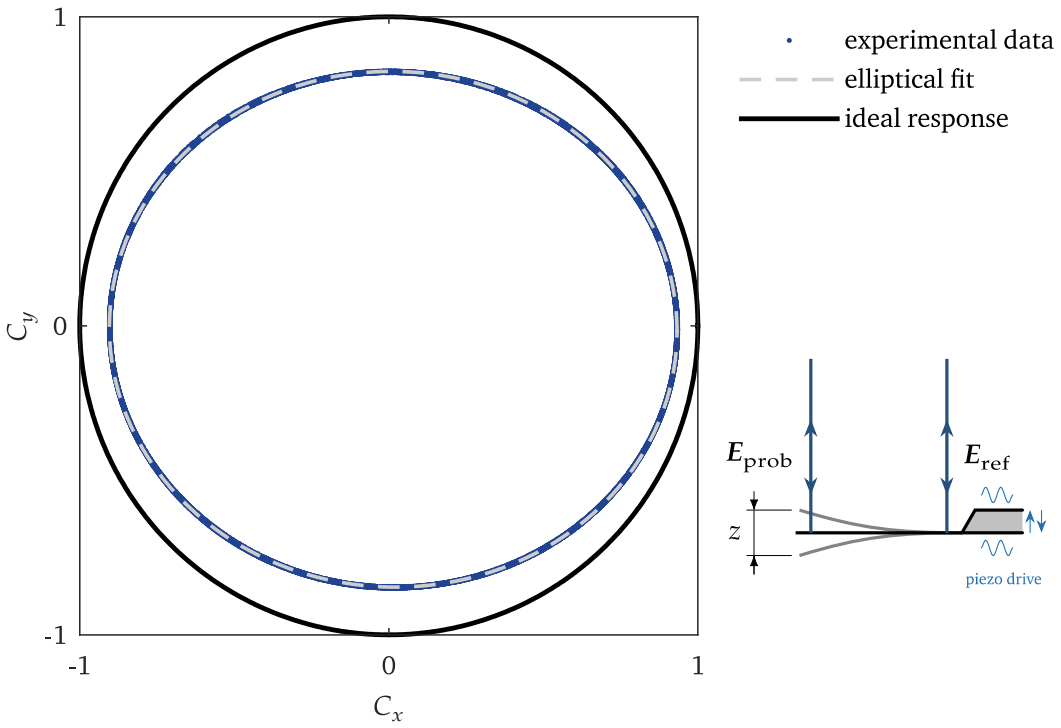

Figure 2.4 An exemple of Heydemann correction applied to the CryoQPDI signal. The thermal noise amplitude of a μcantilever is typically under $1\,\text{nm}$, and is too low to explore the full response range of the interferometer. The cantilever is therefore driven by a piezo element to a deflection amplitude slightly above half the laser wavelength, only during the calibration process. The contrast displayed here was obtained after optimizing the interferometer response, as explained in the main text. The final ellipse parameters were $x_0 = 0.014$, $y_0 = -0.011$, $X = 0.92$, $Y = 0.83$ and $\psi = -0.4°$.

- After this optimization, the piezo excitation is turned off, and the cantilever can ring down to its thermal noise level of deflection. The ellipse fit parameters are then used to correct the subsequent thermal noise measurements.

Both the contrast display and the ellipse curve fit can be made very quickly, making both the contrast pattern and the 5 fit parameters available to the operator in quasi real time. The overall calibration procedure is therefore straighforward and only takes a few minutes to perform.

2.3 Conclusion

In this chapter, a description of the Quadrature Phase Differential Interferometer (QPDI) operating principle was given. The Jones calculus was used to provide a mathematical description of the interferometer in the ideal case. The extraction of phase and deflection information was then presented both for an ideal and a real interferometer, the second case being treated with an Heydemann correction procedure. Following is a summary of the main points of the QPDI concept:

- Two beams are produced using the double refraction of a birefringent element, and are reflected by the base and the free end of the μcantilever. An analysis of the interferences between the two beams leads to a direct, differential sensing of the cantilever deflection.
- This analysis is performed using a quadrature phase detection technique. This technique allows for a complete determination of the optical phase, while not being affected by the laser intensity fluctuation, and with a constant sensibility.
- After a straighforward Heydemann calibration procedure, the optical phase can be precisely related to the cantilever deflection.

3 Thermal noise and dissipation of a microcantilever

In this chapter, the theoretical framework used to describe the mechanical thermal noise of a µcantilever is presented. This framework is based on three cornerstones. The µcantilever is first described as a clamped-free beam in the Euler-Bernoulli framework, leading to a description of its dynamics in terms of normal modes, each mode behaving as an independent harmonic oscillator. The equipartition theorem then establishes a relation between the magnitude of the cantilever thermal noise and its rigidity. Lastly, dissipation is accounted for by describing each mode of the cantilever as a damped harmonic oscillator, and the Fluctuation-Dissipation Theorem is employed to predict the power spectral density of the cantilever thermal noise.
For the most part, the content of this chapter come from references [14, 92, 5], where additional details are provided.

3.1 Free vibration of a microcantilever: the Euler Bernoulli model

To model the bending vibrations of a µcantilever, it is assimilated as a clamped free beam according to the Euler-bernoulli approach (figure 3.1). Its dynamic thus reduce to the transverse displacement $z(x,t)$ of its neutral axis, which is governed by the following differential equation:

$$EI\frac{\partial^4 z(x,t)}{\partial x^4} + \rho S\frac{\partial^2 z(x,t)}{\partial t^2} = F_{ext}(x,t) \tag{3.1}$$

Where ρ and E are the density and Young's modulus and of the cantilever material, S the area of its cross section, and $F_{ext}(x,t)$ the density of external forces applied to the cantilever. The area moment of inertia I of the cantilever is given by:

$$I = \frac{bh^3}{12} \tag{3.2}$$

for a rectangular cross section. Equation 3.1 is solved in absence of external driving ($F_{ext} = 0$) by applying the following separation of variable:

$$z(x,t) = \zeta(x)\,\tau(t) \tag{3.3}$$

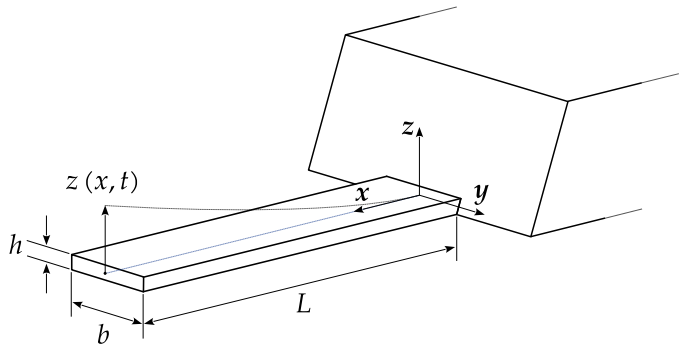

Figure 3.1 Schematics of an Euler-Bernoulli cantilever. The cantilever thickness h is supposed to be much smaller than its width b, itself much smaller than its length L, and the cantilever's deflection is assumed to be much smaller than its thickness. The cantilever bending dynamics is assimilated to the vertical deflection $z\,(x,t)$ of its neutral axis (in blue).

Inserting this relation in equation 3.1, one obtains a system of two differential equations:

$$-\frac{1}{\tau}\frac{\mathrm{d}^2\tau}{\mathrm{dt}^2} = \omega^2 \tag{3.4}$$

$$\frac{EI}{\rho S}\frac{1}{\zeta}\frac{\mathrm{d}^4\zeta}{\mathrm{d}x^4} = \omega^2 \tag{3.5}$$

with $\omega = 2\pi f$ standing for an angular frequency. By solving equations 3.4 and 3.5, it is found that the vibration of a cantilever can be decomposed onto the basis of its orthogonal eigenmodes, each mode being an independent harmonic oscillator:

$$z\,(x,t) = \sum_{n=1}^{\infty} z_n\,(x,t) = \sum_{n=1}^{\infty} \zeta_n\,(x)\,\tau_n\,(t) \tag{3.6}$$

where n is the mode number. The time components $\tau_n\,(t)$ are the solutions of the harmonic oscillator equation 3.4, and takes the following form:

$$\tau_n\,(t) = A_n \cos\left(\omega_n t + \theta_n\right) \tag{3.7}$$

where the amplitude and phase terms A_n and θ_n only depend on the initial conditions.

The spatial components $\zeta_n\,(x)$ correspond to the cantilever mode's shapes (figure 3.2), and are obtained by solving equation 3.5 in conjunction with the clamped-free boundary conditions for a cantilever:

$$\begin{aligned} \zeta\,(0) &= 0 & \frac{\mathrm{d}\zeta\,(0)}{\mathrm{d}x} &= 0 \\ \frac{\mathrm{d}^2\zeta\,(L)}{\mathrm{d}x^2} &= 0 & \frac{\mathrm{d}^3\zeta\,(L)}{\mathrm{d}^3x} &= 0 \end{aligned} \tag{3.8}$$

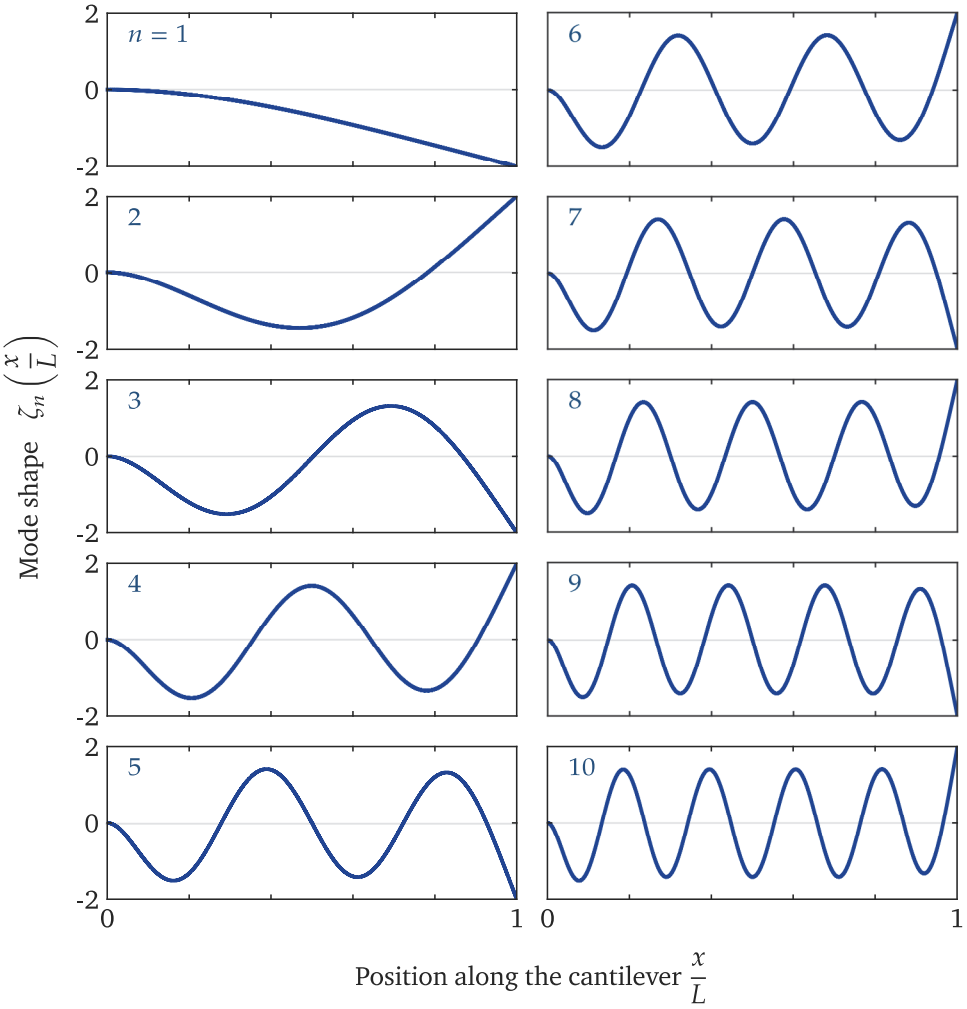

Figure 3.2 Mode shape $\zeta_n\left(\frac{x}{L}\right)$ of the first ten modes of a cantilever. The mode number n corresponds to the number of vibration nodes found along the cantilever

Table 3.1 Eigenvalues and frequency repartition for an Euler-Bernoulli cantilever.

Mode number n	Eigenvalue α_n	Frequency repartition $\left(\frac{\alpha_n}{\alpha_1}\right)^2$
1	1.8751	1
2	4.6941	6.2669
3	7.8548	17.547
4	10.996	34.386
5	14.137	56.843
6	17.279	84.913
7	20.420	118.60
8	23.562	157.90
9	26.704	202.81
10	29.845	253.33

They write as:

$$\zeta_n(x) = \left(\left[\cos\left(\alpha_n \frac{x}{L}\right) - \cosh\left(\alpha_n \frac{x}{L}\right) \right] - \frac{\cos(\alpha_n) + \cosh(\alpha_n)}{\sin(\alpha_n) + \sinh(\alpha_n)} \left[\sin\left(\alpha_n \frac{x}{L}\right) - \sinh\left(\alpha_n \frac{x}{L}\right) \right] \right) \tag{3.9}$$

Note that the mode's shapes ζ_n (equation 3.9) are defined up to a multiplicative constant. They are chosen here to provide an orthonormal basis of the functions fulfilling the boudary conditions 3.8:

$$\frac{1}{L} \int_0^L \zeta_n(x)\, \zeta_m(x)\, dx = \delta_{nm} \tag{3.10}$$

where δ_{nm} is the Kronecker delta. It can be noted in particular that $|\zeta_n(L)| = 2$.

The eigenvalues α_n obeys the relation:

$$1 + \cos(\alpha_n) \cosh(\alpha_n) = 0 \tag{3.11}$$

and can be obtained by numerical methods (table 3.1). For large n, they converge to:

$$\alpha_n \approx \left(n - \frac{1}{2}\right)\pi \tag{3.12}$$

which provides an approximation with an error of less than 0.1 % for $n \geqslant 3$.
The natural angular frequency ω_n of mode n computes as:

$$\omega_n = \frac{\alpha_n^2}{L^2} \sqrt{\frac{EI}{\rho S}} \tag{3.13}$$

with $\omega_n = 2\pi f_n$, and f_n the mode resonant frequency[1].

It is useful to compute the ratio between a reference resonant frequency f_r and the remaining resonant frequencies of the cantilever, to help identifying the modes in an experimental thermal noise spectrum[2]. From the previous expression, the modes frequency repartition is obtained as

$$\frac{w_n}{w_r} = \frac{f_n}{f_r} = \left(\frac{\alpha_n}{\alpha_r}\right)^2 \tag{3.14}$$

In practice, setting the first mode as the reference one ($r = 1$) is advantagous, because in addition to being the easiest to identify, it benefits from the highest spectral signal-to-noise ratio, as explained in the next section. Table 3.1 also provides the modes' frequency repartition relative to the first mode.

3.2 Application of the equipartition theorem to an Euler-Bernouilli microcantilever: thermal noise

In the following, the deflection of the cantilever is always considered at its free end, $z \Leftrightarrow z\,(x = L)$. The static deflection z of an Euler-Bernoulli cantilever subjected to a force F acting at its free end (along the z direction) follow Hooke's law, $F = -Kz$. The cantilever spring constant K is given by:

$$K = \frac{3EI}{L^3} \tag{3.15}$$

The equipartition theorem requires that in thermal equilibrium, the cantilever potential energy has a mean value of $\frac{1}{2}k_BT$, resulting in:

$$\frac{1}{2}K\left\langle z^2\right\rangle = \frac{1}{2}k_BT \tag{3.16}$$

With k_B the Boltzmann constant, T the cantilever temperature, $\left\langle z^2\right\rangle$ the cantilever total mean quadratic deflection due to thermal noise, and $\langle\ \rangle$ standing for average through time. Rearranging this relation yields

$$\left\langle z^2\right\rangle = \frac{k_BT}{K} \tag{3.17}$$

from which the magnitude of the cantilever's fluctuations in bending can be predicted.

[1] In this manuscript, the natural frequency f is used for the experimental data, and the angular frequency $\omega = 2\pi f$ for the theoretical formulas.

[2] In particular, to distinguish bending modes from torsion modes

In reference [16], Butt & Jaschke showed that a similar relation can be written for each bending mode of an Euler-Bernoulli cantilever:

$$\frac{1}{2}k_n \left\langle z_n^2 \right\rangle = \frac{1}{2}k_B T \tag{3.18}$$

$$\left\langle z_n^2 \right\rangle = \frac{k_B T}{k_n} \tag{3.19}$$

where k_n is the effective spring constant of the mode considered, and where $\left\langle z_n^2 \right\rangle$ is its contribution to the cantilever total thermal noise. The mode's effective spring constants and resonant frequencies are linked by :

$$k_n = m_{\text{eff}}\omega_n^2 \tag{3.20}$$

$$m_{\text{eff}} = \frac{m_C}{4} \tag{3.21}$$

Where m_{eff} is the effective mass for all modes, and $m_C = \rho SL$ is the mass of the cantilever. The spring contants K and k_n are related by

$$k_n = \frac{\alpha_n^4}{12}K \tag{3.22}$$

$$\sum_{n=1}^{\infty} \frac{1}{k_n} = \frac{1}{K} \tag{3.23}$$

Equations 3.19 and 3.22 permit to evaluate the contribution of mode n to the cantilever total thermal noise. Equation 3.23 ensure the sum of all these contributions lead to a total thermal noise in agreement with equation 3.16, namely:

$$\sum_{n=1}^{\infty} \left\langle z_n^2 \right\rangle = \left\langle z^2 \right\rangle \tag{3.24}$$

To assess how the total thermal fluctuation is distributed between the different modes of the cantilever, the ratio between the noise contribution of mode n and the total noise can be computed from equations 3.16, 3.19 and 3.22, giving

$$\frac{\left\langle z_n^2 \right\rangle}{\left\langle z^2 \right\rangle} = \frac{12}{\alpha_n^4} \tag{3.25}$$

from which it is found that the first mode contribute to $\approx 97.1\,\%$ of the cantilever mean quadratic deflection, the contribution of higher modes then converging rapidly to zero. Also, the first ten modes account together for $\approx 99.996\,\%$ of the total thermal noise.

3.3 Dissipation of a microcantilever : the Fluctuation Dissipation Theorem

3.3.1 Mechanical response function for a single oscillator

Simple Harmonic Oscillator To take into account the loss of mechanical energy occuring in a real cantilever, each of its modes is modeled as a damped harmonic oscillator. In the classic Simple Harmonic Oscillator (SHO) model, the dissipation is modeled by a viscous damping force proportional to the oscillator velocity. Such an oscillator submitted to thermal fluctuation responds to the following Langevin equation of motion:

$$m\ddot{z} + \gamma\dot{z} + kz = F_{th} \tag{3.26}$$

where m is the mass of the oscillator, γ is a constant friction coefficient, k is the oscillator spring constant, F_{th} is an external stochastic force representing the thermal fluctuations, and where the dotted notation for time derivatives has been used. Rewriting equation 3.26 in the Fourier space gives

$$-m\omega^2 z(\omega) + i\gamma\omega z(\omega) + kz(\omega) = F_{th}(\omega) \tag{3.27}$$

In general, one can define from this kind of equation a mechanical response function $G(\omega)$, as:

$$G(\omega) = \frac{F_{th}(\omega)}{z(\omega)} \tag{3.28}$$

For a SHO, the response function thus writes

$$G^{\mathrm{SHO}}(\omega) = k\left(1 - \frac{\omega^2}{\omega_0^2} + i\frac{\omega}{Q\omega_0}\right) \tag{3.29}$$

where the oscillator resonant angular frequency $\omega_0 = \sqrt{\frac{k}{m}}$ and quality factor $Q = \frac{m\omega_0}{\gamma}$ have been introduced, and where $\omega = 2\pi f$ is the angular frequency at the frequency f.
The SHO model is in good agreement with experiments for a µcantilever immersed in a viscous fluid, such as an AFM cantilever operated in air or water, where the damping coefficient γ represents the viscous drag of the fluid surrounding the cantilever.

Saulson Oscillator As pointed out by Saulson in [103], the SHO model is not adequate for an harmonic oscillator operated in high vacuum, where the viscous damping by the surrounding medium becomes negligible. The remaining "internal damping" can be modeled by an extension of Hooke's law, where the oscillator spring constant

acquire an imaginary part. The corresponding Langevin equation of motion for a Saulson Oscillator (SaO) in Fourier space is

$$-m\omega^2 z + k\left(1 + i\phi\right) z = F_{th} \tag{3.30}$$

where ϕ is the oscillator loss angle, $\phi \ll 1$, and where the dependance in ω have been dropped for simplicity. A complex spring constant is associated with dissipation because a part of the restoring force is out of phase with the displacement: the oscillator loses a fraction $2\pi\phi$ of its stored energy per cycle of vibration. In general, ϕ can be frequency dependant [103, 68]. In equation 3.30, ϕ is assumed to be a constant, where it then represents "structural damping" mechanisms originating from relaxation processes occuring in the cantilever material at the atomic scale.
The response function of a Saulson Oscillator is given by:

$$G^{\mathrm{SaO}}\left(\omega\right) = k\left(1 - \frac{\omega^2}{\omega_0^2} + i\phi\right) \tag{3.31}$$

3.3.2 Fluctuation Dissipation Theorem for a single oscillator

The Fluctuation Dissipation Theorem (FDT) [18, 17] is a generalization of the work of Johnson and Nyquist on the electrical noise of a resistor [60, 91] and the work of Einstein on the brownian motion [34] .
In equations 3.26 and 3.30, F_{th} and z are coupled variables by the system hamiltonian. Any perturbation of F_{th} induces fluctuation of z through a dissipative process. The FDT relates the power spectral density $P_z\left(\omega\right)$ of z, the response function $G\left(\omega\right)$ and the temperature T of the system [68]:

$$P_z\left(\omega\right) = -\frac{2k_B T}{\pi\omega}\,\Im\left\{\frac{1}{G\left(\omega\right)}\right\} \tag{3.32}$$

where $\Im\{\,\}$ denotes the imaginary part. Using the FDT, the power spectral density (PSD) of a SHO and a SaO can be obtained from their respective response function:

$$P_z^{\mathrm{SHO}}\left(\omega\right) = \frac{2k_B T}{\pi k\omega_0}\frac{\frac{1}{Q}}{\left(1-u^2\right)^2 + \frac{u^2}{Q^2}} \tag{3.33}$$

$$P_z^{\mathrm{SaO}}\left(\omega\right) = \frac{2k_B T}{\pi k\omega}\frac{\phi}{\left(1-u^2\right)^2 + \phi^2} \tag{3.34}$$

with $u = \frac{\omega}{\omega_0}$. The thermal noise PSD for a SHO and a SaO are compared in figure 3.3. By setting $u \approx 1$ in equations 3.33 and 3.34, it is deduced that the two models are

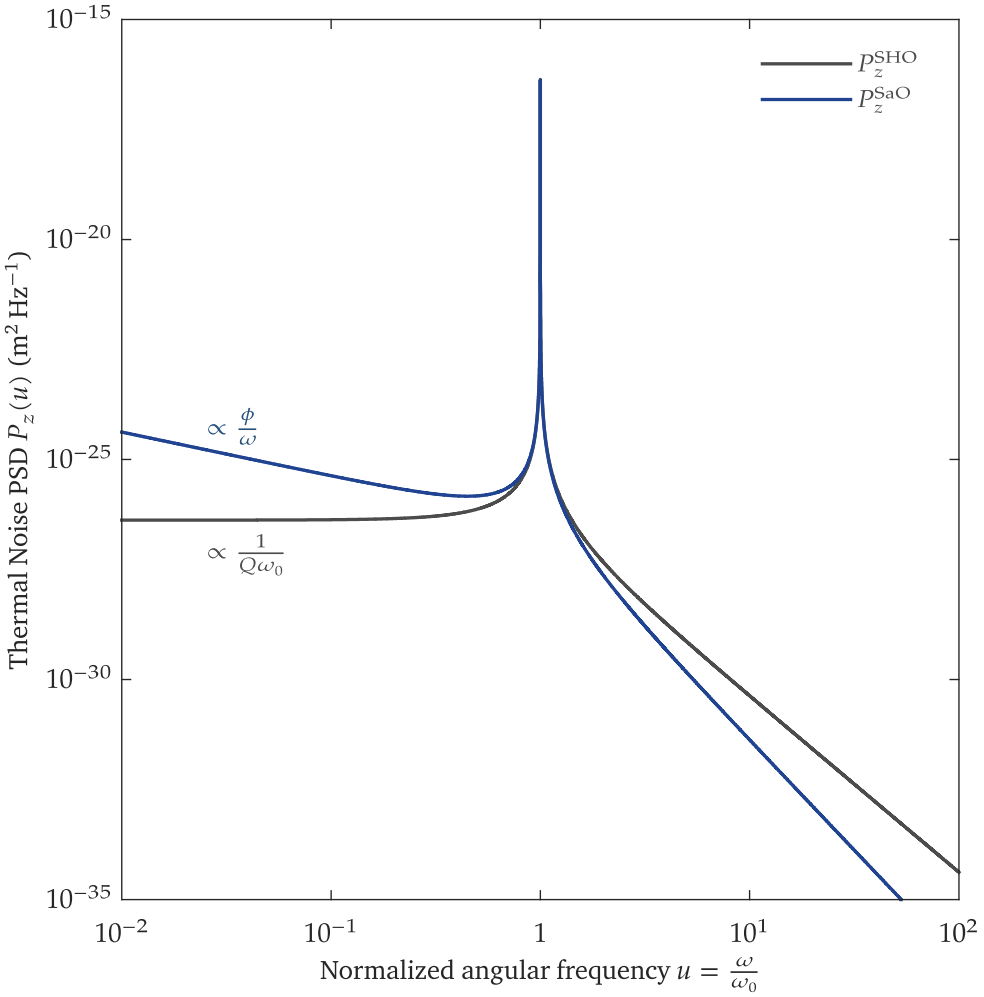

Figure 3.3 Thermal noise power spectral density (PSD) for two damped harmonic oscillators, with equal natural angular frequencies ω_0, equal spring constants $k = 1\,\mathrm{N/m}$, and equal quality factor $Q = \frac{1}{\phi} = 10^5$. The dark grey curve shows the spectrum P_z^{SHO} for a Simple Harmonic Oscillator. The dark blue curve shows the spectrum P_z^{SaO} for a Saulson Oscillator.

equivalent close to resonance, and both spectra presents a similar Lorentzian shape, from which a link can be made between the loss angle and the quality factor:

$$u \approx 1 \Leftrightarrow Q = \frac{1}{\phi} \tag{3.35}$$

Away from resonance, the two models stand apart, especially at low frequency where P_z^{SHO} is constant, whereas P_z^{SaO} exhibit a distinctive $1/f$ behaviour. These tendencies can be inferred from equations 3.33 and 3.34 by setting $\omega \ll \omega_0$ (or $u \ll 1$):

$$P_z^{\mathrm{SHO}}\,(\omega \ll \omega_0) = \frac{2k_BT}{\pi k}\frac{1}{Q\omega_0} \tag{3.36}$$

$$P_z^{SaO}\,(\omega \ll \omega_0) = \frac{2k_BT}{\pi k}\frac{\phi}{\omega} \tag{3.37}$$

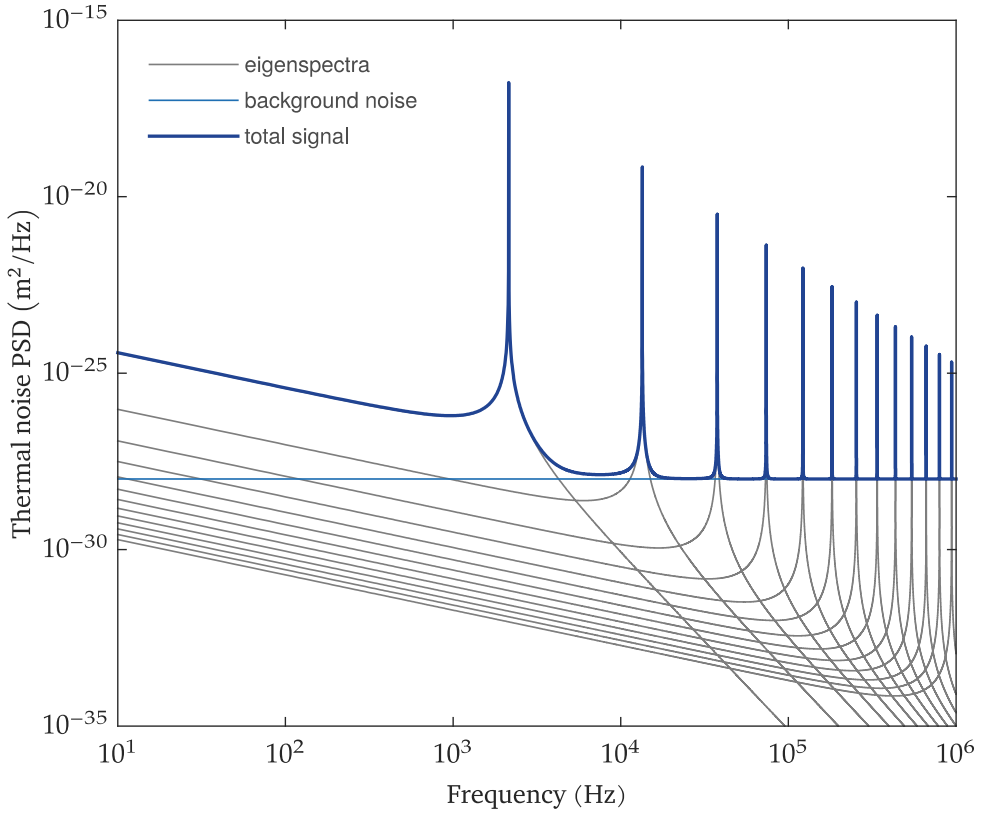

Figure 3.4 Thermal noise power spectral density of a nominal OCTO750S μcantilever at 300 K. The physical parameters of the cantilever are provided in appendix A, page 199. Each mode of the cantilever respond as a Saulson Oscillator with a loss angle of 10^{-5}. The many dark grey curves are the spectra of each individual modes. The light blue line provides a simplified representation of the QPDI background noise, at $10^{-28}\mathrm{m}^2/\mathrm{Hz}$. The dark blue curve is the sum of all the modes contribution and of the background noise of the instrument, and therefore represents the experimentally accessible thermal noise signal for this cantilever.

A $1/f$ thermal noise PSD at low frequency is thus the signature of structural damping [68].

The link between the FDT and the equipartition theorem for a single oscillator is given by:

$$\int_0^\infty P_z(\omega)\,d\omega = \int_0^\infty P_z(f)\,df = \langle z^2 \rangle = \frac{k_B T}{k} \tag{3.38}$$

3.3.3 Application to a microcantilever

A natural way to include dissipation effects in the μcantilever thermal noise modelization made so far is to rewrite each of its vibration mode as a damped harmonic oscillator, for example by replacing the differential equation 3.4 for the time component $\tau_n(t)$ of each mode by one of the two Langevin equations of motion 3.26 or 3.30, and then describing each mode as a SHO or a SaO. In such a frawework, and as a direct consequence of the mode independence (equation 3.10), the total thermal

noise spectrum of the cantilever is obtained as the sum of the spectra of each of its modes:

$$P_z{}^C(\omega) = \sum_{n=1}^{\infty} P_z{}^n(k_n, \omega_n, Q_n | \phi_n, \omega) \tag{3.39}$$

where $P_z{}^C$ is the thermal noise PSD of the whole cantilever, and $P_z{}^n$ is the thermal noise PSD of mode n.

However, as the presence of dissipation distributes the energy of a harmonic oscillator at all frequencies, a particular mode can lose and receive energy to and from all the remaining modes of the cantilever, and such a coupling imply that the independence of the modes cannot hold strictly. To discuss this point, a comparison is made between the PSD of a mode n at its resonance frequency ω_n and the PSD of the next mode $n+1$ at the same frequency, in the particular case where both mode respond as a SaO. The peak amplitude of mode n is expressed by setting $\omega = \omega_n$ ($u = 1$) in equation 3.34:

$$P_z^{SaO\ n}(\omega_n) = \frac{2k_BT}{\pi} \frac{1}{k_n \phi_n \omega_n} \tag{3.40}$$

The amplitude of mode $n+1$ at the same frequency is:

$$P_z^{SaO\ n+1}(\omega_n) = \frac{2k_BT}{\pi} \frac{1}{k_{n+1}\omega_n} \frac{\phi_{n+1}}{\left(1 - \left(\frac{\omega_n}{\omega_{n+1}}\right)^2\right)^2 + \phi_{n+1}^2} \tag{3.41}$$

The PSDs of the two modes are compared by computing the ratio between equations 3.40 and 3.41:

$$\frac{P_z^{SaO\ n}(\omega_n)}{P_z^{SaO\ n+1}(\omega_n)} = \frac{1}{\phi_n \phi_{n+1}} \frac{k_{n+1}}{k_n} \left[\left(1 + \left(\frac{\omega_n}{\omega_{n+1}}\right)^2\right)^2 + \phi_{n+1}^2 \right] \tag{3.42}$$

In this works, we are concerned with loss angles ranging from 10^{-6} to 10^{-4}, so the ϕ_{n+1}^2 term in equation 3.42 can be neglected. Further simplifications are obtained by using

$$\frac{k_{n+1}}{k_n} = \left(\frac{\alpha_{n+1}}{\alpha_n}\right)^4 \qquad \left(\frac{\omega_n}{\omega_{n+1}}\right)^2 = \left(\frac{\alpha_n}{\alpha_{n+1}}\right)^4 \tag{3.43}$$

which are obtained by using equation 3.22 and 3.13 respectively. Equation 3.42 then become:

$$\frac{P_z^{SaO\ n}(\omega_n)}{P_z^{SaO\ n+1}(\omega_n)} = \frac{1}{\phi_n \phi_{n+1}} \left[\left(\frac{\alpha_{n+1}}{\alpha_n}\right)^4 \left(1 + \left(\frac{\alpha_n}{\alpha_{n+1}}\right)^4\right)^2 \right] \tag{3.44}$$

The bracket term in equation 3.44 takes a values of ≈ 53 for $n = 1$, and then converge to 4 for higher modes: for the range of loss angles considered here, the PSD of a mode at resonance is then found to be at least 7 orders of magnitude larger than the PSD of the next mode at the same frequency: for a µcantilever with low dissipation and subjected only to thermal fluctuation, the coupling between modes is expected to

remain negligible for all practical purposes. An example of μcantilever thermal noise spectrum according to equation 3.39 is provided in figure 3.4. It is clear that the peak amplitude of any mode is much larger than the PSD of the remaining modes of the cantilever in the same region of the spectrum, so that the previous conclusion would also have been obtained in another particular case. Figure 3.4 also illustrate the importance of a low measurement noise, which is critical to detect the low frequency region of the first mode and the remaining modes at higher frequencies.

3.4 Conclusion

In this chapter, the tools used to interpret the mechanical thermal noise spectra of a μcantilever have been presented. Modeling the bending vibration of the cantilever within the Euler-Bernoulli framework first led to a description of its dynamic in term of normal modes, and established the relationship between the cantilever physical parameters and the modes' natural frequencies and spring constants. The equipartition theorem was then employed to predict the mean squared deflection of an Euler-Bernoulli cantilever subjected to thermal agitation, elucidating the contribution of each mode to the total thermal noise. Finally, each mode of the cantilever has been subjected either to viscous damping according to the Simple Harmonic Oscillator (SHO) model, or to structural damping following the Saulson Oscillator (SaO) model, and the Fluctuation-Dissipation Theorem (FDT) was used to relate to corresponding response functions to the cantilever thermal noise spectrum. In the low dissipation limit, the thermal noise spectrum of a μcantilever results from the sum of the thermal noise spectra of each of its modes.

4 An overview of the system

The aim of this chapter is to provide an overview of the CryoQPDI steup, with an emphasis on illustrations. It can be considered as an introduction for chapter 5 and chapter 6. The general architecture and the main components of the system are presented. Details on the internal structure and thermal performance of the cryostat are given. Some elements of the interferometer overall design are provided, and the steps involved in a typical measurement cycle are given.

CryoQPDI is an acronym standing for "Quadrature Phase Differential Interferometry on Cryocooled microresonators". The CryoQPDI is the combination of a pulse tube based cryostat and an interferometer, the later being based on the QPDI concept presented in chapter 2. The cryostat is a commercial unit [114] which was tailored for the CryoQPDI needs. Its construction is thus only briefly reviewed here. On the other hand, the majority of the work done during this thesis was devoted to the development of the interferometer, which is therefore described in more detail in the next chapters.

One of the main problematics of any high precision measurement is the need to isolate the instrument from external vibrations. In the CryoQPDI case, apart from the vibrations coming from the floor, two important sources of vibrations are the pumping system and the refrigerator. The designs and methods applied to adress this important problematic are discussed throughout this chapter.

4.1 General architecture

Figure 4.1 is a photograph of the main components of the CryoQPDI. These components are identified in figure 4.2. Besides giving the system's overall dimensions, figures 4.3 and 4.4 are also provide alternative viewpoints on the CryoQPDI setup. As a primary measure against external vibrations, the system's main components are placed on a vibration-isolating optical table. The instrument is located in a white room environnement with controlled temperature and humidity as well as a very low dust level.

As mentioned in this chapter's introduction, the CryoQPDI is mainly an interferometer used in conjunction with a cryostat. The cryostat consists in a vacuum vessel integrating a cryorefrigerator and a cooling circuitry. This cooling circuitry is connected to a cold plate were the sample and a few other elements of the interferometer are

Figure 4.1 Photograph of the CryoQPDI main elements. The cryostat is the main subject of this photograph and is visible at the foreground, while the interferometer sits behind it on the left. From a comparison with the other figures of this chapter, one can recognizes from left to right: the main vaccum vessel of the cryostat, the pulse tube connected via two helium gas lines to its compressor (not shown), the pressure sensor and the ion pump. The cold plate is easily identified by its gold color, with the cryo holder attached on it. Appart from the pulse tube compressor and the acquisition and control electronics, all the apparatus sits on an optical table with self-leveling, active air isolator feets.

placed. The main body of the interferometer is located outside the cryostat on an optical breadboard. A supporting structure is used to position the interferometer at and adequate height above the optical table surface. The light from the interferometer reaches the sample after passing through a set of windows and apertures placed on the side of the cold plate enclosure (see the next section).

The aim of any cryostat design is to mitigate the natural flow of heat from hot parts to cold parts. In this regards, the heat tranfers due to gas convection need to be eliminated. This fact makes the production of a vacuum necessary for cryogenics [**cryobook_vacuum**]. The cryostat is thus operated at a high vacuum, reaching a pressure around 10^{-7} mbar at room temperature and around 10^{-8} mbar at cryogenic temperature, where the pumping is assisted by gas condensation on cold surfaces. This level of vacuum also eliminates any gas damping from the μcantilever.

To reach this pressure level, a set of two pumps connected in series is used. A scroll pump [117] (not shown) is first used to reach a pressure around 10^{-2} mbar, and a magnetic bearing turbomolecular pump [117] is then employed to reach the pressure mentioned before. During initial testing, it was found that the vibrations caused

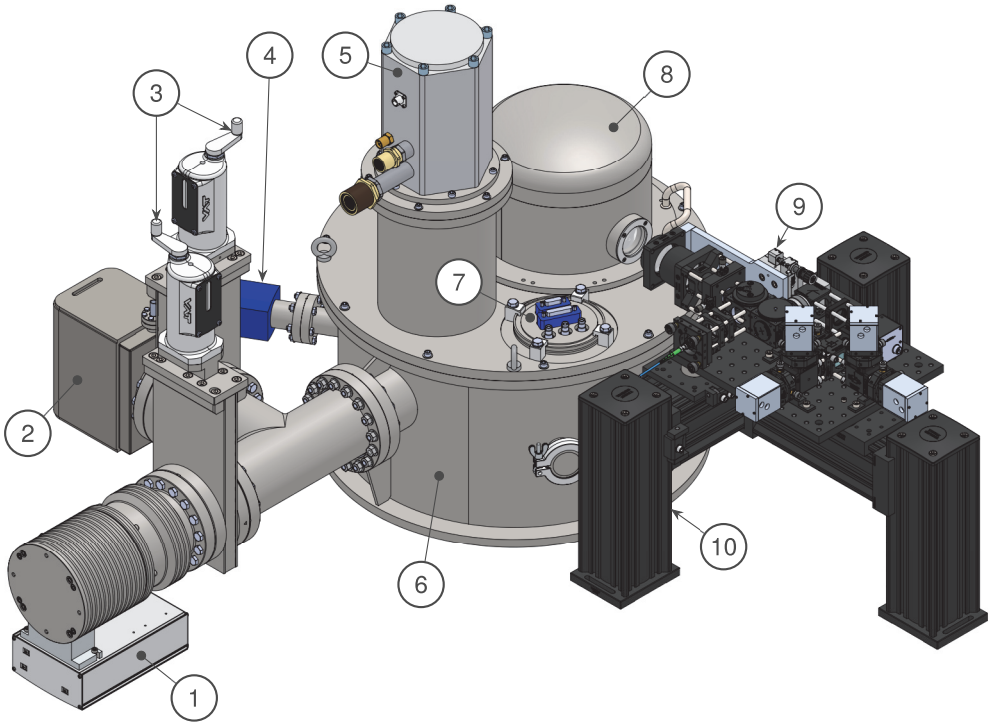

Figure 4.2 General architecture of the CryoQPDI. The instrument consists in the combination of a cryostat (on the left, grey) and a quadrature phase differential interferometer (QPDI, on the right, black).

Item	Description	Item	Description
1	Turbomolecular pump	6	vaccum vessel
2	ion pump	7	cold plate electrical connexions
3	high vacuum valve	8	experiment space
4	pressure sensor	9	interferometer
5	pulse tube cryocooler	10	interferometer support structure

by this main pumping group introduced an important noise in the interferometer signal. To avoid this issue, a ion pump [11] was added to the system. It is a closed pump working on an absorption principle, thus offering the advantages of having no moving part and of not requiring a backing pump to operate. It is used alone below 10^{-6} mbar to maintain the system pressure during data acquisition, allowing the main pumping group to be turned off. Two vacuum valve are used to select which of the main pumping group or the ion pump is used to pump the cryostat.

4.2 Cryostat

Figure 4.5 displays a photograph of the cryostat cold plate. The three enclosures of the cold plate are shown on the photograph of figure 4.6. The cryostat internal structure is provided in figure 4.7. Two typical temperature curves of the system are displayed in figure 4.8.

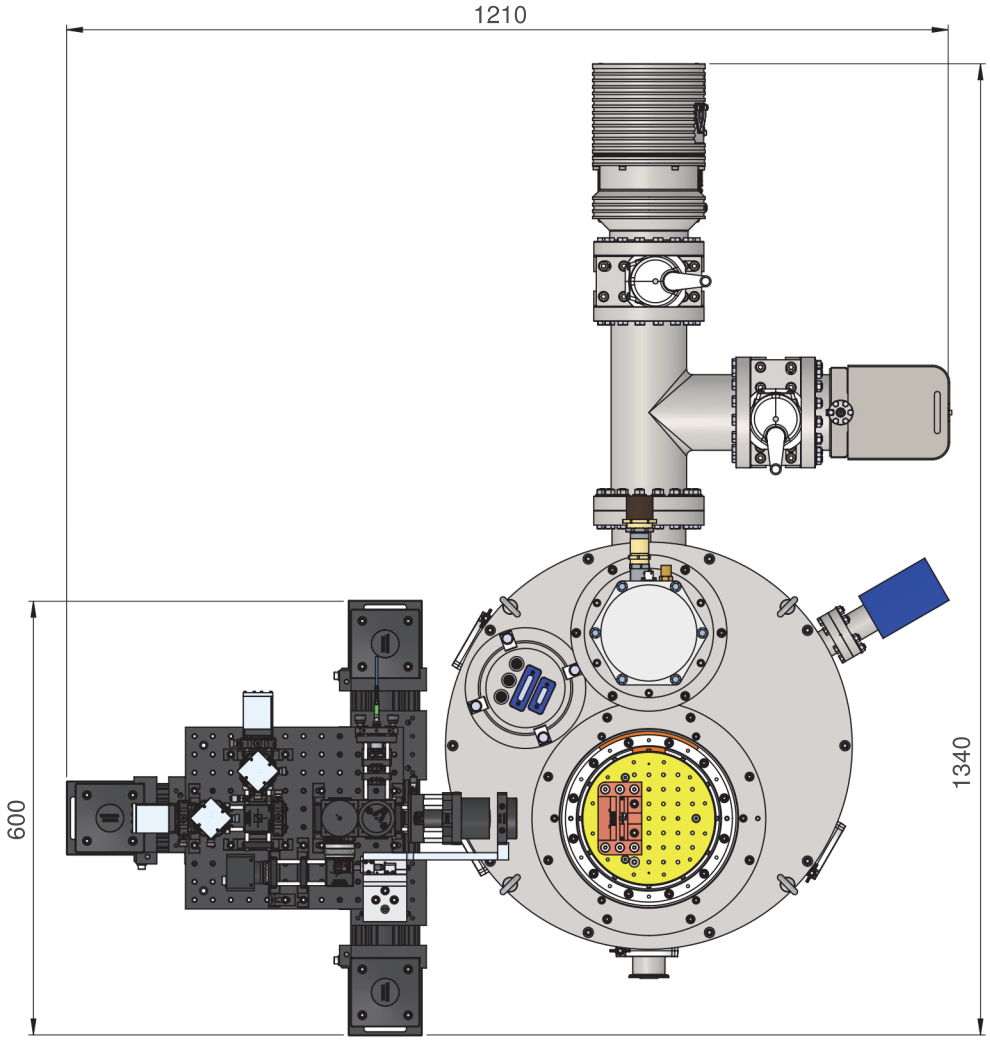

Figure 4.3 Top view of the CryoQPDI. All dimensions are in millimeter, and where rounded to the nearest tens of millimeters.

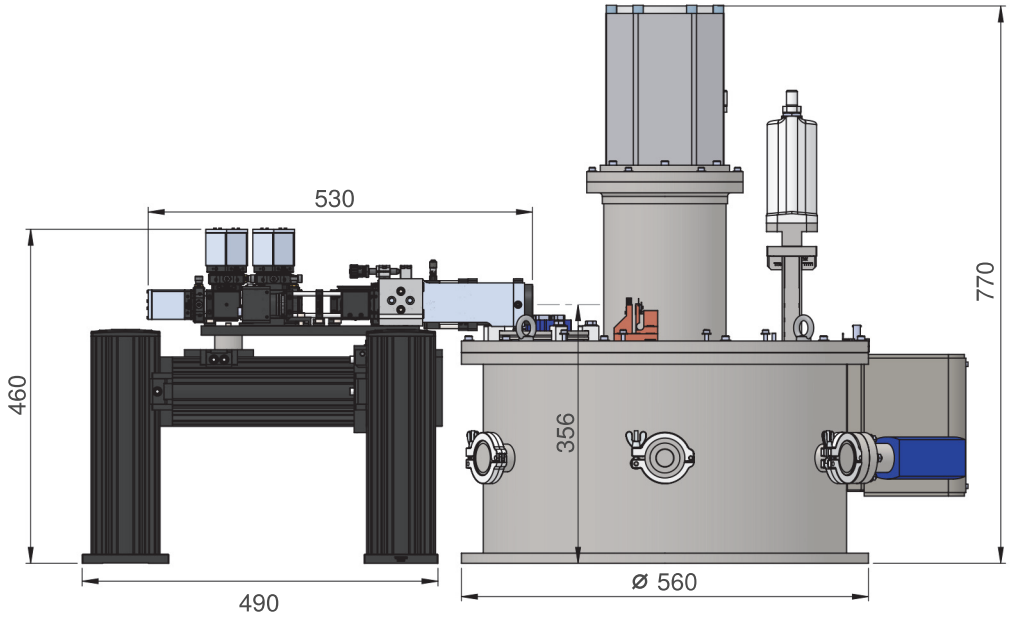

Figure 4.4 Side view of the CryoQPDI. All dimensions are in millimeter. Except for the height of the interferometer's line of sight, all dimensions where rounded to the nearest tens of millimeters.

As mentioned before, the cryostat's cooling function is provided by a pulse tube refrigerator [95, 118] (figure 4.1 and 4.7). Pulse tubes are a type of closed cycle refrigerator, and they therefore have the important advantage of not requiring a supply of cryogenic fluids, making them comparatively easier and less expensive to operate. Compared to the other closed cycle cryocooler technologies, pulse tubes also have the advantage of not having any cryocooled moving part, giving them an increased reliability and life time. In a pulse tube, heat extraction is acheived by the oscillation in flow and pressure of a pressurized helium gas, this oscillation being created by a high power external compressor (not shown).

In the cryostat, the sample and the interferometer's birefringent beam splitter are placed on the cryo holder, a mechanical assembly which is itself fastened to the cryostat cold plate (figure 4.5). The design of the cryo holder is described in the next chapter. The cold plate gives a workspace larger than a cube of $100 \times 100 \times 100$ mm (figure 4.7). The cryo holder occupies around half of this space, leaving the other half for other experiments. During measurements, this workspace is enclosed by two screens and a vacuum lid. The light from the interferometer reaches the sample through a set of optical windows and apertures placed on these enclosures (figures 4.6). The screens are used to mitigate unwanted radiative heat transfers.

Operating the pulse tube generates a large amount of vibration which makes any thermal noise measurement impossible. This problem was anticipated, and it was planned to turn off the pulse tube and acquire data during the following passive warm up of the sample. To slow down this warm up, a lead thermal mass was added to the

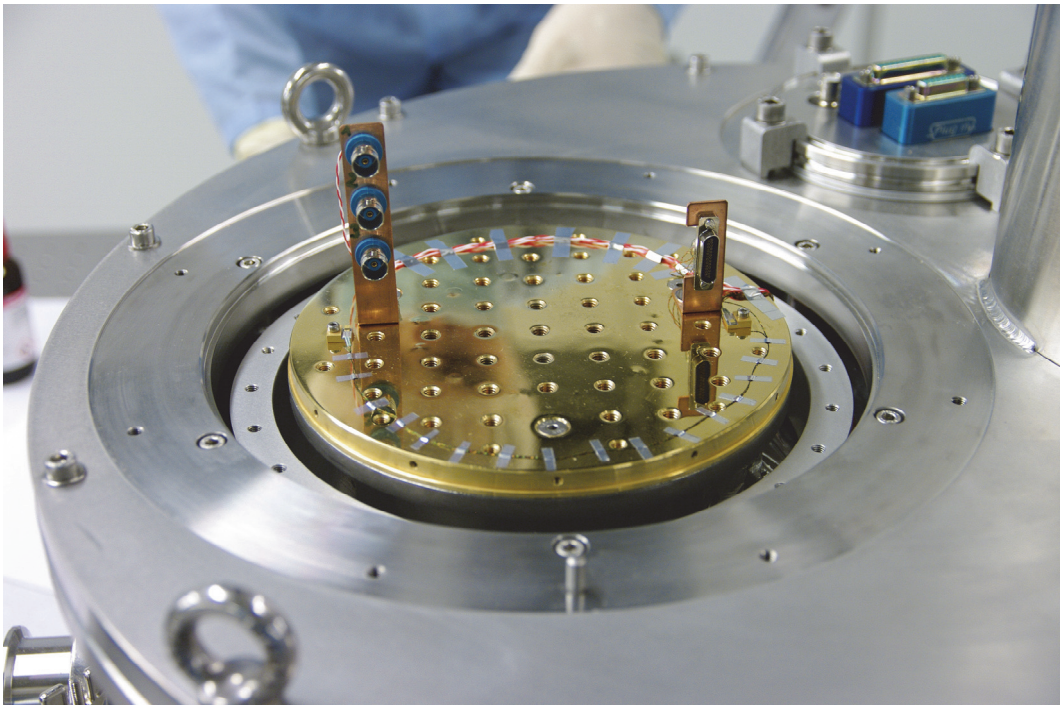

Figure 4.5 Photograph of the cryostat cold plate, as received from the cryostat manufacturer. The cold plate is made of oxygen free high conductivity (OFHC) copper and received a gold coating to reduce radiative heat transfers. It has a diameter of around $180\,\mathrm{mm}$. Three BNC connectors on the right and a generic analog connector on the left provide electrical contacts between the cold environnement and the outside. They are linked to a connector plate visible on the top right corner. Looking closely, the two small temperature sensors of the cold plate can be identified on the left and right sides of the cold plate respectively. In particular, the cable of the left sensor circles around the cold plate on the foreground. During an experiment, this sensor is attached to the cryo holder close to the sample.
Both sensors are of the silicon diode type. They are calibrated with a maximum reading error of $1\,\mathrm{K}$. This reading is done by a dedicated temperature controller. The temperature controller can also send power to a set of resistive heaters to speed up the warm up of the cold plate. This function is used only after the end of a measurement session.

cryostat initial design just below the cold plate, then increasing the system thermal inertia.

Two typical temperature curves of the system are displayed in figure 4.8. During cool down, the temperature first follows an almost linear trend with an average cooling rate of 35 K per hour. A temperature less than 10 K is reached after around 8.5 hour of cooling, above which the cooling rate decreases significantly. A temperature of 7.5 K is obtained after 24 hours of cooling, and the minimum attainable temperature of the system of 6.5 K is reached after 48 hours. During warm up, the temperature increases at an initial rate of 11 K per hour (or 0.18 K per minute) around 10 K. The warm up rate decreases with increasing temperature, taking a value of 5 K per hour (0.08 K per minute) at 120 K.

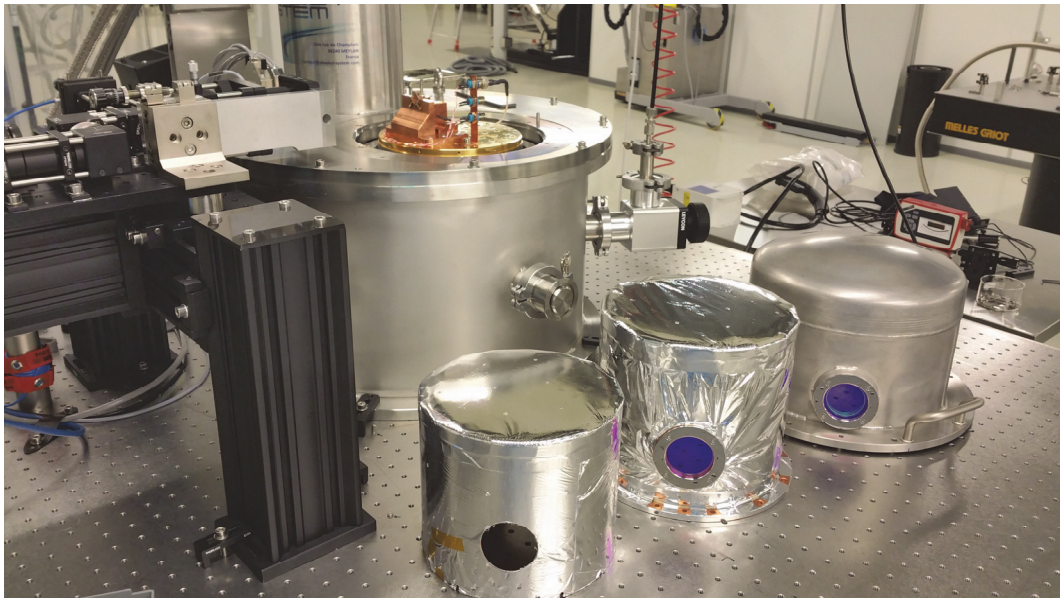

Figure 4.6 Photograph of the cryostat's two radiation screens and vacuum lid. On the bottom right of the photograph, from left to right, these elements are the 4 K screen, the 80 K screen and the vacuum lid, which stays at room temperature. The lid is made of steel like the vacuum vessel, while the screens are made of copper and covered with a multilayered insulator.
The temperatures used to name the screens are just nicknames. In practice, the 4 K screen has the same temperature as the cold plate, which is 6.5 K at best. At this point, the 80 K screen real temperature is rather found around 40 K.
While the 4 K screen just has two open apertures to let the light through, the 80 K screen and the vacuum lid both hold two windows, for a total of four. These windows are all identical. They are made of fused silica and received an home made antireflection coating at four common laser wavelenghs: 532 nm, 633 nm, 1064 nm and 1550 nm. The cryostat manufacturer determined that using windows is also necessary for the 80 K screen for additional radiation isolation, but is not significantly beneficial on the 4 K screen.

4.3 Interferometer

Figure 4.9 displays a photograph of the interferometer. Figure 4.10 highlight the interferometer's sub assemblies.

The interferometer optomechanical assembly was designed to be both very rigid and modular. Several functional subassemblies can be detached from the interferometer's breadboard, worked on and fastened again without disturbing the remaining components of the interferometer. Having a relatively rigid, light and compact assembly is also a measure against external vibration. The general guideline followed in this case is to try to set the resonant frequencies of the interferometer's structure above the cutoff frequency of the optical table. The same principle was applied to the design of the support structure.

As shown in figure 4.10, the interferometer assembly can be divided into five functional blocs. The input bloc determine the beam size and state of polarization. The scanning objective is used to focus and position the beam on the μcantilever. The cryo holder

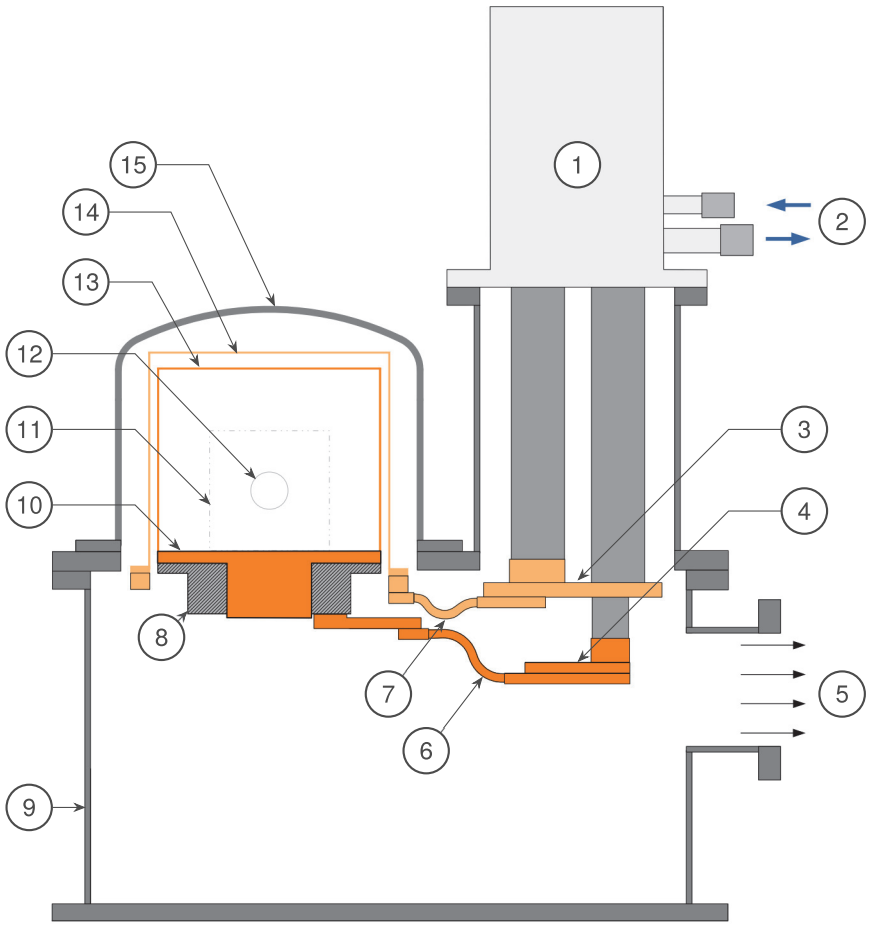

Figure 4.7 Simplifed schematic of the cryostat internal thermal circuit. The structural elements supporting the cold plate and the screens are not displayed for clarity.

Item	Description	Item	Description
1	pulse tube cryocooler	9	vaccum vessel
2	helium gas line	10	cold plate
3	80 K cooling stage	11	cryogenic experimental space
4	4 K cooling stage	12	view port, ⌀=40 mm
5	pumping port	13	4 K radiation screen
6	4 K flexible thermal link	14	80 K radiation screen
7	80 K flexible thermal link	15	vaccum lead
8	lead thermal mass		

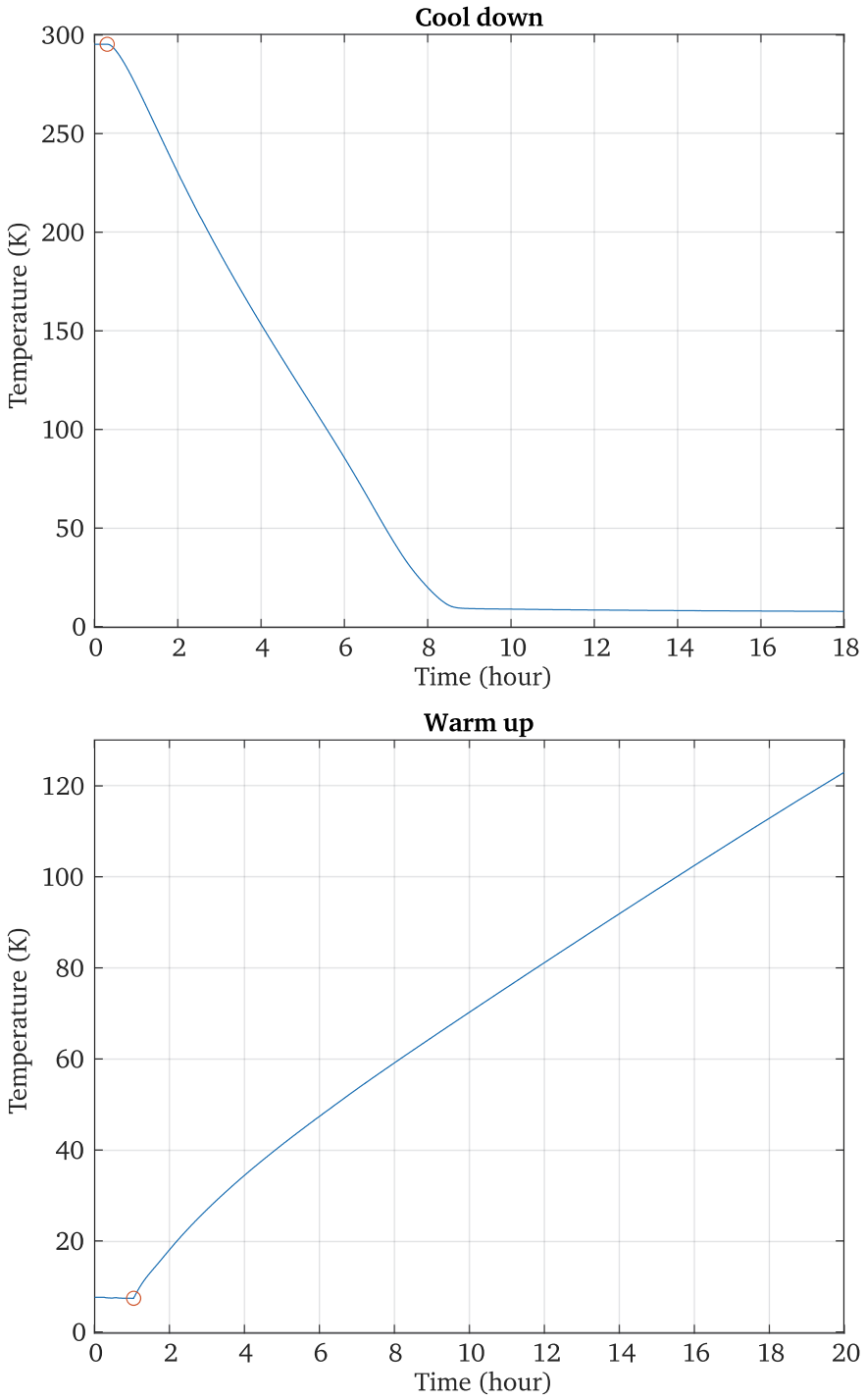

Figure 4.8 CryoQPDI cooldown and warm up sample temperature curves. These curves were acquired from the temperature sensor fastened to the cryoholder. On each curve, the orange circle marks the point where the pulse tube is turned on (cool down) or turned off (warm up).

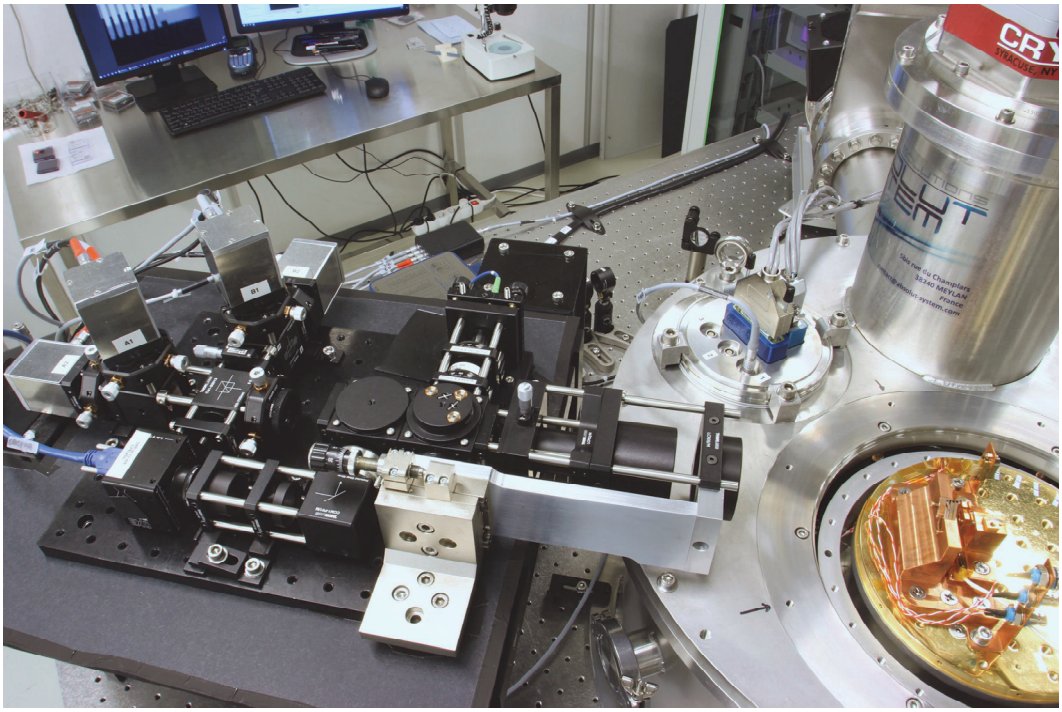

Figure 4.9 Photograph of the CryoQPDI interferometer. The interferometer was build with structural rigidity and modularity in mind. Both of these purposes are achieved by using a so called "cage system" of optomechanical components.
The support structure is partially hidden by a cardboard which constitutes the first part of a box intended to prevent stray light to enter the system. This box was not finished due to time constrains. A curtain is used as a temporary replacement for this box. The two additional rods connecting the ends of the scanning objective are used to prevent the curtain to fall in front of the scanning objective lenses. They dont play any structural role.

holds both the sample and the birefringent beam splitter inside the cryostat. Together with the scanning objective, the imaging bloc is used to form and acquire and image of the sample. At last, the quadrature detection bloc is used to interpret and acquire the interferometer signal.

4.4 CryoQPDI operation

The steps involved in a cryogenic measurement are listed hereafter. It is supposed that the system is initially at room temperature and room pressure.

- A sample is installed on the cryo holder. The two radiation screens and the lid are used to close the cryostat.
- The correct positioning of the sample is checked using the image from the instrument's camera.
- The system is pumped down to 10^{-6} mbar or less using the scroll pump alone first and then the scroll pump and the turbomolecular pump together. At this step, the

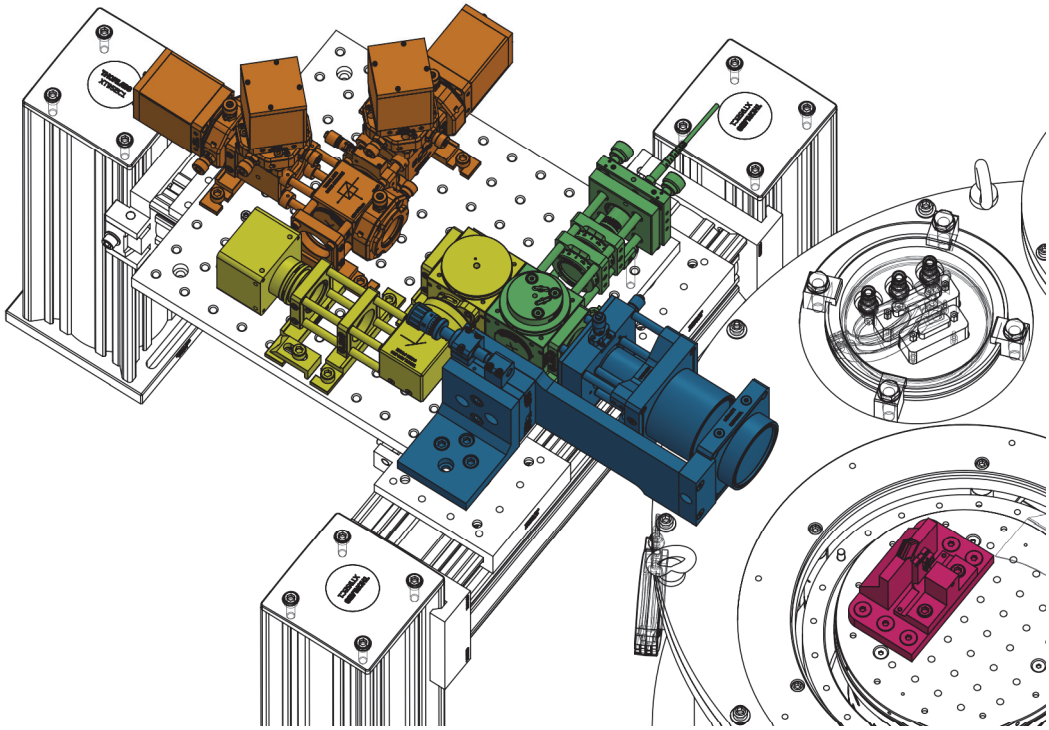

Figure 4.10 Division of the interferometer into logical subassemblies, or blocs. The blocs coloring is as follows. Green: input bloc. Blue: scanning objective bloc. Red: cryo holder. Yellow: imaging bloc. Orange: quadrature detection bloc.

vacuum valve in front of the turbomolecular pump (for the main pumping group) is open and the one in front of the ion pump is closed.

- After reaching the target pressure, the pulse tube is turned on.
- When the sample temperature is found below 10 K, the scanning objective is used to position the laser spots on a sample. The interferometer is then calibrated.
- The valve of the ion pump is opened, and the valve of the main pumping group is closed. The main pumping group is turned off. At this point, the instrument is no longer affected by pump vibrations.
- The pulse tube is turned off. The sample temperature rise slowly while the interferometer's signal is acquired. The system is in its most quiet state of operation.
- Once an adequate temperature range have been covered, the data acquisition is stopped and the main pumping group is again set to pump the cryostat. This is to preserve the ion pump lifetime. The resistive heaters are used to warm up the cold plate faster. The system is brought back to room pressure only after the cryostat internal temperature is close to room temperature to avoid condensation.

4.5 Conclusion

In this chapter, an overview of the CryoQPDI setup was provided. The overall design of the instrument was carried out with the goal of mitigating any disturbance of the interferometer signal from external vibrations. The system is placed on an optical table to reduce the floor's vibrations. An ion pump is used during measurement so that the main pumping group with mechanical pumps can be turned of. The pulse tube cryocooler is turned off during measurement, and the cryostat thermal inertia is increased by a lead mass to slow down the warm up of the system. The interferometer is constructed for a high rigidity. The design of the most critical optical subassemblies of the CryoQPDI as well as the cryo holder are described in chapter 5. The design of the CryoQPDI photodetectors and signal chain is discussed in chapter 6.

5 CryoQPDI optical design

The object of this chapter is the development of the CryoQPDI quadrature phase differential interferometer optical assembly. As a first introduction to its design, the general optical scheme of the interferometer is displayed in figure 5.1.

The interferometer development was conducted with the aim of optimizing two of its important performance metrics, which are its contrast and the spots size on the μcantilever, which determine the interferometer lateral spatial resolution. Achieving a good contrast is important to minimize the spectral noise of the system [92], and provides an additional headroom for the measurement of nonideal samples. With a small spot size, the laser beam on the μcantilever can be considered point like, which allows for the detection of higher vibration modes and simplifies the data analysis process [14]. To optimize these two performance metrics, a particular attention is given to the laser beam wavefront and its interaction with the optical element of the interferometer. The spatial extent of the beam is therefore considered, corresponding to an extension of the ray representation used in chapter 2. The beam reaching a photodetector is the superposition of the wavefronts of two beams giving rise to interferences. If these wavefronts have the same shape and if the beam have the same power, the resulting interference pattern is uniform. In particular, in this case a state of destructive interference causes a complete extinction of the beam and results in zero photodetector signal, which ensures a good contrast for the interferometer. If the two beams have different wavefronts however, fringes will form in the interference pattern and the signal of the photodetector can never fall to zero, which implies a degradation of the interferometer contrast [54].

Thanks to its common path architecture, there is only one place where the wavefront of the two beams of the interferometer can become different: when they are separated by the birefringent beam splitter. Unfortunately, focusing a beam through a birefringent material results in a important differential deformation of the two output beams' wavefronts, which originates from a first order astigmatism linked to the very nature of birefringent crystals.

Even in the case where the wavefronts are identical, any deviation of a wavefront from an ideal spherical shape can disturb the optimal energy concentration of a beam at focus. This deviation, which is called an aberration of the wavefront, can therefore results in a increase of the interferometer spot size. In the CryoQPDI, aberrations

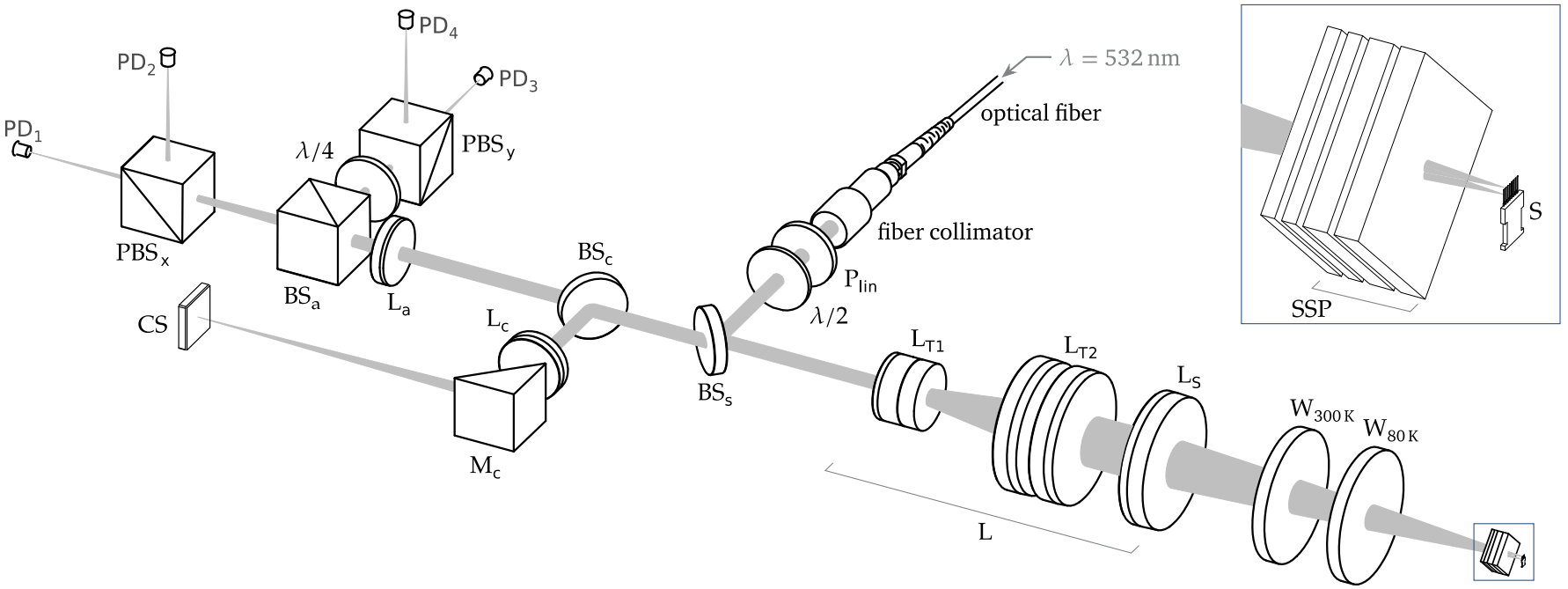

Figure 5.1 CryoQPDI optical scheme. With reference to the diagram of figure 2.2, page 17. The grey beam displays the laser $1/e^2$ diameter. The focal length of the camera lens L_c is 150 mm, and the focal length of the analysis lens L_a is 125 mm.

Symbol	Description
P_{lin}	linear polarizer
$\lambda/2$	half wave plate
$\lambda/4$	quarter wave plate
BS_s, BS_c	non-polarizing beam splitter, 10:90
BS_a	non-polarizing beam splitter, 50:50
PBS_x, PBS_y	polarizing beam splitter
M_c	mirror
CS	camera sensor

Symbol	Description
L_a, L_c, L_S	doublet lens
L_{T1}, L_{T2}	telescope multielement lens
L	scanning objective
$W_{300\,K}$, $W_{80\,K}$	cryostat windows
$PD_{1\to4}$	photodetectors
SSP	Semel-Savart plate
S	μcantilever sample

may be introduced by the system of lenses used to shape and focus the beam on the μcantilever. Here, the simultaneous requirements of a small spot size, a compact assembly and a long working distance to reach the sample from outside the cryostat make this system of lens particularly sensitive to aberrations.

In summary, without a particular attention to their design, the lenses used to focus the laser beam on a μcantilever can be responsible for an increase of the interferometer spot size, and the birefringent beam splitter can be the source of both an increased spot size and a reduction of the interferometer contrast. Accordingly, in this chapter the emphasis is set on the design of these two elements. The system of lenses used to focus the beam was developed as the "scanning objective". It is aberration compensated to optimize the system spot size and also fill another very important role, which is to position the spot on the sample. The birefringent beam splitter of the CryoQPDI is a Semel-Savart plate, a design used to compensate for crystal astigmatism.

The chapter is organized as follow: in a first section, the design of the scanning objective is described. This section start with a brief exposure to the theory of aberration in imaging system, before focusing on the scanning objective case. The design of the scanning objective is then carried out with the help of a dedicated sofware. A second section is then devoted to the design of the Semel-Savart plate. The theory of the interaction of light with birefringent crystals is presented and used to construct beam splitters with increasing levels of aberration correction and complexity. A litterature review is carried out to select an aberration free beam splitter design compatible with the CryoQPDI requirements. The design of the CryoQPDI beam splitter based on the Semel-Savart plate concept is then presented. Given the importance of the scanning objective and the Semel-Savart plate for the interferometer performance, most of the volume of this chapter is dedicated to these two sections. In a third section, the construction of the cryo holder, an assembly used to hold both the Semel-Savart plate and the sample under study, is briefly presented. In the fourth and last part of this chapter, some elements of the design of the imaging bloc are also briefly provided. This subassembly has no influence on the quality of thermal noise data, but considerably simplifies the system usage by streamlining the alignement process.

5.1 Scanning objective

5.1.1 Aberrations

Wavefront function The aberrations of an optical system can be generally defined as the deviations of light rays through this system from the path expected in the paraxial optic approximation [108, 75]. The general effect of aberrations is a degradation of the optical system image forming ability, in the sense that in the presence of aberration, the system is not able to form a point image from a point object. Aberrations are

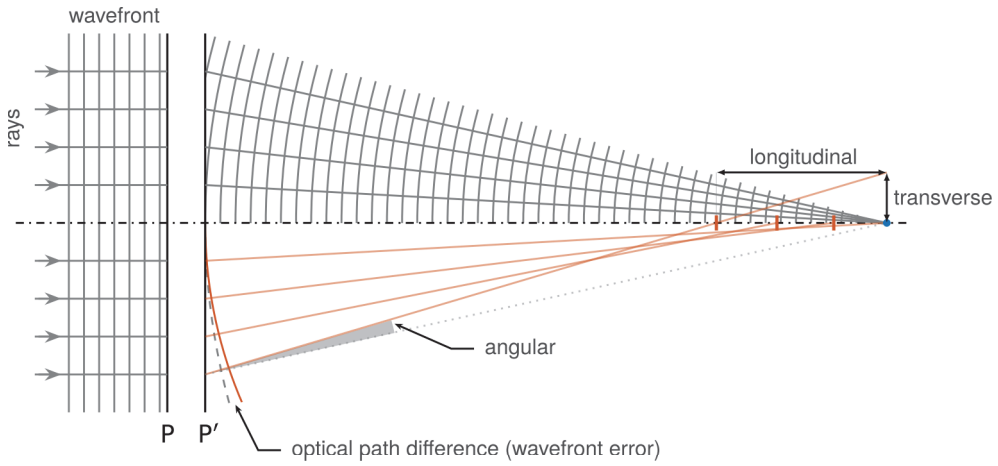

Figure 5.2 Focusing of a planar wavefront by an optical system [120]. The optical system is represented by its two principal planes P and P′. Above the optical axis, the system is perfect (unaberrated) and the incoming rays all converge to the same paraxial image point. The corresponding perfect wavefronts are spherical and centered on the paraxial image point. Below the optical axis, the optical system is aberrated and introduces an additional optical path difference between the on-axis ray and the off-axis rays. The corresponding wavefront deviates from spherical, and the off-axis rays no longer intersect the optical axis at the same location. From the point of view of geometric optics, the rays aberrations are accounted for by either their angular, longitudinal or transverse deviations from the perfect case. The wave aberration (or wavefront error) of a ray is defined as the additional optical path along this ray relative to the spherical reference wavefront.

present even in a perfect optical assembly, where it results from the intrinsic limitations of optical components. In the context of this manuscript, only monochromatic aberrations are discussed.

Figure 5.2 illustrates the concept of aberration. The optical system PP′ is used to focus the light from an infinitely distant point object. All the light rays emitted by this object travel an equal optical path length (OPL) before entering the optical system. The surface connecting rays of equal OPL is defined as the wavefront, and the rays are everywhere normal to the wavefront. In the unaberrated case, the optical system generates a spherical wavefront from the incoming planar wavefront[1], and the rays converge to a point image. From the point of view of paraxial optic, a spherical wavefront is therefore associated with a perfect optical system, and this spherical wavefront serves as a reference. In the presence of aberration, the optical system generates a wavefront which deviates from spherical by introducing an additional OPL between the on-axis and off-axis rays. The optical path difference between the system actual wavefront and the reference spherical wavefront for a particular ray is defined as the wave aberration of that ray. A positive wave aberration means that the ray has to travel an extra path lenght relative to the reference sphere. The optical system wavefront aberration function W gives the wave aberration of any ray transmitted by

[1] Notice that a planar wavefront is a spherical wavefront with an infinite radius of curvature.

the system. For a rotationally symetric optical system of moderate angular aperture, the wavefront function can be described by the following power series expansion [75]:

$$\begin{aligned} \mathrm{W}(r,\theta;h') &= a_\mathrm{s}\, r^4 + a_\mathrm{c}\, h' r^3 \cos\theta + a_\mathrm{a}\, h'^2 r^2 \cos^2\theta \\ &\quad + a_\mathrm{d}\, h'^2 r^2 + a_\mathrm{t}\, h' 3r \cos\theta \end{aligned} \tag{5.1}$$

where r and θ are the radial and angular coordinate of a ray in the (circular) exit pupil, and where h' is the image height from the optical axis. The system exit pupil is defined as its most limiting aperture as seen by looking at it from the image space[1]. Following from its definition, the wavefront aberration function is always equal to zero at the center of the image-forming light cone, where $r = 0$. The peak value of W is found on the edge of the pupil and is usually of a few μm, so that it is commonly expressed in unit of the wavelength considered, i.e. in unit of wave. The wavefront function of a multielement optical system is obtained by adding the wavefront functions of its individual components.

The aberration coefficients a_s, a_c, a_a, a_d and a_t are respectively the coefficients for spherical aberration, coma, astigmatism, field curvature and distortion, in unit of m^{-3}. The inclusion of these aberration terms in the wavefront mathematical description corresponds to an extension of the small angle approximation which defines the paraxial regime [109]:

$$\sin\alpha = \alpha - \frac{\alpha^3}{3!} + \ldots \tag{5.2}$$

Where α is a generic angle of incidence on an optical surface.
The value of the aberration coefficients is in general a complex function of the design considered and the imaging conditions. However, of the five types of aberration mentioned, only spherical aberration, coma and astigmatism affect the point image quality. On the other side, field curvature and distorsion describes a deformation of the image plane [120]. In the context of the scanning objective design, where the goal is to focus the interferometer laser beam to a spot rather than the formation of an extended image, field curvature and distorsion are clearly of minimal importance. Moreover, spherical aberration is the only aberration which does not depends of the image height h' or the field angle θ. Since the scanning objective's main function is to focus the interferometer laser beam on-axis, this is the most important aberration to consider for the system optimization, and the only aberration present when the system is centered. Accordingly, the following discussion is pursued with emphasis on spherical aberration.

For an optical system with a circular pupil of radius a, it is common for simplicity to rewrite equation 5.1 by suppressing the explicit dependance on h' and by using the

[1] For a more complete definition, see reference [75].

normalized radial variable $\rho = r/a$, $0 \leqslant \rho \leqslant 1$. For a configuration with spherical aberration only, this equation becomes:

$$\mathrm{W_s}(\rho) = A_\mathrm{s}\rho^4 \tag{5.3}$$

where $A_\mathrm{s} = a_\mathrm{s}\, a^4$ is the peak spherical aberration coefficient in unit of waves, as $\mathrm{W_s}$. This expression already shows that the amount of spherical aberration introduced by an optical system can be dramatically reduced by reducing its aperture a, as A_s depends on the fouth power of a.

In presence of spherical aberration, the best focus point[1] does not corresponds to the paraxial image point, but is rather found after a shift of the observation plane along the optical axis. Such a shift introduces defocus aberration:

$$\mathrm{W_d}(\rho) = B_\mathrm{d}\rho^2 \tag{5.4}$$

where b_d is the peak defocus aberration coefficient. Compensating an aberration by adding another type of aberration is referred to as aberration balancing. An uncompensated aberration is called a primary aberration. For uniform illumination in a circular pupil, primary spherical aberration is optimally compensated by a defocus of $B_\mathrm{d} = -A_\mathrm{s}$. The expression for balanced spherical aberration is thus:

$$\mathrm{W_s^b} = A_\mathrm{s}\left(\rho^4 - \rho^2\right) \tag{5.5}$$

Aberration and diffraction Up to now, the wave nature of light has not been taken into account. The image of a point object is not a point but rather a pattern of energy distribution determined by diffraction. The system phase aberration Φ is linked to its wave aberration W by:

$$\Phi = (2\pi/\lambda)\,\mathrm{W} \tag{5.6}$$

where λ is the light wavelength. Let the z axis be the optical axis of the system considered, R the distance between the exit pupil and the paraxial image point, and P the total power in the exit pupil. To evaluate the effect of aberrations on an optical system image forming ability, one may consider the following aberrated diffraction integral [76]:

$$I(r';z) = \frac{4P\pi a^2}{\lambda^2 z^2}\left|\int_0^1 e^{i\Phi(\rho)} J_0\left(\pi r'\rho R/z\right)\rho d\rho\right|^2 \tag{5.7}$$

where z is the coordinate of the observation plane relative to the exit pupil, the observation plane is normal to the z axis, r' is the radial coordinate of the observation point with respect to the point of intersection of the observation plane and the line joining the center of the exit pupil and the paraxial image point, and where J_0 is the

[1] According to diffraction.

zero order Bessel function of the first kind. r' is in unit of $\lambda F\#$, where $F\# = R/2a$ is the F-number or focal ratio of the image forming light cone. I is the irradiance distribution or the diffraction point spread function (PSF) of the (point) image. Equation 5.7 is valid only for a rotationally symetric aberration (like spherical aberration). A more general expression can be found in reference [76].

The PSF of a system free of aberration and with uniform illumination is the Airy pattern I_{Airy}. Letting $\Phi = 0$ and $z = R$ in equation 5.7 gives:

$$I_{\text{Airy}}(r'; R) = \frac{P\pi a^2}{\lambda^2 R^2}\left[\frac{2J_1(\pi r')}{\pi r'}\right]^2 \tag{5.8}$$

where J_1 is the first order Bessel function of the first kind. The Airy pattern consists of a central bright spot surrounded by dark and bright rings. The central bright spot is called the Airy disc and is delimited by the first minimum of the Airy pattern located at $r' = 1.22$. It contains around 84 % of the total power P. The factor $P\pi a^2/\lambda^2 R^2$ is the maximum value of the Airy distribution, located in its center at $r' = 0$. From the definition of r', the Airy disc radius r_{Airy} can also be written as:

$$r_{\text{Airy}} = 1.22\,\lambda\,F\# = 1.22\,\lambda\frac{\mathrm{f}'}{D} \tag{5.9}$$

The last expression in equation 5.9 is given for a thin lens of diameter D and focal length f' focusing a collimated beam, for which $F\# = F/D$.

In presence of aberration, the system PSF is distorded relative to the Airy pattern. The general effect of this distorsion is a PSF with a less efficient energy concentration than the one achieved without aberration. The aberrated PSF thus have a central maximum value less than the maximum of the Airy distribution, and the corresponding spot size can be much larger than the Airy disc [120].

The Strehl ratio There is no simple relationship between the wavefront function and the PSF of a system when the amount of aberration is significant, and an aberrated diffraction integral such as equation 5.7 must be evaluated if the PSF is to be determined in this case. For a small amount of aberration however, where the PSF does not deviates too much from the Airy distribution, some simple results can be used and the evaluation of a diffraction integral can be avoided.

The Strehl ratio is defined as the ratio of the PSF central value with and without aberration. For uniform illumination, it writes:

$$S_{\text{r}} = \pi^2\left|\int_0^1\int_0^{\pi} e^{i\Phi(\rho,\theta)}\rho\,d\rho\,d\theta\right|^2 \tag{5.10}$$

Notice that in this expression the aberration function is not required to be rotationally symetric. Since the maximum central value of the PSF is maximum for an aberration free system, the Strehl ratio ranges between 0 and 1.
For small aberrations, the Strehl ratio can be evaluated using the following empirical expression [76]:

$$S_r \approx e^{-\sigma_\Phi^2} = e^{-(2\pi\sigma_W)^2} \tag{5.11}$$

where σ_W is the standard deviation of the wave aberration across the pupil in unit of wave RMS, and where σ_Φ is the corresponding phase aberration standard deviation.

Equation 5.11 yields an error less than 10 % for $S_r > 0.3$, with a smaller errors for a larger Strehl ratio. In this range, the Strehl ratio depends strongly on the aberration variance, but only weakly on the content of the aberration function.

Aberration correction criterion and method An optical system with uniform illumination can be considered diffraction limited for a particular image point if $S_r \geqslant 0.8$. This Strehl ratio is obtained for a wavefront aberration standard deviation equal or less than approximately $1/14$ wave RMS. Under this condition, the optical system PSF does not deviates significantly from the Airy function and its performance can be evaluated as in the aberration free case.

The wavefront aberration standard deviation for balanced spherical aberration $\sigma_{W_s^b}$ is given by [76]:

$$\sigma_{W_s^b} = A_s/13.42 \tag{5.12}$$

The maximum amount of balanced spherical aberration allowed for a diffraction limited performance is

$$A_s = 1 \text{ for } S_r = 0.8 \tag{5.13}$$

The design of an aberration corrected multielement optical system is usually carried out using a ray tracing software. The software is used to determine the path of many rays using exact trigonometric reflexion and refraction equations at the system optical interfaces. At an early stage of developpement, the dispersion of the ray bundle relative to the Airy disc (i.e. the geometric PSF) is usually used as a crude but simple criterion for aberration correction. When the ray bundle dispersion approaches the Airy disc radius, further optimizations are done based on the wavefront standard deviation and the Strehl ratio. This method is referred to as the golden rule of optical design [77].

5.1.2 Aberration for a gaussian beam

From uniform to gaussian illumination So far only uniform illumination have been considered, but the TEM_{00} laser beam used in the interferometer has a gaussian rather than uniform amplitude, with significant consequences on its relation to

Table 5.1 Balanced spherical aberration functions and standard deviations for uniform and gaussian illuminations [82].

Illumination	Aberration function W_s^b	standard deviation $\sigma_{W_s^b}$
uniform	$A_s(\rho^4 - \rho^2)$	$A_s/13.42$
gaussian, $\sqrt{\gamma} = 1$	$A_s(\rho^4 - 0.993\rho^2)$	$A_s/13.71$
gaussian, $\sqrt{\gamma} = 2$	$A_s(\rho^4 - 0.728\rho^2)$	$A_s/18.29$
gaussian, $\sqrt{\gamma} = 3$	$A_s(\rho^4 - 0.444\rho^2)$	$A_s/40.50$

diffraction and aberration. The amplitude G of a gaussian beam entering an optical system with a pupil of radius a can be described by [78]:

$$G(\rho) = G_0 e^{-\gamma\rho^2} \tag{5.14}$$

where G_0 is the central peak amplitude of the beam, and where γ is a truncation ratio defined by:

$$\gamma = \left(\frac{a}{\omega}\right)^2 \tag{5.15}$$

with ω the gaussian beam radius, defined as the radial distance where the beam intensity drop to $1/e^2$ of its central intensity. The balanced spherical aberration functions and standard deviations are given in table 5.1 for an uniform and a gaussian illumination, and for several value of the truncation ratio. For a strongly truncated beam ($\gamma \to 0$), the aberration free PSF is also the Airy pattern, and the gaussian nature of the input beam is lost through diffraction. Even for $\gamma = 1$, where the beam waist is made equal to the pupil radius, the aberration function and standard deviation are almost the same as the ones for an uniform illumination. It is usually desirable to avoid excessively truncating a gaussian beam, to minimize the effect of diffraction and preserve its gaussian shape, but also to mitigate losses of the beam power. The transmitted power is 99.97 % for $\sqrt{\gamma} = 2$, and practically 100 % when $\sqrt{\gamma} \geqslant 3$ [82]. In this range, the gaussian shape of the input beam is preserved, and the system aberration free PSF is also gaussian and corresponds to the one predicted by gaussian beam optics [105]. For large γ, the spherical aberration standard deviation is also reduced: the optical system wavefront function is now weighted by the gaussian amplitude of the beam, and a smaller weight is applied to the edge of the pupil where the beam amplitude is the lowest and the wavefront function is the largest. In other words, reducing the beam radius ω relative to the optical system aperture (increasing γ) has a similar effect that a reduction of the aperture for uniform illumination, but a gaussian beam is at the same time less sensitive to aberrations than an uniform beam. Accordingly, a larger Strehl ratio is obtained with a gaussian beam for the same aberration standard deviation. Another consequence is that for a gaussian beam with $\gamma > 1$, equation 5.11 is valid only for $S_r > 0.9$, and always underestimates the system Strehl ratio otherwise. There is no simple relation between the Strehl ratio of a gaussian beam and the aberration standard deviation in this case. Also, for a gaussian beam affected by spherical

aberration, the amount of balancing defocus is a function of γ, and decreases as γ increases (table 5.1). All of these observations are also true for coma and astigmatism [82].

From gaussian beam optics to classical geometric optics Another concern when using a laser beam is its behavior according to gaussian beam optics [105]. In the general case, the position of the input beam waist ω_0 and the beam Rayleigh range z_R must be accounted for to compute the location and magnification of the imaged waist ω'_0. The input beam waist and Rayleigh range are linked by:

$$z_R = \frac{\pi\omega_0^2}{\lambda} \tag{5.16}$$

There are however two cases where the conjugation relations of gaussian beam optics are equivalent to the classic relations of geometric optics. Let f be the absolute focal length of an element in the optical system considered. This two cases are:

- $z_R \ll f$: this case is encountered when the beam is focused to a tight spot, ω_0 is relatively small, and the beam has to propagate several Rayleigh ranges before the reach the element. The beam wavefront then approximates the one of a point source located at the waist.
- $z_R \gg f$: in this case, the beam is collimated with a relatively large waist, and the beam radius of curvature is large everywhere compared to the element focal length. The beam wavefront is then equivalent to the one of a point source at infinity. In this case, the beam radius ω can be assimilated to its waist radius ω_0, and stays constant for a large propagation length.

The laser beam of the CryoQPDI is always found in either one of these two special cases[1], in particular in the scanning objective. The gaussian nature of the beam can thus be ignored for propagation calculations, and must be remembered only for the computation of the beam waist size at focus (on the µcantilever). The spot radius ω'_0 obtained by focusing a collimated laser beam of radius ω_0 with a positive lens of focal length f′ (figure 5.2) can be computed with:

$$\omega'_0 = \frac{\lambda f'}{\pi\omega_0} \tag{5.17}$$

5.1.3 Spherical aberration of a thin lens

As a first exemple of aberration calculation and to help in the interpretation of the scanning objective design, the spherical aberration of a thin lens is considered. The

[1] For exemple, the measured beam radius at the interferometer input is 4.7 mm, corresponding to a Rayleight range of 130 m.

lens has a refractive index n and a focal length f′, and consists of two spherical surfaces of radius R_1 and R_2. These parameters are linked by the lensmaker equation [79]:

$$\frac{1}{\mathrm{f}'} = (n-1)\left(\frac{1}{R_1} - \frac{1}{R_2}\right) \tag{5.18}$$

The spherical aberration coefficient a_s of a thin lens is given by [79]:

$$a_s = -\frac{c_1}{\mathrm{f}'^3}\left(c_2 + c_3\,p^2 + c_4\,q^2 + c_5\,pq\right) \tag{5.19}$$

where the c_i coefficients are all positive and depend of the lens refractive index only:

$$\begin{aligned} c_1 &= \frac{1}{32n(n-1)} & c_2 &= \frac{n^3}{n-1} \\ c_3 &= (3n+2)(n-1) & c_4 &= \frac{n+2}{n-1} \\ c_5 &= 4(n+1) \end{aligned} \tag{5.20}$$

The Coddington position factor p depends only of the imaging conditions:

$$p = -\frac{2\mathrm{f}'}{s} - 1 = 1 - \frac{-2\mathrm{f}'}{s'} \tag{5.21}$$

with s and s' the object and image positions relative to the lens. The Coddington shape factor q depends only of the lens geometry:

$$q = \frac{R_2 + R_1}{R_2 - R_1} \tag{5.22}$$

Using equations 5.18 to 5.22, the following observations can be made about the spherical aberration of a thin lens [79, 108]:

- There is an infinite number of combinations of R_1 and R_2 to obtain a given focal length f′.
- The lens spherical aberration will however depends of the selected R_1-R_2 combination via the shape factor q.
- For a given imaging condition (a given p), there is an optimal lens shape (an optimum q) which minimize the lens spherical aberration. Such a lens is called a best form lens.
- In the important case where both the object and its image are real ($-1 \leqslant p \leqslant 1$), the spherical aberration of a lens cannot be zero. Even a best form lens will still introduces a finite amount of spherical aberration.
- Since the spherical aberration of a lens is related to the third power of its focal length, an optical system made from a proper combination of lenses having focal lengths of opposite signs can achieve zero spherical aberration.

The focusing of a collimated laser beam by a single positive thin lens in now considered. This is the situation represented in figure 5.2 if the PP′ system simply consists of a thin lens. For simplicity, the gaussian nature of the beam is ignored and equations 5.19, 5.3, 5.12 and 5.11 are used for aberration calculations. The laser beam of radius ω is thus assimilated to a parallel beam of light limited by an aperture $a = \omega$. Equation 5.17 is nonetheless used for computing the gaussian spot size, and the laser wavelength is set at $\lambda = 532\,\text{nm}$.

A parallel input beam correspond to an object at infinity ($s = -\infty$). The lens is therefore used at infinite conjugate, and the position factor is $p = -1$. The refractive index of the lens is set at $n = 1.5$ to be representative of common optical glass materials used in the visible. With $p = -1$ and $n = 1.5$, a plano-convex lens with its convex side facing the parallel beam is almost a best form lens [79], and this type of lens is thus selected. In this case, the lens shape factor is $q = 1$.

If the lens focal length and the beam radius are set to $\text{f}' = 30\,\text{mm}$ and $w = 2\,\text{mm}$, the configuration obtained is similar the one of the reference QPDI[1]. The corresponding peak aberration coefficient is $A_\text{s} = -0.173\,\mu\text{m}$, or $A_\text{s} = -0.325$ waves at 532 nm. This corresponds to a balanced spherical aberration standard deviation of $\sigma_{\Phi_\text{s}^\text{b}} = -0.0242$ wave RMS and a Strehl ratio of $S_\text{r} = 0.98$, from which a diffraction limited performance can be expected. The focused spot diameter is $2\omega_0' = 5.1\,\mu\text{m}$ in this case.

The lens focal length is now increased by a factor of five, to 150 mm. If one wants to obtain the same spot diameter, the input beam radius must be increased by the same factor, to 10 mm. The configuration is now similar to the CryoQPDI one. However, the lens spherical aberration parameters are now $A_\text{s} = -1.624$ waves, $\sigma_{\Phi_\text{s}^\text{b}} = -0.121$ wave RMS and $S_\text{r} = 0.56 < 0.8$, which indicates that the focused spot size is likely increased due to a non negligible amount of spherical aberration. The peak spherical aberration coefficient and the aberration standard deviation were also increased by a factor of five, because A_s vary as a^4/f'^3. Remarkably, the lenses in this two examples does not contribute the same amount of spherical aberration even if they are used with the same F-number of F/7.5. These examples illustrate why a special attention was given to spherical aberration in the design of the CryoQPDI scanning objective.

As a last example, the settings are again $\text{f}' = 30\,\text{mm}$ and $w = 2\,\text{mm}$, but the plano-convex lens is now oriented with its flat side toward the input beam, then changing the lens shape factor from $q = 1$ to $q = -1$. With the lens oriented in this "wrong" direction, the aberration standard deviation is now $\sigma_{\Phi_\text{s}^\text{b}} = -0.0934$ wave RMS, around four time larger than the one obtained in the "right" direction, for a Strehl ratio of $S_\text{r} = 0.71$. This last example illustrates the influence of the lens shape, which can be exploited for spherical aberration compensation in a multielement lens system.

[1] In the reference QPDI, the focusing lens is actually an achromatic triplet, which offers additional correction when the lens is displaced off-axis.

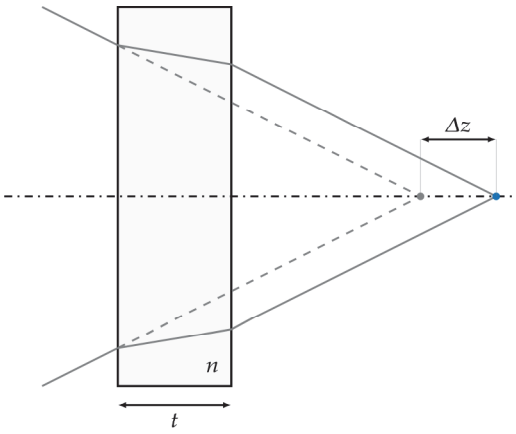

Figure 5.3 Longitudinal focus shift resulting from the insertion of a plane parallel plate in a converging light beam.

5.1.4 Spherical aberration of plane-parallel plate

The spherical aberration introduced by a plane-parallel plate is now discussed. If a light beam is focused through a plane-parallel plate, the plate introduces spherical aberration in the beam because the rays reaching the plate at an angle have to travel an extra optical path length before to exit the plate. The peak spherical aberration coefficient of a plate computes as [80]:

$$A_{\mathrm{s}} = \frac{n^2 - 1}{128 n^3} \frac{t}{\mathrm{F}\#^4} \tag{5.23}$$

where n is the plate refractive index, t is the plate thickness, and where the F# to consider is the one of the image forming light cone. The spherical aberration introduced by a plate does not depend of the plate position in the focused beam, and is zero for a collimated beam (F# $\rightarrow \infty$).

Using equation 5.23, the spherical aberration introduced by the two cryostat windows can be evaluated (figure 5.1). The F# is set at $F/7.5$ as in section 5.1.3. The two windows are identical, with a thickness of 5 mm ($t = 10$ mm) and a refractive index of $n = 1.46$ at 532 nm [28]. The total peak aberration coefficient for the two plates is $A_{\mathrm{s}} = 0.0169$ waves, corresponding to a balanced spherical aberration standard deviation of $\sigma_{\Phi_{\mathrm{s}}^{\mathrm{b}}} = 0.0013$ wave RMS and a Strehl ratio of $S_{\mathrm{r}} = 1$. As a conclusion, the spherical aberration introduced by the cryostat windows is negligible.

The only (first order) effect that should be considered for design is the plate focus shift Δz, which is a translation of the image point along the optical axis resulting from the insertion of the plate (figure 5.3):

$$\Delta z = t \left(1 - \frac{1}{n} \right) \tag{5.24}$$

5.1.5 Scanning objective optical design

Operating principle The working principle of the scanning objective is explained with the help of figure 5.4. This design has two main characteristics: it provides a small spot size on the μcantilever despite a long working distance, and permits a positioning of the focused spot in three dimensions (lateral displacement and focus).

The telescope lens L_{T1} and L_{T2} are arranged as a Galilean telescope which is used as a beam expander [111]. The input radius of the laser beam is enlarged by the telescope magnification M:

$$M = -\frac{f'_{T2}}{f'_{T1}} \tag{5.25}$$

where f'_{T1} and f'_{T2} are the focal lengths of L_{T1} and L_{T2} respectively. Since the focal lengths of the two telescope lenses are of opposite signs, the telescope magnification M is positive. The telescope is used to enlarge the beam before the sample lens L_S. From equation 5.17, increasing the input beam radius by a factor M results in a reduction of the focused spot size by the same factor. The scanning objective assembly is equivalent to a lens L with a focal length f'_L given by [111]:

$$f'_L = \frac{f'_S}{M} \tag{5.26}$$

If ω_0 is the laser beam radius at the scanning objective input, the spot size on the sample is therefore:

$$\omega'_0 = \frac{\lambda f'_S}{\pi M \omega_0} \tag{5.27}$$

Together, equations 5.26 and 5.27 illustrate the main idea of the scanning objective. As shown in figure 5.4, for a given input beam diameter, the scanning objective achieves the same spot size that would be obtained with a lens of focal length f'_S/M, but with a working distance of f'_S. As a result, all the scanning objective elements can be placed outside of the intrument cryogenic environnement, with a significant simplification of the interferometer design. Since expanding the beam also increases the system effective pupil radius, a downside of this approach is an increased sensibility to spherical aberration, as discussed previously.

Another concern is to align the laser spot on the μcantilever. The μcantilever is brought into focus by a translation of the sample lens L_S along the optical axis. Since the beam before L_S is collimated, the lens and the system focal point are displaced by the same amount, with no alteration of the spot size. A lateral displacement of the spot is obtained by translating the first telescope lens L_{T1} normally to the optical axis. By scanning L_{T1} by a distance d, the virtual point image of the beam created by this lens is displaced by the same distance. The second lens of the telescope L_{T2} now collimates the light from a point object located at a distance d above the optical axis, and provides

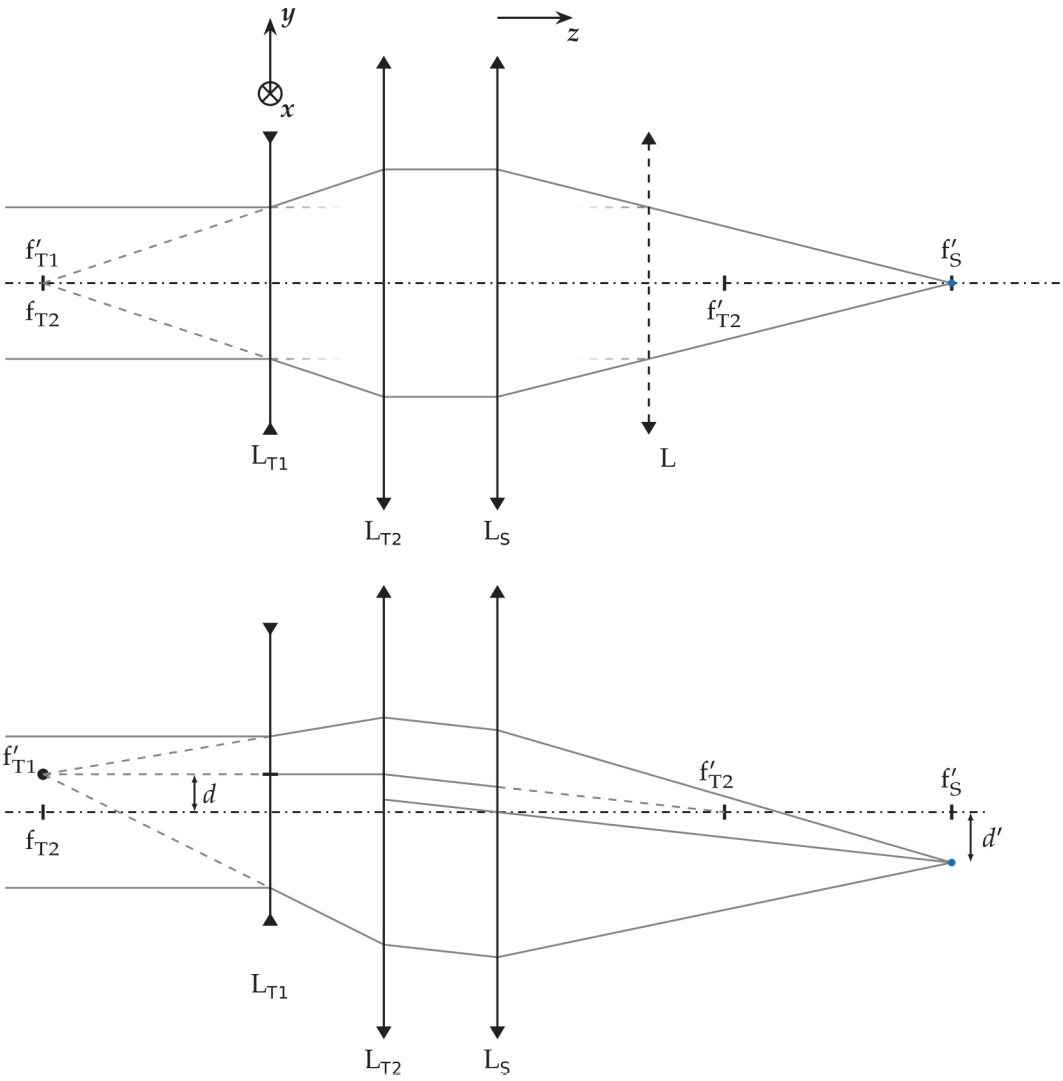

Figure 5.4 Paraxial optical scheme of the scanning objective.
On the top: the scanning objective consists of an assembly of three lens. The first two lenses $\mathrm{L_{T1}}$ and $\mathrm{L_{T2}}$ form a galilean telescope which is used as a beam expander. With an enlarged input beam, the last lens $\mathrm{L_S}$ is able to focus to a smaller spot. The system is equivalent to a lens L whose equivalent focal length is $\mathrm{f'_S}/M$, where $M = -\mathrm{f'_{T2}}/\mathrm{f'_{T1}}$ is the telescope magnification. A longitudinal displacement z of $\mathrm{L_S}$ is used to focus the beam on the sample.
On the bottom: The lateral positioning of the laser spot is acheived by translating $\mathrm{L_{T1}}$ off the optical axis. The relation between the displacement d of $\mathrm{L_{T1}}$ and the spot displacement d' is $d'/d = -\mathrm{f'_S}/\mathrm{f'_{T2}}$.

a parallel beam at an angle α to the optical axis. The spot produced by L_S is thus translated laterally by an amount d'. Using the construction of figure 5.4, one can obtain the following expression:

$$\alpha = -\frac{d}{f'_{T2}} = \frac{d'}{f'_S} \tag{5.28}$$

From which the relation between the two displacements d and d' follows immediately:

$$d' = -\frac{f'_S}{f'_{T2}} d = l_{disp}\, d \tag{5.29}$$

where the lateral displacement coefficient $l_{disp} = -f'_S/f'_{T2}$ have been introduced. The three translation direction of the spot are linear and independent.

Expressed in another way, the lateral positioning or scanning function of the scanning objective accomplished by displacing L_{T1} is a deliberate misalignement of the system. This is not the most direct approach which can be employed to align the laser and the sample. However, if the lens of the scanning objective where fixed, one would need to move the cantilever and the interferometer relative to each other. In this case, with the cantilever fixed, the entire interferometer assembly would need to be displaced, which is impractical. On the other hand, leaving the interferometer fixed and moving the µcantilever would have required motorized actuators able to operate at cryogenic temperature. Such actuators are very expensive, and come with an additional design and setup complexity. At the end, the solution offered by the scanning objective appears both simpler to implement and less expensive. Displacing the optical elements of the objective is comparatively easier to achieve, and since the complete objective assembly is located outside of the cryostat, this displacements can be done with manual rather than motorized stages[1], further reducing the system cost. Understandably, misaligning the system also introduces aberrations into the beam: this issue is treated in the next paragraph.

Ray tracing Even if it consists of only three lenses, the problem of correcting the spherical aberration of the scanning objective can only be managed by the use of a ray tracing sofware, given the large number of parameters involved. Accordingly, the selection of the scanning objective lenses was carried out using the Zemax version 12 ray tracing software [125].

[1] The motorization of the scanning objective displacements was also considered, but was not retained in the final CryoQPDI design due to time and budget constrains. Motorizing the objective instead of the µcantilever or the entire interferometer would still have resulted in a lower system cost.

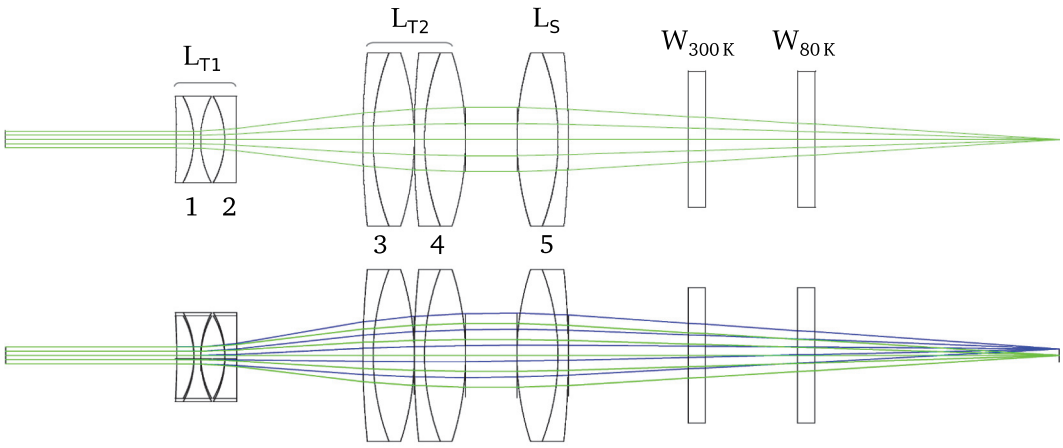

Figure 5.5 Application of ray tracing to the scanning objective design. The software was used to assist the selection of the system's lenses. The diagram on the top displays the rays path with the L_{T1} lens on axis ($d = 0$). The diagram on the bottom is a superposition of the previous diagram (green rays) with a second diagram where L_{T1} is displaced below the optical axis (blue rays). The first telescope lens L_{T1} is the combination of a negative achromatic doublet and a negative plano-concave singlet (element n°1 and n°2). The second telescope lens L_{T2} is an assembly of two positives achromatic doublet (element n°3 and n°4), and the sample lens L_S consist of one of the element of L_{T2}, but with an opposite orientation (element n°5). The relevant optical parameters of the system are provided in table 5.2. The influence of the two cryostat windows $W_{80\,K}$ and $W_{4\,K}$ was also evaluated during this design.

Under normal circumstance, the optical designer would be free to select the number of lenses involved as well as their refractive indices and radii of curvature. However, the scanning objective design was done with the additional constraint of using only commercially available stock lenses. This choice was made with the aim of reducing the system cost and development time. This strong constraint is allowed by the relative simplicity of the aberration correction problem considered: the scanning objective needs to be corrected for only one wavelength and only at infinite conjugate (only for a collimated input beam), and its design involves only moderate F-numbers.

The software interface was used to test several candidate combinations of lenses until a design with negligible spherical aberration was found, with the L_{T1} lens on-axis ($d = 0$). The L_{T1} lens was then displaced to assess the system performance when the scanning function is used, and a range of acceptable displacement was determined. The input beam was left to the default uniform illumination setting: since the ray tracing software employed is primarily intended for the development of imaging systems, it was difficult to use it outside of an uniform illumination context. To account for the gaussian nature of the laser beam, the input beam radius was set to 2.5 mm, close to the measured CryoQPDI input beam $1/e^2$ radius. As explained is section 5.1.2, a system corrected for aberration with an uniform beam in this manner will also perform well for a laser beam because a gaussian beam is comparatively less sensitive to aberration.

Table 5.2 Optical parameters of the scanning objective. The truncation ratio is computed using the expanded beam radius and the sample lens mount clear aperture of 48.3 mm in diameter.

Element n°	Reference	diameter	nominal f′
1	ACN-254-040-A	25.4 mm	−40.1 mm
2	LC1715-A	25.4 mm	−50 mm
3, 4, 5	AC508-150-A	50.8 mm	150 mm
Scanning objective lenses		Scanning objective assembly	
f_{T1}	−20.6 mm	M	3.77
f_{T2}	77.6 mm	l_{disp}	-1.93
f_{T2}	150 mm	f_L	39.8 mm
Beam parameters			
ω_0	2.35 mm	$M\omega_0$	8.86 mm
$\sqrt{\gamma}$	2.73	ω'_0	2.87 μm

The scanning objective design resulting from this procedure is displayed in figure 5.5. Besides using the information of section 5.1.3, the scanning objective lens selection process was conducted following two design principles [110, 112]:

- Lens splitting : the aberration of a lens can be reduced by substituting it with two lenses with larger focal lengths. This method can reduce the aberration of the lens being replaced by approximately a factor 5. This method was used for L_{T1} and L_{T2}, which both consist in a combination of two lenses. In the case of L_{T1}, this method also permitted the use of lenses with larger diameters, since it is not possible to find a single lens with a diameter smaller than its focal length.
- Use achromatic doublet and triplet lenses. The use of achromatic lenses in a monochromatic application may be surprising. However, besides chromatic aberrations, these lenses are also designed to minimize spherical aberration and coma at a specific conjugate ratio. Using an achromatic lens then gives a lower aberration to start with. In the scanning objective, all but the second element are cemented achromatic doublets corrected at infinite conjugate.

To obtain a relatively compact assembly, the first step was to use a relatively large beam diameter in the interferometer. The beam diameter is set by the fiber collimator at the interferometer input (figure 5.1). Doing so, the necessary telescope magnification and thus the telescope length, one of the main determinant of the system size, were kept to moderate values. Following the discussion of section 5.1.2, the largest possible lens diameters were used to preserve the beam power and limit the effect of diffraction.

The system optical parameters are provided in table 5.2. The equivalent focal length of L_{T1} and L_{T2} was determined with the sofware for a better accuracy, and the remaining parameters were computed using equations 5.25 to 5.29. The resulting values of the telescope magnification M and the displacement coefficient l_{disp} were also verified in software. The scanning objective theoretical spot diameter is 5.74 μm.

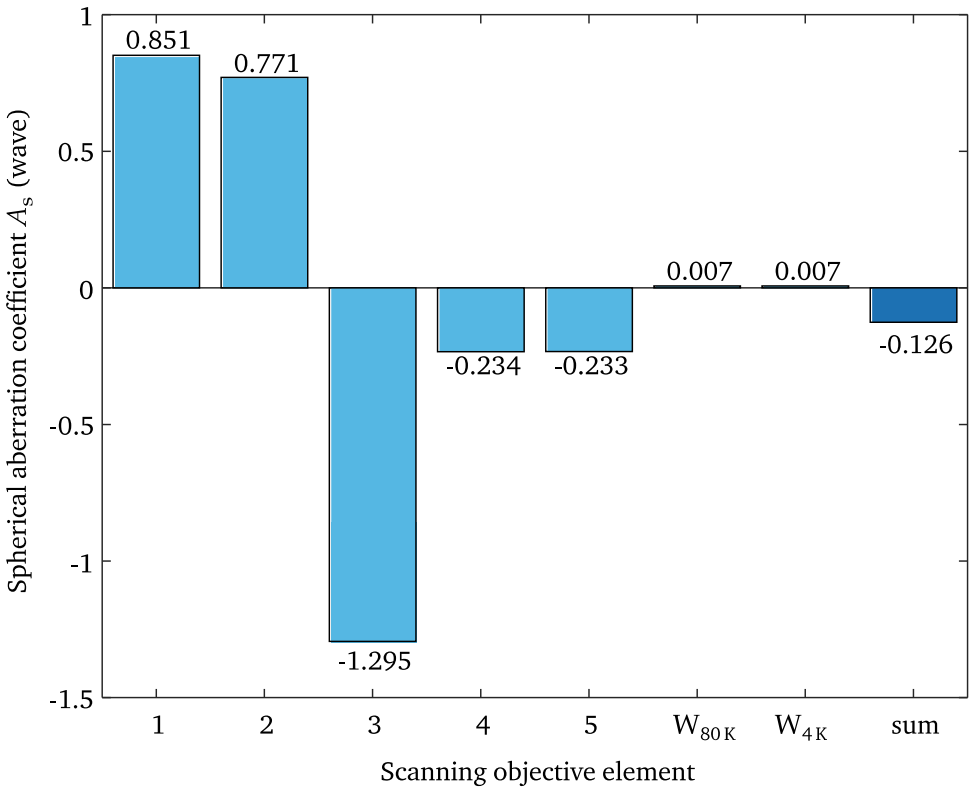

Figure 5.6 Spherical aberration contribution of the scanning objective elements. The elements are identified in figure 5.5.

Figure 5.6 shows the contribution of the scanning objective lenses as well as the cryostat windows to the total system spherical aberration, in the case where L_{T1} is on-axis. As expected from the result of section 5.1.4, the contribution of the cryostat windows is negligible. The two negative lenses of L_{T1} introduce positive spherical aberration to compensate the negative spherical aberration introduced by the remaining positive lenses. Since the number of negative lenses in the scanning objective is lower that the number of positive lenses, the aberration contributions of the negative lenses was increased on purpose, first by using a singlet plano concave lens as the second element, and then by using the first element in the "wrong" orientation. Even if the same lens model is used for the elements n°3, n°4 and n°5, the aberration contribution of the third lens is larger because it is not used at infinite conjugate in this case.

The system spot diagram is displayed in figure 5.7 for three value of the L_{T1} lens displacement d. These diagram where recorded after a research of the best image plane: the best geometric focus for which the ray bundle dispersion is minimum was first determined, and a minimization of the wavefront standard deviation was then executed. This procedure is an application of the golden rule of optical design mentioned at the end of section 5.1.1. These spot diagrams can be used for a qualitative evaluation of the effect of a L_{T1} displacement on the system aberration performance. As the lens is displaced, the input beam is set to travel in the scanning objective at an angle which increases with larger displacement. The system is then affected by

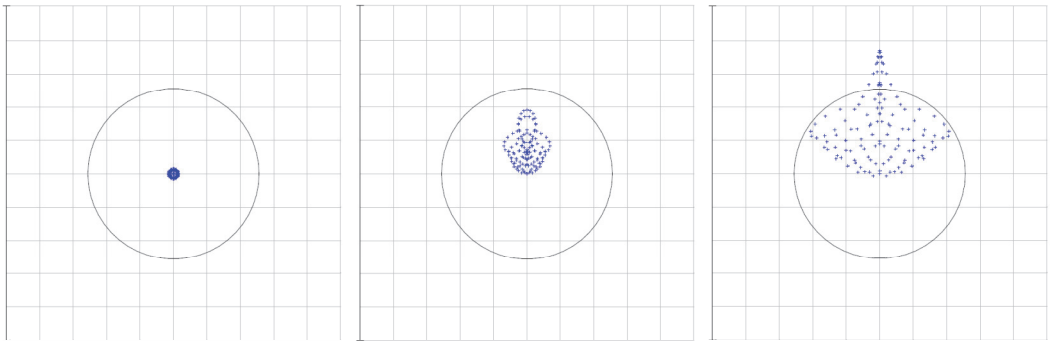

Figure 5.7 Spot diagram of the scanning objective as a function of the displacement d of the first telescope lens. The small blue crosses displays the point of intersection of a ray with the image plane at best focus. The spot diagram of an aberration free system is a single point. For the three diagrams, the grid lines are spaced by $2\,\mu\mathrm{m}$ and the circles mark the Airy disk which has a radius of $5.1\,\mu\mathrm{m}$ in this case. The applied displacement is $d = 0\,\mathrm{mm}$ on the left, $d = 0.5\,\mathrm{mm}$ on the center and $d = 1\,\mathrm{mm}$ on the right.

Table 5.3 Aberration performance of the scanning objective as a function of the scanning lens displacement ($\lambda = 532\,\mathrm{nm}$).

Displacement d (mm)	Wavefront standart deviation σ_W (wave)	Strehl ratio S_r
0	0.0037	0.9995
0.5	0.0630	0.8550
1	0.1335	0.4948

a mix of spherical aberration, coma and astigmatism (equation 5.1). Accordingly, the observed rays dispersion increases for larger values of d. The system wavefront standard deviations corresponding to the three spot diagrams of figure 5.7 are given in table 5.3. In each case, the corresponding Strehl ratio for uniform illumination was computed using equation 5.11. For $d = 0\,\mathrm{mm}$ and $d = 0.5\,\mathrm{mm}$, the system Strehl ratio is larger than 0.8. In this displacement range, the amount of aberration introduced by the misalignement of $\mathrm{L_{T1}}$ can be tolerated, and a diffraction limited performance can be expected. At $d = 1\,\mathrm{mm}$, the Strehl ratio of around 0.5 indicates that the amount of aberration is significant in this case. However, as discussed in section 5.1.2, the corresponding Strehl ratios for a gaussian beam are larger than the one displayed in table 5.3. Due to a software limitation, it was not possible to determine the system aberration component with the $\mathrm{L_{T1}}$ lens displaced off-axis, and a precise calculation of the Strehl ratio would also requires a determination of the system wavefront function on its full aperture, not only up to the uniform beam radius. However, the results of reference [82] can be used for a rough estimate of the gaussian beam Strehl ratio. With a truncation ratio of $\gamma = 2.73$ and a wavefront standard deviation of 0.1335 wave RMS, the Strehl ratio of the scanning objective is probably at least between 0.7 and 0.8 when $d = 1\,\mathrm{mm}$. At this point, there are two more reasons to expect a smaller wavefront standard deviation than the one mentionned in the previous sentence. First, the $1/e^2$ diameter of the CryoQPDI input beam is measured at 4.7 mm, smaller than the 5 mm diameter that was used for ray tracing. Second, since a uniform illumination

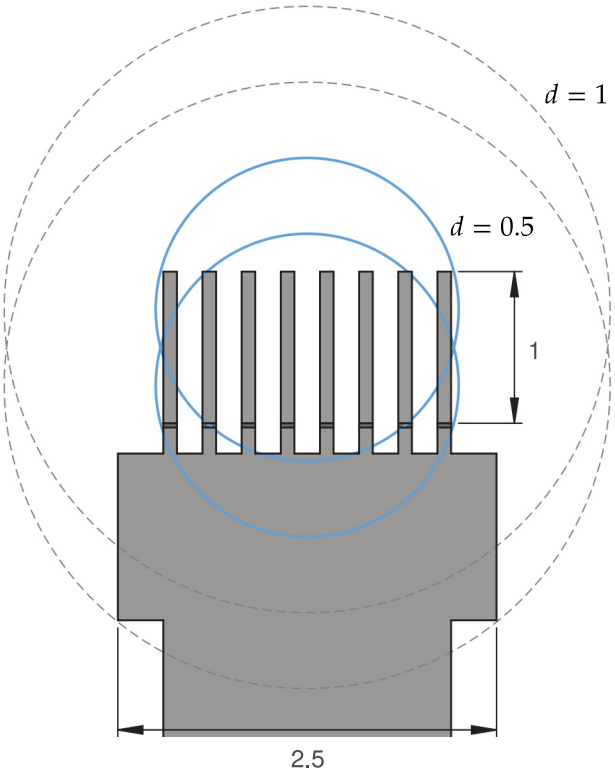

Figure 5.8 Aberration corrected lateral positioning range of the scanning objective. For each value of the displacement d, the two circles represent the corresponding range of position for the two spot generated by the birefringent beam splitter.

was used, the best focus point found by the software is not the one that would have been found with gaussian illumination (table 5.1). For these two reasons, the actual Strehl ratio of the scanning objective for $d = 1$ mm is probably larger than 0.7-0.8. As a conclusion, a small focused spot diameter can be expected even with such a large displacement of the L_{T1} lens.

The range of accessible spot positions is compared to the size of a µcantilever sample in figure 5.8. The sample displayed supports eight 1 mm long µcantilevers, which are the longest cantilevers available among the samples used in the context of this work (appendix A). It therefore represents the worst use case for the scanning objective. With a lateral displacement coefficient $\left|l_{\text{disp}}\right|$ of almost 2, the scanning objective aberration corrected lateral positionning range is a circle with a radius d' of around 1 mm or 2 mm, for $d = 0.5$ mm and $d = 1$ mm respectively. In figure 5.8, this range is found to cover all the µcantilevers of the sample. As a final conclusion, the scanning objective is expected to provide a small focused spot size for all the common use case of the CryoQPDI.

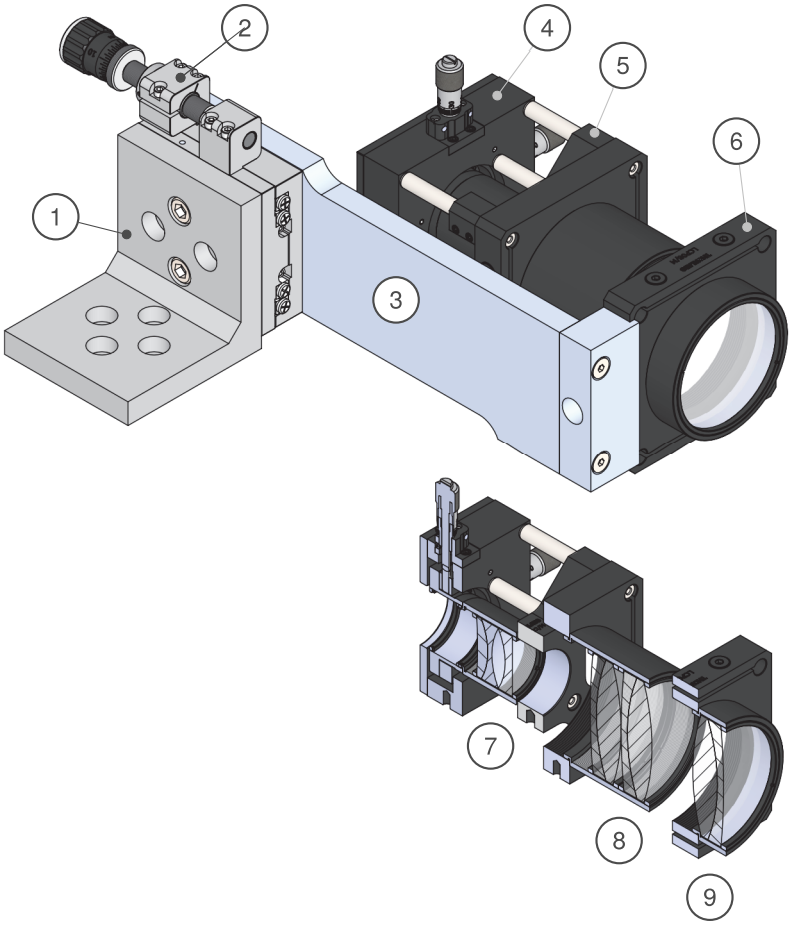

Figure 5.9 Overview of the scanning objective mechanical assembly.

Item	Description	Item	Description
1	Vertical mounting bracket	6	Focus assembly
2	Linear stage (focus)	7	L_{T1}
3	Focus arm	8	L_{T2}
4	XY translation mount (lateral positioning)	9	L_S
5	Telescope assembly		

5.1.6 Scanning objective construction

An overview of the scanning objective construction is provided in figure 5.9. The displacement of the first telescope lens is done using a lateral lens translation mount. The sample lens mount is attached to a linear translation stage via a plate called the focus arm, which is also the only custom component of the assembly. Another possibility would have been to use a lens zoom mount, but no commercially available zoom mount were found without a significantly limited clear aperture. A translation stage with crossed roller bearings was selected to provide adequate load capacity and rigidity even when mounted in a vertical position. In practice, the focusing action does not result in any appreciable lateral displacement of the laser spot. The system dimensions are given in figure 5.10. Thanks to the use of a large input beam and a sofware for aberration correction, it was possible to achieve a relatively compact design.

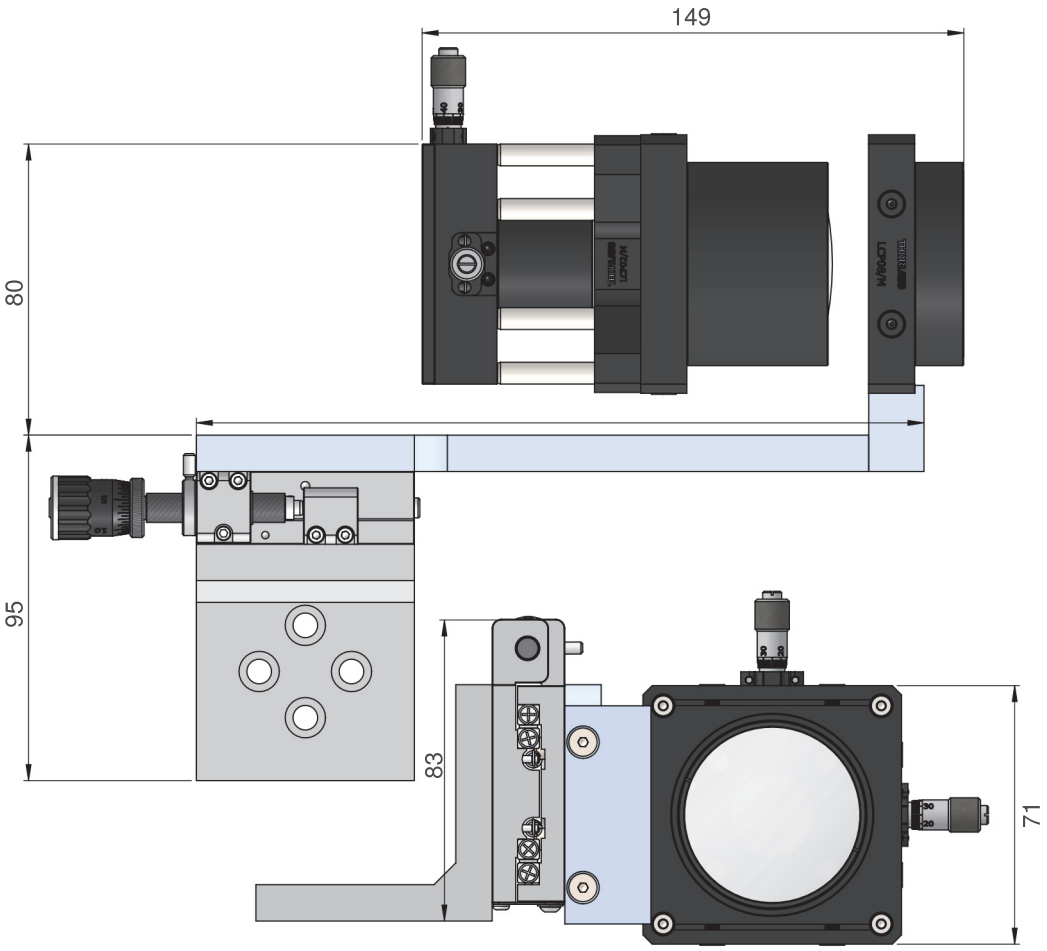

Figure 5.10 Top view and front view of the scanning objective. The dimensions are in millimeters, and were rounded to the nearest millimeters.

The orientation of the three manual positioning actuators makes them accessible to the operator[1].

5.2 Semel-Savart plate

In this section, a brief description of the birefringence phenomenom is provided, with an emphasis on how to exploit this effect for the construction of polarizing beam splitters. The propagation of a light ray incident on a birefringent plane-parallel plate at normal incidence is adressed first. A description of the crystal astigmatism encountered away from normal incidence is then provided, using both an analytical model and several illustrations. From there, birefringent beam splitters with increasing levels on complexity are elaborated to correct for this astigmatism. Several possible solutions are reviewed and a choice is made regarding the constraints of cryogenic

[1] If one consider replacing the manual actuators with motorized ones, this replacement can also be done directly without redesigning the scanning objective.

operation. A beam splitter based on the choosed design is constructed. At last, the results obtained both in terms of spot size and contrast are birefly exposed.

5.2.1 Single plate

Birefringence Birefringence is a property exhibited by several transparent materials, especially by crystals possessing an anisotropic lattice structure [15, 39]. In these crystals, the birefringence is manifested by a refractive index which depends on light's polarization and direction of propagation.

A ray of light striking the surface of an arbitrarily oriented birefringent crystal is generally refracted into two rays having orthogonal polarizations, different propagation directions and different velocities. This phenomenom is termed double refraction, and makes birefringent crystals natural polarizing beam splitters.

There may be one or two special propagation directions inside a anisotropic crystal for which the double refraction is not observed. Such a special direction is called an optical axis of the crystal. Crystals possessing one optical axis are described as uniaxial, and crystals with two optical axes are described as biaxial. In the context of this manuscript, only devices made of uniaxial crystals are considered.

The double refraction of a light ray by a plane-parallel plate cut into an uniaxial crystal is illustrated in figure 5.11 and 5.12, for normal incidence. One of the two refracted rays passes through the crystal without deviation and is called the ordinary ray (o ray). It behaves as in an isotropic media and experiences a constant index of refraction n_o, the ordinary index of the crystal. The other ray is the extraordinary ray (e ray), and does not obey Snell's law. Despite normal incidence, it is refracted at an angle by the plate, inducing a lateral displacement d between the two rays, and exits the plate parallel to the o ray. The index of refraction for the e ray is a function of its propagation direction inside the crystal, and varies between n_o and n_e, where n_e is the crystal's extraordinary index.

Birefringent uniaxial crystals can further be classified as negative (N) or positive (P) according to the sign of their birefringence $n_e - n_o$. For a negative uniaxial crystal $n_e - n_o < 0$, and for a positive uniaxial crystal, $n_e - n_o > 0$.

The two refracted rays are contained within the plate principal plane, defined by the optical axis and the z axis. As the optical axis corresponds to a direction inside the crystal (and not to a particular axis), any plane parallel to the principal plane is also a principal plane. In figure 5.11, the plate is cut so that its lateral faces are principal planes. The extraordinary ray is linearly polarized with its polarization direction parallel to the principal plane, and the ordinary ray is linearly polarized with its polarization perpendicular to the principal plane. Both rays exist because the incident

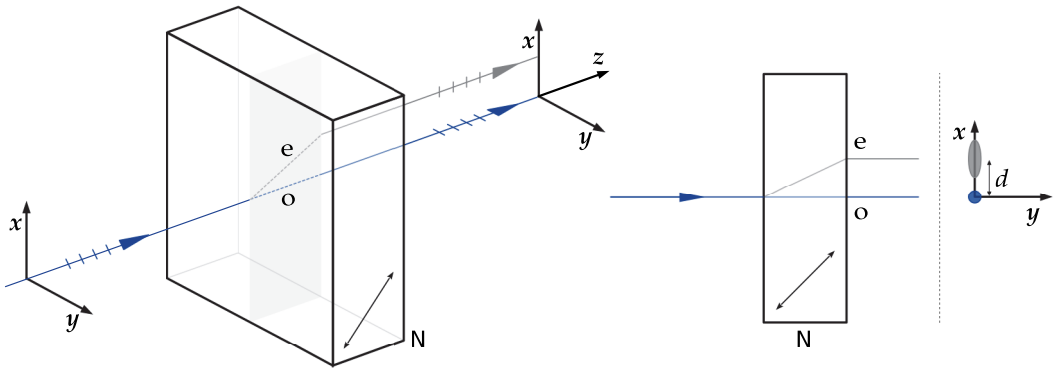

Figure 5.11 Double refraction of a light ray normally incident on a plane-parallel plate made of a negative uniaxial crystal.
On the left: the plate is cut so that its lateral faces are principal planes. The crystal optical axis is indicated by the black double arrow on the right face. The N label designates a negative uniaxial crystal. The grey plane inside the plate marks the principal plane at the point of incidence. Dashed lines are used to display rays propagating inside the plate. The coordinate system is oriented so that the xy plane is parallel to the plate's entrance face, the x axis belongs to the principal plane, and the y axis is perpendicular to it. The z axis is oriented along the (normally) incident ray propagation direction. The incident light is linearly polarized at an angle to the principal plane. The ordinary and extraordinary rays are labelled o and e respectively. The propagation direction of all the rays is pointed out by an arrow, and their polarization directions is indicated by an inclination of both the propagation arrow and the small segments before it.
On the right: on this simplified representation, the principal plane is in the plane of the page, and the polarization directions are not indicated. Upon double refraction, the e ray is displaced by a distance d with respect to the o ray. The coordinates have been rotated to display the displacement direction and sign. The spot geometry obtained when focusing a beam of light through the plate is roughly approximated by either an elongated ellipse or a circle, the meaning of which being explained at the end of section 5.2.1.

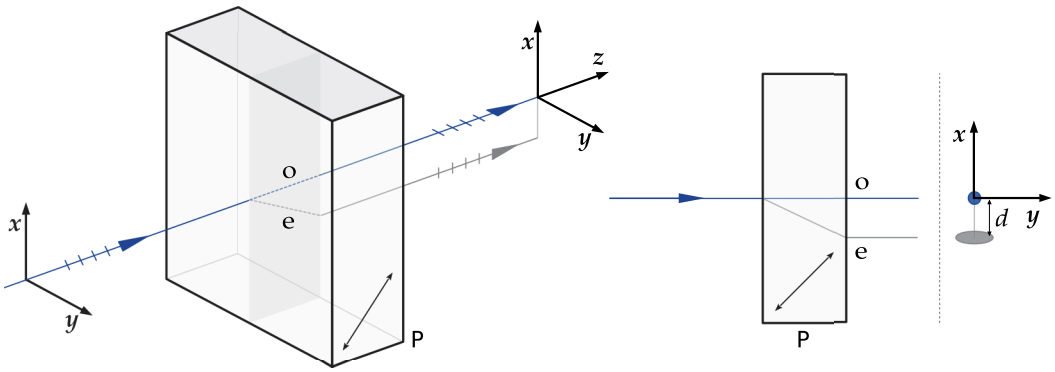

Figure 5.12 Same as figure 5.11, but for a positive uniaxial cristal (P). The displacement between the two refracted beams is in the opposite direction of the one obtained with a negative cristal. On the right, also notice the different orientation of the ellipse spot for the extraordinary beam, compared to a negative crystal.

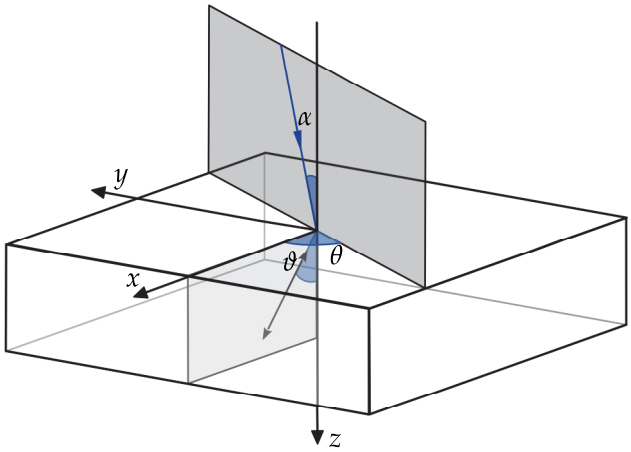

Figure 5.13 Definition of the angles ϑ, θ and α. The optical axis of the crystal is contained in the principal plane, which is displayed as the grey plane inside the plate. The plane of incidence is the grey plane at the top of the plate. Both of these planes contain the z axis, which is normal to the plate (entrance) surface. ϑ is the angle made by the optical axis with the z axis, α is the angle of incidence, and θ is the angle between the plane of incidence and the principal plane. The angles ranges are $\alpha, \vartheta \in [0°, 90°]$ and $\theta \in [0°, 360°]$.

ray contains energy in both of these priviledged polarization directions of the crystal. A linearly polarized incident ray with a polarization direction parallel or perpendicular to the principal plane would only give rise to an e or an o ray respectively. An incident beam of light does not need to be linearly polarized for the e and o beams to behave as explained here, but this offers a simple mean to balance the power between the two beams, as with any polarizing beam splitter.

Lateral displacement For normal incidence, the lateral displacement d between the e and the o rays is a function of the plate thickness t, the ordinary and extraordinary refractive indices n_o and n_e of the crystal, and the angle ϑ between the optical axis and z (figure 5.13). It is given by the following relation [40]:

$$d(\vartheta) = \frac{\sin 2\vartheta}{\frac{n_o^2 + n_e^2}{n_o^2 - n_e^2} - \cos 2\vartheta} t \tag{5.30}$$

There is zero lateral displacement for $\vartheta = 0°$ and $\vartheta = 90°$. The first case corresponds to an optical axis normal to the entrance face of the plate: the axis is then aligned with the incident ray propagation direction, and there is no double refraction. The index of the crystal is n_o for any polarization. The case $\vartheta = 90°$ corresponds to an optical axis laying in the plate entrance surface. Double refraction occurs, but the e and o rays are superimposed, and the crystal index for the e ray is equal to n_e. This last case is the arrangement used for the construction of waveplates.

For a given plate thickness and a given material, the lateral displacement is maximum when the optical axis angle obeys the following relation:

$$\cos 2\vartheta = \frac{n_o^2 - n_e^2}{n_o^2 + n_e^2} \tag{5.31}$$

The angle ϑ for maximum separation is found close to 45° for many uniaxial crystal[1]. For this reason, and for simplicity, the kind of birefringent beam splitter discussed here are often designed with plates cut at 45° to the optical axis. For ϑ =45°, equation 5.30 becomes:

$$d = \frac{n_o^2 - n_e^2}{n_o^2 + n_e^2}\, t \tag{5.32}$$

In the same way as for this equation, a dependance in ϑ not indicated means that ϑ=45°. From equation 5.30 or 5.32, it can be seen that the displacement direction is opposite for opposite signs of the crystal birefringence. For example, in figures 5.11 and 5.12 and with the chosen coordinate system, the plate made of a negative uniaxial crystal generates a positive displacement along the x axis, but the plate made of a positive crystal gives a negative displacement along the same axis.

In addition to the lateral displacement, the plate also introduces an optical path difference Δ between the two refracted rays. The optical path difference is taken as the optical path length of the extraordinary beam minus the optical path length of the ordinary beam ($\Delta = \mathrm{OPL}_e - \mathrm{OPL}_o$). For normal incidence, Δ computes as [116, 41]:

$$\Delta_{\alpha=0°}(\vartheta) = (n_\epsilon - n_o)\, t \tag{5.33}$$

where n_ϵ is an effective refractive index defined by:

$$\frac{1}{n_\epsilon^2} = \frac{1}{n_e^2}\sin^2\vartheta + \frac{1}{n_o^2}\cos^2\vartheta \tag{5.34}$$

Focusing through a birefringent plate: crystal aberration The more general case where the incidence is not normal is now studied. As a consequence, the angle of incidence α and the angle θ between the plane of incidence and the principal plane of the crystal (figure 5.13) must be considered. The optical path difference Δ now computes as [116, 41]:

$$\begin{aligned}\Delta(\vartheta,\alpha,\theta) = {} & \Delta_{\alpha=0°}(\vartheta) + d(\vartheta)\cos\theta\sin\alpha \\ & + \frac{1}{2}\left[\Delta_x(\vartheta)\cos^2\theta + \Delta_y(\vartheta)\sin^2\theta\right]\sin^2\alpha \\ & + \text{terms in } \sin^4\alpha, \text{etc.}\end{aligned} \tag{5.35}$$

[1] At 532 nm, the optical axis angle for maximum lateral displacement is ϑ =41.83° degree for calcite and ϑ =48.13° for YVO_4 (see table 5.4 for the corresponding indices).

where the path differences Δ_x and Δ_y are given by

$$\Delta_x(\vartheta) = t\left(\frac{1}{n_o} - \frac{n_\epsilon^3}{n_o^2 n_e^2}\right) \tag{5.36}$$

$$\Delta_y(\vartheta) = t\left(\frac{1}{n_o} - \frac{n_\epsilon}{n_e^2}\right) \tag{5.37}$$

In equation 5.35, the second term in simply the optical path difference due to the plate lateral displacement [41]. Since this lateral displacement is one of the desired effect of the plate, it is not an issue. The last terms are negligible under paraxial conditions and can be ignored.

The two remaining term of equation 5.35, however, have important effects when a beam of light is focused through an uniaxial plate. The first term in equation 5.35, namely the finite optical path difference introduced by the plate at normal incidence (equation 5.33), already implies that for a focused incident beam, the foci of the ordinary and extraordinary beams are not located at a same distance away from the plate, and thus dont have the same coordinate along the z axis.

In figure 5.14, let z_c be the coordinate of the incident light beam focal point along the z axis in the absence of the plate. After the plate is inserted, for the ordinary beam the plate has the same effect as an isotropic plate, which is to first order only a longitudinal translation of the focus of the incident beam (equation 5.24). The ordinary focus longitudinal position z_o is thus given by:

$$z_o = z_c + t\left(1 - \frac{1}{n_o}\right) \tag{5.38}$$

The extraordinary beam is additionally affected by a first order astigmatism which results directly from the crystal anisotropy, namely a crystal aberration. Away from normal incidence, the extraordinary ray is located in the plane of incidence only when it also contains the principal plane ($\theta = 0°, 180°$) or is normal to the principal plane ($\theta = 90°, 270°$) [107]. The effect of this crystal astigmatism on an extraordinary focus is illustrated in figure 5.14. After being refracted by the crystal, the extraordinary beam no longer focuses at the same location along or normal to the principal plane. Instead of being focused to a point, this beam gives rise to two foci lines. One of them lays in the principal plane, the other one is normal to it. The z coordinates of the two foci lines are given by:

$$z_e^x = z_c + t\left(1 - \frac{n_\epsilon^3}{n_o^2 n_e^2}\right) \tag{5.39}$$

$$z_e^y = z_c + t\left(1 - \frac{n_\epsilon}{n_e^2}\right) \tag{5.40}$$

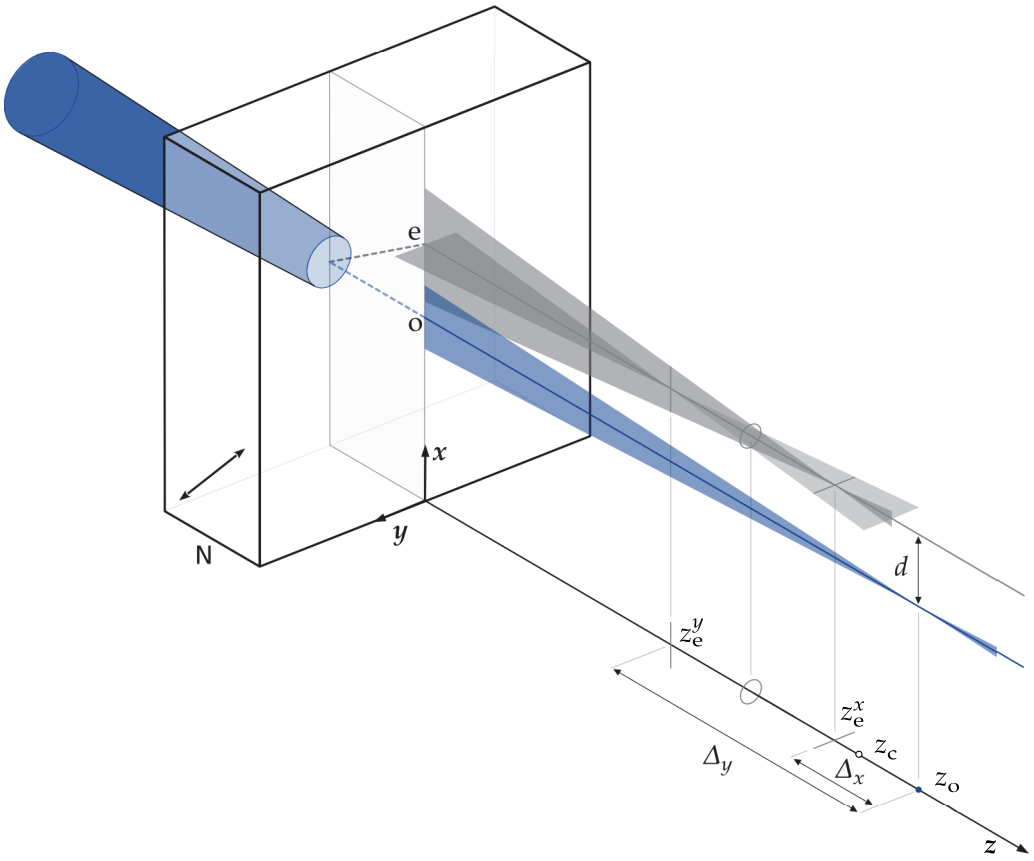

Figure 5.14 Focusing of a light cone through a uniaxial plane-parallel plate under paraxial conditions. The e and o beam generated by the plate double refraction are displayed by cross sections parallel and perpendicular to the plate principal plane (parallel to the xz and yz planes). The o beam is unaberrated and gives a point focus located at z_{o}. Accordingly, only a section parallel to the principal plane is displayed. However, the e beam is affected by a crystal astigmatism resulting from the peculiarities of the extraordinary refraction. Under the effect of this astigmatism, the extraordinary focus is split along the beam propagation direction, so that the focus in x and y no longer occurs at the same z position. The e beam thus converges to two foci lines: the x-focus, located at z_{e}^{x}, is a focus line along the y axis, and the the y-focus, located at z_{e}^{y}, is a focus line along the x axis. The best geometric focus, or circle of least confusion [120], is marked by a circle and is located midway between the two foci lines. Δ_x and Δ_y are the longitudinal optical path differences between the ordinary point focus and the two extraordinary foci lines. The relative position of the o and e foci displayed is for to a calcite plate at $532\,\mathrm{nm}$, for $\vartheta = 45°$.

where z_e^x is the longitudinal position of the x-focus, giving a focus line along the y axis, and where z_e^y is the longitudinal position of the y-focus, corresponding to the other focus line oriented along the x axis. The longitudinal path differences between the ordinary focus and the two extraordinary foci lines are thus:

$$z_e^x - z_o = \Delta_x(\vartheta) \tag{5.41}$$

$$z_e^y - z_o = \Delta_y(\vartheta) \tag{5.42}$$

where the two path differences Δ_x and Δ_y are retrieved from their expression in equations 5.36 and 5.37. The third term in equation 5.35 therefore expresses the optical path difference induced by the first order crystal astigmatism experienced by the extraordinary beam.

From this analysis, Δ can be interpreted under paraxial conditions as the optical path difference between two wavefronts, one spherical, unaberrated wavefront centered on the ordinary focus at z_o, and an astigmatic wavefront corresponding to the superposition of two cylindrical wavefronts centered on the two foci lines at z_e^x and z_e^y [116]. The first two terms in equation 5.35 respectively account for the relative longitudinal and transversal translations of these two wavefronts due to the plate beam splitting effect.

Regarding the interferometer performance, the first and third term in the expression of Δ (equation 5.35) are the problematic ones, and should be corrected to obtain a birefringent beam splitter free of aberration. Since the wavefronts of the two beams produced by the birefringent plate are not equal, these terms are associated with a degradation of the interferometer contrast and of the focus quality in the extraordinary beam case (figure 5.14).

Simplified representation of the crystal astigmatism To make a drawing like the one of figure 5.14, one must know the relative position of z_o, z_e^x and z_e^y along the z axis, which is given by the signs of the path differences Δ_x, Δ_y and $\Delta_y - \Delta_x$. Here this sign study was done only for the case $\vartheta = 45°$. From equations 5.36, 5.37 and 5.34, one can find that both Δ_y and $\Delta_y - \Delta_x$ have the same sign as the crystal birefringence $n_e - n_o$. The sign of Δ_x, however, is very difficult to obtain analytically, but can easily be evaluated numerically in special cases. For the materials used in our polarizing beam splitter, it is found that Δ_x also have the sign of the birefringence at 532 nm (table 5.4). As a result, the relative positions of the foci are not the same for a plate made of a positive or a negative uniaxial crystal:

$$z_e^y < z_e^x < z_o \quad \text{for} \quad n_e - n_o < 0 \qquad \text{(Calcite at 532 nm)} \tag{5.43}$$

$$z_e^y > z_e^x > z_o \quad \text{for} \quad n_e - n_o > 0 \qquad \text{(YVO}_4\text{ at 532 nm)} \tag{5.44}$$

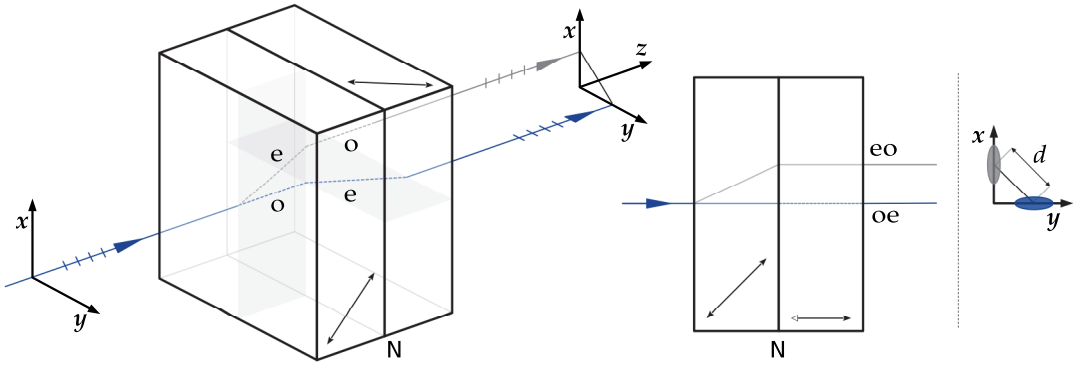

Figure 5.15 Beam splitting by a Savart plate made of a negative uniaxial crystal. A Savart plate consists of two plates of equal thickness made of the same birefringent material, with their optical axis at 45° to the entrance face normal. The second plate is rotated so that its principal plane is perpendicular to the principal plane of the first plate. In the simplified representation on the right, a horizontal double arrow indicates that the optical axis lies in a plane perpendicular to the plane of the page. The arrow end marked with an empty arrow head is the farthest from the plane of the page. A dashed horizontal line indicates a beam propagating away from the plane of the page and coming closer to the reader.

The first case (equation 5.43) is the one displayed by figure 5.14. This results stems from the fact that the crystal aberration of a positive or a negative uniaxial plate have opposite signs, which is exploited in section 5.2.3 to construct a beam splitter free of first order crystal astigmatism.

This result is also used in all the polarizing beam splitter schematics of this section to provides a simplified representation of the crystal aberration effect on the focus. Here, an unaberrated focus is represented by a circle, while a focus affected by the crystal astigmatism is represented by an elongated ellipse, roughly mimicking the beam shape at the line focus the closest to the plate.

5.2.2 Savart plate

The first term of equation 5.35 can be eliminated by using a Savart plate[1]. As shown in figure 5.15 and 5.16, a Savart plate consists of two identical birefringent plates with perpendicular principal planes, and with their optical axes set at $\vartheta = 45°$. Doing so, the ordinary beam of the first plate become the extraordinary beam of the second plate (oe beam), and vice versa. The two plates produce equal lateral displacements in perpendicular direction, so that the total displacement is $\sqrt{2}$ times the displacement d of a single plate. From equation 5.32, the lateral displacement of a Savart plate thus writes [40]:

$$d_{\text{Savart}} = \sqrt{2}\,\frac{n_{\text{o}}^2 - n_{\text{e}}^2}{n_{\text{o}}^2 + n_{\text{e}}^2}\,t = \sqrt{2}d \tag{5.45}$$

In equation 5.35, setting $\vartheta = 45°$ and neglecting the last term provides the optical

[1] Also refered to as a Savart polariscope.

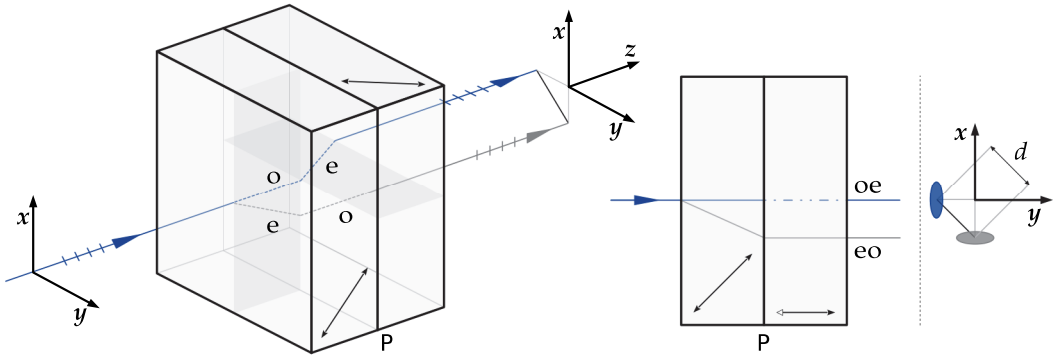

Figure 5.16 Same as figure 5.15, but for a positive uniaxial crystal. In the simplified representation, a dash-dotted horizontal line indicates a beam propagating away from the plane of the page and going away from the reader.

path difference introduced by the first element of the Savart plate [67]:

$$\Delta_1(\alpha,\theta) = \Delta_{\alpha=0^\circ} + d\cos\theta\sin\alpha + \frac{1}{2}\left[\Delta_x\cos^2\theta + \Delta_y\sin^2\theta\right]\sin^2\alpha \tag{5.46}$$

The optical path difference of the second element is obtained by replacing θ with $\theta + \pi/2$ in equation 5.46 [67]:

$$\Delta_2(\alpha,\theta) = \Delta_{\alpha=0^\circ} - d\sin\theta\sin\alpha + \frac{1}{2}\left[\Delta_x\sin^2\theta + \Delta_y\cos^2\theta\right]\sin^2\alpha \tag{5.47}$$

The total optical path difference between the two beam generated by the Savart plate is thus given by [40, 67]:

$$\begin{aligned}\Delta_{\text{Savart}} = \Delta_1 - \Delta_2 = {} & \frac{d_{\text{Savart}}}{\sqrt{2}}\left(\cos\theta + \sin\theta\right)\sin\alpha \\ & + k_\Delta\left(\sin^2\theta - \cos^2\theta\right)\sin^2\alpha\end{aligned} \tag{5.48}$$

with

$$k_\Delta = \frac{t}{\sqrt{2}}\frac{n_o\left(n_o^2 - n_e^2\right)}{n_e\left(n_o^2 + n_e^2\right)^{3/2}} \tag{5.49}$$

With no constant term in this expression, the path difference is zero for normal incidence and the foci of the two beams are brought in the same plane. However, now that the two beams are extraordinary each in turn, they are both affected by crystal astigmatism (figures 5.14 and 5.16), and a term in $\sin^2\alpha$ remains. The effect of this term is studied in figure 5.17. To obtain the experimental interferogram of this figure, the interferometer optical scheme of figure 5.1 was modified by replacing the μcantilever by a mirror and by inserting a linear polarizer between the BS_s and BS_c. This polarizer is needed to allow the two superimposed and orthogonally polarized beams to interfer. The interferogram was observed on a screen placed after the polarizer. The observed fringe pattern is the one expected for pure astigmatism [81].

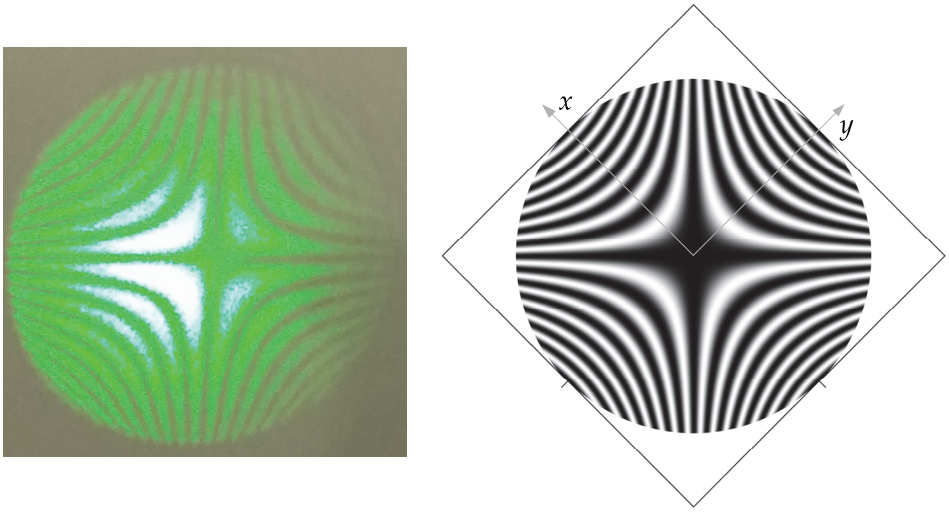

Figure 5.17 Fringe pattern of the interferometer beam generated by the crystal astigmatism of a Savart plate. On the left: experimental interferogram resulting from two passes of the focused beam in a Savart plate. This picture is simply a photograph of the interferogram which was observed on a screen. On the right: corresponding numerical interferogram (equation 5.51).

As the experimental interference pattern was obtained after the recombination of the two beams by the Savart plate, the $\sin\alpha$ term of equation 5.54 associated with lateral displacement is eliminated. A model for the observed optical path difference is thus the $\sin^2\alpha$ term:

$$\Delta_{\text{exp}} = k_\Delta \left(\sin^2\theta - \cos^2\theta\right)\sin^2\alpha \tag{5.50}$$

The Savart plate used in this case was made of calcite and had a total thickness of $2t = 6.4\,\text{mm}$, corresponding to a lateral displacement of $500\,\mu\text{m}$ at 532 nm. Using this thickness value and the refractive index of calcite provided in table 5.4, the coefficient k_Δ is $k_\Delta = 125\,\mu\text{m}$. The numerical interferogram of figure 5.17 is computed using (equation 2.21, page 20):

$$I_{\text{exp}} = \frac{1}{2}\left[1 + \cos\left(\Phi_c + \frac{2\pi}{\lambda}\left(2\times\Delta_{\text{exp}}\right)\right)\right] \tag{5.51}$$

For $\alpha \in [0°, 7°]$ and $\theta \in [0°, 360°]$. The factor of 2 applied to Δ_{exp} accounts for the two passes in the Savart plate. A constant phase shift between the two beam of $\Phi_c = \pi$ was added to reproduce the dark fringe observed in the center of the field, and the interferogram was rotated by 45° to correctly represent the Savart plate orientation. In figure 5.17, the experimental and numerical interferograms are in good agreement, which confirms that the observed fringe pattern was generated by crystal astigmatism in the Savart plate.

From the numerical interferogram of figure 5.17, it is also possible to compute the expected contrast of the interferometer in these conditions. The interferogram was first normalized by a gaussian amplitude profile with a $1/e^2$ radius set at the edge of the

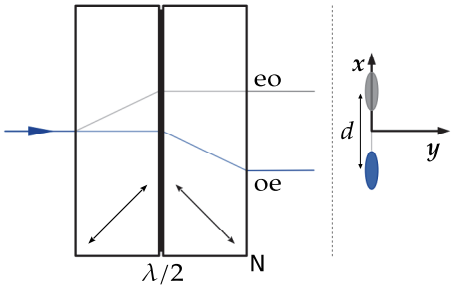

Figure 5.18 Françon modification of the Savart plate [42].

angular aperture, at 7°[1]. The resulting pattern was then integrated for several value of Φ_c between 0 and 2π to reproduce the signal of a photodetector during calibration, and the corresponding local contrast was extracted. Using the same local contrast for the four photodetectors in equations 2.27 and 2.28 (page 21), the computed contrast of the interferometer is circular and centered with a radius of 0.27. This contrast is in good qualitative agreement with the experimental contrast of ≈ 0.18 which was observed using this Savart plate[2]. These results confirmed that the crystal astigmatism of a birefringent beam splitter is the main source of contrast degradation for a quadrature phase differential interferometer. Since it is a first order effect, the astigmatism of a plate only a few millimeters in thickness cannot be neglected, even for a light cone of only a few degrees in aperture.

5.2.3 Aberration corrected birefringent beam splitters

To eliminate both the relative defocus of the two beams and the effect of crystal astigmatism represented by the first and third terms of equation 5.35, a birefringent beam splitter design more elaborated than the one of a Savart plate is required. Several such designs have been proposed in the litterature, among which five possible designs suitable for monochromatic operation are reviewed here [42, 67, 71]. Based on this review, a design for the CryoQPDI birefringent beam splitter is selected and the corresponding design equations are used to construct it. An approximate measurement of the system spot size is then performed to assess the proper operation of both the scanning objective and the birefringent beam splitter.

A review of aberration corrected birefringent beam splitter designs The first design considered is presented in figure 5.18, and is a modification of the Savart plate proposed by Françon [42]. The plates are oriented so that their optical axes lie in

[1] This imaging conditions were obtained with a previous version of the scanning objective.

[2] The use of a Savart was considered in the CryoQPDI design primarily because of its ability to eliminate the relative defocus between the two beams of the interferometer. At this point, the issue of crystal astigmatism was not yet clarified. There, the poor experimental contrast that was observed motivated deeper investigations, and the fringe pattern of figure 5.17 revealed the crystal astigmatism problem, and motivated the use of an aberration corrected birefringent plate

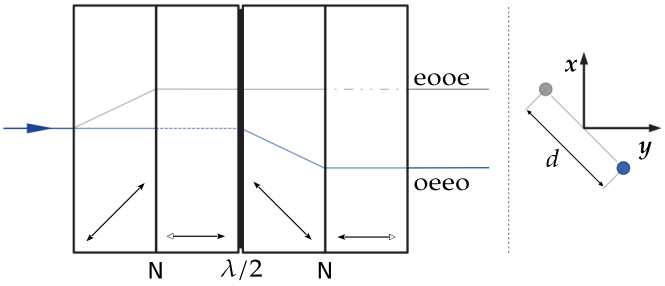

Figure 5.19 Semel "standard solution" for a birefringent beam splitter free of aberrations [71].

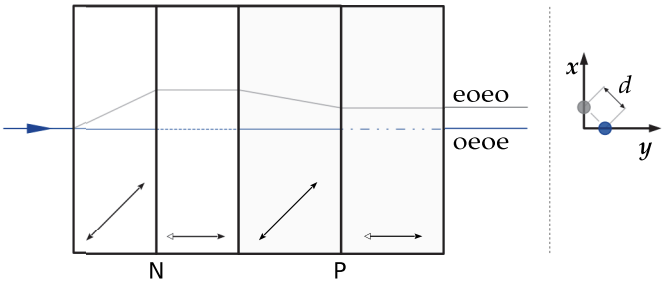

Figure 5.20 Enhanced Savart polariscope design proposed by Li, Zhu and Hou [67].

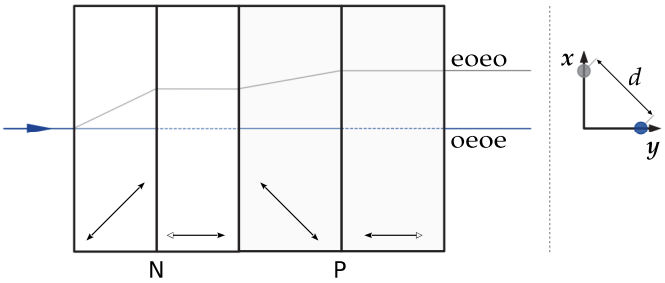

Figure 5.21 Semel aberration free beam splitter "heterogeneous solution 1" [71].

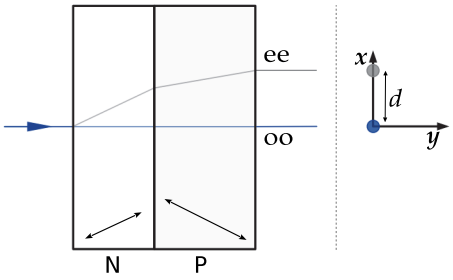

Figure 5.22 Semel aberration free beam splitter "heterogeneous solution 2" [71].

the same plane and are perpendicular to each other. An half wave plate is inserted between the plate and its axis is oriented at 45° to the plane containing the plate axes. The polarizations of the two beams exiting the first plate are rotated by 90° before entering the second plate: their role are thus exchanged and the second plate is able to introduces an additionnal displacement between the beams. As with a Savart plate, both beams are affected by a finite amount of crystal astigmatism, but this astimatism now have the same orientation for both beams. The third term of equation 5.35 is effectively eliminated, but the focus of each beam is still affected by crystal astigmatism. Using this design, a good contrast can be expected, but with an important degradation of the focus quality.

The second design reviewed was proposed by Semel [71] and is refered to as a "standard solution" by this author. Here this design is called standard with reference to the Françon design. As shown in figure 5.19, these design share important similarities. Instead of individual plates, two Savart plates are separated by a half wave plate. For each beam, the second Savart plate introduces an astigmatism which is perpendicular to the one introduced by the first Savart plate. The total crystal astigmatism of each beam is thus cancelled, and this design is free of aberration. Both a good contrast and good focus quality can be expected.

The third design under consideration is displayed in figure 5.20, and was proposed by Li, Zhu and Hou [67]. The general idea remains the same: cancel the aberration of a first Savart plate by using a second Savart plate. However, here the second Savart plate is made of a birefringent material with a birefringence sign opposite to the one of the first Savart plate. This design exploit the fact that two birefringent plates with opposite signs of birefringence and with parallel principal planes introduce astigmatisms in perpendicular directions. This fact can be appreciated by comparing the simplified representations of figures 5.11 and 5.12, or of figures 5.15 and 5.16. Doing so, the design proposed by Li, Zhu and Hou does not requires an half wave plate. The total astigmatism of this beam splitter is set to zero at a particular wavelength after the determination of a specific thickness ratio between each plate. However, with the orientation of figure 5.20, the second Savart plate partly cancel the lateral displacement of the first Savart plate, so that for a given lateral displacement, this design is much thicker that the other designs reviewed here. It is again a beam splitter design free of aberration.

The fourth design was also proposed by Semel [71] and was named "heterogeneous solution 1" by the author, where the term "heterogeneous" refers to the use of both a positive and a negative uniaxial crystal. As shown in figure 5.21, it is identical to the previous design, only that the two Savart plates are now in antiparallel orientation. The advantages in terms of aberration correction is retained, but now both Savart plates contribute to the total lateral displacement so that a much smaller total plate thickness can be used.

At last, the fifth design considered is again due to Semel [71], and is called "heterogeneous solution 2" in the cited reference. It is displayed in figure 5.22. It can be seen as a Françon design where the half wave plate is removed by using opposite birefringent material, only that here the extraordinary beam is also free of crystal astigmatism, with no degradation of the focus. With only two elements, this design is the simplest of all the design reviewed here. However, to cancel both the relative defocus between the beam and the plates astigmatism, the plates optical axes must be set away from the $\vartheta = 45°$ condition.

Selection of a beam splitter design The main advantage of using a birefringent beam splitter with parallel beam separation is that the beam splitter can be positioned very close to the μcantilever, giving the interferometer a short arm length which was found to provide stability against external disturbance [93]. For this reason, the CryoQPDI birefringent beam splitter is the only optical element placed in the cryostat cryogenic environment, to be close to the sample under study. This constraint suggests the use of a simple and compact beam splitter design.

As mentioned at the beginning of section 5.2.1, setting the optical axis at 45° of the birefringent plate surface normal provides close to optimum lateral displacement for many birefringent material. This has the important consequence of making such birefringent plates available as standard component. A birefringent plate cut at an angle away from this standard can be expected to be more expensive.

Of the five birefringent beam splitter designs reviewed in the previous paragraph, the Françon design is the only one which is not aberration free, and is therefore not suitable to preserve both the focus quality and the contrast of the interferometer. The "standard solution" of Semel appears impractical because it demands an half wave plate and a mounting solution for this plate which are both compatible with cryogenic temperatures. The Semel "heterogeneous solution 2" is desirable for its simplicity and its compactness, but has the important drawback of requiring non standard birefringent plates. As pointed out before, the design proposed by Li, Zhu and Hou and the "heterogeneous solution 2" by Semel are identical except for the relative orientation of the two Savart plates, which makes the Semel proposition much more compact. Based on these arguments, the "heterogeneous solution 1" proposed by Semel and displayed in figure 5.21 was considered the best aberration free birefringent beam splitter design for the CryoQPDI. In other word, this design was selected because it is the most compact design using only standard birefringent plates. Because it is based on the Savart plate concept, this birefringent beam splitter is called a "Semel-Savart plate" in other parts of the present dissertation.

Design of the CryoQPDI Semel-Savart plate Let t_N be the thickness of an individual plate made of the negative uniaxial crystal, and t_P the thickness of an individual

plate made of the positive uniaxial crystal. The total thickness of the Semel-Savart plate t_{tot} is simply:

$$t_{tot} = 2\left(t_P + t_N\right) \tag{5.52}$$

The total lateral displacement d_{tot} generated by the plate is

$$d_{tot} = d_{Savart\,P} + d_{Savart\,N} = \sqrt{2}\left(-t_P\left(\frac{n_o^2 - n_e^2}{n_o^2 + n_e^2}\right)_P + t_N\left(\frac{n_o^2 - n_e^2}{n_o^2 + n_e^2}\right)_N\right) \tag{5.53}$$

From equation 5.54, the total optical path difference $\Delta_{Semel-Savart}$ of the Semel-Savart plate computes as:

$$\begin{aligned}\Delta_{Semel-Savart} = &\frac{d_{tot}}{\sqrt{2}}\left(\cos\theta + \sin\theta\right)\sin\alpha \\ &+ \left(k_{\Delta P} + k_{\Delta N}\right)\left(\sin^2\theta - \cos^2\theta\right)\sin^2\alpha\end{aligned} \tag{5.54}$$

where the subscript N and P respectively refer to the first and second Savart plate. In this expression, the term in $\sin^2\alpha$ which is responsible for the plate crystal astigmatism can be eliminated the relative thickness of the positive and negative plates is chosen to obey the following condition:

$$k_{\Delta P} + k_{\Delta N} = 0 \Leftrightarrow \frac{t_P}{t_N} = -\frac{\left(\dfrac{n_o\left(n_o^2 - n_e^2\right)}{n_e\left(n_o^2 + n_e^2\right)^{3/2}}\right)_N}{\left(\dfrac{n_o\left(n_o^2 - n_e^2\right)}{n_e\left(n_o^2 + n_e^2\right)^{3/2}}\right)_P} \tag{5.55}$$

The design process start with the selection of two high birefringence uniaxial materials. From their indices at the working wavelength considered, the plates thickness ratio is determined using equation 5.55, and the total thickness of the Semel Savart plate is adjusted to achieve the targeted lateral displacement. Ideally, this displacement should be slightly shorter than the length of the µcantilevers to be measured. If several µcantilever lengths are to be encountered, the beam separation should be shorter than the length of the shortest µcantilever considered, to ensure that the two beams of the interferometer can be focused on the cantilever surface in all cases. In our case, this requirement corresponds to a beam separation below but close to 500 μm (appendix A).

The thicknesses of the CryoQPDI Semel-Savart plate elements was determined by the availability of two 1 mm thick calcite plates at the laboratory. Calcite is a negative uniaxial crystal commonly used to build polarizing optical components. Yttrium orthovanadate YVO_4 was selected as the pairing positive uniaxial crystal mainly thanks to its availability. The design parameters of the CryoQPDI Semel-Savart plate are listed in table 5.4. The plate design beam separation is 419.4 μm, and is achieved with less

Table 5.4 CryoQPDI Semel-Savart plate design at $\lambda = 532\,\mathrm{nm}$.

Material		Calcite (N)	YVO_4 (P)
ordinary index [94]	n_o	1.6629	2.0177
extraordinary index [94]	n_e	1.4885	2.2508
birefringence	$n_e - n_o$	-0.1744	0.2331
lateral displacement coefficient	$d = t \times (\cdot)$	0.1103	-0.1089
thickness ratio	t_P/t_N	1.7101	
plate thickness	t [mm]	t_N =1.0000	t_P =1.7101
total thickness of the combination	t_{tot} [mm]	5.4202	
total lateral displacement	d_{tot} [µm]	419.4	

than 6 mm of total plate thickness.The beam separation is relatively low compared to 500 μm, but was kept as is to accomodate the vertical drift of the µcantilever during cryogenic measurements (chapter 8).

As mentioned earlier, the solution retained for the design of the CryoQPDI birefringent beam splitter [71] and the design proposed by Li, Zhu and Hou [67] differ only by a rotation of one of the Savart plate. One can find that equation 5.55 is the same for both references, except for the use of a different notation. This mean that one can build a birefringent beam splitter based on the concept presented here and select two differents beam separation only by a rotation of one of the Savart plate.

Spot size measurement As quick assessment of the system lateral resolution, the interferometer laser spots were brought into focus on a µcantilever and the spots were scanned up to its edge. The spots were then displaced outside of the µcantilever while monitoring both the total optical power on the photodetectors and the position of the scan lens. The photodetectors signals went to zero after a single 10 μm step of the scan lens actuator for both spots, which is also the actuator resolution. Taking into account the absolute scanning objective displacement ratio of almost 2, the spot was displaced by around 20 μm. While this result does not allow for an accurate determination of the spots $1/e^2$ diameter, it shows that this diameter is certainly much smaller than 20 μm. Also, in the last chapter of the dissertation dedicated to experimental results, the detection of both the higher bending modes of the µcantilever and of several of its torsions mode demonstrates than the system lateral resolution in sufficient for this purpose.

Contrast The important benefit of the Semel-Savart plate for the interferometer contrast is displayed in figure 2.4, page 24. An average ellipse radius above 0.8 is routinely achieved by the instrument. It is the highest contrast ever achieved with a QPDI based on the concept presented in chapter 2.

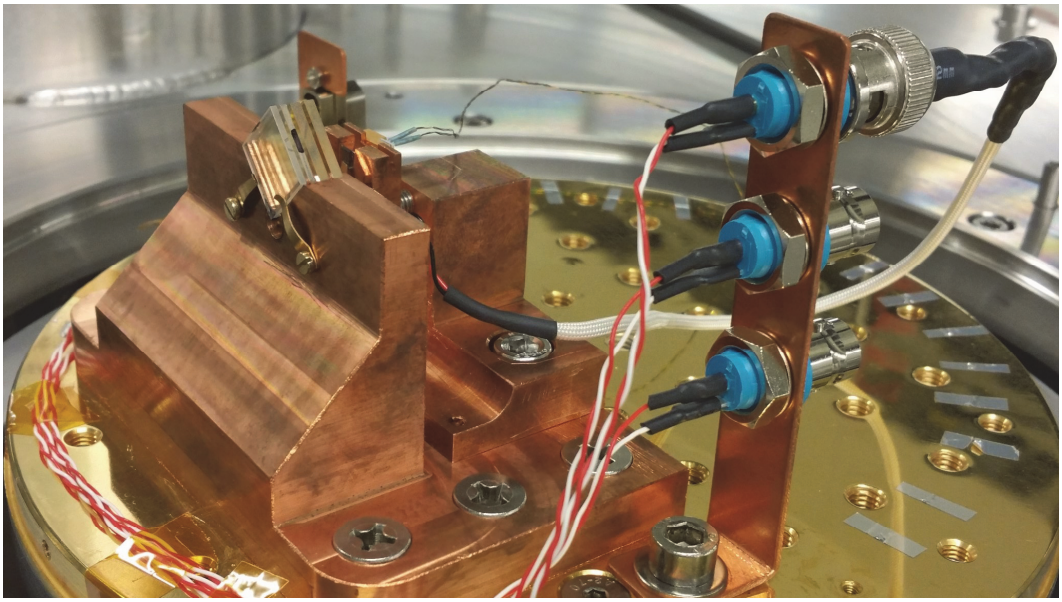

Figure 5.23 Photograph of the cryo holder installed on the cryostat cold plate. The holder is made of a cryogenic grade, high purity copper, and occupies around half of the cold plate surface. The white cable connects the piezo ceramic to one of the available BNC connectors.

5.3 Cryo holder

The cryo holder is a mechanical assembly used to hold the cryocooled element of the CryoQPDI inside the cryostat. Its two main functions are to place the Semel-Savart plate and the μcantilever sample at an adequate height above the cold plate surface, in the center of the cryostat's windows aperture, and to provide an adequate thermal conductivity between the sample and the cold plate.

The problem of cooling the sample and therefore the cryo holder design is relatively simple for two reasons. First, the system minimum operating temperature of ≈7 K is relatively high, avoiding many practical problems encountered at lower temperatures, say at or below 1 K [96]. Second, the thermal mass of a μcantilever sample is very small, making it easy to cool. In this context, the cryo holder design was carried out following only two guidelines: use a high thermal conductivity material for the holder body, and ensure a good thermal contact between individual elements. A photograph of the cryo holder is displayed in figure 5.23. The main components of the cryo holder are made of oxygen free high conductivity (OFHC) copper, which is commonly used for its very high thermal conductivity at cryogenic temperature [89, 97].

The main components and features of the cryo holder are presented in figure 5.24 and 5.25. The cryo holder assembly consists of two main parts, which are the Semel-Savart plate holder and the sample holder. Under normal condition, the Semel-Savart plate holder is permanently attached to the cold plate, which avoid unnecessary manipulations of the fragile crystal components of the beam splitter. On the other

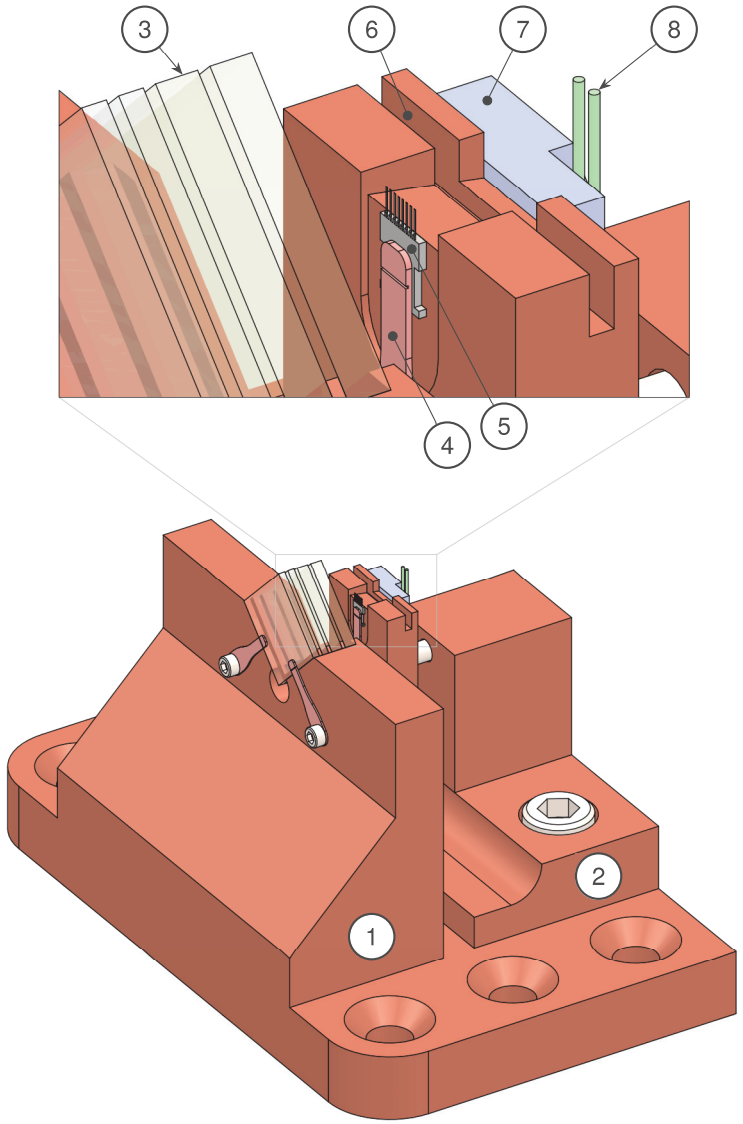

Figure 5.24 Overview of the cryogenic holder, first perspective.

Item	Description	Item	Description
1	Semel-Savart plate holder	5	μcantilevers sample
2	sample holder	6	sample back notch
3	Semel-Savart plate	7	temperature sensor support
4	sample clamp	8	temperature sensor connection

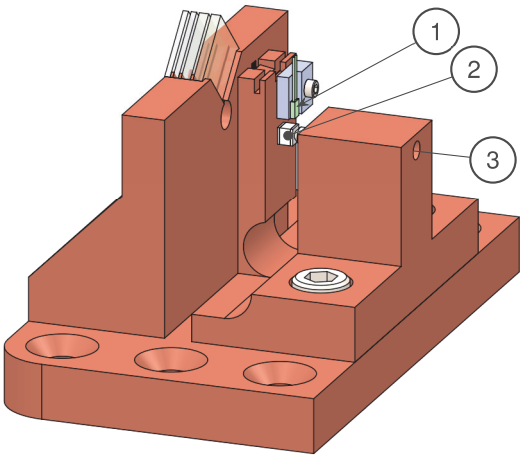

Figure 5.25 Overview of the cryogenic holder, second perspective.

Item	Description	Item	Description
1	temperature sensor	3	adjustement screw
2	piezo ceramic		

hand, the sample holder was made easy to remove from the cryogenic workspace to ease the exchange of samples.

The sample holder have a main body which can be grabbed easily by the operator, and a vertical beam-like section (or sample section) where the sample is clamped using a copper-beryllium spring clip. To help in the identification of these two regions, item n°6 in figure 5.24 belongs to the sample section, and item n°3 in figure 5.25 belongs to the main body of the sample holder.

On the sample section, a temperature sensor is attached very close to the sample to provide an almost direct reading of the µcantilever temperature. The sample holder also hosts the piezoelectric ceramic mentioned at the end of section 2.2.2, which is used for mechanical excitation of the µcantilever during the calibration phase. The piezo ceramic is caught between the rear face of the sample section and the tip of a screw which goes through the main body (figure 5.25; see also figure 5.26). The base of the sample section beam was made narrower with the idea of increasing its compliances to the piezo excitation. In some sens, this narrowed region is a form of "small length flexural pivot" [1] [59]. A notch was created behind the sample to host a small plate used as a diffusive background for imagery. In other experiments,

[1] This feature is also essential for the initial alignment of the interferometer. The piezo ceramic screw can be used for angular alignements of the sample surface in the vertical plane. This alignment is done only during the initial assembly of the CryoQPDI, not after every sample exchange.

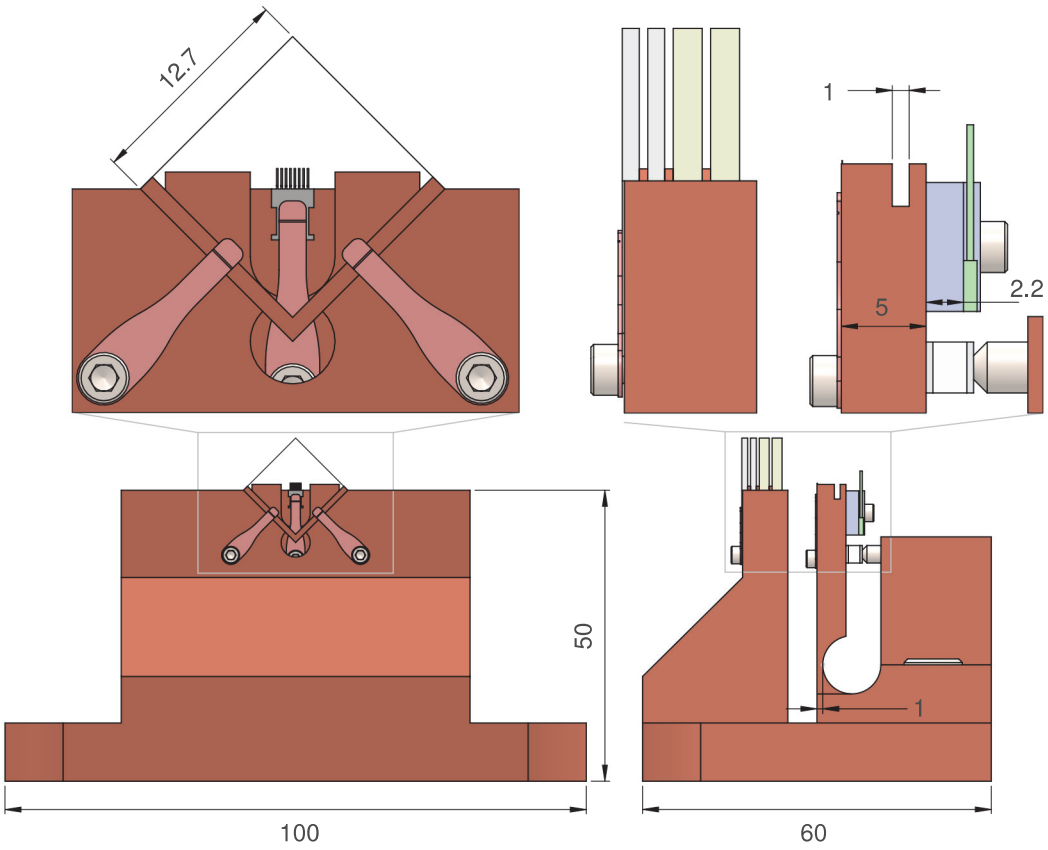

Figure 5.26 Front view and side view of the cryogenic holder. Dimensions are in millimeters. On the side view, a light blue color is used for the two calcite plates and a light yellow color is used for the two YVO_4 plates.

this notch may be used to hold a photodiode and detect the light transmitted by the μcantilever.

The cryo holder dimensions are provided in figure 5.26. The interface between to different mechanical parts in a thermal circuit is always the source of an additional thermal boundary resistance. This thermal resistance decrease linearly with the pressure exerted to close the interface [96]. The cryo holder was made much larger than the held elements to increase the contact area between it and the cold plate, and have more opportunity to screw it down to the plate. The intrument main optical axis, which goes though the center of the cryostat windows, is located 50 mm above the cold plate surface and also goes through the center of the Semel-Savart plate. At its narrowest point, the base of the sample section is only 1 mm thick without compromising the sample cooling. Figure 5.27 gives additional details of the Semel-Savart plate assembly. The birefringent plates are square with a standard width of 12.7 mm (half an inch). The Semel-Savart plate receptacle was drawn around this standard dimension. The four birefringent plates are separated by three spacers and clamped with two of the same spring clips used for the sample. This spring mounting was used instead of a rigid mounting to eliminate any possibility of failure due to

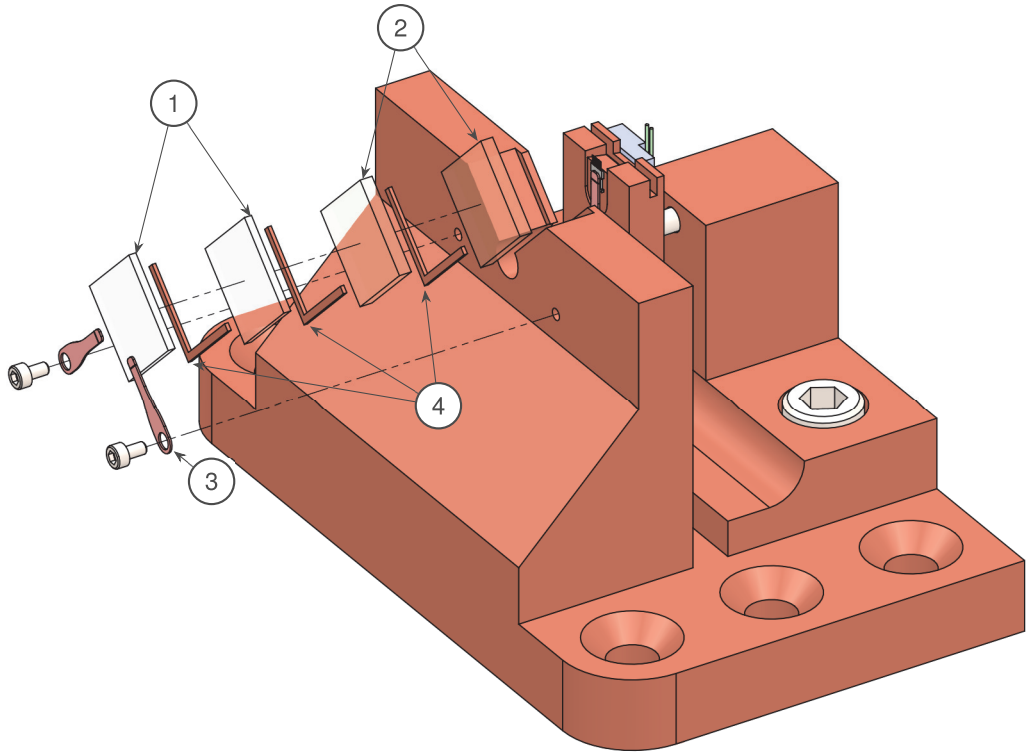

Figure 5.27 Detail of the Semel-Savart plate assembly on the cryo holder.

Item	Description	Item	Description
1	calcite plate	3	clamps
2	YVO_4 plates	4	spacers

differential thermal expansion [65]. In the same vein, no cement is employed and the upper part of the space between the birefringent plates is open for air evacuation during pump down.

To test the proper cooling of the sample, two temperature cycles of the cryostat were executed; The cycles consisted in a cool down to less than 8 K followed by a warm up to room temperature. The first cycle was done with the two temperature sensors of the cold plate attached to it, and the second cycle was carried out with one sensor attached on the cold plate and the other sensor fastened on the cryo holder as shown previously. The sensor remaining on the cold plate is located at its coldest point. During the first cycle, a difference in the temperature reading of the two sensors was observed, with a maximum discrepancy of 1 K at room temperature and smaller otherwise. The result of the second cycle displayed almost the same discrepancy. Below 8 K, the reading of the sensor on the cryo holder was less than the on located on the cold plate, by 0.5 K. As a conclusion, the difference in reading between the two temperature sensors of the cryostat is attributed to a calibration uncertainty, and the temperature difference between the sample and the coldplate is much less than this calibration uncertainty, namely below 0.5-1 K. This result demonstrates that the cryo holder design is successful in providing an adequate cooling of the sample.

5.4 Imaging bloc

The primary goal achieved with the CryoQPDI imaging bloc is to simplify and accelerate the alignment and focus of the interferometer laser beams on a μcantilever before a measurement of its thermal noise. It also proved being an invaluable help for the initial alignment of the setup.

The design of this bloc involves an adequate selection of the camera lens and magnification given the size of the object to be imaged, and of the camera sensor and pixel size knowing the optical resolution of the system. This is a common imaging problem, the rationals of which are provided in the technical litterature [115] and are not repeated here. Accordingly, in this section the design of the imaging bloc is only briefly presented, with reference to the general optical scheme of the CryoQPDI provided in figure 5.1, page 52.

The optical configuration of the CryoQPDI imaging system is similar to the one of a microscope using an infinity-corrected objective. The complete imaging system is the combination of the scanning objective and the imaging bloc. The objective in this case is the scanning objective characterized by its equivalent focal length f'_L of 39.8 mm and the camera lens L_c is a simple achromatic doublet with a focal length f'_{L_c} of 150 mm. The scanning objective produces an image at infinity, and the camera lens is used to reform a real image. The lateral magnification M_c of the imaging system is simply

$$M_c = -\frac{f'_{L_c}}{f'_L} = -3.77 \tag{5.56}$$

As the magnification is negative, the image is inverted, and this inversion is removed by rotating the camera. The beam splitter BS_c has a reflection:transmission ratio of 10:90 to preserve the majority of the signal for interferometry. The mirror M_c is used to fold the optical path of the imaging bloc for a more compact design. The reflection occuring on the mirror also compensates the revertion due to the reflection on the beam splitter, retaining a non-reverted inverted image.

The CryoQPDI camera is a model exo4000MU3 from SVS-VISTEK [113]. Since no additional information is expected from the color in an image from the camera, a monochrome camera was selected. The camera is build around a square CMOS sensor with a sensor size of 11.26 × 11.26 mm and a pixel size of 5.5 × 5.5 μm, corresponding to a full frame size of 2048 × 2048 pixels.

The image covers a field equal to the sensor size divided by the system magnification, almost 3 × 3 mm. This field is slighty larger than a μcantilever sample (figure 5.8) and allows the imaging of all the μcantilevers of the sample at the same time (figure 5.28).

The aberration of the imaging system was evaluated using the same ray tracing software used for the scanning objective design, only in the case where the scanning lens is centered. This evaluation revealed that the imaging system is diffraction limited for an aperture almost equal to the laser beam radius at the sample lens of the scanning objective, around 9 mm (table 5.2), but is limited by spherical aberration for larger aperture. This corresponds to a F-number of $F/8.33$. The Rayleigh criterion states that two adjacents point of an image can be resolved if there are separated by at least one Airy disc radius. Using equation 5.9 at the laser wavelength and the previously mentioned F-number, the system optical resolution is equal to 5.4 μm, or 20.4 μm after magnification. The Nyquist sampling criterion demands a pixel size less than or equal to half the (magnified) optical resolution of the system. In this case, the camera pixel size should be equal or less than 10.2 μm. With a pixel size of 5.5 μm, the system resolution is therefore limited by diffraction, not by the camera pixel size. The Nyquist criterion would also be met approximately if the imaging system was corrected for the full angular aperture of the scanning objective, where the F-number of the system would be $F/3.1$. In the imaging bloc, a diaphragm can be inserted between the beam splitter and the camera lens to limit the system aperture, providing an adjustment for the usual trade-offs between resolution, depth of focus and image brightness.

A typical image acquired with the CryoQPDI camera is displayed in figure 5.28. The image size and resolution are adequate for the interferometer alignment, meaning that the primary goal of the imaging bloc has been achieved. In its current state, the imaging system is not complete, because it lacks an adequate sample illumination method. The initial design of the system included a quasi monochromatic light source to shine light on the sample and a set of narrowband optical filters to balance the laser power on the camera and avoid contaminating the interferometer quadrature signals. These elements were not implemented due to time and budget constraints, and their inclusion in the CryoQPDI optical scheme is left as a perspective of this work. An important consequence is that the images and the thermal noise signal cannot be acquired at the same time. The picture of figure 5.28 was taken after placing a neutral density filter just after the laser output, which would otherwise blind the camera.

An image like the one of figure 5.28 can also be used to estimate the lateral displacement of the Semel-Savart plate. By comparing the length of a µcantilever to the observed image shift, the plate displacement is measured at 417 μm, close to the design displacement of 419.4 μm.

5.5 Conclusion

In this chapter, the optical design of the CryoQPDI interferometer was presented. This presentation was done with emphasis on two important sections of the interferometer optical scheme, which are the scanning objective and the Semel-Savart plate.

The scanning objective is used to shape and focus the laser beam to small spots on the μcantilever, and also permits a positioning of these spots in three dimensions for alignment purposes. The scanning objective was compensated for aberrations using a ray tracing software, and the theory required to perform this compensation and interpret the sofware results was presented. A criterion for aberration compensation based on the Strehl ratio was used with an account for the gaussian nature of the laser beam. The scanning objective retains an adequate level of aberration compensation when its positioning function is used in a range covering the typical size of a sample.

The Semel-Savart plate consists in the combinaison of two Savart plates in antiparallel orientations and made of birefringent crystals with opposite birefringence signs. The relative defocus between the ordinary and extraordinary beams generated by a birefringent plate is eliminated using the Savart plate concept. The crystal astigmatism introduced in extraordinary beams by the first Savart plate is compensated by an astigmatism of opposite sign generated by the second Savart plate. This compensation is achieved for a specific thickness ratio between the individuals birefringent plates forming the beam splitter.

Thanks to their respective aberration corrections, these two elements give a theoretical $1/e^2$ spot diamter of around $6\,\mu$m to the system. A spot diameter less than $20\,\mu$m was experimentally confirmed.

The other important benefit of the Semel-Savart plate is to preserve the interferometer contrast. The contrast achieved by the CryoQPDI is the highest contrast ever achieved with QPDI.

Additionally, the designs of the system's cryo holder and imaging bloc where briefly exposed. The cryo holder is a mechanical assembly located inside the cryostat. It is used to hold the sample under study as well as the Semel-Savart plate. Its cryogenic grade copper construction ensure an adequate cooling of the sample. The imaging bloc uses a small portion of the light coming from the sample to form an image which is used as an important source of information during the initial alignment of the system. The completion of this imaging system with a proper lighting apparatus is left as a perspective of this thesis.

Figure 5.28 Image of a µcantilever sample from the CryoQPDI camera. The µcantilevers nominal dimensions are $500 \times 90 \times 1\ \mu\mathrm{m}$. The bright dot on the fifth µcantilever (from left to right) is the laser spot of the interferometer. As shown in figure 2.1, page 14, the laser beam of the interferometer is separated in two beams on its forward path to the sample. The image on the camera, observed on the beam return path, displays a reciprocal situation. As the beams are recombined by the Semel-Savart plate, only a single spot is visible. The light coming from the µcantilevers, which is not polarized in a particular direction relative to the Semel-Savart plate axes, is however split in two by the beam splitter. In other words, instead of a µcantilever with two laser spots, the image acquired by the camera displays a single spot with two µcantilevers. Looking at one of the µcantilever image at a time, one can indeed infer the position of the reference beam at the base of the µcantilever from the top image and the position of the probe beam at the top left corner of the µcantilever from the bottom image.
Even if the lighting conditions of this image are clearly suboptimal, the most important informations researched with the CryoQPDI imaging bloc, which is the position and focus of the laser spots on a specific µcantilever, are available immediatly to the operator. The correct alignment of the sample relative to the direction of separation of beam splitter can also be verified. In this case, the sample is slightly rotated to the right.

6 CryoQPDI signal chain design

This chapter deals with the design of the CryoQPDI signal chain. The term “signal chain” refers to all the electronic components located between the surface of the interferometer four photodiodes and the digitized data in the control computer. As such, each of the four channels of the CryoQPDI signal chain is constitued of three main elements. The first two element are a photodiode transimpedance amplifier used to convert the photodiode’s current into a manageable voltage and a lowpass filter used to avoid the effect of aliasing. These two elements together constitute the interferometer photodetector. The last element of the signal chain is a data acquisition card, responsible for converting the photodetector analog voltage into digital data.

Given the very low amount of signal expected from a μcantilever thermal noise measurement, it is critical for every element of the signal chain to contribute a minimum amount of noise to the interferometer signal. Since this signal primarily consists of a light intensity, the maximum signal to noise ratio is set by the shot noise of this light itself. Ensuring that this shot noise dominates the electronic noise of the signal chain is then an important guiding principle for the signal chain design, providing an important measure of optimality.

In the first section of this chapter, the operating principle of photodiodes is presented, and is used to construct a relevant photodiode circuit model. The principle of the photodiode transimpedance amplifier is then presented, and a complete theoretical model of this circuit operation in terms of frequency response and noise is then developed. This model is used afterwards to elaborate a specific photodetector design strategy.

The second section of this chapter present the design and selection of the three main element of the signal chain mentioned before. The photodetector’s design was assisted by SPICE simulation, and the bandwidth and quantization noise of an ADC was considered for the selection of an adequate data acquisition card.

In the third and last section of this chapter, the experimentaly achieved noise performance of the CryoQPDI signal chain is presented, and a comparison is made between circuits based on two operational amplifiers. The investigations carried out during this work revealed an excess of high frequency noise from the photodetector, which is also discussed in this section. A comparison is made between the electronic noise acheived by the signal chain of the CryoQPDI and the reference QPDI.

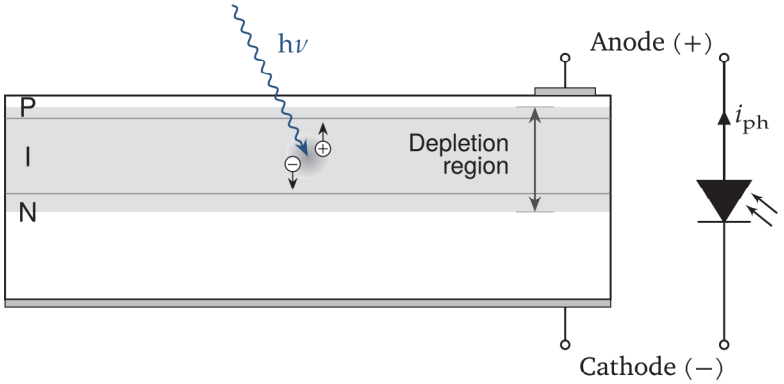

Figure 6.1 Simplified schematic of a silicon PIN photodiode cross section. The P-layer at the photodiode active surface forms a P-N junction with the N-type substrate. The absorption of photons in the depletion region contributes the majority of the reverse diode photocurrent i_{ph}. Inserting an intrinsic I-layer at the P-N junction interface increases the volume of the depletion region, improving the photodiode performances.

6.1 The photodiode transimpedance amplifier

6.1.1 Photodiodes

Photodiodes characteristics Photodiodes are light sensors that mainly consist of a shallow semiconductor P-N junction operated as a photoelectric converter [50] (figure 6.1). When a light ray strikes a photodiode, and if the light energy is greater than the band gap energy of the photodiode constitutive semiconductor material, the absorption of photons releases electron-hole pairs, that act as the charge carriers inside the device. Close to the junction interface, the depletion region built-in electric field separates the electron-hole pairs and accelerates them toward the photodiode terminals. As carriers released outside the depletion region do not benefit from this charge separation effect, the light absorbed inside the depletion region contributes to the majority of the diode photocurrent i_{ph} [47].

As photodiodes perform a direct photon-to-electron conversion, they are a type of quantum light sensor [55]. The most basic measure of a quantum sensor sensitivity at a given wavelength is its quantum efficiency η_λ, defined as the fraction of incident photons that contributes to the photocurrent:

$$\eta_\lambda = \frac{N_e}{N_{ph}} \tag{6.1}$$

Where N_{ph} is the number of incident photon in a given time interval, N_e the number of released electron in the same time interval, and $0 < \eta_\lambda < 1$. The quantum efficiency of a particular photodiode mainly depends on the semiconductor material used and on details of the photodiode internal construction. Photodiodes for the visible spectral

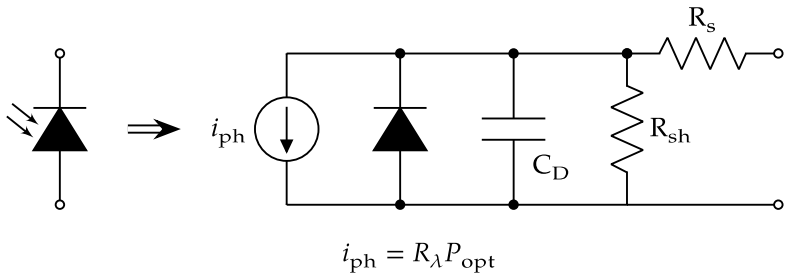

Figure 6.2 Circuit model of a photodiode. An ideal current source i_{ph} in parallel with a diode represent the photodiode ideal attributes. The junction capacitance C_D together with the shunt and serie resistance R_{sh} and R_s are the photodiode parasitic elements. For a silicon photodiode operated in photoconductive mode, the diode, R_{sh} and R_s can usually be ignored for both noise and bandwidth analysis.

range are made of silicon, and tend to have a rather constant quantum efficiency, that can be as high as $\eta_\lambda = 0.9$ [55].

A more practical characteristic for design calculations is the photodiode responsivity, defined as the ratio of the diode output photocurrent to the incident light power:

$$R_\lambda = \frac{i_{ph}}{P_{opt}} = \frac{\lambda \eta_\lambda e}{h c_0} \tag{6.2}$$

where R_λ is the responsivity in A/W, P_{opt} is the optical power in W, e is the elementary charge, h the plank constant and c_0 the speed of light in vacuum. The responsivity of silicon photodiodes ranges between 0.1 A/W and 0.6 A/W in the visible, with a typical value of ≈ 0.3 A/W at 532 nm.

Photodiode circuit model The quantized nature of the photon-to-electron conversion in photodiodes ensures that they behave as extremely linear current sources. Their intrinsic speed is also very high, and is mainly determined by the carriers transit time from the depletion region to the device terminals, which is not a concern for a bandwidth below several GHz [50]. However, it is often necessary to convert the photocurrent to a voltage, as most electronic instruments accept a voltage measurand[1]. Here, unwanted interactions between the photodiode and the external circuitry required for this current-to-voltage conversion usually sets the limit to the resulting photodetector's bandwidth, linearity and noise level. To permit an analysis of these interactions, the photodiode non-ideal characteristics are modeled with discrete circuit components [47]. The corresponding photodiode circuit model is shown in figure 6.2 and is described hereafter.

[1] Photodiodes can also output a voltage v_{ph}, but v_{ph} is a much less desirable measurand than i_{ph}: it is a logarithmic function of the incident light intensity, is very sensitive to temperature variation, and photodiode's voltage monitoring circuits suffer from additional limitations [47].

In a photodiode, charges stored in the high conductivity P and N layers are separated by the low conductivity depletion region. This stored charge effect gives a capacitive behaviour to the P-N junction, where the P and N layers act as the capacitor's plates. This capacitive response is modeled by an effective junction capacitance C_D. As explained in the following, C_D has a profound impact on the transimpedance amplifier noise and bandwidth, and a lower C_D value results in an overall better photodetector performance.

In the PIN photodiode variation, an intrinsic I-layer is inserted between the P and N layers. The resulting expansion of the depletion region increases the separation between the junction capacitor's plates, and results in a reduced diode capacitance [50, 55].

Further capacitance reduction is commonly achieved by applying a reverse bias voltage V_b across the photodiode[1]. This bias voltage adds to the depletion region built-in voltage and increases its electric field. As a result, the charges stored in the P and N layers are repelled, thickening the depletion region and reducing C_D. The bias voltage and the junction capacitance are linked by [47]:

$$C_D = \frac{C_{D0}}{\sqrt{1 + \frac{V_b}{V_{bi}}}} \tag{6.3}$$

Where C_{D0} is the photodiode capacitance at zero bias, and V_{bi} is the junction built-in voltage (illustration in figure 6.3). Operating a photodiode at zero bias is called the photovoltaic mode of operation, while a reverse biased photodiode is operated in the photoconductive mode of operation. The C_{D0} of a particular photodiode depends on the details of its construction, but is generally proportional to its active area, lower junction capacitance being achieved in small-area devices. C_{D0} range from a few tens of pF for small area photodiodes to several thousand of pF for large area photodiodes. Importantly, the larger electric field in the depletion region of a photodiode operated in photoconductive mode also improves its carrier separation and collection efficiency, resulting in an improvement of its linearity, especially at higher light power [50, 55], and resulting in a slight enhancement of its responsivity[2] [50, 47].

However, applying a reverse bias voltage also causes a small leakage current to flow through the photodiode. As this current flow even without any light irradiating the sensor, it is called the dark current i_{dark}. This dark current and its shot noise together set the lowest detectable photocurrent and the fundamental noise level of a photodiode used in the photoconductive mode. The photodiode dark resistance, or shunt resistance

[1] For both PN and PIN photodiodes

[2] The thicker depletion region obtained with a PIN photodiode and/or with photoconductive operation also favours the absorption of longer wavelengths, but as the corresponding increase in responsitivy occurs mainly between 900 nm and 1100 nm, it is not a concern here.

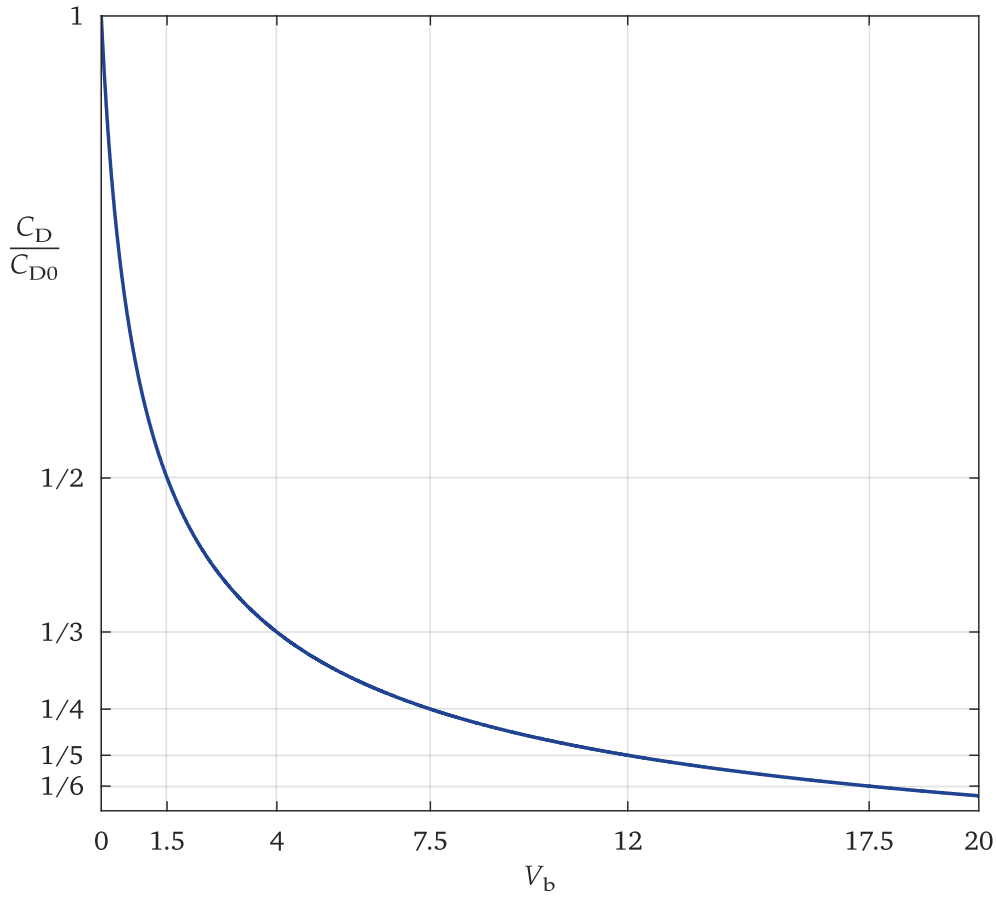

Figure 6.3 Normalized photodiode junction capacitance as a function of the applied reverse bias voltage (equation 6.3, for $V_{bi} = 0.5\,V$)

R_{sh}, represents the leakage path of the dark current through the photodiode. It is defined as :

$$R_{sh} = \frac{V_B}{i_{dark}} \tag{6.4}$$

for a typical bias value of $V_B = 10\,mV$. The shunt resistance is specified primarily for noise calculations in the photovoltaic mode of operation. Equation 6.4 is in general not valid for higher value of V_B, but gives a correct order of magnitude [55]. The value of i_{dark} as a function of V_B is provided in the photodiode's specification. The dark current of a silicon photodiode is usually very low, so that its effect can be ignored except for very low signal level.
At last, the photocurrent encounters a finite resistivity while crossing the photodiode and its terminal contact, which is accounted for by a serie resistance R_s.

A light controlled current source i_{ph} in combination with a regular diode and the parasitic elements described above form the photodiode circuit model of figure 6.2. For a silicon photodiode, R_{sh} is very high[1], typically from $10\,M\Omega$ to $10^5\,M\Omega$, and

[1] This is not always the case for other semiconductor materials, such as those used for infrared photodiodes.

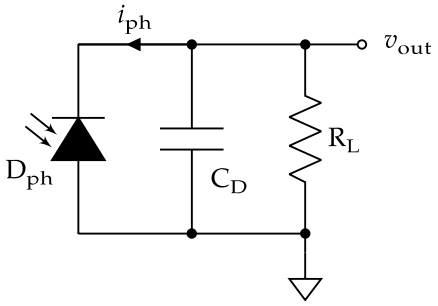

Figure 6.4 The direct connexion of a photodiode D_{ph} and to a load resistor R_L forms the simplest transimpedance circuit, but provides a slow and nonlinear response.

R_s is very low, with values ranging from 10 Ω to 10^3 Ω , so that their effects on a photodetector circuit response can usually be ignored [85]. The diode has been included to model the behaviour of the photodiode in its forward biased state. As this situation is not encountered in a nominal photodetector operation, it can also be removed from figure 6.2. A simplified photodiode model which is valid for silicon photodiode then consists only in the current source i_{ph} in parallel with the junction capacitance C_D.

Effect of the junction capacitance: an example The importance of the photodiode junction capacitance is illustrated with the example of figure 6.4. The simplest way to convert the photocurrent to a voltage is to connect a photodiode D_{ph} to a load resistor R_L [56]. At DC frequency, the output voltage v_{out} of this circuit is simply given by Ohm's law:

$$v_{out} = i_{ph} R_L \tag{6.5}$$

But as the frequency increases, the photodiode capacitance shunts the signal away from the load resistor, giving this circuit a RC lowpass filter response with a −3 dB cutoff frequency of:

$$f_{RC} = \frac{1}{2\pi R_L C_D} \tag{6.6}$$

The typically large R_L value required to obtain a manageable voltage often severely limits the bandwidth of this circuit[1]. Additionally, as the output voltage is impressed on the photodiode, a variation of the input light level leads to a variation of both its junction capacitance and its responsivity, resulting in a nonlinear response.

6.1.2 Principle of the photodiode transimpedance amplifier (TIA)

To adress the limitations of the circuit of figure 6.4, the photodiode should ideally be able to deliver its photocurrent to a load while being isolated from the resulting output voltage. The photodiode transimpedance amplifier (TIA) of figure 6.5 approximates

[1] For instance, with $C_D = 4$ pF and $R_L = R_f = 100$ kΩ, the resulting f_{RC} is close to 400 kHz, 10 times slower than the CryoQPDI transimpedance amplifier theoretical bandwidth.

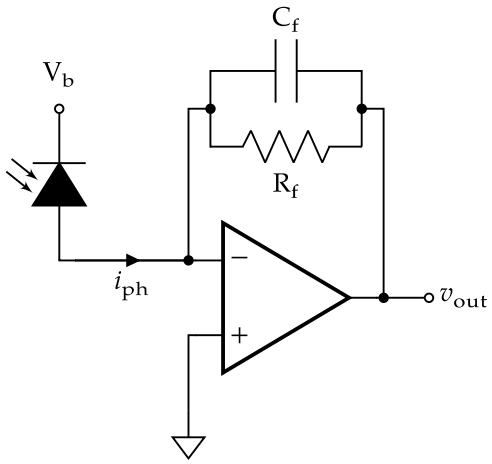

Figure 6.5 Basic schematic of a photodiode transimpedance amplifier (TIA). The operational amplifier forces the photocurrent to flow through the feedback network while isolating the photodiode from the resulting output voltage, largely avoiding the limitations of the circuit of figure 6.4. Simply connecting a voltage source to the photodiode allows for a photoconductive mode of operation.

this ideal condition. To explain the operating principle of the TIA circuit, an ideal voltage feedback operational amplifier (opamp) is considered first. While the inverting input of the opamp does not accept any current, the feedback imposes the voltage at this point to remain at the ground level. The photodiode is therefore presented to a virtual ground with zero impedance. The opamp accomplishes this by developping an output voltage v_{out} which forces the photocurrent through the feedback impedance Z_f. Z_f results from the parallel combinaison of the feedback resistor R_f and the feedback capacitor C_f:

$$Z_\text{f} = \frac{R_\text{f}}{1 + sR_\text{f}C_\text{f}} \tag{6.7}$$

where the Laplace variable s have been introduced to simplify notations:

$$s = j\omega = j2\pi f \tag{6.8}$$

In the ideal opamp case, the output signal voltage v_{out} and the input photocurrent i_{ph} are then related by:

$$v_{\text{out}} = -i_{\text{ph}}Z_\text{f} \tag{6.9}$$

The transimpedance amplifier is a current to voltage converter[1], with a transimpedance gain in unit of Ohm determined primarily by the feedback resistor R_f (at low frequency). In the ideal opamp case, the circuit bandwidth would be determined by the cutoff frequency f_{RC} resulting from the combinaison of R_f with C_f, with no influence of the photodiode capacitance C_D. In practice, the speed of a photodiode TIA is mainly determined by the opamp limited ability to isolate the photodiode due to its finite open-loop gain A_OL, and a large photodiode capacitance also plays a role in reducing the TIA bandwidth. The TIA circuit also permits a simple connexion of the reverse bias

[1] Also sometime referred to as a transresistance amplifier.

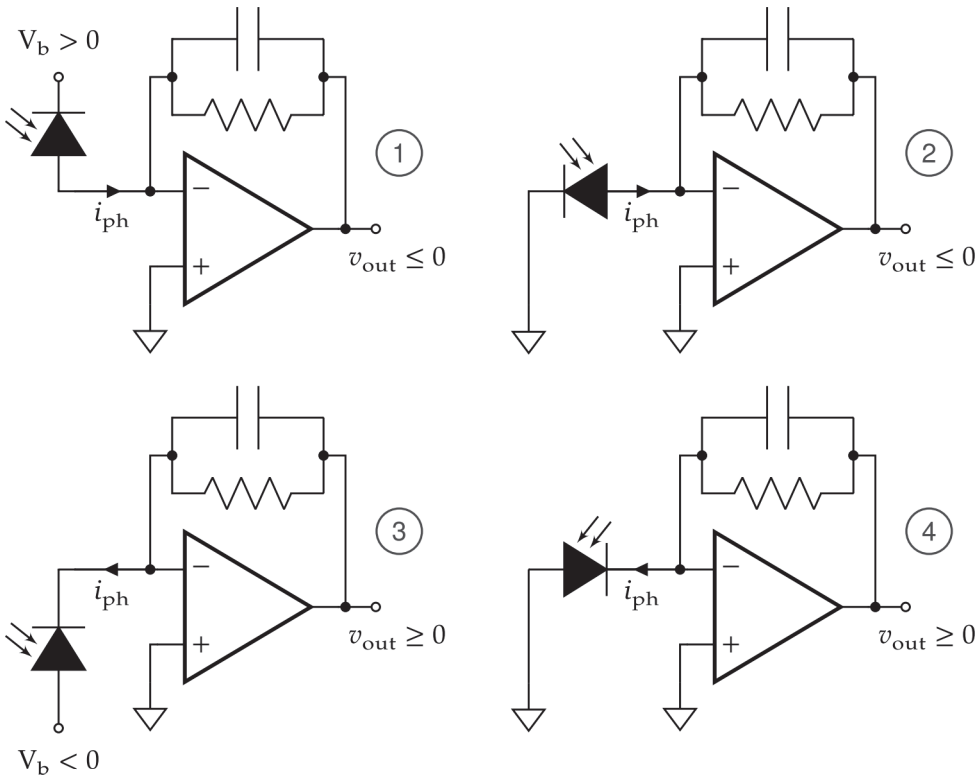

Figure 6.6 Schematics of the four possible TIA circuit configurations. The two circuits on the top (1 and 2) produce a positive voltage, while the two circuits on the bottom (3 and 4) are arranged to deliver a negative voltage. The two circuits on the left (1 and 3) operate the photodiode in photoconductive mode, whereas the two circuits on the right (2 and 4) corresponds to the photovoltaïc mode of operation.
The transimpedance amplifier frequency response is described by the same set of equations for all these configurations, but with a reduced photodiode capacitance C_D in the photoconductive cases (figure 6.3). The application of a reverse bias voltage V_b introduces additional error and noise sources which are discussed in section 6.1.4.

voltage V_b used to reduce this capacitance. On the other side, the feedback capacitor C_f is primarily introduced to restore the circuit stability [47]. The relation between the circuit parameters and the circuit transfer function is determined in the next section.

In a real TIA, the output signal is also affected by several error and noise sources. In particular, the opamp input voltage noise and its interaction with the circuit components introduce important design constraints, which are discussed in section 6.1.4.

The four possible TIA circuit configurations are presented in figure 6.6, from which the output signal polarity can be determined. In the following analysis, the minus sign of equation 6.9 will therefore be dropped for simplicity.

6.1.3 TIA frequency response

Transfer function The transfer function H_{TIA} of the transimpedance amplifier is determined from the circuit model of figure 6.7 [47]. In this circuit, the photodiode

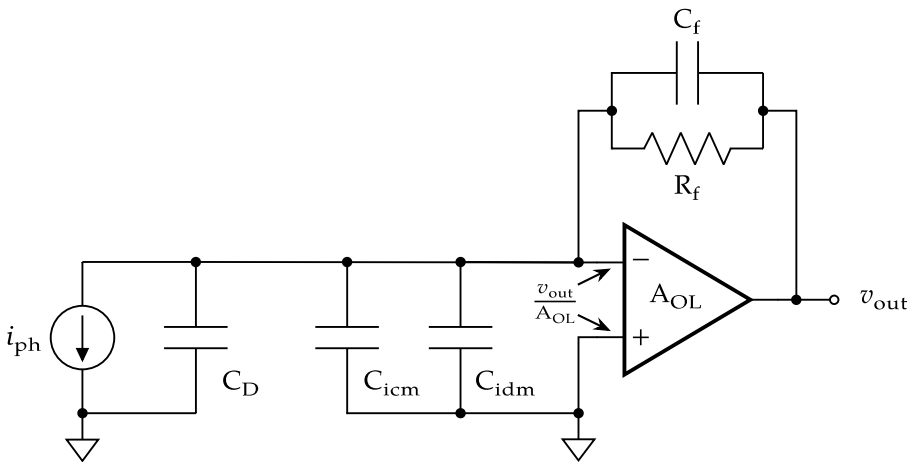

Figure 6.7 TIA circuit model for bandwidth analysis. The photodiode is modeled by the current source i_{ph} in parallel with the junction capacitance C_D. The opamp displays a finite open-loop gain A_{OL}, and contributes to the total input capacitance C_{in} of the circuit with its common mode input capacitance C_{icm} and its differential mode input capacitance C_{idm}.

have been replaced by the simplified model discussed at the end of section 6.1.1, which combines a current source i_{ph} in parallel with a junction capacitance C_D. The operational amplifier input capacitance is represented by its common mode input capacitance C_{icm} and its differential mode input capacitance C_{idm}. The circuit total input capacitance C_{in} is then given by:

$$C_{in} = C_D + C_{icm} + C_{idm} \tag{6.10}$$

With a finite open-loop gain A_{OL}, the opamp requires an error signal v_{out}/A_{OL} between its input to support the output voltage v_{out}. A fraction $\frac{1}{\beta}$ of this error voltage is substracted from the output, where β is the circuit feedback factor. Writing a loop equation for v_{out} gives:

$$v_{out} = i_{ph}Z_f - \frac{1}{\beta}\frac{v_{out}}{A_{OL}} \tag{6.11}$$

Rearanging this expression provides the general form of the transimpedance amplifier transfer function:

$$H_{TIA} = \frac{v_{out}}{i_{ph}} = \frac{Z_f}{1 + \frac{1}{A_{OL}\beta}} \tag{6.12}$$

The feedback factor β is the fraction of the amplifier output signal fed back to the amplifier input [45, 46]. The quantity $1/\beta$ is the circuit noise gain, and is called so because it is the main part of the gain received by the opamp input voltage noise (see section 6.1.4). The noise gain is also an important parameter for bandwidth and stability consideration. β takes the form of a voltage divider ratio from the output to the input:

$$\beta = \frac{Z_{in}}{Z_{in} + Z_f} \tag{6.13}$$

where the expression of the feedback impedance Z_f was given in equation 6.7, and where the input impedance Z_{in} is determined by the circuit input capacitance:

$$Z_{in} = \frac{1}{sC_{in}} \tag{6.14}$$

Inserting equation 6.7 and 6.14 in equation 6.13 provides an expression of the TIA noise gain as a function of the circuit components:

$$\frac{1}{\beta} = \frac{1 + sR_f\left(C_{in} + C_f\right)}{1 + sR_fC_f} \tag{6.15}$$

From equation 6.15, the noise gain is found to exhibit a zero frequency ω_z and a pole frequency ω_p:

$$\omega_z = \frac{1}{R_f\left(C_{in} + C_f\right)} \tag{6.16a}$$

$$\omega_p = \frac{1}{R_fC_f} \tag{6.16b}$$

Using these relations in equation 6.15, the noise gain is expressed in terms of its characteristic frequencies:

$$\frac{1}{\beta} = \frac{1 + \frac{s}{\omega_z}}{1 + \frac{s}{\omega_p}} \tag{6.17}$$

The open-loop gain A_{OL} of a voltage feedback opamp can be approximately described by a single pole, lowpass frequency response [47]

$$A_{OL} \approx \frac{A_{DC}}{1 + \frac{s}{\omega_{dom}}} \tag{6.18}$$

where A_{DC} is the open-loop gain value at DC frequency, and where ω_{dom} is the open-loop gain dominant pole. A_{DC} is typically very high, around 10^5 to 10^6, and f_{dom} is usually set to a relatively low frequency, typically under 1 kHz. The most usefull frequency range of the open-loop gain is located far above f_{dom}, where equation 6.18 is well approximated by:

$$A_{OL} \approx \frac{\omega_c}{s} \tag{6.19}$$

where f_c is the unity gain crossover frequency of the opamp, specified as its gain-bandwidth product (GBW).

By inserting equation 6.17 and 6.19 in equation 6.12, the transimpedance amplifier transfer function is written in terms of the circuit noise gain and the opamp open-loop gain characteristic frequencies:

$$H_{TIA} = R_f \frac{1}{\frac{s^2}{\omega_z\omega_c} + s\left(\frac{1}{\omega_p} + \frac{1}{\omega_c}\right) + 1} \tag{6.20}$$

From this expression, the photodiode transimpedance amplifier is found to display a second order (or two-pole) frequency response, and equation 6.20 can be rewritten to take the following general form:

$$H_{\mathrm{TIA}} = R_{\mathrm{f}} \frac{1}{-\frac{\omega^2}{\omega_{\mathrm{r}}^2} + j\frac{1}{Q}\frac{\omega}{\omega_{\mathrm{r}}} + 1} \tag{6.21}$$

where the TIA natural resonant frequency ω_{r} and quality factor Q[1] are given by:

$$\omega_{\mathrm{r}} = \sqrt{\omega_{\mathrm{z}}\omega_{\mathrm{c}}} \tag{6.22a}$$

$$\frac{1}{Q} = \omega_{\mathrm{r}}\left(\frac{1}{\omega_{\mathrm{p}}} + \frac{1}{\omega_{\mathrm{c}}}\right) \tag{6.22b}$$

From equation 6.21, the circuit normalized power transfer function is determined as:

$$\left(\frac{|H_{\mathrm{TIA}}|}{R_{\mathrm{f}}}\right)^2 = \frac{1}{\left(\frac{\omega}{\omega_{\mathrm{r}}}\right)^4 + \left(\frac{\omega}{\omega_{\mathrm{r}}}\right)^2\left(\frac{1}{Q^2} - 2\right) + 1} \tag{6.23}$$

Bandwidth The bandwidth of the transimpedance photodiode amplifier corresponds to the cutoff frequency $f_{3\,\mathrm{dB}}$ for which the circuit amplitude gain fall -3 dB below its DC value. Accordingly, the cutoff frequency can be determined from equation 6.23 by solving $\left(|H_{\mathrm{TIA}}|/R_{\mathrm{f}}\right)^2 = \frac{1}{2}$, which leads to:

$$\left(\frac{\omega_{3\,\mathrm{dB}}}{\omega_{\mathrm{r}}}\right)^4 + \left(\frac{\omega_{3\,\mathrm{dB}}}{\omega_{\mathrm{r}}}\right)^2\left(\frac{1}{Q^2} - 2\right) - 1 = 0 \tag{6.24}$$

Solving this equation for $\omega_{3\mathrm{db}}$ provides a relation between the circuit's bandwidth, resonant frequency and quality factor:

$$f_{3\,\mathrm{dB}} = f_{\mathrm{r}}\sqrt{1 + \frac{1}{2Q^2}\left(\sqrt{8Q^4 - 4Q^2 + 1} - 1\right)} \tag{6.25}$$

The normalized power transfer function of the transimpedance amplifier is displayed in figure 6.8 for several values of the circuit quality factor Q (equation 6.23). The quality factor is an important figure of merit which influences the shape of the transfer function as well as the circuit bandwidth and stability. The circuit bandwidth is primarily determined by its resonant frequency f_{r}, which results from the selection of the photodiode, feedback resistor and operational amplifier (equation 6.22a). Its quality factor can then be tuned through the feedback capacitor C_{f}, a larger C_{f} value resulting in a lower Q. As explained below (figure 6.11), a maximum quality factor Q_{max} of around 1.19 is allowed before threatening the circuit stability, giving around

[1] In the context of this chapter, Q always refers to the circuit quality factor, not to be confused with the quality factor of a simple harmonic oscillator.

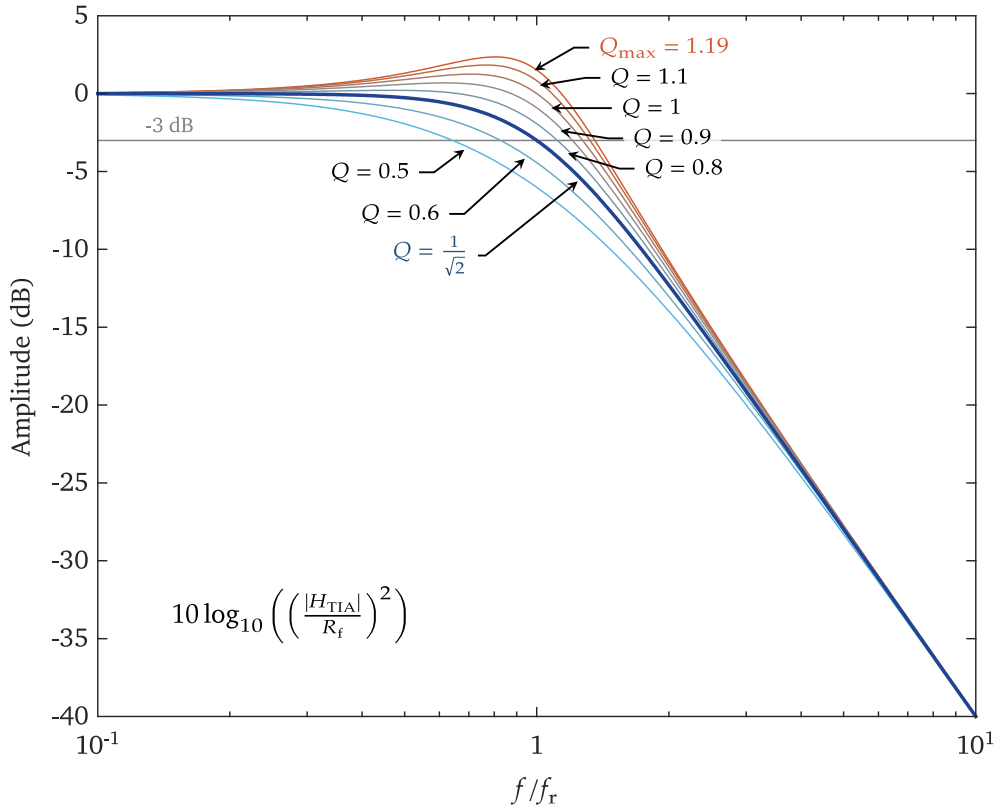

Figure 6.8 Normalized amplitude transfer function of the transimpedance amplifier for several quality factors between $Q = 0.5$ and $Q = 1.19$ (equation 6.23).

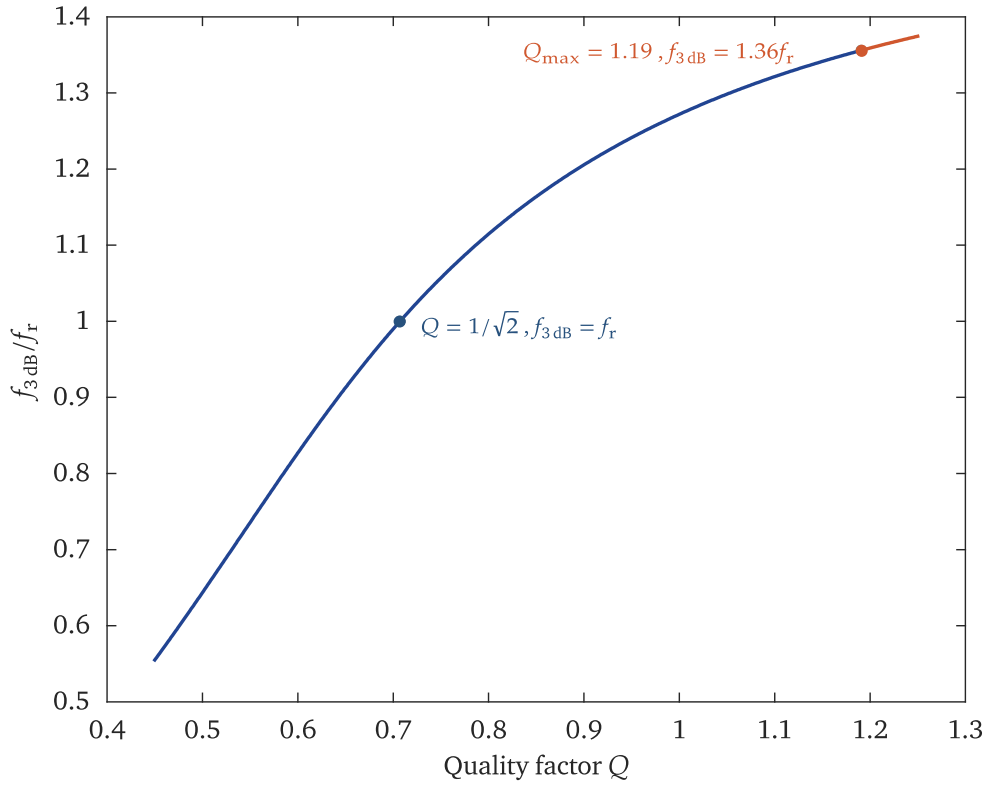

Figure 6.9 Bandwidth of the transimpedance amplifier relative to its resonant frequency as a function of the circuit quality factor (equation 6.25).

31 % of gain peaking as well. The special value $Q = 1/\sqrt{2}$ provides a maximally flat, Butterworth frequency response, which yields the most uniform sensitivity in the circuit passband.

Figure 6.9 displays the normalized frequency $f_{3\,\mathrm{dB}}/f_\mathrm{r}$ as a function of the quality factor Q (equation 6.25). For $Q = 1/\sqrt{2}$, the circuit −3 dB bandwidth equals its resonant frequency. For a quality factor ranging between 0.5 to 1.19, the TIA −3 dB bandwidth vary approximately ±35% around f_r.

Design equation for C_f An effective design strategy is to select the feedback capacitor C_f to achieve a predetermined quality factor, after selecting the remaining components of the circuit. To simplify the following formulas, a virtual capacitance C_c is defined to relate the feedback resistor R_f to the opamp unity gain crossover frequency f_c:

$$C_\mathrm{c} = \frac{1}{R_\mathrm{f}\omega_\mathrm{c}} \tag{6.26}$$

Using this virtual capacitance in equation 6.22b along with the definitions of the circuit characteristic frequencies lend to an alternative expression for Q:

$$Q = \frac{\sqrt{C_\mathrm{c}\,(C_\mathrm{in} + C_\mathrm{f})}}{C_\mathrm{c} + C_\mathrm{f}} \tag{6.27}$$

This expression can be used to establish a quadratic equation for C_f:

$$C_\mathrm{f}^2 + C_\mathrm{f}\left[C_\mathrm{c}\left(2 - \frac{1}{Q^2}\right)\right] + \left[C_\mathrm{c}^2\left(1 - \frac{1}{Q^2}\frac{C_\mathrm{in}}{C_\mathrm{c}}\right)\right] = 0 \tag{6.28}$$

and the solution of this equation is:

$$C_\mathrm{f} = C_\mathrm{c}\left(\frac{1}{2Q^2} - 1 + \frac{1}{Q}\sqrt{\frac{1}{4Q^2} - 1 + \frac{C_\mathrm{in}}{C_\mathrm{c}}}\right) \tag{6.29}$$

Stability In an opamp circuit configured for negative feedback, instability may results from an excessive delay of the output signal fed back to the input. If the corresponding phase shift reaches on cycle, or −360°, the feedback will become positive and the circuit will be unstable [47].

The complex quantity $\mathrm{A_{OL}}\beta$, called the loop gain, is the only parameter to take into account for stability consideration. In equation 6.12, if the loop gain is allowed to come near to −1 (with $|\mathrm{A_{OL}}\beta| = 1$ and $\angle\mathrm{A_{OL}}\beta = 180°$), the TIA transfer function will become infinite. With infinite gain, the circuit is able to support an output signal without an input signal, and will oscillate as a consequence [46].

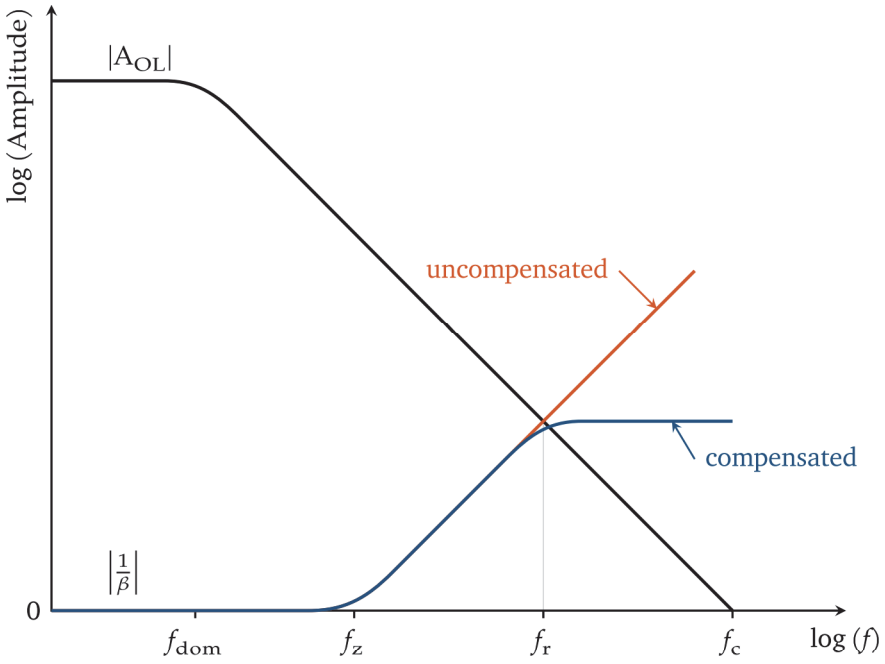

Figure 6.10 Bode plot for a graphical analysis of the transimpedance amplifier stability. The magnitude of the opamp open-loop gain A_{OL} and of the circuit noise gain $1/\beta$ are plotted together for the most common case $f_z \ll f_r$, and the circuit stability can be evaluated from the curves slopes at their intersection. The noise gain is displayed for two cases: in orange, the uncompensated case corresponds to a circuit without feedback capacitor, with a highly probable instability. In blue, the noise gain is modified by the addition of the feedback capacitor, implementing phase compensation.

To avoid this unstable state, it must be insured that the phase shift around the feedback loop dont reach $-180°$ when the loop gain reaches unity magnitude[1]. The phase margin Φ_m is defined as the difference between $-180°$ and the loop phase shift for $|A_{OL}\beta| = 1$. A phase margin of 45° is often recommended in practice to ensure stability in an actual circuit, for instance to establish a safety margin against tolerances in the circuit components parameters. This stability criterion can be discussed from a response plot like the one of figure 6.10 [45]. The magnitude of the opamp open-loop response and of the circuit noise gain are displayed together for the most common conditions found in a transimpedance amplifier circuit. The noise gain is drawn for two cases: the uncompensated case is encountered when no feedback capacitor is added to the circuit ($C_f = 0$), while a feedback capacitance is added for the compensated case. The circuit loop gain magnitude is available indirectly through the vertical distance between the $|A_{OL}|$ and $\left|\frac{1}{\beta}\right|$ curves. With a logarithmic scale, this distance is:

$$\log\left(|A_{OL}|\right) - \log\left(\left|\frac{1}{\beta}\right|\right) = \log\left(|A_{OL}\beta|\right) \tag{6.30}$$

[1] The phase inversion from the opamp inverting input add $-180°$ to the loop phase, so that the total phase shift equals the $-360°$ needed to sustain oscillations.

The frequency at which $|A_{OL}\beta| = 1$ is defined as the intercept frequency f_{int}, as it corresponds to the frequency at which the A_{OL} curve intercept the $\frac{1}{\beta}$ curve:

$$|A_{OL}| = \left|\frac{1}{\beta}\right| \Leftrightarrow |A_{OL}\beta| = 1 \tag{6.31}$$

The loop gain phase and the phase margin can be determined approximately from the relative slopes of the open-loop gain and noise gain magnitude curves. The link between slope and phase shift stems from the effects of response poles and zeros [47, 46]. A pole introduces a -20 dB/decade response slope and up to a $-90°$ phase shift far above the pole frequency. At the pole frequency, the phase shift equal $-45°$. A zero have the same effects with opposite sign.
The phase margin writes [47]:

$$\Phi_m = 180° + \Phi_{A_{OL}} - \Phi_{1/\beta} \tag{6.32}$$

where $\Phi_{A_{OL}}$ is the phase shift introduced by the opamp open-loop response and $\Phi_{1/\beta}$ is the phase shift due to the input and feedback networks. From equation 6.17 and 6.19, $\Phi_{A_{OL}}$ and $\Phi_{1/\beta}$ are rewritten as a function of the phase shifts associated with their respective zeros and poles. Equation 6.32 then become:

$$\Phi_m = 180° + \Phi_{f_{dom}} - \Phi_{f_z} + \Phi_{f_p} \tag{6.33}$$

where $\Phi_{f_{dom}}$ is the phase shift associated with the open-loop gain dominant pole, and where Φ_{f_z} and Φ_{f_p} are the phase shifts associated to the noise gain zero and pole. Equation 6.33 can be evaluated approximately from a comparison of the characteristics frequencies of A_{OL} and β and the interceipt frequency f_{int}. f_{dom} is located far below f_{int}, so that the opamp A_{OL} response can develops almost its full $-90°$ phase shift at f_{int}. In most practical cases of interest[1], f_z is also located far below f_{int} ($f_z \ll f_{int}$). This is ensured by the relatively large value of R_f and C_{in} found is most TIA (equation 6.16a). The noise gain zero is thus able to introduce almost a 90° phase shift. At this point, equation 6.33 becomes:

$$\Phi_m = \Phi_{f_p} \tag{6.34}$$

This expression illustrates the phase compensation performed by the feedback capacitor to restore the circuit stability. In the uncompensated case, $\Phi_{f_p} = \Phi_m = 0$, predicting instability. In figure 6.10, this unstable condition translates to the curves relative rates of closure of -40 dB/decade. The pole introduced in the noise gain by the feedback capacitor is used to compensate for the phase lag due to the noise gain zero and restore the circuit stability. In figure 6.10, the curves relative rates of closure lies between -40 dB/decade and -20 dB/decade, indicating a non zero phase margin.

[1] The remaining cases are discussed in references [85, 47].

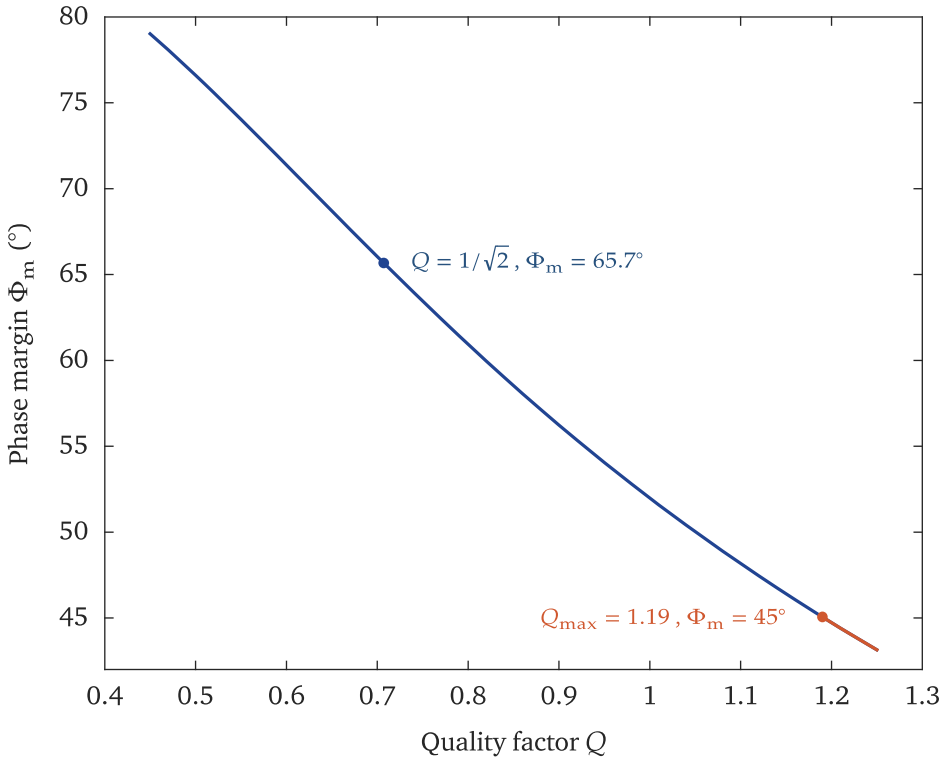

Figure 6.11 Phase margin Φ_m of the transimpedance amplifier as a function of its quality factor Q. To preserve a phase margin of at least 45°, the quality factor must not be set higher than $Q_{max} \approx 1.19$. The Butterworth case $Q = 1/\sqrt{2}$ provides a phase margin of 65.7°.

The actual value of the phase margin acheived through this phase compensation then relies on an adequate selection of the feedback capacitor value. A common approximate expression for C_f is provided by the following two step approach:

- Without C_f, the intercept frequency f_{int} is equal to the circuit resonant frequency f_r [47]. Setting the pole frequency f_p at f_r, where f_r is first computed for $C_f = 0$, then lets the pole develops around half of its full phase lead, yielding $\Phi_{f_p} \approx 45°$.
- The $f_p = f_r$ relation is solved after neglecting the feedback capacitance compared to the input capacitance ($C_f \ll C_{in}$), an approximation which is valid when a relatively large area photodiode is selected.

The resulting equation for C_f is:

$$C_f \approx \sqrt{\frac{C_{in}}{2\pi R_f f_c}} \quad \text{for} \quad C_{in} \gg C_f \tag{6.35}$$

Including the resulting C_f to the circuit lets the intercept frequency occur above f_r, and as a result, the provided phase margin is not equal to 45°, as it is often stated in the technical litterature [85]. However, the phase margin will be found above 45°, so that equation 6.35 provides a conservative value for C_f.

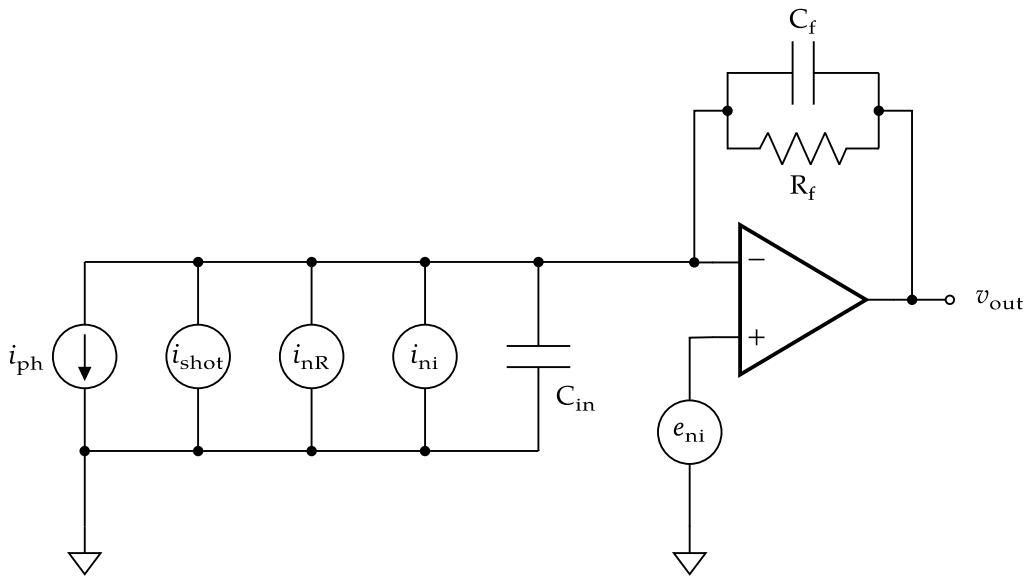

Figure 6.12 TIA circuit model for noise analysis [56]. The major random noise sources in the transimpedance amplifier are the signal shot noise i_{shot}, the feedback resistor Johnson-Nyquist thermal noise i_{nR}, the opamp input current noise i_{ni} and the opamp input voltage noise e_{ni}. The first three noise sources appear at the output through the TIA signal transfert function, but the input voltage noise is amplified by the TIA non inverting gain H_{NI}. In general, the input current noise is made negligible by choosing a JFET input operational amplifier.

Nonetheless, as the feedback capacitor value also has an important impact on the circuit bandwidth and noise, directly using the value provided by equation 6.35 will likely results in a suboptimal design, particularly when the conditions $f_{\mathrm{z}} \ll f_{\mathrm{int}}$ and $C_{\mathrm{f}} \ll C_{\mathrm{in}}$ are not well satisfied. While this value of C_{f} can be further optimized through simulation and trials and errors, a more accurate expression is still desirable to obtain a better starting point for these optimization procedures and for a better insight into the circuit behaviour. In this regards, it is useful to relate the phase margin to the circuit quality factor. An analytical treatement does not leads to a simple relation between these two quantities, but it can be established numerically. Accordingly, the design curve of figure 6.11 was constructed using the numerical tools provided in [84]. It is found that a maximum quality factor $Q_{\mathrm{max}} \approx 1.19$ is allowed to preserve at least 45° of phase margin. Targeting a quality factor lower that Q_{max} and selecting the corresponding feedback capacitor with equation 6.29 should then ensure a stable circuit response. The Butterworth case $Q = 1/\sqrt{2}$ is found to be associated with a phase margin of 65.7°.

6.1.4 TIA noise

Like any measurement device, the photodiode transimpedance amplifier ability to detect a signal is set by its noise, the term “noise” designating any unwanted signals that may hinder the detection of the desired signal.

This section deals with the random noise generated by the TIA during the detection and amplification process. This noise is generally of physical origin, and is usually generated within the circuit itself, with the notable exception of the shot noise due to the light signal. This random noise cannot be avoided completely, but can be optimized by an adequate selection of the circuit components. Another form of noise comes from interferences, corresponding to unwanted coupling between the circuit and its environnement. Some common sources of interferences are power supplies, electromagnetic radiations, vibrations, or external light sources in the context of light detection. The effects of interferences can be reduced to a negligible level by applying a number of circuit design, layout, and construction methods, including (but not limited to) grounding and shielding. The application of these methods to the CryoQPDI photodetectors is briefly mentioned in section 6.2.4. The application of a bias voltage can also inject power supply noise in the system, a problem treated in section 6.1.5.

The main contributors to the total transimpedance amplifier random noise and their relations to the circuit output signal are described using the circuit model of figure 6.12. Following the common convention [57], a current noise source is accounted by its current spectral density i_n, in unit of $\mathrm{A}/\sqrt{\mathrm{Hz}}$, and a voltage noise source is accounted by its voltage spectral density e_n, in unit of $\mathrm{V}/\sqrt{\mathrm{Hz}}$. For calculation purposes, these noise sources are better represented by their power spectral densities P_{i_n} and P_{e_n}, in unit of A^2/Hz and V^2/Hz respectively, where $P_{i_\mathrm{n}} = i_\mathrm{n}^2$ and $P_{e_\mathrm{n}} = e_\mathrm{n}^2$.

Shot noise Shot noise results directly from the quantum nature of light [55]. The detection of light consists in the independant detection of discrete photons, which is a random Poisson process submitted to statistical fluctuations. These fluctuations constitute the shot noise, which appears as a random noise afflicting the photocurrent. In figure 6.12, the photocurrent's shot noise is modeled by the random current source i_shot. Its power spectral density is uniform (white), and depends only on the average photocurrent:

$$P_{i_\mathrm{shot}} = 2eI_\mathrm{ph} \tag{6.36}$$

where P_{i_shot} is the shot noise PSD expressed in A^2/Hz, e is the electron charge and I_ph is the DC component (average) of i_ph.
Since shot noise derives from the nature of light, it is intrinsic to the light signal itself and sets the maximum signal to noise ratio achievable in a light detection experiment[1]. A goal in photodetection is thus to ensure that the signal to shot noise ratio is not significantly degraded by additional noise sources, meaning that the measurement is shot noise limited. From there, the signal to shot noise ratio can only be improved by capturing more signal, and increases as $\sqrt{P_\mathrm{opt}}$, as a direct consequence of the shot noise obeying a Poisson statistic.

[1] The recent developments about the squeezing of light are ignored on purpose, since they are not relevant in the context of this manuscript.

Johnson-Nyquist noise The Johnson-Nyquist noise of a resistor, or simply the Johnson noise, is the noise caused by the thermal agitation of the electrons in a resistor at thermal equilibrium [60, 91, 57]. In figure 6.12, the Johnson noise of the feedback resistor is modeled by the random current source i_{nR}. It also displays a flat PSD, and depends only on the resistor's value and temperature:

$$P_{i_{\mathrm{nR}}} = \frac{4k_{\mathrm{B}}T}{R_{\mathrm{f}}} \tag{6.37}$$

where $P_{i_{\mathrm{nR}}}$ is the feedback resistor Johnson noise PSD in A^2/Hz, and where T is the feedback resistor temperature[1].

Input current noise The random current source i_{ni} represents the equivalent input current noise generated by the operational amplifier's internal components[57]. Its value depends on the opamp design, and is specified by the manufacturer. For TIA applications, i_{ni} can usually be made negligible by selecting a FET input operational amplifier, but may not be so for very low light level or when using another type of opamp.

Input voltage noise The random voltage source e_{ni} represents the equivalent input voltage noise generated internally by the operational amplifier. For most opamp, the voltage noise displays a $1/f$ power spectral density up to a corner frequency f_{f}, from which it reach a flat noise floor[2] [57]:

$$P_{e_{\mathrm{ni}}} = P^{\mathrm{f}}_{e_{\mathrm{ni}}}\left(1 + \frac{f_{\mathrm{f}}}{f}\right) \tag{6.38}$$

where $P_{e_{\mathrm{ni}}}$ is the opamp input voltage noise PSD in V^2/Hz, and where $P^{\mathrm{f}}_{e_{\mathrm{ni}}}$ is the voltage noise PSD in its flat region.

Total output noise From figure 6.12, it can be seen that the current noise source i_{shot}, i_{nR} and i_{ni} are treated like the signal i_{ph}, so their respective power spectral densities appear at the output multiplied by the circuit power transfer function (equation 6.23). However, unlike the other noise sources of figure 6.12, the input voltage noise is transfered to the output through the circuit non inverting voltage gain H_{NI}. From feedback analysis [47, 46], H_{NI} is given by:

$$H_{\mathrm{NI}} = \frac{1}{\beta}\frac{1}{1 + \frac{1}{\mathrm{A}_{\mathrm{ol}}\beta}} \tag{6.39}$$

[1] In this chapter only, not to be confused with the cantilever temperature.

[2] Below f_{f}, $P_{e_{\mathrm{ni}}} \propto 1/f$, so that the noise spectral density $\sqrt{P_{e_{\mathrm{ni}}}} \propto 1/f^{1/2}$.

At high frequency, the $A_{ol}\beta$ term in equation 6.39 introduces an additional pole in the non inverting gain response at the intercept frequency f_{int} [47, 46]

$$H_{NI} = \frac{1}{\beta}\frac{1}{1+\frac{s}{\omega_{int}}} \tag{6.40}$$

Using equation 6.17, this last expression can be rewritten in term of the circuit characteristic frequencies:

$$H_{NI} = \frac{1+\frac{s}{\omega_z}}{\left(1+\frac{s}{\omega_p}\right)\left(1+\frac{s}{\omega_{int}}\right)} \tag{6.41}$$

From which the circuit non inverting power transfer function $|H_{NI}|^2$ can be determined:

$$|H_{NI}|^2 = \frac{1+\left(\frac{\omega}{\omega_z}\right)^2}{\left(1+\left(\frac{\omega}{\omega_p}\right)^2\right)\left(1+\left(\frac{\omega}{\omega_{int}}\right)^2\right)} \tag{6.42}$$

Neglecting the input current noise i_{ni}, and considering that all the previouly described noise sources are uncorrelated, the transimpedance amplifier total output voltage noise PSD $P_{v_{no}}^{total}$ can thus be evaluated using:

$$P_{v_{no}}^{total} = |H_{TIA}|^2\left(P_{i_{shot}} + P_{i_{nR}}\right) + |H_{NI}|^2\left(P_{e_{ni}}\right) \tag{6.43}$$

Output noise PSD in the passband In most texts about transimpedance amplifier design (or low noise analog circuit design), one is concerned with the magnitude of the output noise fluctuations in the time domain, which is accounted for by its band-limited root mean squared (RMS) amplitude. For the transimpedance amplifier, the output noise RMS amplitude v_{no}^{RMS} can be computed from equation 6.43 as:

$$v_{no}^{RMS} = \sqrt{\int_0^{f_{3\,dB}} P_{v_{no}}^{total}\,df}\,\sqrt{B} \tag{6.44}$$

where B is the equivalent noise bandwidth of the system used to measure v_{no}^{RMS} [57]. In the context of this work however, where the signals of the interferometer are to be analysed in the frequency domain, this quantity is of little significance: one shall considers the photodetector's noise PSD directly, more particularly up their cutoff frequency $f_{3\,dB}$.

Below $f_{3\,dB}$, the circuit power transfer function is almost constant[1], and is approximately equal to $|H_{TIA}|^2 \approx R_f^2$. For common TIA quality factor values, the intercept frequency f_{int} is found close to $f_{3\,dB}$, so that the circuit non inverting gain H_{NI} is almost

[1] This is especially true for $Q = 1/\sqrt{2}$.

solely determined by the noise gain $1/\beta$. Accordingly, in the TIA passband, equation 6.43 can be simplified to:

$$P_{v_{\mathrm{no}}} = P_{v_{\mathrm{shot}}} + P_{e_{\mathrm{nR}}} + P_{e_{\mathrm{no}}} \tag{6.45}$$

where $P_{v_{\mathrm{no}}}$ is the total noise PSD in the passband. $P_{v_{\mathrm{shot}}}$ is the output voltage noise PSD due to the signal shot noise in the passband:

$$P_{v_{\mathrm{shot}}} = R_{\mathrm{f}}^2 \, P_{i_{\mathrm{shot}}} = 2eI_{\mathrm{ph}}R_{\mathrm{f}}^2 \tag{6.46}$$

and the two remaining terms of equation 6.45 are setting the circuit dark noise in the passband, which is the circuit noise in the absence of any signal:

$$P_{e_{\mathrm{nR}}} = R_{\mathrm{f}}^2 \, P_{i_{\mathrm{nR}}} = 4k_{\mathrm{B}}TR_{\mathrm{f}} \tag{6.47a}$$

$$P_{e_{\mathrm{no}}} = \left|\frac{1}{\beta}\right|^2 P_{e_{\mathrm{ni}}} = P_{e_{\mathrm{ni}}}^{\mathrm{f}} \left(1 + \frac{f_{\mathrm{f}}}{f}\right) \frac{1 + \left(\frac{f}{f_{\mathrm{z}}}\right)^2}{1 + \left(\frac{f}{f_{\mathrm{p}}}\right)^2} \tag{6.47b}$$

where $P_{e_{\mathrm{nR}}}$ is the output voltage noise PSD due to the feedback resistor Johnson noise, and where $P_{e_{\mathrm{no}}}$ is the output voltage noise PSD due to the opamp input voltage noise.

Ideally, in the absence of amplifier noise, the TIA dark noise would be set by the feedback resistor Johnson noise only. It is useful to compute the DC output voltage required for the signal shot noise to equal this Johnson noise, which is found by making equations 6.46 and 6.47a equal [56]:

$$v\left(P_{v_{\mathrm{shot}}} = P_{e_{\mathrm{nR}}}\right) = \frac{2k_{\mathrm{B}}T}{e} = 52\,\mathrm{mV} \tag{6.48}$$

at a temperature of $T = 300\,\mathrm{K}$. The noise of any output signal much larger than 50 mV will thus be shot noise dominated.

However, the effect of the opamp input voltage noise often degrades this simple figure dramatically, especially at high frequency, where the rising opamp voltage noise may dominate a large proportion of the TIA passband. Indeed, the gain experienced by the opamp input voltage noise follows the behaviour displayed by $1/\beta$ in figure 6.10 (blue curve, up to f_{int}). The simultaneous demands of high sensitivity, high gain and high bandwidth suggests the use of a large area photodiode, a large feedback resistor and a fast opamp combined with a small feedback capacitor. As a result, f_{z} is placed far below $f_{3\,\mathrm{dB}}$ and the rising opamp voltage noise is allowed to severely degrade the TIA dark noise on the majority of the circuit passband. This noise issue, which is characteristic of the transimpedance amplifier circuit, is the main issue which need to be dealt with in optimizing the TIA dark noise power spectral density. Following reference [57], this noise is referred to as the "$e_{\mathrm{n}}C$" noise in the rest of the chapter,

since it results from an interaction between the opamp input voltage noise and the circuit input capacitance. In the following, a clearer picture of the TIA dark noise is worked out.

Below f_z, the circuit noise gain is unity, and the opamp input voltage noise $P_{e_{ni}}$ appears unchanged at the output. For common TIA configurations, the $1/f$ corner frequency f_f of $P_{e_{ni}}$ is found far below f_z, and the input voltage noise level in its flat region $P^f_{e_{ni}}$ is much lower than the feedback resistor Johnson noise. $P_{e_{ni}}$ thus dominates $P_{e_{nR}}$ only in its $1/f$ region from DC up to a low frequency noise crossover f_{n1}, where they are equal. Accordingly, setting equations 6.38 and 6.47a equal and solving for the frequency gives:

$$f_{n1} = f_f \frac{P^f_{e_{ni}}}{4k_B T R_f - P^f_{e_{ni}}} \tag{6.49}$$

Starting at f_z, $P_{e_{no}}$ rises as f^2 up to f_p. Using equation 6.47b in this frequency range, $P_{e_{no}}$ writes as:

$$P_{e_{no}}\left(f_z < f < f_p\right) = P^f_{e_{ni}}\left(1 + \left(\frac{f}{f_z}\right)^2\right) \tag{6.50}$$

Setting this expression equal to equation 6.47a and solving for f provides an expression for the high frequency noise crossover f_{n2}, above which the $e_n C$ noise dominates:

$$f_{n2} = f_z \sqrt{\frac{4k_B T R_f}{P^f_{e_{ni}}} - 1} \tag{6.51}$$

Above f_p, the noise gain flatten of and $P_{e_{no}}$ reaches a maximum of:

$$P_{e_{no}}\left(f > f_p\right) = P^f_{e_{ni}}\left|\frac{1}{\beta}\right|^2_{max} = P^f_{e_{ni}}\left(1 + \frac{C_{in}}{C_f}\right)^2 \tag{6.52}$$

this relation being found for $f \gg f_z, f_p$ in equation 6.47b.

Within its passband, the TIA dark noise can therefore be separated into four frequency segments, depending on which of $P_{e_{nR}}$ or $P_{e_{no}}$ dominates (figure 6.13, see the next section):

- From DC to f_{n1}, the dark noise is dominated by $P_{e_{no}}$, and display its $1/f$ behaviour.
- Between f_{n1} and f_{n2}, the dark noise is mainly determined by $P_{e_{nR}}$, and diplays its flat power spectral density. This is the shot noise dominated frequency band which should be maximized.
- Between f_{n2} and f_p, the $e_n C$ noise comes to dominates the total dark noise again, which then increases as f^2.

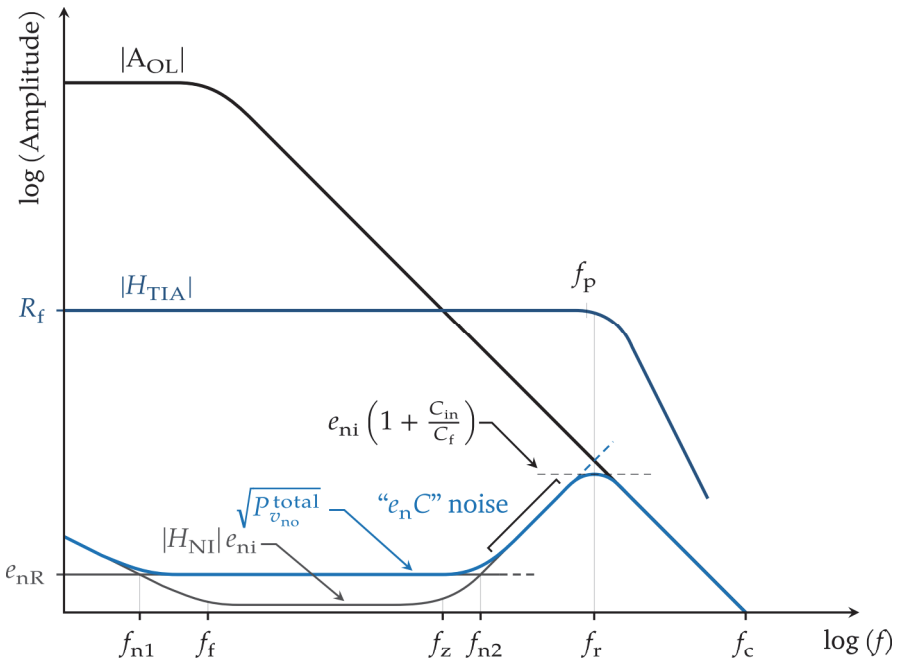

Figure 6.13 Design curves for a photodiode transimpedance amplifier. Note that these curves have different units. The two noise densities $|H_{NI}|\,e_{ni}$ and $\sqrt{P_{v_{no}}^{total}}$ displayed at the bottom of the figure are in unit of $\mathrm{m}/\sqrt{\mathrm{Hz}}$, the circuit gain $|H_{TIA}|$ is in Ω, and the open-loop gain A_{ol} is in V/V (unitless).

- Finally, from f_p to f_{int}, the dark noise is still dominated by $P_{e_{no}}$, which now displays a flat PSD, reaching the plateau value given by equation 6.52[1].

At a frequency where $P_{e_{no}}$ dominates, the results of equation 6.48 can be extended easily: if at a given frequency the dark noise PSD is N times larger than the feedback resistor Johnson noise PSD, the circuit output voltage must be N times 52 mV for the signal shot noise to equal the dark noise at this frequency.

6.1.5 Photodetector design strategy

Design curves Summarizing the analytical model of the transimpedance amplifier presented so far, figure 6.13 provides a synthetic schematic representation of the circuit signal response, stability and noise and their relations to the various circuit characteristic frequencies, for the case $Q = 1/\sqrt{2}$. As explained before, this particular value of Q provides a maximally flat signal response as well as an adequate level of stability. A flat response is desirable in this context since it results in a simplification of the interferometer frequency domain data analysis.

[1] Note that above f_{int}, the noise will decrease again thanks to the additional pole at f_{int} in equation 6.40.

Since for $Q = 1/\sqrt{2}$, the circuit resonant frequency f_r and cutoff frequency $f_{3\,dB}$ are equal, the vertical line at f_r in figure 6.13 marks the circuit signal bandwidth together with the validity range for the passband noise analysis carried out before, from equation 6.45 to equation 6.52. The behaviour of the total circuit dark noise spectral density $\sqrt{P_{v_{no}}^{total}}$ below f_r thereby follows from this analysis, and figure 6.13 illustrates the four frequency segments delimited by f_{n1}, f_{n2}, f_p and f_r.

Below f_r then, were $H_{NI} = 1/\beta$, and above f_f, were the opamp input voltage noise is flat, the $|H_{NI}|\, e_{ni}$ curve on the bottom of figure 6.13 reproduces the behaviour of the TIA noise gain $1/\beta$, and its intersection with the opamp open loop gain magnitude $|A_{OL}|$ somehow repeats the stability considerations illustrated by figure 6.10.

Components selection To achieve a low dark noise PSD, and then obtain a shot noise limited measurement on a large bandwidth even for low light levels, it is desirable to place f_z, and thus f_{n2}, at a frequency as high as possible, ideally so that f_{n2} ends above $f_{3\,dB}$. From equation 6.51, if all the parameters but R_f remain fixed, one can found that f_{n2} vary as $1/\sqrt{R_f}$, which suggest reducing the feedback resistor to increase f_{n1}. Since reducing R_f also reduce the output signal and shot noise level, the benefit of this R_f reduction in terms of signal to noise ratio is not immediate. To help clarify this point, another noise crossover frequency f'_{n2} can be defined, this time using the output shot noise PSD. Setting equations 6.46 and 6.50 equal, the expression for f'_{n2} is:

$$f'_{n2} = f_z \sqrt{\frac{2ei_{ph}R_f^2}{P_{e_{ni}}^{f}} - 1} \tag{6.53}$$

from which it is found that f'_{n2} is only weakly affected by a change of R_f. In other word, increasing R_f does not help in making the shot noise overcomes the $e_n C$ noise, because the resulting shift of f_z to a lower frequency counteracts the higher gain applyed to the shot noise, leaving f'_{n2} almost unchanged. Although increasing R_f alone does not improves the signal to shot noise ratio, it helps in making the shot noise overcomes the noise of the remaining elements of the signal chain. Generally, it appears that the use of a moderate R_f value is preferable, as long as the retained value allows for a shot noise limited operation, ideally on the full TIA bandwidth, considering both the TIA noise alone and the noise of the complete signal chain.

The most effective mean of mitigating the $e_n C$ noise through an increase of f_{n2} is to minimize the input capacitance C_{in}, by selecting an opamp with a low input capacitance $C_{icm} + C_{idm}$, and by using a reverse biased photodiode with a small area to acheive a low C_D. Reducing the size of the photodiode also implies practical alignement difficulties, and does not offers additional advantages if the photodiode is already small enough for C_D to be comparable or lower than $C_{icm} + C_{idm}$. The input capacitance of an opamp typically ranges between 1 pF to 20 pF. As fast opamps tend to displays lower input capacitance [57], this C_{in} reduction strategy suggests the selection of an opamp

with a high f_c (a high gain bandwidth product GBW). Usually, fast opamps also display better dynamic performance[1], which are desirable for a better overall performances. Faster opamp, however, also tend to display higher input voltage noise en [57]. The observation made during this work is that if the photodiode and opamp input capacitance are comparable, this effect mitigates but does not eliminates the advantage of a reduced opamp input capacitance, making a faster opamp still desirable.

In choosing an opamp and a feedback resistor value, the following consideration must also be kept in mind. For a fixed circuit quality factor Q, a larger R_f value also reduces bandwidth, because reducing f_z also reduce f_r, meaning that an even faster opamp may be required to attain the same bandwidth. Both a larger R_f and a higher f_c results in the use a small feedback capacitor C_f, which may become impractical, in the sense that the value required may be comparable to the printed circuit board's parasitic capacitances[2]. The selection of R_f and the opamp also define the TIA dynamic range, which is the difference between the highest and lowest measurable light intensity. The highest measurable light intensity is determined by the saturation of either the opamp or the following elements of the signal chain, while the lowest measurable light intensity is set by noise. At last, fast opamps also tend to display higher f_f, increasing f_{n1} and the TIA low frequency dark noise. This last constrains is not of the most restrictives, because an opamp input voltage noise PSD increases as f toward lower frequency, while the e_nC noise increases as f^2.

On the whole, the selection of the feedback resistor involves a noise versus bandwidth and stability compromise, with an arguably nonintuitive relation with the circuit dark noise and shot noise. The selection of the opamp, in addition to the clear bandwidth implication, also involves a low frequency versus high frequency noise compromise.

At this point, it should be emphasized that the usual opamp selection recommandation for noise reduction in the TIA, which adress the integrated RMS noise, can conflict with the objective of minimizing the dark noise PSD in the passband when a small area photodiode is employed. From equation 6.43, and as shown in the design curves of figure 6.13, the opamp input voltage noise and the signal are transferred to the output through two differents transfer functions. In particular, the opamp input voltage noise receives a much larger bandwidth than the signal, since it is mainly determined by the opamp f_c. For a large area photodiode, where the opamp input capacitance is negligible in front of the diode capacitance ($C_{in} \approx C_D$), only the opamp e_n and f_c are relevant, and it is preferable to select an opamp just fast enought to attain the required TIA bandwidth, so as to reduce the input voltage noise bandwidth and be able to use an opamp with a lower e_n. In this case, it is usually not possible to set the e_nC noise

[1] Here, better dynamic performance mean for example lower harmonic distorsion and higher slew rates [19].

[2] The nature of this parasitic capacitances and a mitigation method is briefly discussed in section 6.2.4.

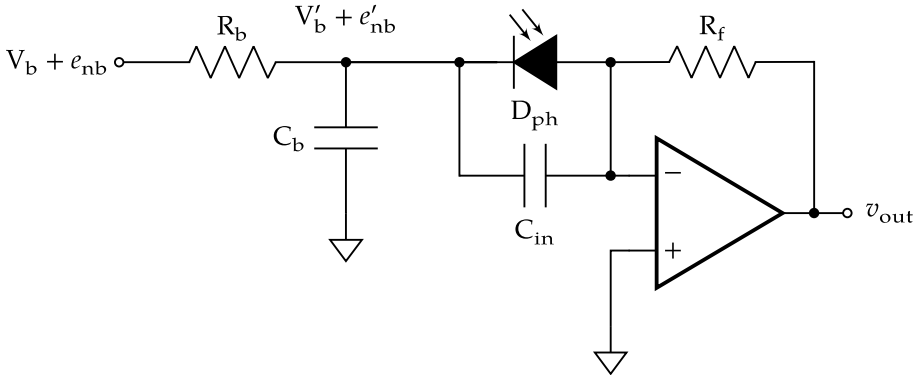

Figure 6.14 The application of the R_bC_b bias filter to the bias voltage V_b diverts a large portion of the bias voltage noise e_{nb} to the ground [47]. The impedances of the filter's components are selected for a minimal perturbation of the TIA operation.

outside of the passband, and the advantage of a lower e_n is the only remaining way of minimizing its effect. In contrast, when the photodiode and opamp input capacitance are comparable, selecting a faster opamp with lower input capacitance can lead to a reduction of the passband dark noise, as explained before.

Bias noise filtering In the TIA circuit, noise on the powerlines may affect the output voltage in two ways. On the one hand, voltage fluctuations in the opamp supply rails are coupled to the output signal, but the opamp resists this coupling thanks to its power supply rejection ratio (PSRR) [57, 19]. When using a reasonably quiet power source in combination with a proper capacitive bypassing of the supply rails, the opamp PSRR should reduce the effect of supply rails fluctuations to a negligible level [47]. On the other hand, the noise caused by fluctuations of the bias voltage requires special attention.

Figure 6.14 displays the application of a RC filter to the bias voltage. The noise component e_{nb} represents the fluctuations of the bias voltage V_b. Without the filter components R_b and C_b, e_{nb} is impressed across the circuit input capacitance C_{in}, producing a noise current $e_{nb}C_{in}s$. This current flow through the feedback resistor, resulting in a new output voltage noise component $e_{nb}R_fC_{in}s$. In other words e_{nb} receives amplification through the bias voltage noise gain A_{nb}:

$$A_{nb} = R_fC_{in}s \tag{6.54}$$

with a response zero at $1/2\pi R_fC_{in}$, which is usually close in frequency to the noise gain zero f_z. This result in a high level of high frequency amplification of the bias voltage noise, not unlike the e_nC noise described earlier. But where the later resulted from amplification of the opamp input voltage noise, the former results from a bias voltage noise which is commonly several order of magnitude larger: if nothing is done to mitigate this noise source, it will likely severely degrades the circuit noise up to an unacceptable level.

The R_bC_b bias filter is added in figure 6.14 accordingly. With the filter in place, the initial bias voltage $V_b + e_{nb}$ becomes $V'_b + e'_{nb}$. The goal is to ensure only a little DC voltage loss, which translates into $V'_b \approx V_b$, while significantly reducing the AC bias voltage noise component, so that $e'_{nb} \ll e_{nb}$. Following reference [47], these conditions are met with the following design rules:

$$\begin{aligned} R_b &\ll R_f \\ C_b &\gg C_{in} \\ R_f C_{in} &\ll R_b C_b \end{aligned} \tag{6.55}$$

With bias filtering, the bias noise gain becomes

$$A'_{nb} = \frac{R_f C_{in} s}{1 + R_b (C_b + C_{in}) s} \tag{6.56}$$

At high frequency, with $C_b \gg C_{in}$, this gain turns into

$$A'^{HF}_{nb} = \frac{R_f C_{in}}{R_b C_b} \tag{6.57}$$

The presence of the filter introduces a response pole to counteract the zero of A_{nb} (equation 6.56), flattening the noise gain at high frequency (equation 6.57). Applying the R_bC_b bias filter and following the design rules of equation 6.55 should ensures a significant high frequency attenuation of the bias voltage noise while minimizing disturbance of the TIA operation.

On the need for a lowpass antialiasing filter Up to now, the discussion was focused on the optimization of the TIA dark noise in the passband only. This does not mean that the circuit signal and noise above $f_{3\,dB}$ can be ignored.

The CryoQPDI photodetectors output voltage is ultimately digitized by an analog to digital converter (ADC). In the Fourier domain, the maximum resolvable frequency of the spectrum, i.e. the Nyquist frequency, is equal to $f_s/2$, where f_s is the sampling frequency. The discrete time sampling inherent to the analog to digital conversion process creates an ambiguity between the signal (or the noise) below and above the nyquist frequency. This ambiguity, called aliasing, has the important practical consequence of making the spectral content located above the Nyquist frequency "fold back" at below the Nyquist frequency [70]. If f_0 is a frequency between DC and $f_s/2$, any spectral content at $(f_0 + nf_s)$, where n is an integer, is added to the spectrum at f_0. For the TIA, the consequence of aliasing is a contamination of the passband signal by the circuit high frequency dark noise, which is severely compounded by the both the large bandwidth allowed to this noise and the usually large amplification applied to the opamp e_n between f_p and f_{int} (equation 6.52).

As aliasing is a direct consequence of sampling, it cannot be avoided, but its effect can usually be reduced to a negligible level by the application of an analog lowpass antialiasing filter. The purpose of such a filter is to attenuate the spectral content above $f_s/2$ so that when aliasing occurs, only an insignificant quantity is added to the spectrum of interest below $f_s/2$.

In practice, the CryoQPDI data acquisition card (DAQ) have an integrated first order lowpass antialiasing filter. During initial testing, the DAQ filter proven to provide insufficient attenuation of the TIA high frequency noise. In response, an order five filter was built an inserted in the signal chain between the TIA and the DAQ. The filter, whose design is briefly described in section 6.2.2, is found to yield an efficient antialiasing effect while adding a negligible amount of noise in the signal chain.

Circuit simulation The analytical model developed in this chapter is a necessary approximation of the behaviour of a real world circuit. Real circuit components have imperfections, the printed circuit board presents stray inductances and capacitances [10], and in particular, the response of an operational amplifier is expectedly more complex than what equation 6.19 suggest [56].

In this regard, circuit simulation is an important part of the circuit design process. It allows verification of the analytical model with a more accurate description of the circuit elements. It also offers a flexible interface were the design can be quickly altered and optimized. Accordingly, circuit simulations where performed during the CryoQPDI photodetectors' development to limit the amount of prototyping work and to obtain a more accurate representation of the circuits response.

Simulations where done using the LTSpice XVII software [32] based on the SPICE language [86]. All the transimpedance amplifier simulations where carried out on the schematic of figure 6.7, with opamp macromodels [12, 6] provided by the manufacturers[1]. As a trade of between accuracy and simulation speed, an opamp macromodel is a simplified mathematical description of its characteristic rather than a complete physical representation. For this reason, and because it is elusive to include all the many effects that can be encountered in a real circuit, simulation cannot replace prototyping, but as mentioned above, it anyway remains an important intermediate step between analytical modeling and the real world circuit implementation.

Design strategy From the discussion carried out sor far, the following design strategy was applied to the developpment of the CryoQPDI photodetectors:

- select a small area PIN photodiode, and apply a reverse bias voltage to further reduce its capacitance;

[1] The opamp input capacitance is included in its macromodel, and was not added to the circuit schematics

- select a suitable feedback resistor, providing a sufficient amount of amplification without compromizing on noise and bandwidth;
- select a FET-input opamp with a large f_c and a correspondingly low input capacitance. The opamp should also displays a low input voltage noise spectral density, a low input voltage noise $1/f$ corner frequency, and have an output voltage range equal or higher than the DAQ input voltage range to maximize dynamic range;
- select a feedback capacitor for a quality factor of $1/\sqrt{2}$, providing adequate stability as well as a flat frequency response. At this point, following the selection of a fast opamp, the TIA likely present a signal bandwidth larger than required, and produces a significant amount of high frequency noise;
- use a low pass antialiasing filter to set the bandwidth of the photodetector and eliminates aliasing, while adding a negligible amount of noise relative to the TIA;
- verify the transimpedance amplifier and antialiasing filter with LTSpice simulations;
- among several method to reduce the effect of external interference, apply an *RC* filter to the photodiode bias voltage to reject the noise caused by its fluctuations.

At the opamp selection step, with both the feedback capacitor value and the opamp input capacitance and unity gain crossover frequency being unknown, it is not immediatly clear how a particular opamp may be adequate, but choosing a relatively fast opamp also simplify this step so that a trial and error selection method is sufficient.

6.2 Signal chain design

The CryoQPDI signal chain was developped with two main requirements: a target bandwidth of 1 MHz, and a combination of signal gain and dark noise allowing for a shot noise limited operation at all frequency within this passband for the thermal noise measurement of an uncoated silicon µcantilever. The 1 MHz bandwidth requirement stems from the experience gained on the reference QPDI; it allows for the detection of many vibration modes on a soft cantilevers, and also permits the detection of a few modes on the more rigid ones. The noise requirement, which motivated the elaboration of the previouly described design strategy, was set to obtain an optimally flat measurement background noise even with the relatively low light level obtained with the reflectivity of an uncoated µcantilever.

The global schematic of the CryoQPDI signal chain is represented in figure 6.15 for one of the four channels of the interferometer. Each channel consists in three mains elements: a photodiode transimpedance amplifier, a low pass antialiasing filter and the "analog input" of the data acquisition card. The combination of a TIA and a lowpass filter forms one of the four photodetectors of the system. All the photodetectors are powered by a pair of 12 V lead-acid battery, which deliver one of the lowest possible power supply noise [57]. The same 12 V potential is applied as the photodiode bias

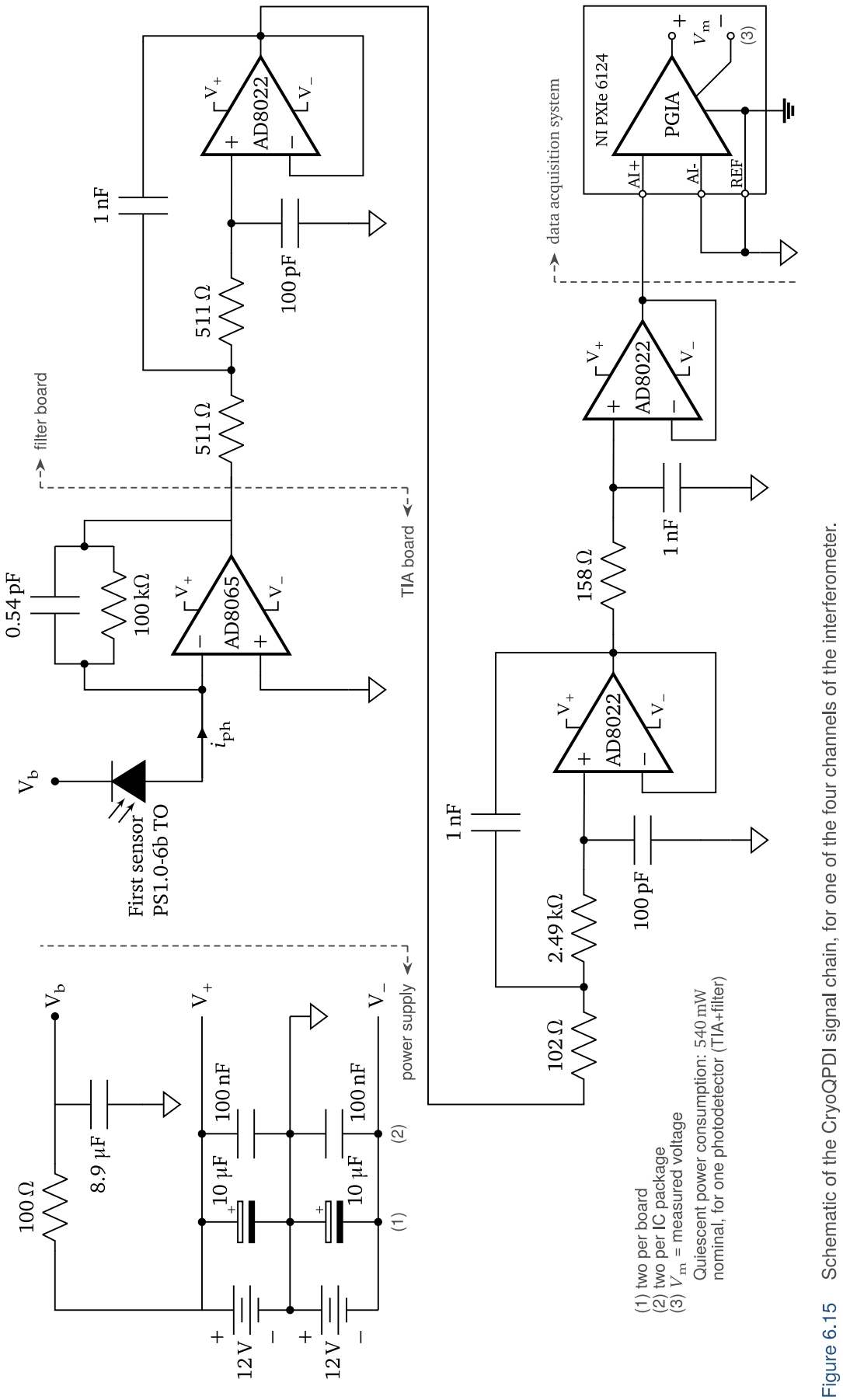

Figure 6.15 Schematic of the CryoQPDI signal chain, for one of the four channels of the interferometer.

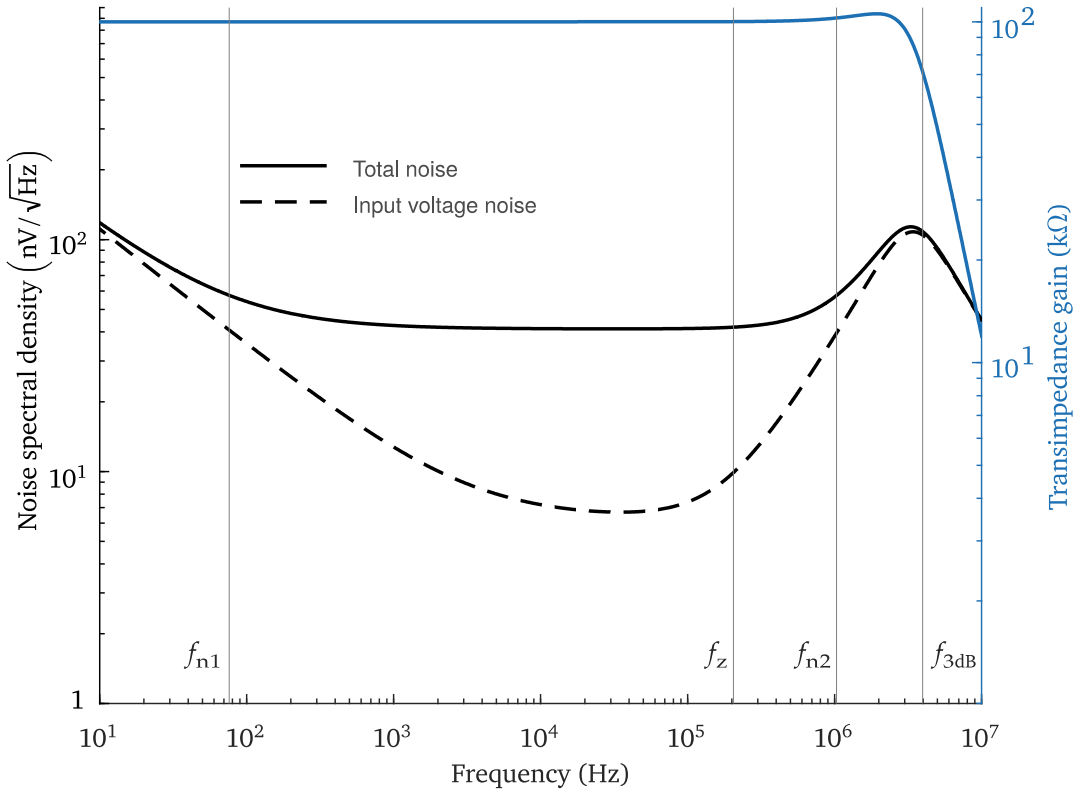

Figure 6.16 LTSpice noise and gain simulation of the transimpedance amplifier employed in the CryoQPDI photodetectors. The general behaviour of both the circuit gain and noise is compatible with the analytical model developped in section 6.1 and displayed by the TIA design curve of figure 6.13. With a relatively low total input capacitance of 10.6 pF, the simulation indicates that the $e_n C$ noise becomes dominant only around 1 MHz.

voltage: as shown in figure 6.3, an higher bias voltage would have only resulted in a slight additional reduction of the photodiode capacitance and is not worth the additional circuit complexity, particuly here with the photodiode capacitance already of the same order as the opamp input capacitance. The measured signal on each channel range between 0 V and −10 V, limited by the DAQ input range. In this section, the design, selection and arrangement of each element of the signal chain is presented.

6.2.1 Transimpedance amplifier

The CryoQPDI transimpedance amplifiers (figure 6.15) are based on a First sensor PS1.0-6b TO PIN photodiode [101] and an Analog Device AD8065 operational amplifier [3]. The relevant specifications for these two parts are listed in table 6.1. Beside its low C_D of 4 pF when reverse biased, the photodiode was selected for its slightly enhanced responsivity at 532 nm. The TIAs have a nominal total input capacitance of $C_{in} = 10.6$ pF. With a 100 kΩ feedback resistor, the peak output voltage of the photodector is around 1 V when measuring an uncoated silicon cantilever under nominal

Table 6.1 Specifications for the photodiode and operational amplifier employed in the CryoQPDI TIA. The opamp parameters are given for a supply voltage of $\pm$ 12 V.

PS1.0-6b TO photodiode		AD8065 opamp	
parameter	value	parameter	value
active aera	$1 \times 1\ \mathrm{mm}^2$	f_c (GBW)	145 MHz
$R_{532\,\mathrm{nm}}$	0.38 A/W	$C_{\mathrm{icm}} + C_{\mathrm{idm}}$	6.6 pF
C_D ($V_b = 0$ V)	16 pF	e^f_{ni}	$7\ \mathrm{nV}/\sqrt{\mathrm{Hz}}$
C_D ($V_b = 12$ V)	4 pF	f_f	2 kHz
		output voltage range	$\pm$ 11.9 V

Table 6.2 Comparison of some of the CryoQPDI TIA characteristic frequencies obtained by theoretical calculation and simulation.

characteristic frequency	theory	simulation	difference
f_{n1}	61 Hz	76 Hz	+25 %
f_z	143 kHz	205 kHz	+44 %
f_{n2}	0.843 MHz	1.03 MHz	+22 %
f_{3dB}	4.04 MHz	3.97 MHz	−2 %

conditions[1]. The theoretical C_f required for $Q = 1/\sqrt{2}$ in this configuration (equation 6.29) is equal to 0.48 pF, and a feedback capacitor with a closest matching value of 0.5 pF was selected, bringing the total feedback capacitance at 0.54 pF when taking into account the nominal parasitic capacitance of 0.04 pF of the feedback resistor (reference [43], table 1, case size 0603). With $C_f = 0.54$ pF, the circuit theoretical quality factor is reduced to $Q = 0.63$. The AD8065 opamp have a rail to rail out (RRO) output stage, meaning that it can output a voltage almost as high or as low as its supply voltage [19]. With the TIA arrangement chosen (figure 6.15), the TIA output voltage can range nominaly between 0 V and −11.9 V (figure 6.6).

Figure 6.16 displays simulation results for the TIA gain and noise. Both the circuit noise and gain display the general behaviour expected from the analytical model (figure 6.13). Despite a theoretical quality factor below $1/\sqrt{2}$ ($\approx$ 0.707), where no gain peaking is expected, the simulated gain present a slight 5 % gain peaking, suggesting a effective quality factor above $1/\sqrt{2}$. This moderate gain peaking still suggest an adequate phase margin for the circuit, and the feedback capacitor value was left as is as a consequence. As expected, the simulated circuit total noise spectral density is essentially flat between f_{n1} and f_{n2}, where it is dominated by the feedback resistor Johnson noise of $40.7\ \mathrm{nV}/\sqrt{\mathrm{Hz}}$. By design, the $e_n C$ noise dominates only at a very high frequency, leaving the majority of the passband almost unaffected.

In table 6.2, a comparison is made between the theoretical and simulated value for the four TIA characteristic frequencies represented in figure 6.16. The higher f_{n1} value obtained in simulation can be explained by the inaccuracy in extracting the f_f frequency

[1] For an optical power of 0.5 mW incident on the cantilever, adjusted to avoid an excessive temperature gradient in the cantilever due to absorption.

from the AD8065 input voltage noise curve. The relatively large deviation found between theory and simulation for f_z and f_{n2} as well as the gain peaking observed on the simulated gain curve does not lend themself to such trivial explanations. They are interpreted as a consequence of the simulation being based on a likely more complete model of the AD8065 opamp. Nevertheless, not only does the simulated f_{n1} value remains very low, indicating that the $1/f$ input voltage noise of the AD8065 have little impact on the TIA total noise, but the simulated f_z and f_{n2} are higher than expected from theory, meaning that simulation predicts a overall lower noise spectral density in the circuit passband. The $f_{3\,\mathrm{dB}}$ bandwidth predicted by theory and simulation are in good agreement, but this finding is likely not significant since the comparison is made between circuit having different quality factors. The circuit bandwidth is much larger than the target bandwidth of the signal chain, in agreement with the proposed design strategy: the bandwidth of a photodetector is to be set by its lowpass antialiasing filter.

6.2.2 Antialiasing filter

The schematic of the CryoQPDI photodetectors' lowpass antialiasing filter is displayed in figure 6.15. The filter is an order 5 Butterworth lowpass active filter built around three AD8022 opamps [2] The first two opamps implements order 2 lowpass active filters based on the Sallen-Key topology, while the last filter stage simply consists in an order 1 lowpass *RC* filter followed by an opamp configured as an unity gain buffer. The design of active filters and the Sallen-Key topology have been thoroughly described in the litterature [8, 66, 51], and it is not useful to repeat them here. In practice, the filter have been designed using an automated online design tool [31]. The schematic of figure 6.15 was obtained using the preset "low noise" method and the filter order was selected as a tradeoff between attenuation and noise. The design tool selected both the opamp and the value of the passive components used. Using the AD8022 opamp, the filter accept input voltages ranging between $-11\,\mathrm{V}$ and $12\,\mathrm{V}$ and can output voltages in the $\pm$ 11 V ranges.

Figure 6.17 shows the filter gain and noise simulation results. The employed filter topology provides an unity gain in the passband independent of the value (and tolerance) of the passive components used. The design nominal -3 dB cutoff frequency is 978 kHz, adjusted for the availability of discrete components and with an acceptable deviation from the signal chain 1 MHz target bandwidth.

The simulated gain and noise of a photodetector assembly is given in figure 6.18, illustrating the effect of the filter on the TIA output voltage. As expected, the filter eliminates the TIA e_nC noise and signal above its cutoff frequency to avoid the effect of aliasing, while adding a negligible amount of noise of its own. The total noise spectral density of the photodetector in the flat region equal $42.4\,\mathrm{nV}/\sqrt{\mathrm{Hz}}$, less than $2\,\mathrm{nV}/\sqrt{\mathrm{Hz}}$ above the feedback resistor Johnson noise contribution. At low frequency,

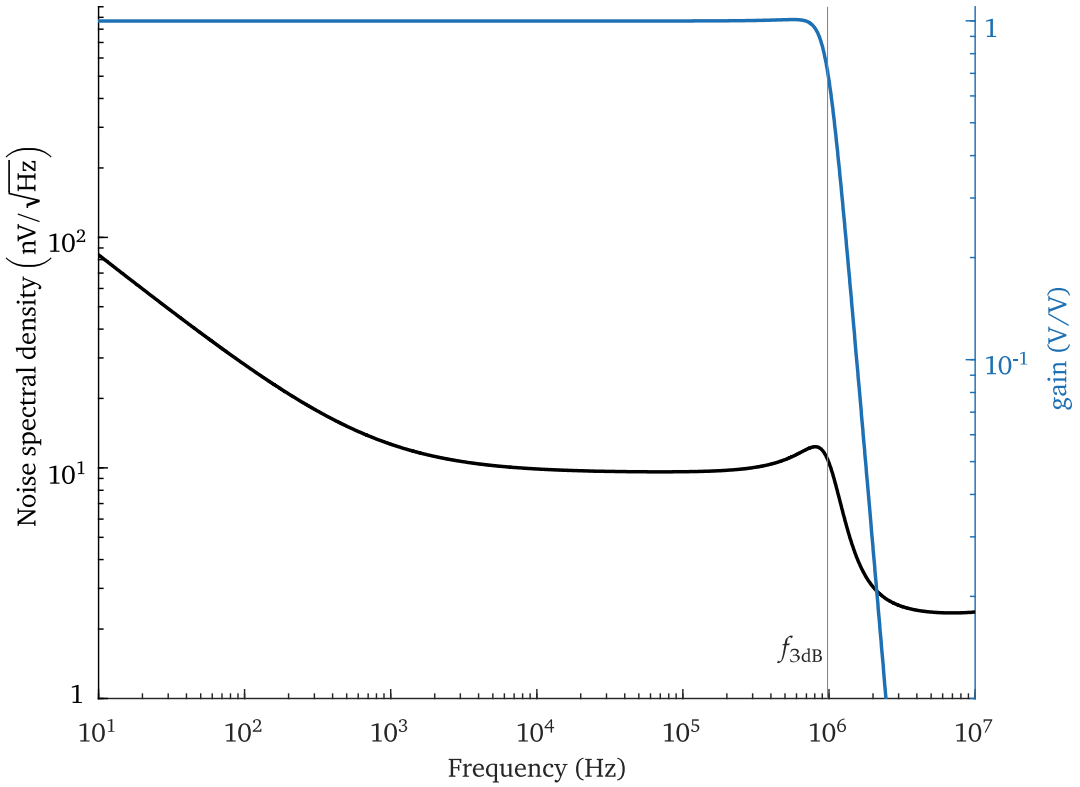

Figure 6.17 LTSpice noise and gain simulation of the low pass antialiasing filter implemented in the CryoQPDI photodetectors. The filter topology provides unity gain with no dependance on the value of the used resistors and capacitors. At 2 MHz, the Nyquist frequency of the signal chain, the filter attenuates its input signal by a factor of 36.

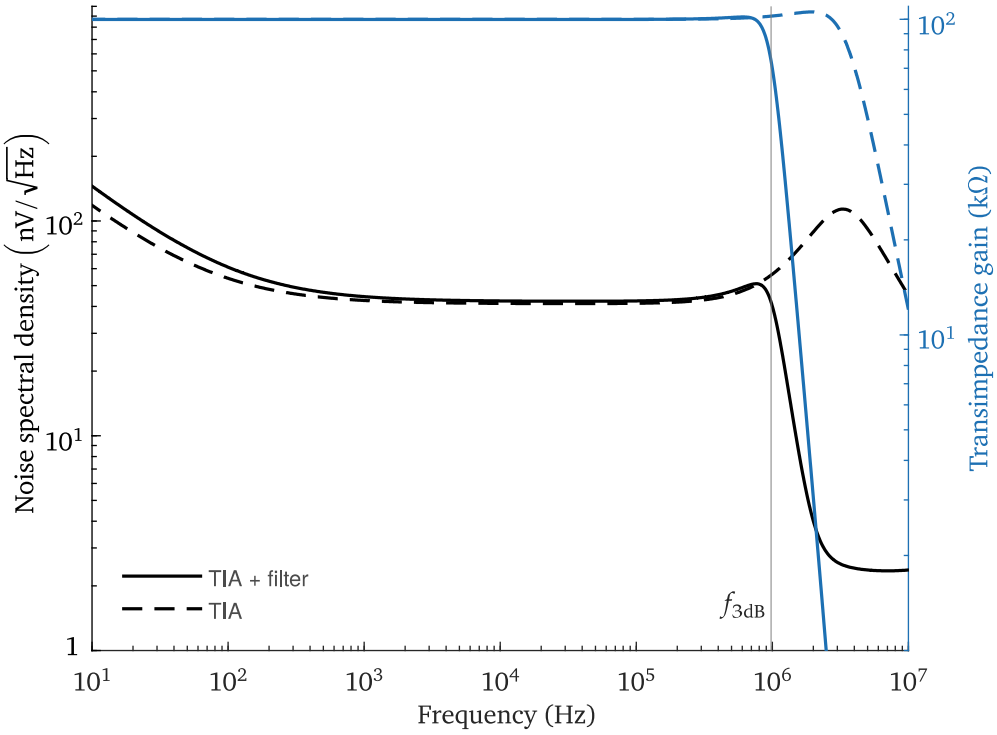

Figure 6.18 LTSpice noise and gain simulation of a complete CryoQPDI photodetector assembly. The TIA total noise and gain curve from figure 6.16 are also displayed for comparison.

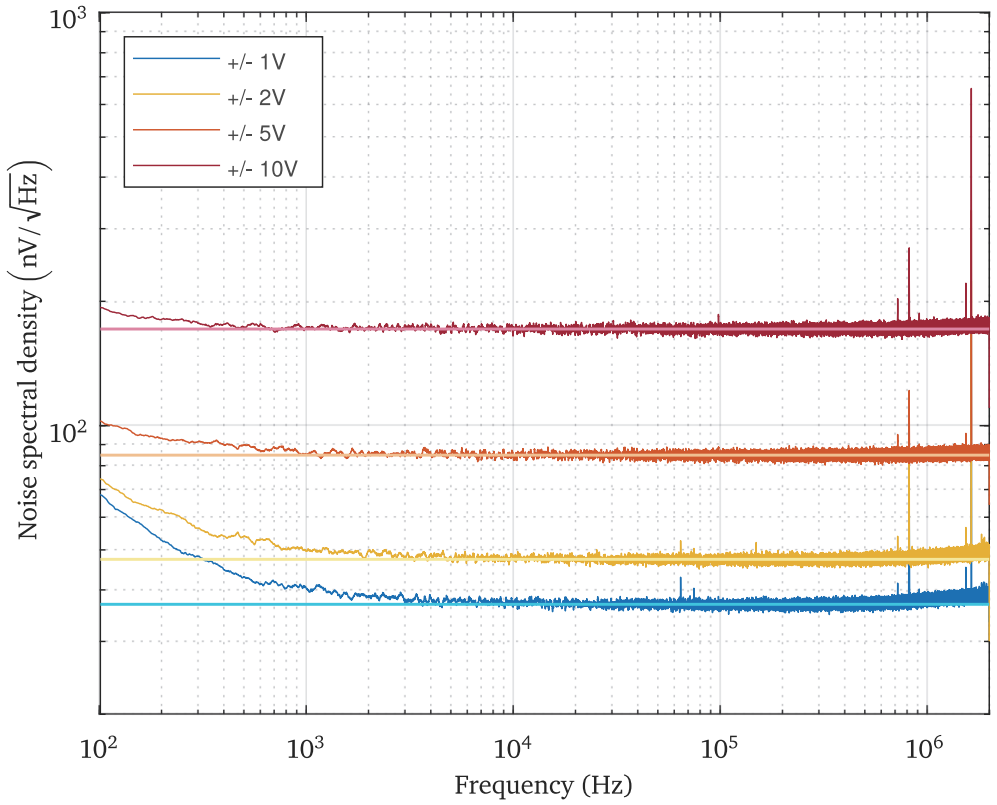

Figure 6.19 Experimental quantization noise spectral density of the CryoQPDI DAQ analog inputs (NI PXIe 6124). For each range, the noise density value was taken as the average of the experimental spectrum between 10 kHz and 500 kHz. The this average noise level is displayed at all frequency for comparison.

f_{n1} is effectively increased to 125 Hz, which still predicts a very good low frequency noise performance.

6.2.3 Data acquisition card (DAQ) selection

In selecting an analog to digital convertion system, both the maximum sampling frequency and the noise introduced by the analog to digital converter (ADC) must be considered. The Nyquist criterion mentioned in section 6.1.5 requires an ADC sampling frequency f_s at least equal to two times the maximum frequency of the signal to be digitized. Translated to the signal chain target bandwidth of 1 MHz, this criterion requires a sampling frequency of at least 2 MHz. Understandably, a larger sampling frequency is required in practice to give the antialiasing filter a frequency band for attenuation.

The smallest voltage variation detectable by an analog to digital converter, namely its voltage resolution, is equal to one least significant bit (LSB, in volt) [98]. An ADC LSB is related to its bit resolution and input voltage range by:

$$LSB = \frac{V^+ - V^-}{2^N - 1} \tag{6.58}$$

where V^+ and V^- are respectively the higher and lower bound of the ADC input voltage range. During the quantization process inherent to analog to digital convertion, the analog input voltage is rounded to the nearest voltage level accomodated by the ADC. A maximum digitization error of $\pm$ 1 LSB is thus added to the real input voltage value, which translates into the addition of a quantization noise to the quantized signal. In average, the quantization noise of a perfect ADC sampling a random signal is equal to $1/\sqrt{12}$ LSB RMS [62, 72]. In practice, the quantization noise of a perfect ADC can be strongly correlated with the input signal if this signal is not purely random, and as a consequence, a perfect ADC is potentially nonlinear. To avoid this artifact of the quantization process, a small amount of random noise is added on purpose to the input signal, a method called dithering [62, 121]. In other word, the addition of the dither noise remove the ADC nonlinearity by randomizing the quantization noise. Consequently, the RMS noise of a commercial DAQ analog input is found closer to 1 LSB RMS.

Taking this distinction into account, a good approximation for the power spectral density of quantization noise of an ADC is given by:

$$P_{\mathrm{e_n\,DAQ}} \approx 1 \times (LSB)^2 \frac{2}{f_\mathrm{s}} \tag{6.59}$$

The quantization noise PSD of an ADC is thus flat in frequency, and depends on its input voltage range, bit resolution and sampling frequency. Since it leads to an higher voltage resolution, a lower quantization noise is achieved with a smaller input voltage range and a higher bit resolution. A higher sampling frequency also results in a lower noise PSD, because the quantization noise is spread on a larger bandwidth. Accordingly, in systems with variable sampling rate, the highest sampling rate available must be selected to reach the lowest possible ADC quantization noise PSD. This noise model is at least valid for succesive approximation register (SAR) ADC [63], as shown below.

Equation 6.59 and the Nyquist criterion, linking the DAQ resolution and sampling frequency to the system bandwidth and noise, are the basic factors to take into account in selecting a data acquisition card. Importantly, in addition to these two factors, quadrature interferometry requires the signal of the four photodetectors to be acquired synchronously, which disqualifies multiplexed ADC architecture [29].

Following these constrains, a National Instrument PXIe 6124 multifunction DAQ [88] was selected as the CryoQPDI acquisition device. The NI PXIe 6124 have four

Table 6.3 Comparison between the measured and specified noise spectral density of the CryoQPDI DAQ analog input. The equivalent resistance producing a Johnson noise equal to the measured noise is computed for $T = 300\,\mathrm{K}$.

	specification		measurement	
input range	LSB RMS	$\mathrm{nV}/\sqrt{\mathrm{Hz}}$	$\mathrm{nV}/\sqrt{\mathrm{Hz}}$	equivalent resistance
$\pm 1\,\mathrm{V}$	1.9	41	37	$83\,\mathrm{k\Omega}$
$\pm 2\,\mathrm{V}$	1.3	56	47	$130\,\mathrm{k\Omega}$
$\pm 5\,\mathrm{V}$	1.0	108	85	$436\,\mathrm{k\Omega}$
$\pm 10\,\mathrm{V}$	0.95	205	171	$1.8\,\mathrm{M\Omega}$

synchronously sampled, differential analog input channels. Each channel is based on the same SAR ADC, with a maximum sampling frequency of 4 MHz and a resolution of 16 bits. On each channel, four possibles voltage ranges can be selected, which are $\pm 1\,\mathrm{V}$, $\pm 2\,\mathrm{V}$, $\pm 5\,\mathrm{V}$ and $\pm 10\,\mathrm{V}$.

Figure 6.19 shows the experimental quantization noise PSD of the CryoQPDI DAQ. These measurements where carried out after putting the DAQ analog inputs in short circuit, thus setting the input voltage to exactly 0 V. The sampling frequency was set to 4 MHz in all case, and the measurements where done on each of the four possible input ranges. The noise displayed by all of the four availables channels was identical, so only the results for one channel is presented.

The measured noise spectra are essentially flat for each input voltage ranges, as expected from equation 6.59. Some additionnal noise is found below 1 kHz, with a relatively higher added noise for the lowest input voltage ranges. A few additional noise spikes are also found at high frequency, with only two spikes laying in the signal chain passband, around 700 kHz and 800 kHz. In table 6.3, a comparison is made between the DAQ specified noise and the result of figure 6.19. In every case, the measured noise spectral density is found lower, but close to the one expected from equation 6.58 and 6.59 and the specified noise in unit of LSB RMS. This results validate the ADC noise theory presented in this paragraph for SAR ADC.

In table 6.3, the equivalent resistance producing a Johnson noise equal to the measured noise is also computed for each input voltage range of the CryoQPDI DAQ. A comparison between these equivalent resistance and the TIA feedback resistance of 100 kΩ shows that the DAQ quantization noise is very close to the photodetectors dark noise when the DAQ is used with its $\pm$ 1 V and $\pm$ 2 V input ranges, and much larger for the remaining input ranges. However, the higher input ranges are to be employed with correspondingly large photodetector output voltages, which still allow for a shot noise limited operation. This point is discussed in more detail in section 6.3.

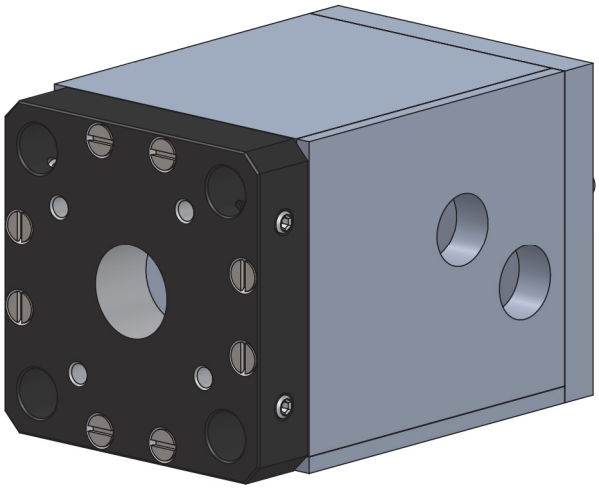

Figure 6.20 CryoQPDI photodetector enclosure. The enclosure is entirely made of aluminium. The enclosure front plate, in black, belong to the same family of optomechanical components used to construct the interferometer. It was employed to guarantee a correct assembly between the interferometer and the photodetectors. Beside providing a protection against shock, dust, etc. ,the enclosure is connected to ground to serve as a shield against external interferences.

6.2.4 Photodetector construction

Figure 6.20 displays the CryoQPDI photodetector enclosure. The central hole in the front plate, in black, is an aperture for the light signal. The two lateral holes permits the insertion of two connectors, one for the input power supply and the other for the output signal. Besides protecting the internal circuitry of the photodetector, the enclosure is also connected to the signal ground as a shield against external interferences. The concept of shielding is described in [57].

An overview of the photodetector internal assembly and PCB layout is given in figure 6.21. With a relatively large feedback resistor and the very low capacitance involved, the TIA circuit is sensitive to the PCB stray capacitance. This capacitance exist between any two nearby traces with a potential difference, in particular between the signal traces and the ground plane. The ground plane of the PCB is a large copper area at ground potential, which is intended to serve as the common ground reference point for all the components of the circuit. The use of a large area copper plane minimizes the resistance of the ground return path, a potential source of noise [57]. Following [10], a ground plane was applied everywere on the TIA PCB, except around the opamp, feedback network and photodiode (figure 6.21), in an effort to minimize the PCB stray capacitance at the opamp input and output.

The aperture made to let the input light reach the photodiode is also a necessary weak point of the enclosure shield. The TIA PCB ground plane, which is also connected to the photodiode case, was oriented facing this aperture with the idea of mitigating this

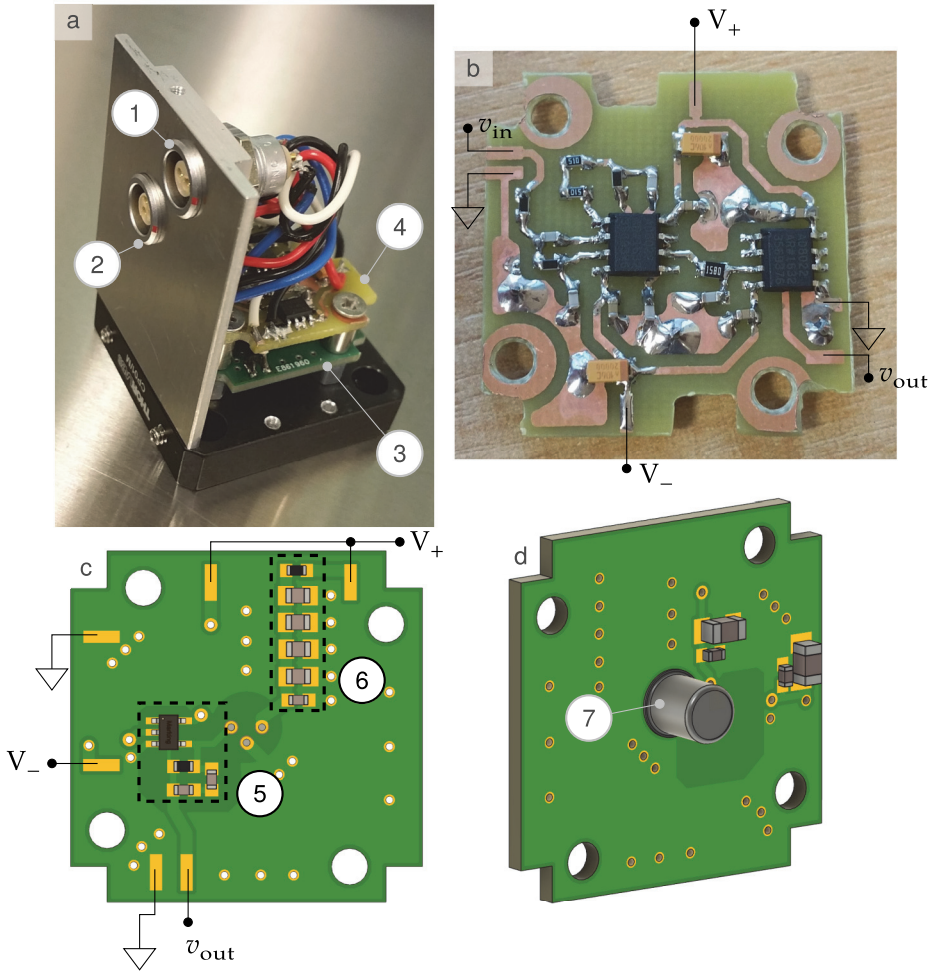

Figure 6.21 Overview of the CryoQPDI photodetectors' construction.
- a: final assembly of one photodetector, with enclosure open. The photodiode transimpedance amplifier and the filter are implemented on two separatates PCB.
- b: a filter board with the component soldered, before final assembly inside the photodetector enclosure. The AD8022 comes with two opamps per package, among which three are used for the antialiasing filter. As this PCB does not requires as much precision as the TIA one, it was etched at the laboratory.
- c: front view of the TIA PCB. This PCB was ordered from a PCB manufacturer, with the goal of making all the four TIA identical and to position the photodiodes precisely in the center of the board. Notice the absence of ground plane around the TIA components.
- d: back view of the TIA PCB. Beside the photodiode and power supply bypass capacitors, this side of the PCB mainly consists of one continuous ground plane, and faces the light aperture in the enclosure . This is intented as an additional shielding measure.

Item	Description	Item	Description
1	signal output	5	TIA opamp and feedback network
2	power supply input	6	bias filter
3	TIA PCB	7	photodiode
4	filter PCB		

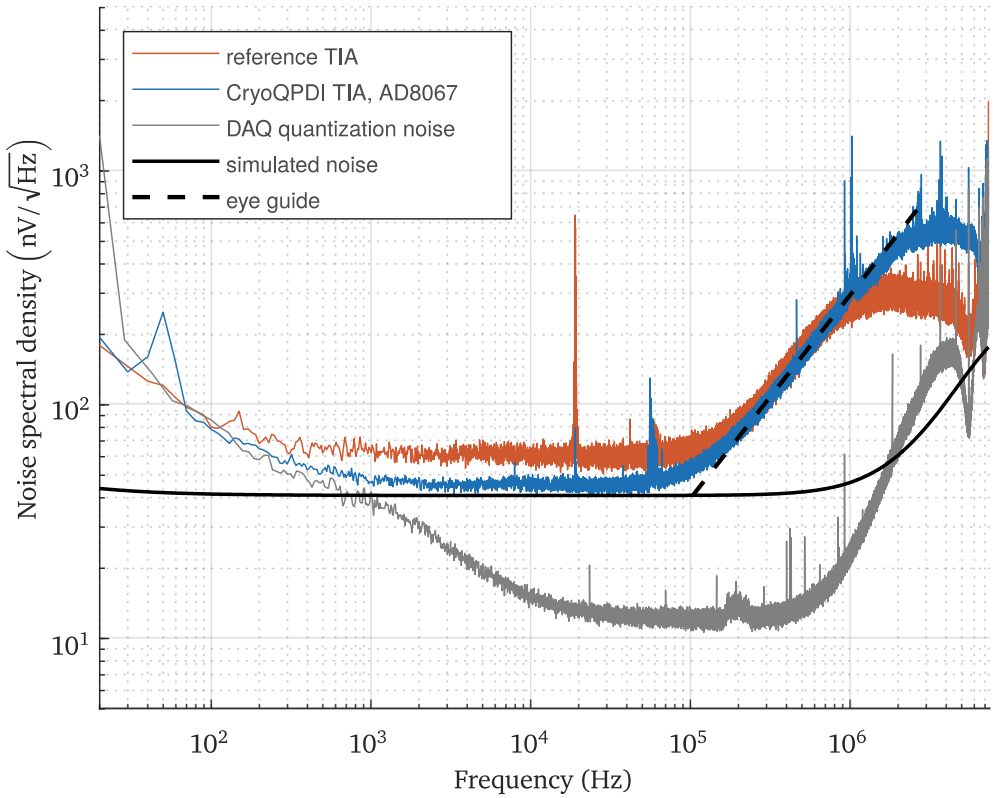

Figure 6.22 Dark noise measurement on the reference QPDI TIA and of the CryoQPDI TIA. In this case, both circuit employs the AD8067 opamp with the same feedback resistor of $100\,\mathrm{k\Omega}$. $C_\mathrm{f} = 1\,\mathrm{pF}$ for the reference TIA and $C_\mathrm{f} = 0.5\,\mathrm{pF}$ for the CryoQPDI TIA. The input capacitance is $C_\mathrm{in} \approx 8\,\mathrm{pF}$ for both circuit. These measurement where carried out using a NI PXI 5922 data acquisition card, which provides a negligible quantization noise above $10^3\,\mathrm{Hz}$.

situation. As such, the application of a ground plane is both a grounding and shielding technique [57, 10].

One last consideration for the mitigation of external interference is the connection between instruments having different ground reference point. In this regard, the differential input of the CryoQPDI DAQ provides an additional noise rejection measure. The connection between the photodetector and the DAQ, which employs a shielded, twisted pair cable, follows the description of reference [58].

6.3 Test of the signal chain

In an earlier stage of developpement, the CryoQPDI TIA design was based on the AD8067 rather than the AD8065 opamp. With both a lower input capacitance and a lower input voltage noise [4], this opamp appeared as a better choice for a lower $e_\mathrm{n}C$ noise. For this reasons, the AD8067 also happens to be used with a $100\,\mathrm{k\Omega}$ feedback in the reference QPDI photodetectors. During measurements however, an excess of $e_\mathrm{n}C$ noise was found in both the AD8067 TIA under developpement and the reference QPDI photodetectors, an issue that went unnoticed before. The AD8065 opamp, with similar

specifications and sharing the same package and the same pinout as the AD8067, was tested as a first step in investigating on this excess noise. While an excess of $e_n C$ noise was also found using the AD8065, the measured noise in this case was lower, and the AD8065 was retained as the opamp of the CryoQPDI TIA. Similarly, the tests also revealed a power supply dependant excess of dark noise despite the application of the bias filter described before, an issue that was solved by using battery power supplies.

In this section, the noise performance of the CryoQPDI signal chain is presented. A comparison is made between the experimental and simulated noise level for both AD8065 and AD8067 TIAs to discuss the excess $e_n C$ noise issue. The noise improvement realized during this work and its impact on the interferometer performance is highlighted. The mentioned power supply related excess noise is also briefly illustrated. For all practical purposes the performance of every four photodetectors where identical in each case, so the data are displayed for one channel only.

Figure 6.22 displays the results of dark noise measurement realized on the reference QPDI TIA as well as on the previous CryoQPDI TIA. These measurement where made using the reference QPDI data acquisition system which is based on the NI PXI 5922 DAQ [87]. Relative to the CryoQPDI DAQ, the NI PXI 5922 have three distinctive advantages:

- It employs $\Sigma - \Delta$ rather than SAR ADC [63], and displays a quantization noise much lower than the one predicted by equations 6.59;
- Its maximum sampling frequency is higher, at 15 MHz, resulting in a Nyquist frequency of 7.5 MHz;
- It has a built in, high order antialiasing filter, and then does not requires an additional filter to reject the TIA high frequency noise.

These advantages were exploited here to have access to the noise of the TIAs alones on a larger bandwidth. The schematic of the reference QPDI TIA is the one of reference [4], page 18. As mentioned before, both of the TIA compared in figure 6.22 are based on the AD8067 opamp and use a 100 kΩ feedback resistor, but the reference QPDI TIA also have the same resistor inserted between the opamp non inverting input and ground. As a result, its noise spectral density in the flat region between 10^3 Hz and 10^5 Hz, where the dark noise of both circuits is dominated by Johnson noise, is $\sqrt{2}$ times larger than the one of the CryoQPDI TIA, around 60 nV/$\sqrt{\text{Hz}}$.
The dark noise of both circuit increases at high frequency, but this increase start at a frequency much lower that expected. Ignoring the additional Johnson noise of the reference circuit, the simulated noise is the same for both TIAs since they have a very similar input capacitance of around 8 pF, with an expected f_{n2} of 1.2 MHz. However, the observed f_{n2} is around 10 times lower, around 100 kHz in both case. Even if the maximum dark noise spectral density reached by both circuits is larger than predicted by simulation in both cases, the high frequency noise gain flattening appears to still

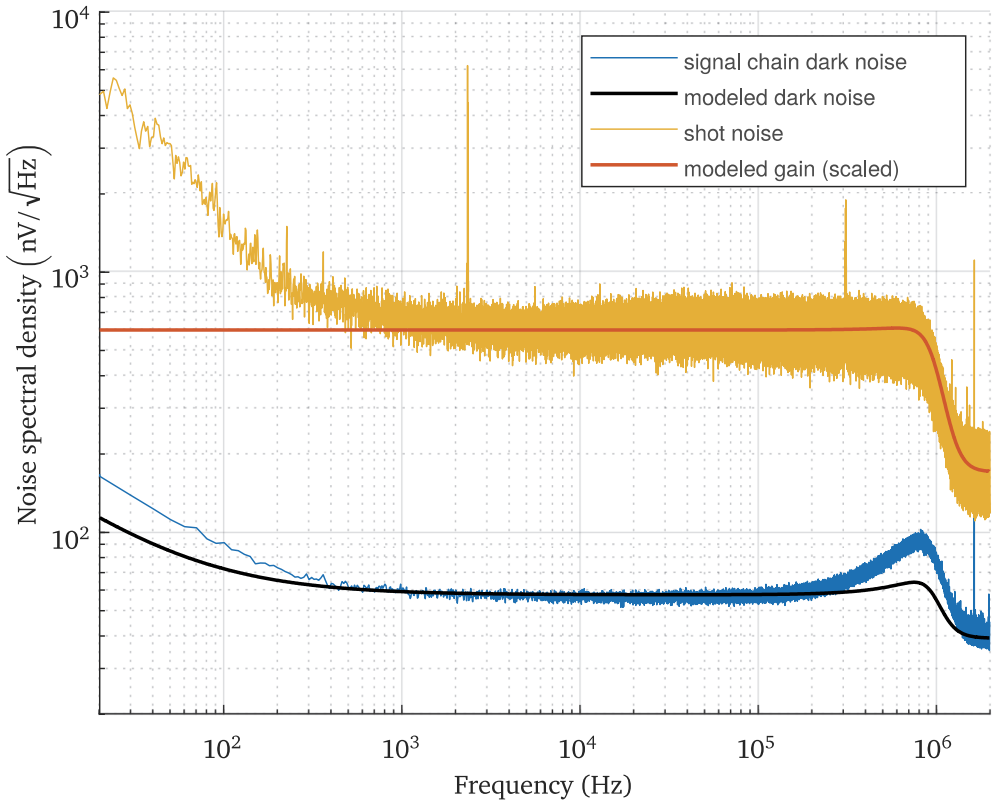

Figure 6.23 Dark noise and shot noise measurement of the CryoQPDI final signal chain.

occurs at f_p in each case, where $f_p = 1.6\,\text{MHz}$ for the reference QPDI TIA and $f_p = 3\,\text{MHz}$ for the CryoQPDI TIA. For both circuits, the observed high frequency noise appears to come from a f_z much lower that expected, hence the name excess $e_n C$ noise.

A first hypothesis to explain this excess noise is an input capacitance larger than expected. With an f_{n2} and thus an f_z 10 times lower, the input capacitance should be around 80 pF. Such a large increase in input capacitance seems unreasonnable, and cannot be explained by board parasitics. Moreover, the same excess noise is observed in two TIAs using different photodiodes and having different PCB layouts. Another hypothesis is an unexpected effect of the bias filter. Both TIA employs a bias filter, but the reference circuit uses $R_b = 1\,\text{k}\Omega$ and $C_b = 1\,\text{nF}$, where the CryoQPDI TIA uses $R_b = 100\,\Omega$ and $C_b = 8.9\,\mu\text{F}$ (figure 6.15). It seems unlikely that the same excess noise would have been obtained with two differents bias filter. By elimination, the excess $e_n C$ noise observed in figure 6.22 appeared related to an unexpected behavior of the AD8067 opamp, an assumption that can be verified only by using a different opamp.

Figure 6.23 shows the experimental dark noise of the CryoQPDI signal chain in its final version, as presented in figure 6.15. The modeled dark noise is the noise of a photodetector (TIA+filter, black solid curve of figure 6.18) plus the measured quantization noise for the $\pm$ 1 V input range used for this dark noise measurement (table 6.3).

Between 10^3 Hz and 10^5 Hz, the dark noise is flat and in good agreement with the model, with a value of 58 nV/$\sqrt{\text{Hz}}$. An excess of noise is observed below 10^3 Hz, which is expected since the noise model does not take into account the excess quantization noise observed in figure 6.19. At high frequency however, an excess of $e_\text{n}C$ noise is also found in this case, with an observed $f_{\text{n}2}$ of around 400 kHz. As shown later, even if the excess noise was not eliminated using the AD8065 opamp, the resulting noise reduction is still a significant improvement relative to the AD8067 TIA. The measured dark noise is also free of any spurious peaks, which indicates a proper application of the grounding and shielding methods mentioned in section 6.2.4 and validates this aspect of the signal chain design.

To assess the signal chain passband, the noise spectral density of the light coming from a flashlight can measured. As this light is emitted from a battery powered thermal light source, it is the best experimental realization of a light source containing only shot noise [57]. The noise spectrum of shot noise follows the frequency response of the signal chain (6.43), hence a shot noise measurement can be used to measure this frequency response, as long as it is much larger than the signal chain dark noise. The result of such a shot noise measurement is also displayed in figure 6.23. To ensure that shot noise dominates, the measured DC voltage was set at 9.30 V, close to the limit of the DAQ. The obtained shot noise spectrum indeed reminds the shape of the photodetectors gain curve. For a direct comparison, the simulated gain of the photodetector (figure 6.18, solid blue curve) was scaled by the average of the shot noise spectrum between 10^3 Hz and 7×10^5 Hz, and the measured quantization noise for the $\pm$ 10 V range was added to this result. The resulting modeled gain of figure 6.23 is in good agreement with the measured shot noise spectrum, except below 10^3 Hz where some excess noise was introduced by drift in the measurement. The modeled flat shot noise level equal 600 nV/$\sqrt{\text{Hz}}$, very close to the 570 nV/$\sqrt{\text{Hz}}$ expected from the measured DC voltage.

A comparison is made in figure 6.24 between the dark noises spectrum using either the photodetector lead acid battery power supply or a laboratory power supply. This figure self-explains why a battery power supply was prefered. While this result also shows an excessive sensitivity of the photodetectors to power supply noise, no attempt has been made to explain this behavior nor to improve on this aspect due to time constrains.

To further investigates on the excess $e_\text{n}C$ issue, the measured and simulated dark noise for the two versions of the CryoQPDI photodetectors are displayed together in figure 6.25. The frequency range was choosed to highlight the point were the $e_\text{n}C$ noise start to dominates in every case. The signal chain for both case is identical (figure 6.15) except for the use of a different opamp. As stated before, the theoretical dark noise performance expected from the AD8067 opamp is superior to the one expected from the AD8065 opamp, but the experimental results show the contrary. The maximum dark noise obtained with the AD8065 opamp is around 90 nV/$\sqrt{\text{Hz}}$

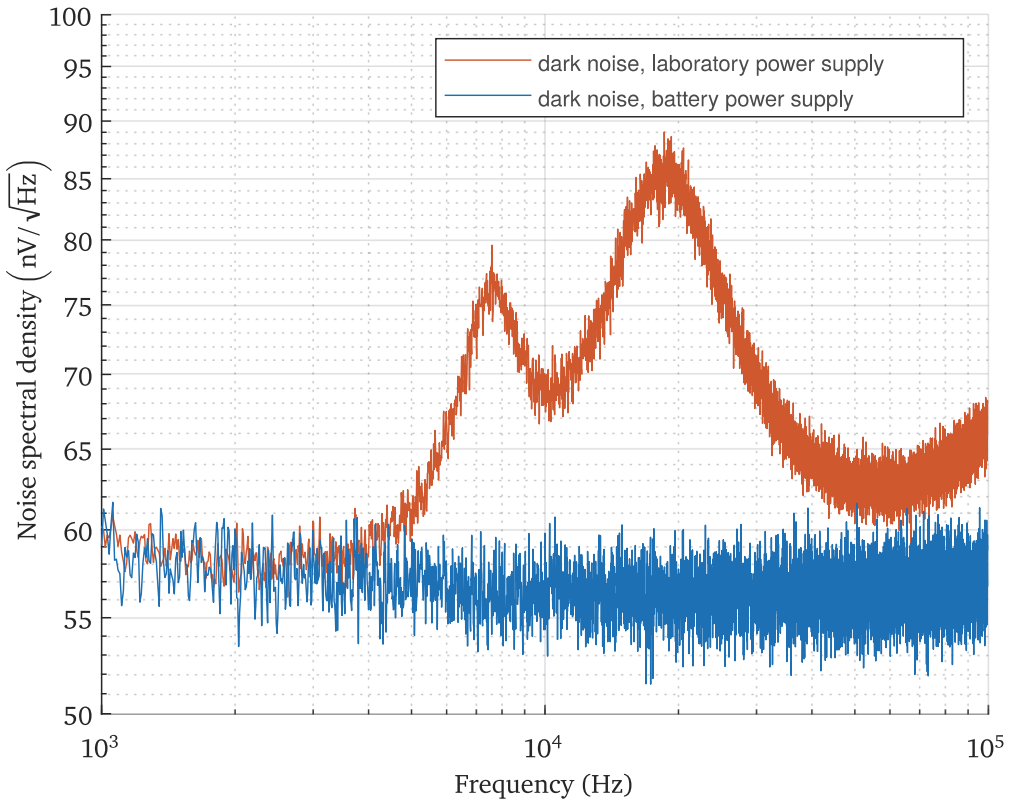

Figure 6.24 Influence of the power supply on the signal chain dark noise. An excess dark noise is observed when using a laboratory power supply. Two broad peaks are found around 7.5 kHz and 20 kHz. This excess noise was not investigated due to time constrains.

at 800 kHz, where the AD8067 TIA displays a dark noise larger than 200 $\mathrm{nV}/\sqrt{\mathrm{Hz}}$ at the same frequency. The AD8067 and AD8065 opamp are closely related part, since the AD8067 is a decompensated version of the AD8065 [3, 4, 56]. This fact may explain why an excess of $e_\mathrm{n}C$ noise is observed with both opamp. As mentioned before, the AD8065 was tested mainly because this test was possible without a time consuming redesign of the TIA schematic and PCB layout. Although the origin of the excess $e_\mathrm{n}C$ is not completely determined, the results obtained here suggest that using another alternative opamp is the path to follow if this issue is to be fully understood and mitigated. This work is however beyond the scope of this thesis.

At last, a comparison is made between the CryoQPDI signal chain noise performance and the noise performance of the reference QPDI signal chain. In figure 6.26 and 6.27, the experimental dark noise of figure 6.22 for the reference TIA (orange curve) and of figure 6.23 for the CryoQPDI TIA (blue curve) are displayed together. Figure 6.26 and 6.27 are identical, except that the second one uses a linear rather than logarithmic frequency axis. From figure 6.26, it can be seen that the dark noise level achieved in both case is essentially the same up to 10^5 Hz. On the other hand, figure 6.26 better expresses the importance of the observed excess $e_\mathrm{n}C$ noise. It dominates from 70 % to 90 % of the 1 MHz frequency range for both instrument.

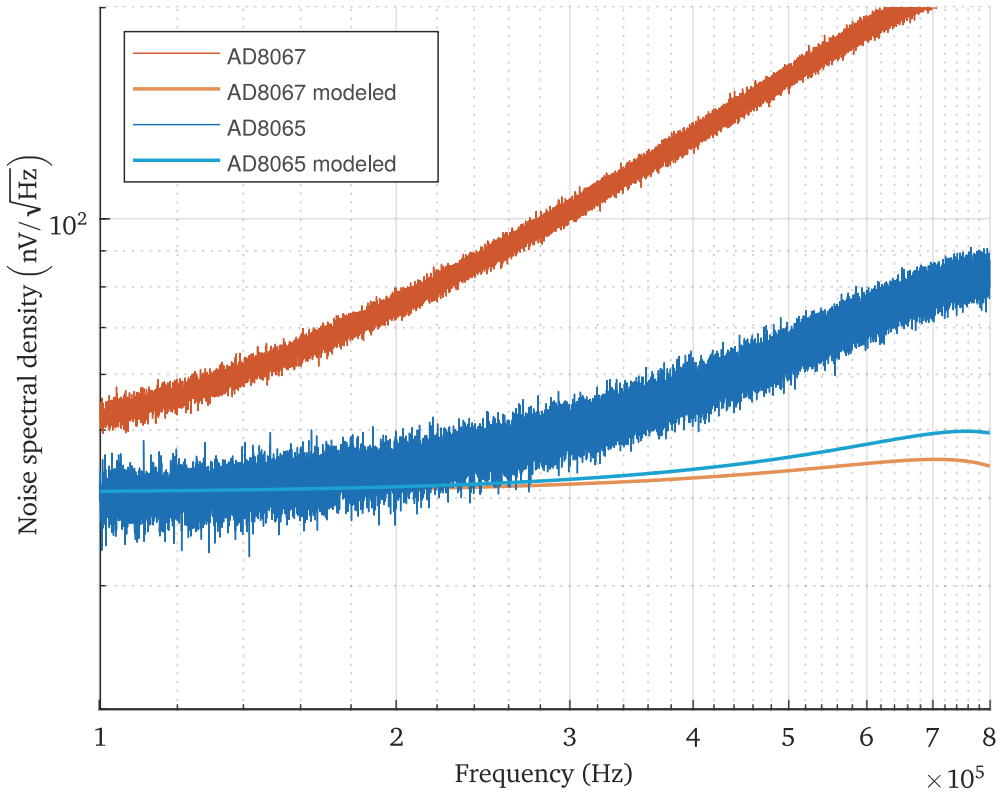

Figure 6.25 Comparison of the CryoQPDI signal chain dark noise using the AD8065 or the AD8067 opamp.

Using equation 6.46, one can find that with a maximum dark noise of 90 nV/$\sqrt{\text{Hz}}$, the signal shot noise start to dominates the CryoQPDI dark noise on the whole passband for an output voltage of 250 mV: despites the remain of an excess $e_{\text{n}}C$ noise, using the AD8065 opamp the dark noise level of the CryoQPDI signal chain is low enough for a shot noise limited operation on its full passband when a uncoated cantilever is measured, where the average voltage on the four channels is around 0.5 V. This means that the objectives fixed at the beginning of section 6.2 have been reached. On the other side, with a maximum dark noise of 270 nV/$\sqrt{\text{Hz}}$, the output voltage required for shot noise to dominates in the full 1 MHz passband in the reference QPDI case is 2.3 V. The maximum measurable photodetector voltage is 5 V for the reference QPDI (NI PXI 5922 max input range), corresponding to an average voltage of 2.5 V on the four photodetectors. Such a high signal voltage can only be reached for a cantilever coated with a high reflectivity coating, or requires an increase of the light power on the cantilever. In other words, the excess $e_{\text{n}}C$ noise for the reference QPDI is never negligible, and always degrades the instrument noise in the high frequency range.

6.4 Conclusion

In this chapter, the design and test of the CryoQPDI signal chain is presented. After a complete development of the transimpedance amplifier theoretical frequency response

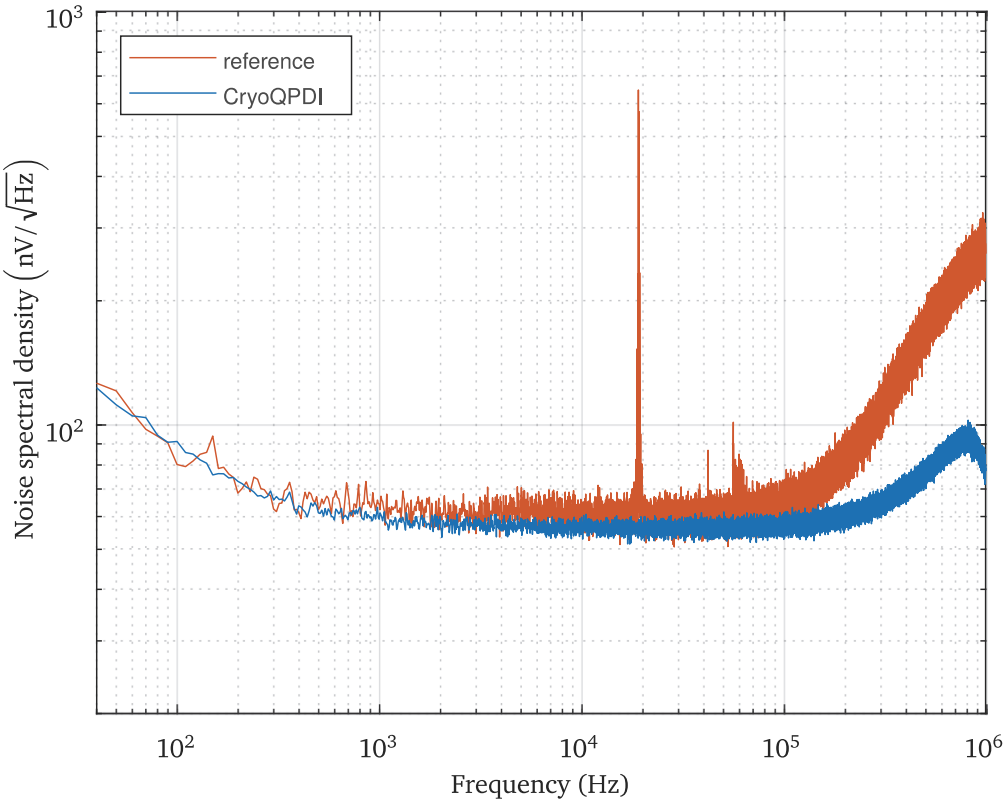

Figure 6.26 Comparison between the signal chain dark noise of the reference QPDI and the CryoQPDI

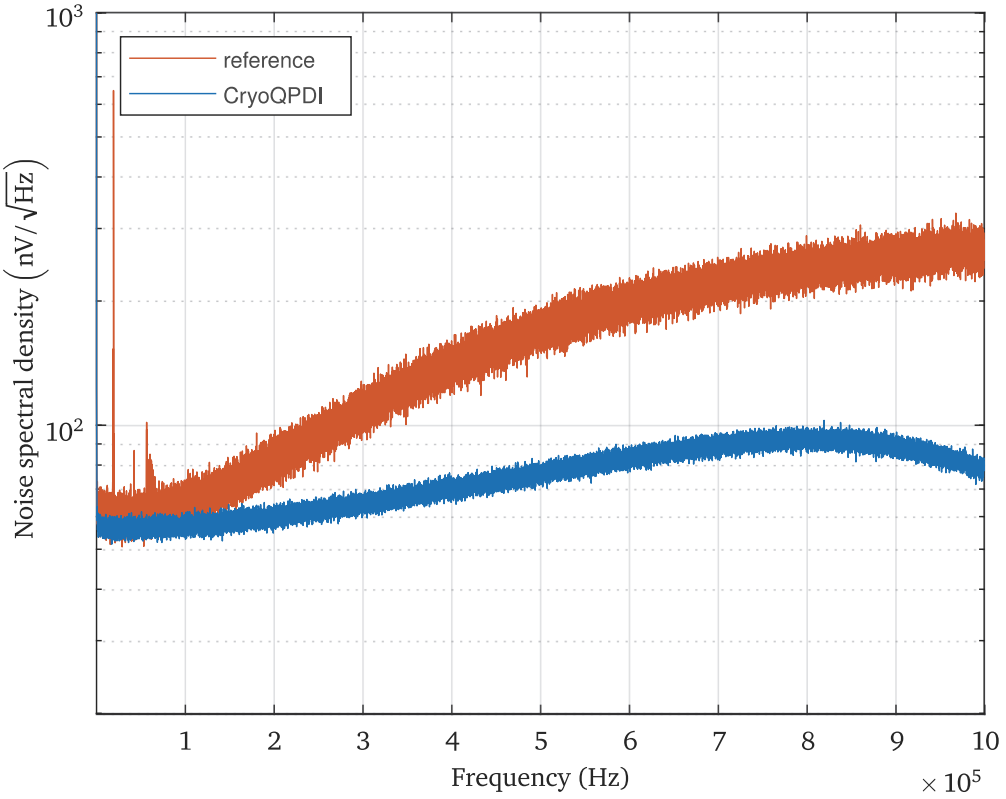

Figure 6.27 Same as figure 6.26, but with a linear frequency axis.

and noise, a design strategy was devised to minimize the passband electronic noise of this circuit, accounting for the spectral domain data analysis of the instrument. The design of a transimpedance amplifier and a lowpass antialiasing filter was then carried out with the assistance of circuit simulations, and the selection of a data acquisition card was presented. Upon testing, an excess of $e_{\mathrm{n}}C$ noise was found, which was related to the AD8067 operational amplifier used to build the photodetectors transimpedance amplifiers. A significant improvement of the reference QPDI noise level was obtained using a AD8065 opamp, allowing the CryoQPDI to achieve a shot noise limited operation in its full passband for the most common expected measurement configurations.

7 Ion Beam Sputtering on microcantilevers

This chapter deals with sample preparation, and details how we place the optical coatings on the µcantilevers. The optical films studied in this manuscript were all deposited using the Spector®, a commercial Ion Beam Sputtering (IBS) deposition system. Owing to their very low stiffness, µcantilevers are very sensitive to the warping induced by coating stress, an effect only aggravated by the tendency of IBS coating to exhibit a very high intrinsic compressive stress. As a µcantilever distorted by the film stress are likely to be impossible to measure, a stress compensation strategy was devised where material is deposited on both sides of the cantilever for the stress effects to compensate. The implementation of this strategy required a new device able to flip the samples inside the Spector when requested. This chapter details the design of this device, called the Recto Verso Deposition System (RVDS). It start with a presentation of the IBS method, with special attention to its implementation by the Spector. Based on this knowledge and on a previous attempt to construct a RVDS, the constraints related to this device are listed, and the design and working principle of the RVDS are detailed.

7.1 Ion Beam Sputtering

7.1.1 IBS principle

The principle of Ion Beam Sputtering[122] is explained in figure 7.1, which displays a simplified diagram of the Spector IBS system.
In a vacuum chamber, a collimated ion beam is generated from a diluted noble gas (most often argon) by an ion source, and is directed toward a target attached to a caroussel. After collision and through momentum transfer, particles from the target are sputtered by the ions, generating a flux of matter toward one or several substrates attached to a fixture, where the matter deposits to form a film. The Spector caroussel can hold up to three targets, allowing several different materials to be deposited during the same coating cycle. Any excessive heating of the target caused by the ion bombardment is prevented by a water cooling circuit.

Inside the sputtering ion source, an additional beam of electron is generated by a neutralizer and is projected together with the ion beam. As the density of electrons is

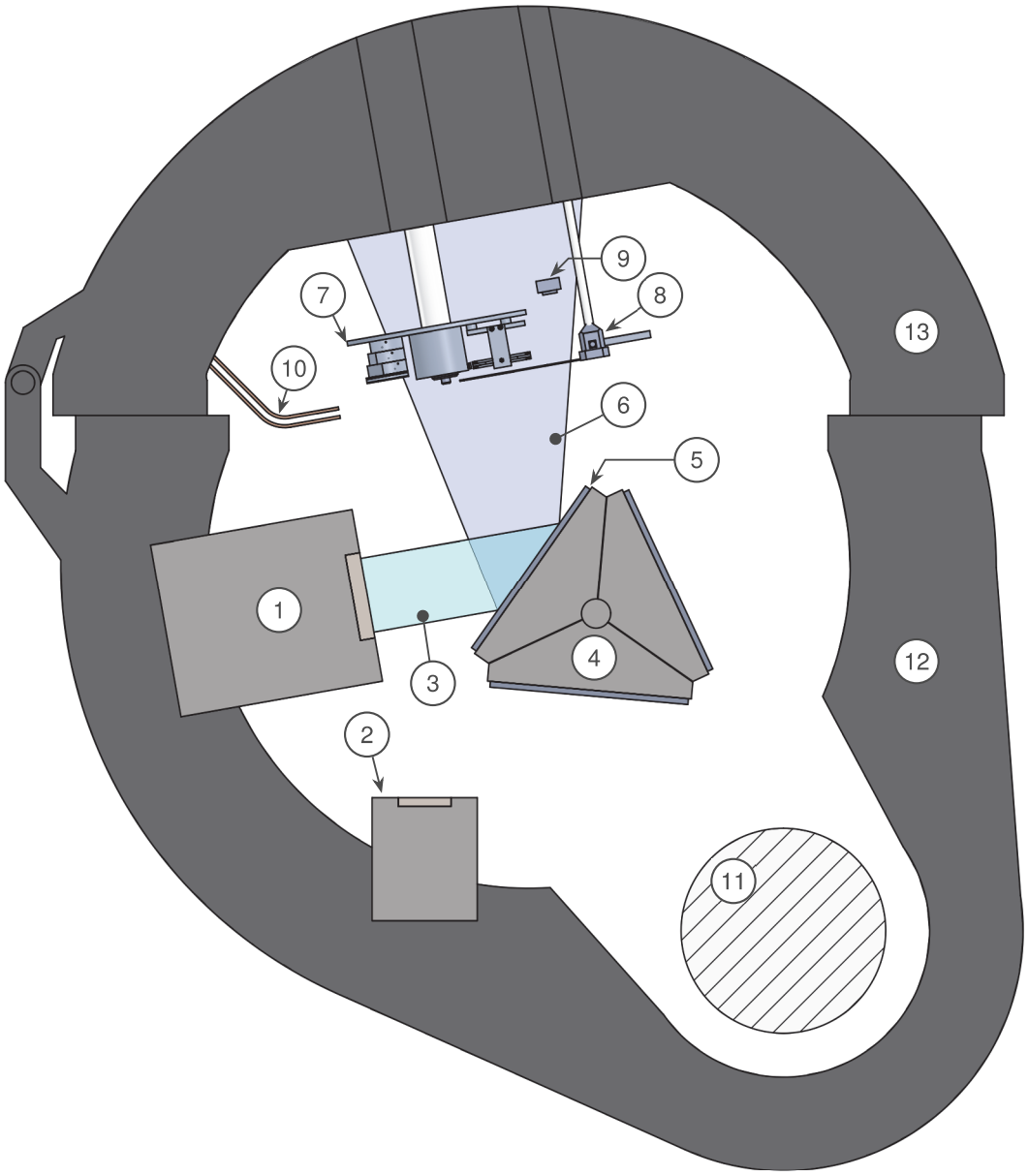

Figure 7.1 Simplified diagram of the Spector Ion Beam Sputtering (IBS) system.

Item	Description	Item	Description
1	sputtering ion source	8	uniformity mask positioner
2	assistance ion sourc	9	quartz rate monitor
3	collimated ion beam	10	gas line
4	three sided target caroussel	11	pumping port
5	target	12	stainless steel vacuum chamber
6	sputtered matter flux	13	vacuum chamber's door
7	rotating fixture		

made equal to the ions density, space-charge neutralization of the sputtering beam is achieved. This neutralization feature prevents charge build-up at the target's surface and allows the use of nonconductive target materials. An additional ion source, similar to the sputtering source and aiming directly at the fixture, can be used to transfert momentum to the growing film, a procedure called assisted deposition, or simply assistance. A partial pressure of reactive gas can be introduced in the chamber through a gas line, where it can combine with the sputtered material to form a polyatomic compound[1]. This combined physical and chemical process is called reactive sputtering. As the Spector employs filamentless radiofrequency sources, reactive sputtering can also be achieved by introducing the reactive gas in one or both of the ion sources. Both reactive sputtering and neutralization are essential for the deposition of optical coatings, as most of the transparent films deposited by IBS[2] are made of dielectric materials belonging to the oxyde and nitride family.

Another concern is the control of the deposited thickness and thickness uniformity, because the layers thicknesses in an interference coating is directly linked to the coating optical functionality. In a cross-section of the sputtered matter beam, the deposition rate possesses in general a smooth 2D profile, with a complex functional dependance on the setup geometry, the materials involved and the deposition parameters.

In the Spector, uniformity is achieved using a combination of two methods. The fixture is attached to a motorised shaft, and is rotated at a typical speed of several hundreds rotations per minute during deposition. The deposition rate thus acquires a circular symmetrical profile, whose revolution axis is the rotation axis of the fixture. This first method transforms the initial 2D uniformity problem in a 1D one, as now the deposition rate must be corrected along a radius only. This radius uniformity correction is done by positioning a mask a few millimeters above the substrate's surface (see figure 7.10). The mask is made wider where the deposition rate is higher, and the actual geometry of a particular mask is determined experimentally for each material, and for a set of deposition parameters. Accordingly, the Spector mask positioner can hold up to three different masks, one for each target attached to the carousel. A fourth position without a mask can be used to facilitate the access to the substrate's fixture, easing the exchange of samples between deposition cycles.
To achieve a given film thickness, the growth of each layer is monitored continuously via the signal of a quartz microbalance, and the deposition is stopped when the desired thickness is reached. The thickness deposited on the balance is usually different from

[1] This reaction can occur at the target surface, at the substrate surface, or both depending on the chemical species considered.

[2] As it is often the case for a deposition technic with many variation, IBS can be found with many different names in the literature: Ion Beam Sputtering Deposition (IBSD) or simply Ion Beam Deposition (IBD), Reactive Ion Beam Sputtering when a reactive gas is used, Dual Ion Beam Sputtering (DIBS) when assistance is employed, etc.

the thickness on the substrate, so that their ratio, called the tooling factor, must be determined by a calibration procedure.

7.1.2 Operation

A typical IBS deposition cycle is divided in three phases:

- A preprocessing phase: after installing one or more samples on the fixture, the vacuum vessel is closed and pumped down to a pressure around 10^{-6} mbar. This step is followed by a bakeout procedure, where the chamber's interior is heated typically above 100 °C by a set of infrared lamps. The bakeout accelerates the outgassing of species adsorbed on the chamber's walls, allowing their evacuation by the pumping stage, and preventing this outgassing to occur during deposition. The targets to be employed for deposition are then presputtered, eliminating contaminants adsorbed on their surfaces. This preclean operation is done while the subtrates are shielded from the matter flux by a shutter positionned between the fixture and the targets. The preclean step also serves two additionnal purposes: it allows the ion sources to warm up, for a stable operation during the subsequent coating step, and the sputter products generate a getter action on the background contaminants, helping the system to reach a lower pressure than the one achievable using the pumping stage alone. The pressure before deposition can be as low as 10^{-8} mbar, further improving the system's environment purity before deposition. The main goal of this preprocessing phase is to reduce contamination of the coating, and is critical in achieving the highest optical performances.
- The coating phase: the relevant targets are alternately sputtered following a pre-programmed recipe. If required, reactive gases are fed to the vacuum chamber at the same time. The growth of each layer is monitored continuously via the quartz microbalance signal, and is stopped when the desired thickness is reached.
- A postprocessing phase: the system's components, and especially the ion sources, are allowed to cool down before to vent and open the vacuum chamber. This prevent the immediate exposure of hot parts to the atmosphere and the associated damages from oxydation, to preserve the machine's integrity.

Importantly, the preprocessing and postprocessing phases generally occupy together the majority of a deposition cycle duration. In the Spector's case, they take about three hours combined, when the coating phase often lasts less than half an hour. For the reasons described above, they cannot be avoided without compromising the coating's optical quality or the setup integrity.

7.1.3 IBS parameters and film properties

Beside the processing improvements mentioned above, the excellent optical properties of optical coatings produced by IBS are largely traceable to the availability of optimized sputtering ion sources [30, 61]. They can operate at a relatively low processing pressure, which is usually close to 10^{-4} mbar, for a lower background gas contamination, and are able to provide a broad ion beam that is highly directional, monoenergetic, and with a fairly uniform ion current density. The incident ions kinetic energy and flux can be varied independantly over a wide range. This, combined with a setup geometry where the ion beam generation, the target and the substrate are physically separated, allows for both a considerable latitude for controlling the deposition process (e.g. film growth rate and stoichiometry) and a simplified study of the film growth condition. The ions kinetic energy is typically set around 1 keV, which is close to an optimum for the sputtering yield of many material. On the other hand, many sputtered particles leave the target with a kinetic energy on the order of 10 eV. At the low IBS working pressure, these particles have a mean free path exceeding the chamber's size, resulting in a very few scattering from the background gas. As a consequence, they transit between the target and the substrate without reduction of their relatively high kinetic energy[1], with a profound impact on the growing film properties: they can penetrate several atomic layers and bound tighly into the film, improving adhesion between the coating and the substrate. They can also knock atoms from the film surface to a nearby void or vacancy as the film grow, a densification process known as atomic peening [122, 20]. At the same time, the subtrate is usually heated only a few tens of degrees above room temperature under the influence of the matter flux: although it allows the selection of a wider variety of substrate's material, the main avantage of a cold substrate is to impede the growth of crystalline region in the film, avoiding the associated increase in light scattering. In the end, owing to these advantageous deposition conditions, IBS optical coatings are grown as dense, amorphous films without voids and with very low surface roughness, making them ideal for demanding optical applications.

7.1.4 IBS film stress and its consequences for IBS microcantilever coating

Unfortunately, IBS coatings also tend to exhibit a high intrinsic compressive stress [64, 23]. Because of the atomic peening densification mechanism described above, the deposited films acquires an overtight atomic packing and tries to relax by taking a larger volume. However, the film expansion is counteracted by the substrate which resists deformation, in such a way that the film-substrate system reaches a new mechanical equilibrium where the film stress is in balance with the substrate strain. Consequently, the deposition of a stressed coating can induce warping of its substrates, the extent of

[1] Compared to alternative physical vapor deposition processes like magnetron sputtering or evaporation

this warping being a function of the substrate rigidity and of the film thickness and stress level.

The very low rigidity of μcantilevers, which makes them appealing for the study of thermal noise, also makes them very sensitive to coating stress induced bending. Working with bent μcantilevers comes with important experimental and theoretical difficulties: when measured with the QPDI, and if their deformation is kept relatively small, bent μcantilevers reflect the probe beam at an angle from the reference beam, causing an imperfect recombination associated with a degradation of the interferometer constrast. If this bending is made larger, the beams may not be able to overlap or reach the photodetectors together, making the affected μcantilever impossible to measure. In both cases, it comes with additional mechanical modeling difficulties, as the majority of the physical models used for this purpose consider only straight cantilevers.

Some early μcantilevers coating experiments conducted at LMA showed that the deposition of even a quarter-wave monolayer, corresponding to as low as 50 nm to 70 nm at the CryoQPDI working wavelength, results in unusable samples. While the magnitude of the bending induced by a given film stress may be reduced by the use of stiffer μcantilevers, it also implies a reduction of the available thermal noise signal, as explained in section 3.2, and does not constitutes a workable solution for the study of thicker multilayer coatings.

7.2 The Recto Verso Deposition System

In order to obtain straight coated μcantilevers measurable with the CryoQPDI, the strategy adopted here is to deposit material on both of their sides, for the two corresponding film stress contributions to balance out and cancel. For this stress compensation strategy to succeed, it was observed that the bending induced by the coating on one side should not be too pronounced, supposedly because the deposition made on the other side would then be done in a configuration which is too far from the one of an initially straight μcantilever. Accordingly, if a monolayer is to be deposited on both sides of a μcantilever, each of them must be deposited in several steps and by alternating between each side. By default, it is necessary to access the inside of the Spector to reposition a substrate, an operation that can only be done between coating cycles after venting and opening the chamber. This render this strategy highly impractical as is, because too many time consuming coating cycles would then be required, especially for multilayer coatings. As most of a deposition cycle duration is devoted to the preprocessing and postprocessing phases, putting in practice this stress compensation method can be done using a device with the ability to return a cantilevers sample inside the Spector at the coating phase, and with no external intervention or any need to open the machine.

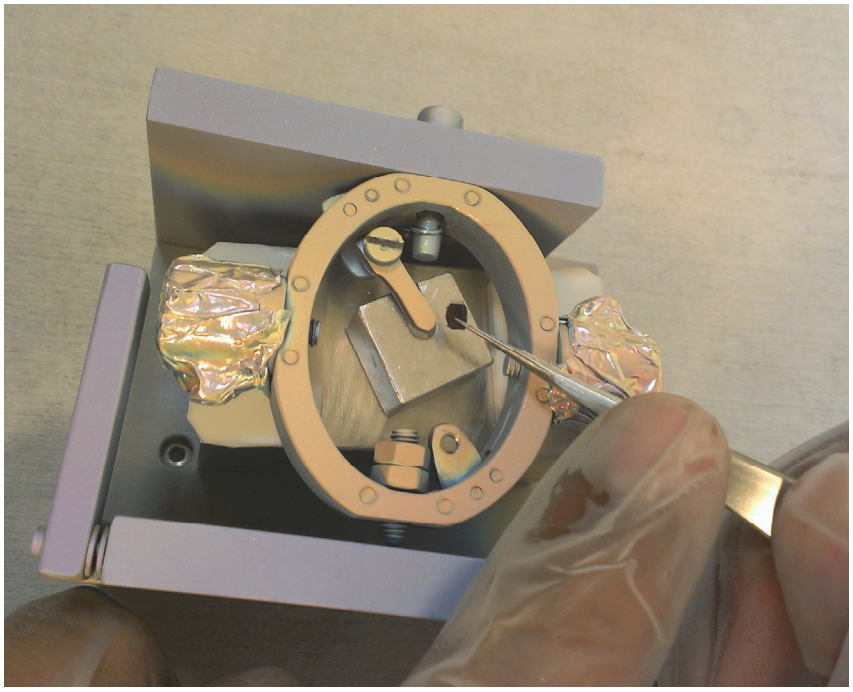

Figure 7.2 Photograph of the first version of the RVDS sample holder. The operator is installing a cantilever sample. Even if a few coating experiments had been conducted successfully using this setup, it quickly showed severe limitations and needed to be replaced by a more reliable design.

7.2.1 Early work and system specifications

The photograph of figure 7.2 shows an early attempt to build such a device, called the Recto Verso Deposition System (RVDS). As explained in more detail later, the main idea behind this system is to exploit the attraction and repulsion between a set of magnets and a ferromagnetic soft iron bar to control the flip of a rotatable structure where μcantilever samples can be attached, exposing either of their side to the matter flux. The rotation axis of the sample holder of 7.2 was subjected to an excessive amount of friction, and exhibited a severe lack of reliability. Material was allowed to deposit inside the axle mechanism, which increased friction after a few coating cycles to the point where the rotatable structure would hang before to achieve a complete half turn, which as will become clear in the following, would lead to collisions inside the Spector. Even before this problem became apparent, the rotation operation was found unreliable, needing several attempts to place the rotatable structure in the desired position, without a complete guarantee of success. A new version of the RVDS, which is described in the remaining of this chapter, was thus developped with the main goal of achieving a more predictable and deterministic behaviour, and preserve the Spector integrity. While a commercial solution was available to return a substrate inside the Spector, it was rejected because of its prohibitive cost.

The new RVDS was developped through a complete redesign of the first one, which was seen as an opportunity to include additional features. The corresponding specifications and contraints are listed hereafter, and are explained in the next paragraph:

- Operation in a clean high vacuum of 10^{-8} mbar
- Operation from room temperature to 300 °C
- No access to the Spector control software
- Be able to attach both wafers 3 inches in diameter and µcantilever samples
- Provide a reliable, low friction rotation of the samples holding structure

A compatibility with high vacuum is needed to not degrade the Spector environment at the coating phase, with the usual limitation on the material selectable to build the system. The maximum operating temperature of the RVDS was extended to permit the study of the substrate's temperature influence on the coatings properties. The upper temperature limit given corresponds to the maximum theoretical temperature acheivable in the Spector.

The Spector being a commercial deposition system, it is controled by a proprietary software which does not allow the addition of new features. For instance, it is not possible to control an extra powered actuator to flip the samples. On of the main advantage related to the RVDS principle is the reuse of the motorized axles already present in the Spector, employing its default control subroutines in doing so.
In contrary to µcantilevers, the wafer samples used in the GeNS instrument [22] does not typically suffer from an excessive coating stress induced bending. If a flat sample is to be obtained, the deposition of a thick coating on both of the wafer's faces can be done by two successive cycles, without special hardware. Even so, a hability to coat both wafers and µcantilever at the same time was included in the RVDS specifications as a mean to compare the charasteristics of coatings produced in the exact same conditions. As by using the RVDS only one coating cycle is required for both of the wafer side to be coated, it also comes with a save of cost and time.

The need of a trustworthy, low friction rotation mechanism was understood from experience gained with the RVDS earlier version. Going along with this requirement is a need to protect the sample holder's axis mechanism from the matter flux.

7.2.2 RVDS design and construction

Overview of the system An overview of the RVDS main components is given in the diagram of figure 7.3 and in the photograph of figure 7.4.

As explained in section 7.1.1, a rotating fixture, a set of uniformity masks attached to a mask positioner and a quartz rate monitor together form the standard Spector setup for coatings uniformity and thickness control. Moreover, all the deposition

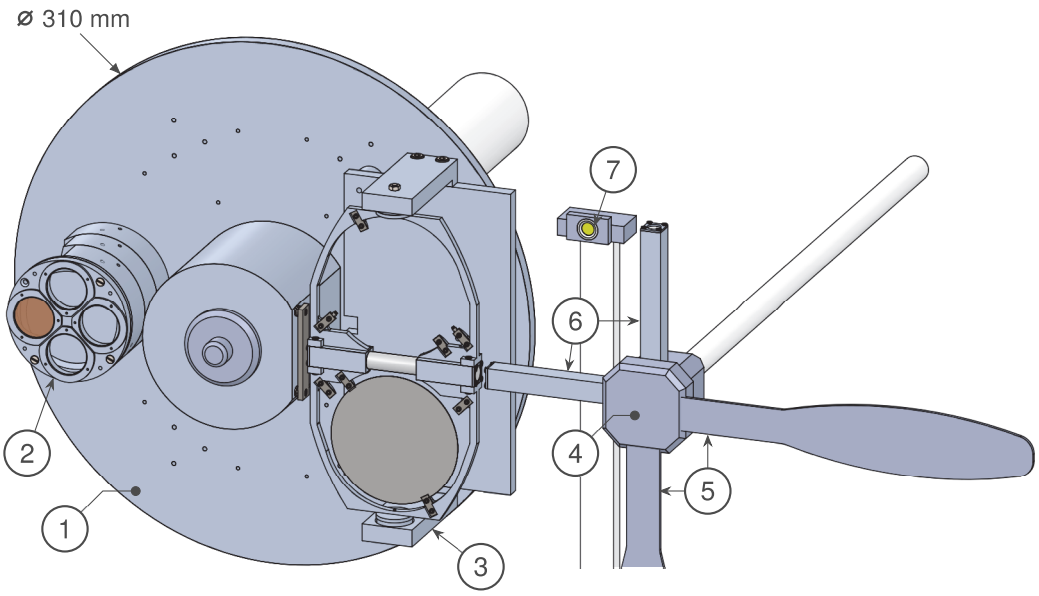

Figure 7.3 Overview of the Recto Verso Deposition System (RVDS). One of the key feature of this setup is to exploit the Spector's built-in hardware and software functionalities to control which side of a specimen is exposed to the matter flux.

Item	Description	Item	Description
1	rotating fixture	5	uniformity masks
2	mount for witness optics	6	control magnets
3	recto verso sample holder (RVSH)	7	quartz rate monitor
4	uniformity mask positioner		

cycles are carried out with at least one witness optics mounted on the fixture, which generally consists in a 1 inch in diameter optical flat. After deposition, the witness transmittance is evaluated ex situ using a spectrophotometer, for calibration and control purposes. On the one side, after a calibration cycle where a single monolayer is deposited, the transmittance data are used to retrieve the deposited thickness and compute the tooling factor mentioned earlier. One the other side, a comparison can be made after a standart deposition cycle between the theoretical and the experimental optical response of the witness to assess the coating functionality[1].

If an additional substrate holder was added to the components cited above to accomodate a specimen to be coated, one would obtain the standard Spector setup for optics manufacturing. In the Recto Verso Deposition System, it is replaced by the Recto Verso Sample Holder (RVSH, figure 7.5), an assembly comprising a hollow structure which is rotatable around an axis. Wafers 3 inches in diameter as well as µcantilevers can be secured to this structure using a set of integrated clamps, with both of their faces uncovered. The structure also hold a rod magnet in its central part, called the overturn magnet, and has two equilibrium positions induced by the attractive forces between this magnet and a soft iron plate placed nearby. These positions are called recto and

[1] The optical response of a component cannot always be measured directly after deposition, often as a consequence of its peculiar geometry. This is the case for µcantilever samples.

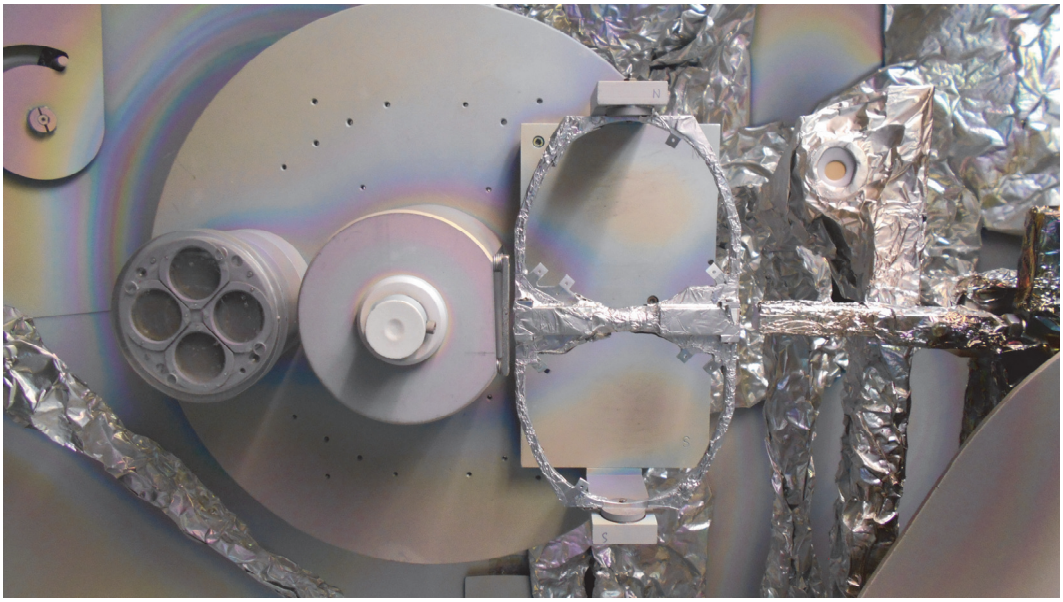

Figure 7.4 Photograph of the RVDS installed inside the Spector. The displayed RVDS configuration is identical to the one of 7.3, but the system is in its verso position. Parts repeatedly exposed to the matter flux over successive deposition cycles end up being covered by a thick deposit which eventually flakes off, potentially polluting the optical components being processed. During the maintenance of the vacuum chamber, these parts are removed and sandblasted to prevent this issue. Alternately, the components which cannot be removed easily or that are to fragile for sandblasting, including the hollow structure of the RVDS, are protected with aluminium foils which are replaced periodically.

verso, and the recto position corresponds to the one of figures 7.3 and 7.9, with the sample clamp's screws visible.

Two additional magnets are attached to the mask positioner, and are used to flip the hollow structure and expose the opposite side of a sample to the matter flux. They are called the control magnets, and have opposite poles facing the rotating fixture. As described in figure 7.6, when both the mask positioner and the rotating fixture are oriented as in figure 7.3, the interaction between a control magnet and the overturn magnet is used to rotate the structure, but also serves to stop it after half a turn, as this interaction transitions from repulsive to attractive. In other words, approching the control magnet makes the hollow structure possess only one equilibrium position, which is always chosen as the opposite of the current one.

The rotating fixture of the RVDS have been constructed specifically for this system, primarily to cope with the large RVSH footprint, which is itself a direct consequence of the wafer's size. The fixture disc was built with the same diameter than the default Spector one to stay in the uniformity corrected region delimited by the masks and avoid the need to replace them. However, the hub linking the disc to the motorised shaft have been made deeper and slightly narrower than the original one, and had a recess milled in its cylindrical body to make more room for the RVSH, also offering a

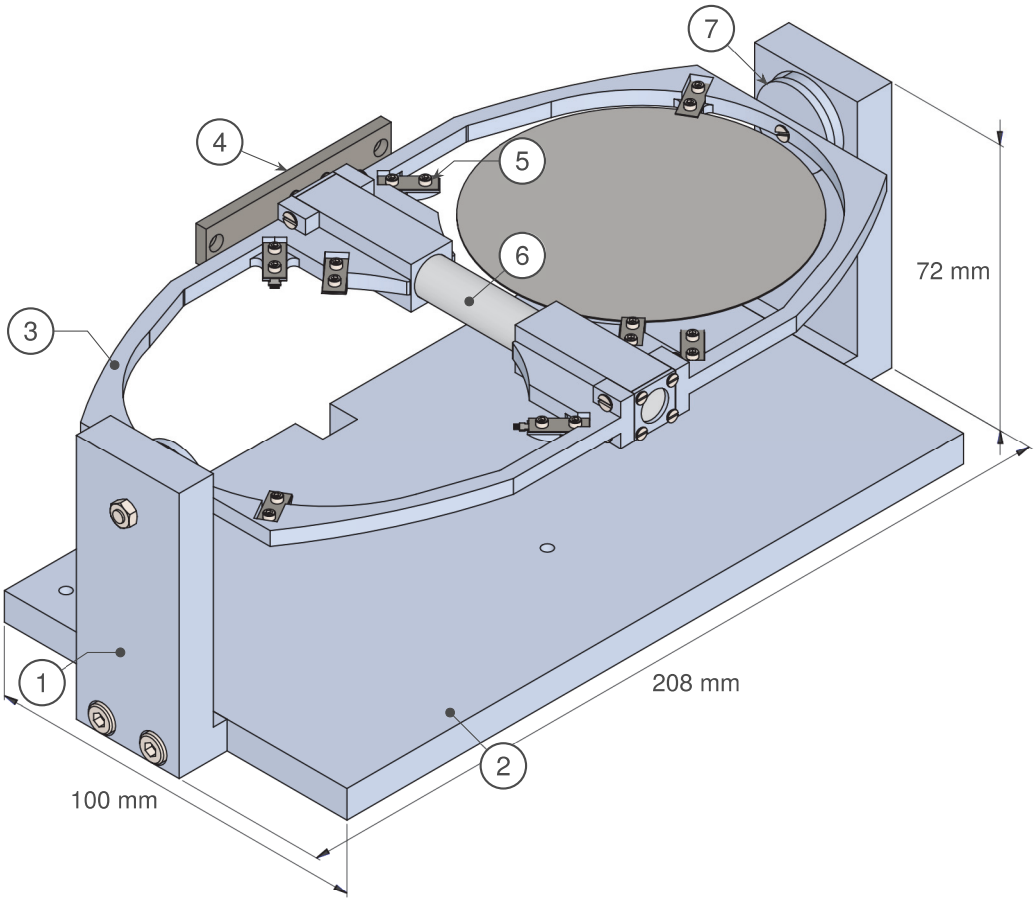

Figure 7.5 Details of the Recto Verso Sample Holder (RVSH).

Item	Description	Item	Description
1	support for the hollow structure	5	sample clamp
2	base plate	6	overturn magnet
3	hollow structure	7	ball bearing assembly
4	soft iron plate		

flat surface where the soft iron plate can be fastened. All the main parts of the system where precision machined from a 2017A aluminium alloy.

For the RVDS to operate as described above, the forces acting on the hollow structure must be carefully tuned. By a trial and error testing procedure, it has been found that besides ensuring that the interaction between the overturn magnet and a control magnet is stronger than the one between the overturn magnet and the soft iron bar, all these forces should be maximized on the whole to guarantee that the residual friction in the rotation axis has negligible effect on the system dynamic. Accordingly, the distance between all the magnetic elements have been made adjustable, by using a set of washers between the soft iron plate and the hub, and by making the fixation of the control magnets repositionable. In the same vein, it is advantageous to employ stronger magnets, which also permit a proper operation at a greater working distance, and to minimize friction in the rotation axis at the same time.

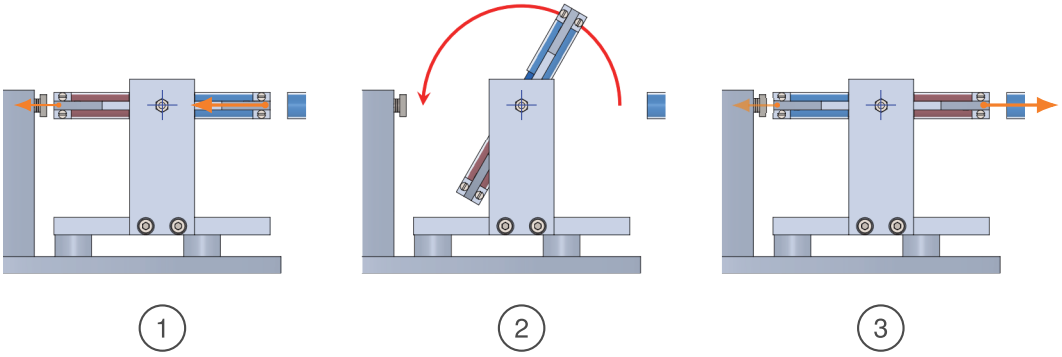

Figure 7.6 Simplified description of the flipping action of a control magnet on the hollow structure. The pieces holding the magnets have been made transparent, and the magnets north and south poles have been colored in blue and red respectively. The forces acting on the system are represented by orange arrows, the hollow structure displacement by a red arrow, and its axis of rotation is marked by a blue cross. 1-When the magnets face each other with the same polarity, the repulsive force between them is greater than the stabilizing interaction between the overturn magnet and the iron bar, so that the current position of the hollow structure become unstable. 2-Being repelled by the control magnet, the hollow structure start rotating around its axis. 3- After half a turn, the two magnets are aligned with opposite polarities and are therefore attracted to each other. The control magnet action now cooperates with the soft iron bar interaction to retain the hollow structure in this orientation, which remains positionned in this way after a few oscillations.

Magnets selection The force or magnetic field provided by a particular magnet is a complex function of its geometry, orientation, and environment, and can only be computed analytically in simple cases. While more difficult problems may be solved quantitatively using numerical tools such as the finite element method, the relatively simple operating principle of the RVDS favors a trial and error approach, as it is not necessary to know the actual values of the forces involved, nor to solve the full dynamics of the system. Selecting a magnet therefore comes down to choosing the most compact and strong one compatible with the RDVS operating environment.

Table 7.1 provides a relevant set of properties for the four major family of permanent magnet materials commercially available [74]. The first figure of merit of a magnet is its maximum energy product BH_{max}, and quantify the maximum amount of magnetic energy it can store. To operate at its BH_{max} point, a magnet must have a particular geometry, corresponding for example to a particular length to diameter ratio for a rod magnet. Roughly speaking, a material with a higher BH_{max} provides a stronger magnets for a comparable footprint. Another figure of merit useful in comparing the relative strength of different magnet materials is their maximum pole face flux

Table 7.1 Magnetic and thermal performances of the four main magnet materials.

Material (grade)	$BH_{max}\,[kJ\,m^{-3}]$	$B_{max}\,[mT]$	$T^{op}_{max}\,[°C]$	$\alpha_{B_r}\,[\%\,°C^{-1}]$
Ferrite (anisotropic)	26	100	250	0.19
Alnico (Alcomax III)	42	130	550	0.02
SmCo (2:17)	208	350	300	0.03
NiFeB (N38H)	306	450	120	0.12

density B_{max}, namely the magnetic flux density provided by a magnet close to its poles surface when it is operated at its BH_{max} point. When heated above room temperature, a magnet material partly looses its magnetization, that may be represented by the temperature coefficient of its remanence α_{B_r}. This loss is recovered from after a cooldown, provided the maximum temperature of operation T^{op}_{max} of the material haven't been exceeded. In this case, the temperature behavior of a magnet depends only on its composition.

All the materials listed in table 7.1 are vacuum compatible, and the specific design of the RVDS does not require a particular resistance to demagnetization by a external magnetic field. Then, only two materials, namely Alnico and SmCo, are compatible with the RVDS maximum working temperature of 300 °C. As they also display similar temperature coefficients, a comparable temperature stability can be expected from the two of them. Thus a choice between these two materials was initially made based on their relative intrinsic strength. As SmCo shows a maximum energy product around five time higher than the one of Alnico, SmCo made magnets appeared as the best candidates for the RVDS, and were tested in a previous version of the system. However, SmCo is also an extremely brittle material, which combined with its high magnetic strength resulted in significant handling issues. For exemple, it was noticed that a SmCo magnet could easily shatter itself after impacting an iron part it was attracted to. SmCo magnets are also much more difficult to manufacture than Alnico magnets, making these latters available in a wider variety of sizes and shapes, which provided more freedom for design. Accordingly, the use of a set of Alnico magnets was eventually prefered, as Alnico gives the best compromise between availability, mechanical resistance, temperature stability and magnetic strength for this application. Both the overturn magnet and the two control magnets are Alcomax III grade Alnico rods, that are 98 mm long and 10 mm in diameter[73].

RVSH rotation axis The design of the RVSH rotation axis is described in figures 7.7 and 7.8. To achieve a rotation with low friction, the RVSH axis was designed around a set of two identical ball bearings, which are integrated in two bearing assemblies linking the hollow structure to its support. The bearings maximum load capacity and maximum rotation speed are of no concern, so the two mains remaining constraints in their selection are compatibility with high temperature and high vacuum operation. The bearings in use in the RVSH are entirely constructed in a ZrO_2 ceramic and do not include any cage, shield or lubricant. Thanks to this construction, they are rated for a high vacuum operation up to 500 °C [21].

The ball bearing assemblies also serve to protect the bearing from the matter flux, preventing any change in their behaviour over successive coating cycles. This task is accomplished by two protective caps. One of them, called the internal protective cap, is also supporting the bearing outer ring, and the other one, called the external protective cap, is inserted between the hollow structure and a spindle supported by

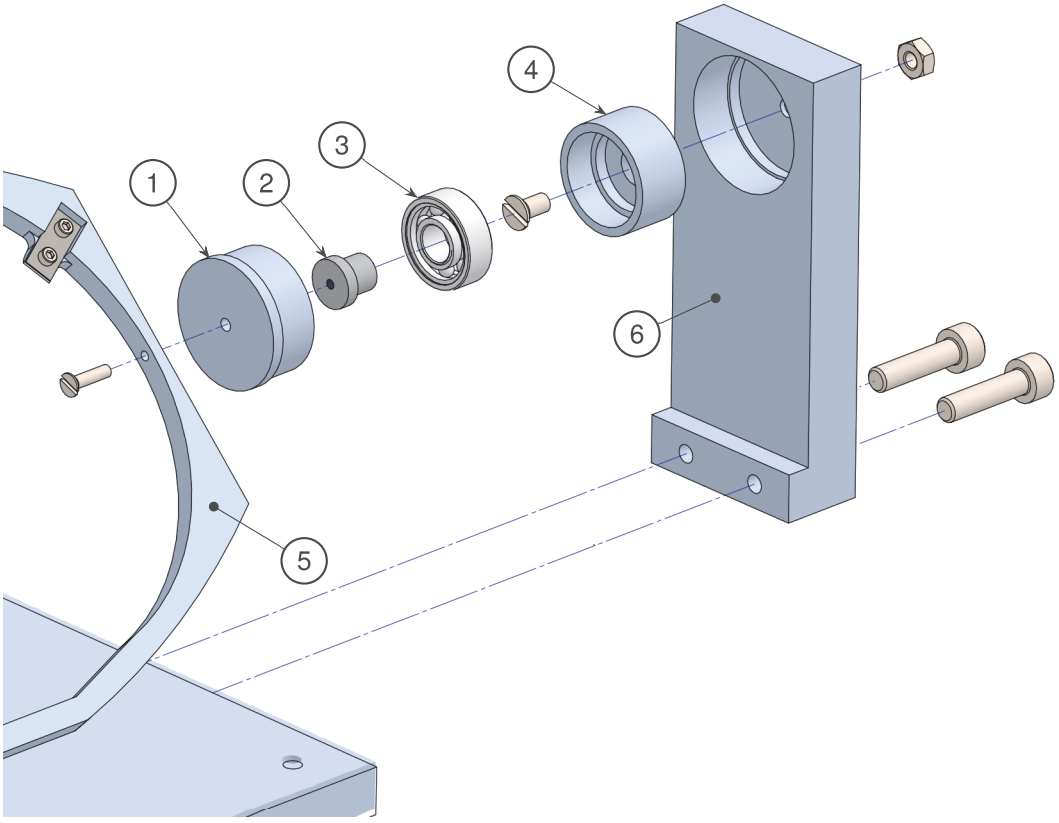

Figure 7.7 Exploded view of a ceramic ball bearing assembly. The design of this subsystem prevent deposition of material inside the bearing.

Item	Description	Item	Description
1	External protective cap	4	Internal protective cap
2	Splindle	5	Rotatable structure
3	Ceramic ball bearing	6	Support for the hollow structure

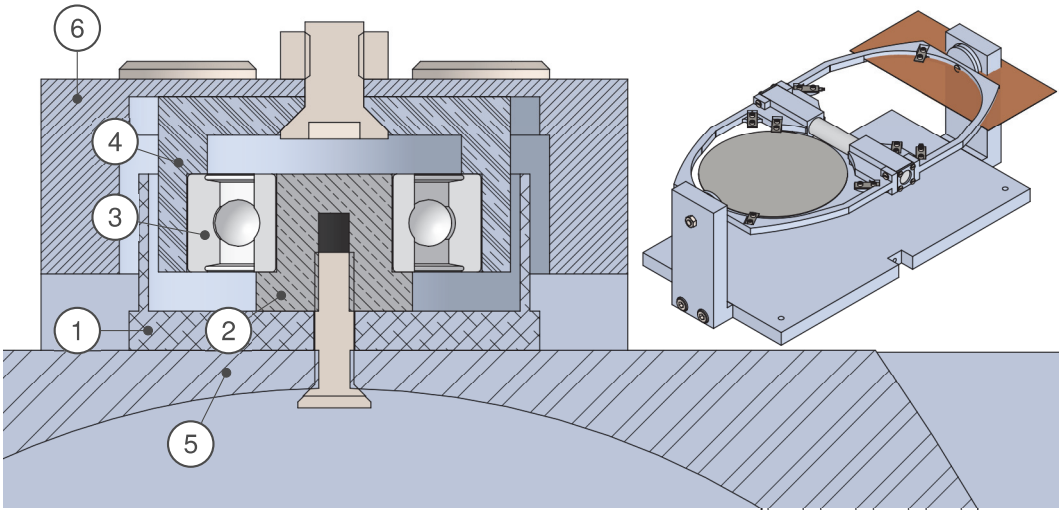

Figure 7.8 Sectional view of a ceramic ball bearing assembly. The insert at the top right corner indicate the cut plane position. The item numbering is identical to the one of figure 7.7.

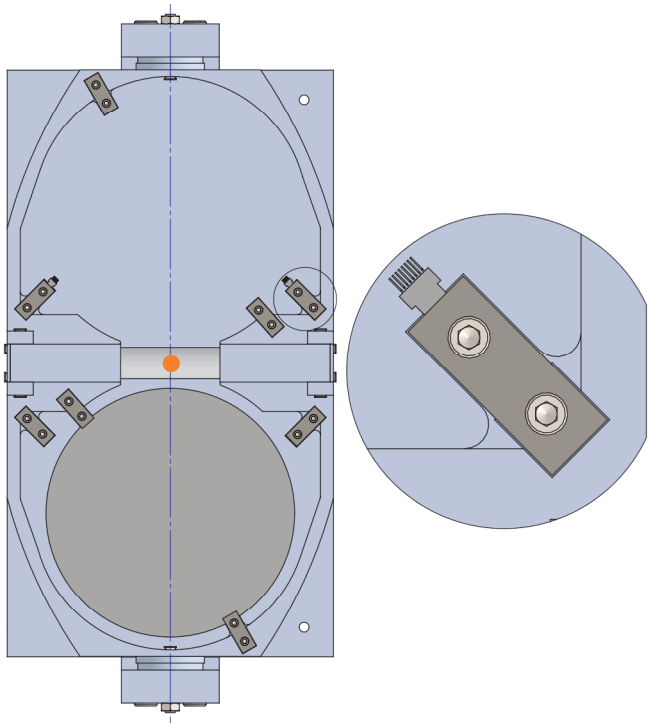

Figure 7.9 Top view of the RVSH. On the left : thanks to its symmetrical design, the center of gravity of the RVSH, marked with a orange dot, is located very close to its rotation axis, indicated by the blue vertical line. This was done to prevent unwanted rotation of the hollow structure caused by the centrifugal force coming from high speed rotation of the fixture. On the right : Detail of a sample clamp, holding a microcantilever sample. The RVSH allows the coating of two 3 inches wafers and four cantilever samples at the same time.

the bearing inner ring. The external protective cap move inside a clearance between the internal protective cap and the hollow structure support piece, so that the matter flux have no direct path to the bearing. None of the parts in contact with the bearing have been designed for a tight fit, so that the RVSH can be entirely assembled by hand, without the need of special equipments.

Symmetry When the fixture is rotated at high speed, the RVSH is submitted to centrifugal forces perpendicular to the hollow structure rotation axis. If these forces, applying to the structure center of gravity, are allowed to translate into a torque, they may result in an unwanted flip of the structure at the deposition phase, and lead to a collision between it and the uniformity mask. To minimize this torque, the hollow structure was given a highly symetrical design, making its center of gravity lie very close to its rotation axis (figure 7.9). When attached to the hollow structure, a wafer also have its center of gravity placed in the rotation axis, to preserve this equilirium. The very low mass of µcantilevers samples gives them a negligible influence in regard of this issue, so that the clamps used to attach them where placed at the structure periphery.

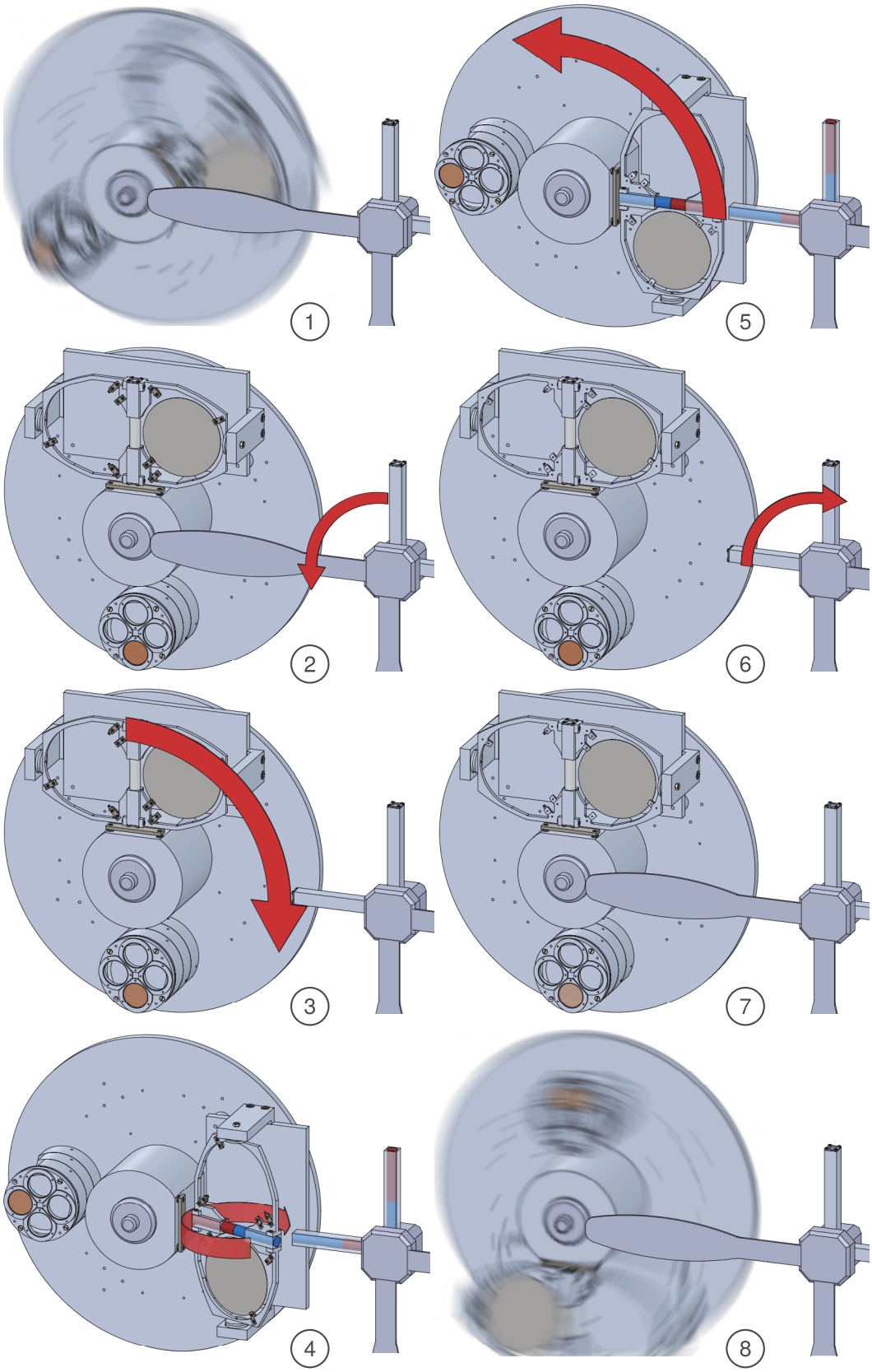

Figure 7.10 Description of a RVDS recto to verso flip sequence. The description of each step is done in the main text.

Rotation sequence The steps involved in a RVDS flip operation are listed hereafter, with reference to figure 7.10.

1. During deposition, the fixture is rotated at high speed and is partially shadowed from the matter flux by a uniformity mask. When the target thickness has been deposited, the sputtering ion beam is shut down, the fixture's motor is turned off, and the fixture is allowed to slow down to a complete stop. Then, as the overturn fixture shaft is equipped with an incremental rather than an absolute rotary encoder, a preprogrammed referencing procedure, that was already available in the Spector® software, must be executed in order to make the angular position of the fixture's shaft available. This referencing is needed after every deposition step, because information on the shaft angular position are lost everytime the fixture is set in high speed rotation. Only after such a referencing procedure can the fixture be placed at a specified angular position, which is required in the next steps.
2. The fixture is rotated to place the RVSH away from the mask positioner, and while this position is maintained, one of the two control magnets is positioned next to the fixture.
3. The RVSH is placed in front of the control magnet.
4. When they are close enough, the repulsive force between the control magnet and the overturn magnet makes the hollow structure flip away from its previous equilibrium position.
5. After the hollow structure have done half a turn, the overturn magnet is attracted by the control magnet and the hollow structure stops in this new equilibrium position. Notice that for the two diagram associated with step 4 and 5, the magnet poles have been colored like in figure 7.6.
6. The RVSH is moved away from the control magnet influence, and its orientation is preserved by the remaining attractive force between the overturn magnet and the soft iron plate.
7. While the RVSH is maintained away from the mask positionner, a uniformity mask is put back in front of the fixture.
8. The fixture is accelerated again, and the sputtering ion beam is switched on. A new layer can be deposited on the opposite side of the substrates attached to the RVSH.

7.2.3 Test of the RVDS

To verify the correct operation of the RVDS, a dedicated Spector cycle was settled, including the default preprocessing and postprocessing phases. At the coating phase, a succession of 100 flipping sequences like the one of figure 7.10 where programmed, but without extraction of the sputtering ion beam. The entire process was filmed, and the film analysed after the cycle. At the beginning of each flipping sequence, the quartz

lamp heaters where turned on to light up the dark vacuum chamber, and the system temperature was raised gradually at the same time. The flipping sequences where thus performed from room temperature to 150 °C. After analysis of the recorded video, it was found that all the flipping sequence succeeded at the first try.

The RVDS was then employed in a few µcantilever coating cycles. While these were not filmed, no apparent signs of a flipping failure or a collision have been found. The RVSH was then dismounted, and the ceramic ball bearings examinated, with no evidence of deposition on any of their parts.

Even if more experience needs to be gained with the RVDS, these result suggest that its main problematic, that is to allow a deterministic, reliable mean of flipping sample inside the machine, have been successfully adressed.

7.3 Conclusion

A device, called the Recto Verso Deposition System (RVDS), was developped to return wafers and µcantilevers inside the Spector, a commercial IBS deposition system. Thanks to this device, a coating stress compensation strategy was implemented to avoid the excessive bending of coated µcantilevers. The RVDS was designed to be vacuum compatible with a theoretical maximum operating temperature of 550 °C using an aluminium construction, ZrO_2 ball bearings and Alnico magnets. When tested, the device worked properly up to 150 °C, and was succesfully used for a few subsequent coating experiments.

8 Analysis of cryogenic noise measurement on a Tantala coated microcantilever

We study the dissipation ϕ of a tantala coated cantilever from 10 K to 150 K. From the thermal noise spectra, a fit of 10 resonances for bending modes, and 6 resonances for torsion modes can be performed, giving access to ϕ from 2 kHz to 600 kHz. Dissipation presents a weak maximum around 50 K in temperature, and is a slowly increasing function of frequency (power law f^{α} with $\alpha \sim 0.06$). An extrapolation of this behaviour to lower frequencies (down to 10 Hz) agrees reasonably well with the thermal noise measurements, even if external noise peaks hinder direct exploitation of the thermal noise datas in this frequency range.

8.1 Experiment protocol and calibration

8.1.1 Sample and temperature ramp description

In this chapter we present the analysis of a thermal noise measurement on a cryocooled tantala coated cantilever. The sample is a rectangular silicon cantilever, $L = 741$ m long, $b = 90$ m wide, $h_s = 0.93$ m thick, coated with $h_c = 310$ nm of tantala and annealed at 500 °C for 10 hours. The scanning electron microscope (SEM) images of figures 8.1 and 8.2 are used to measure the size of the substrate, and check that the thickness of the coating corresponds to the deposition parameters. The measurement corresponds to a temperature raising from 10 K to 151 K. Because of the thermal dilatation of the cryostat internal structure, the position of the laser on the cantilever is slowly drifting throughout the measurement, so it was repositioned between 60 K and 61 K. The two images on figure 8.3 show the spot position right after alignment (initial and after repositioning)

The temperature is saved directly from the controller to the computer. The time allows linking a specific thermal noise measurement to the temperature of the sample. Unfortunately, this recording was limited to 65 000 samples (18 h at 1 Hz), so temperatures above 117K where not recorded. The dependence in time being very smooth, we extrapolate the missing temperatures from a second order polynomial fit (see figure 8.4).

8.1.2 Calibration of the interferometer

During the warming of the cantilever, around 14 000 files where acquired, each corresponding to 2^{22} samples acquired at a sampling rate of 4 MHz of every of the four photodiodes of the interferometer (around 1 s). We process this raw data using the initial calibration of the interferometer for the first files. Each time a measurement presents a large enough oscillation (due to random kicks or self-oscillation of the cantilever), we use the data to recalibrate the interferometer, and subsequently use this ellipse (till the next oscillation larger than $\lambda/2$...) Calibration ellipses are shown on figure 8.6. The distance between the measurements and the calibration ellipse is in average around 5 %, which is acceptable: the error on sensitivity of the interferometer is probably around 10 %, which leads to a similar uncertainty in the power spectra density (PSD) vertical scale, thus in the estimation of the stiffness of each mode. We tried to use the long time drift of the interferometer as a calibration method as well (see figure 8.5), but the uncertainty is still of the same order, so we gave up on this strategy. As we will see later, this error bar is not significant for our measurements. Moreover, the measurement of thermal noise is free of any non-linearity (the benefit of measuring minute signals), so the frequency axis is extremely precise, as are the determination of resonance frequencies and dissipation coefficients.

8.1.3 Data processing

A typical example of time signal is presented in figure 8.7(a). As mentioned, some other datasets present large oscillations due to random external kicks or self-oscillation of the cantilever. Examples of such datasets are presented in figure 8.24. To avoid artifacts during data processing, we discard those sets, as shown on figure 8.8. This corresponds to less than 4% of the recordings. A PSD is computed for each file (using the highest frequency resolution possible, i.e. using 2^{22} points for the Fourier transform, leading to a spectral resolution of 0.95 Hz. An example of such a PSD is shown in figure 8.7(b). We save only a fraction of this PSD: a 4 kHz range around each of the 16 identified resonances. We also compute the background electronic white noise by averaging the PSD over frequencies in the 45 kHz − 75 kHz interval.

8.2 Statistical analysis of the spectra

Each spectrum looks rather noisy due to the lack of averaging, so we study the distribution of noise around the mean spectrum. Appendix B presents a theoretical analysis of this statistics. For the experimental data, we average the spectra around the same temperature (1 K intervals), and compute the histogram (over all files and frequencies) of the ratio between a single spectrum and the mean spectrum. As illustrated in figure 8.9, this ratio follows almost exactly the theoretically expected exponentially decaying

distribution $p(x) = e^{-x}$ (no free parameters in the comparison), except for a bump at high values of the ratio. A closer look at the spectra and time signals corresponding to these extreme positive events shows that they corresponds to external perturbations (kick in the signal, peaked external noise) or low amplitude self oscillations. Figure 8.10 displays a few examples of these events. We therefore discard any dataset having an outlier (defined as the ratio greater than 12) in the ratio between its spectrum and the mean spectrum in neighbouring temperatures. Statistically, this criterium has a probability of 6.1×10^{-6}, and since each spectrum we analyse around each mode contains 4194 frequency bins (4 kHz with 0.95 Hz resolution), this should lead to dropping only 2.6 % of the spectra. Due to the presence of external perturbations, using this criterium we eventually end up discarding 4 % of the recordings (on top of the 4 % of data already discarded with the large oscillations criterium).

8.3 Fit of the resonances with the Saulson model

8.3.1 Fitting procedure

We analyse each resonance by fitting the spectra in a $\pm\Delta f = \pm 1$ kHz range around each resonance, for the mean spectra every 1 K from 10 K to 150 K. The model for the fit is a Saulson model (section 3.3.2, page 34), with 4 free parameters: the resonance frequency f_n, the stiffness k_n, dissipation ϕ_n, and background noise BG of the measurement:

$$P_z^{SaO}(f) = \frac{2k_BT}{\pi f k_n} \frac{\phi_n}{(1-(f/f_n)^2)^2 + \phi_n^2} + BG \tag{8.1}$$

We plot an example of those fits in figure 8.11 for flexion modes 1 to 10 and in figure 8.12 for torsion modes 1 to 6. Expect for flexion mode 1 which is quite noisy, the fits look in general very good. From time to time, due to the slow drift of the laser spots on the cantilever during the measurement, we cross a node of the mode under study. In this case, the thermal noise peak disappears under the background noise. To avoid this issue, we define a spectral signal to noise ratio (SNR) by comparing the amplitude of the measured thermal noise (mean of the spectrum in a $\pm\Delta f = \pm 1$ kHz range around resonance) to the amplitude of the background noise:

$$\mathrm{SNR} = \frac{1}{2\Delta f} \int_{f_n-\Delta f}^{f_n+\Delta f} \frac{P_z(f)}{BG} df \tag{8.2}$$

When this SNR is lower than 1.1, we discard the fit result.

To further assess the validity of the fits, we compute a χ^2 statistics for each. As show in figure B.1 and B.2 in appendix B, the χ^2 value is very close to 1 for every temperature and resonances, except a few exceptions: mode 1 in flexion for all temperatures (as

already commented, noisy spectra), and some other modes in limited temperature ranges.

8.3.2 Fit parameters uncertainty estimation

Let us now estimate the statistical uncertainty on the fit parameters. We start for each resonance and temperature with the theoretical spectrum corresponding to the Saulson model obtained by the fit. This spectrum is noiseless, so we simulate a noise corresponding to the experimental conditions: same number of datasets with a noise distributed according to an exponentially decaying law, temperature drifting by 1 K, etc. We then fit this noisy spectrum by a Saulson model, and get a new estimation of the parameters. We perform this operation for 50 different realisations of the noise, and compute the mean and standard deviation of each parameter of the model. We finally check that we recover the initial parameters within the standard deviation. This is always true in our case as long as the spectral SNR is greater that 1.1. In the following, we will use the standard deviation computed this way to represent the statistical uncertainty on each parameter extracted from the fit. This method obviously doesn't include any uncertainty which would be linked to systematic errors, like errors due to the model being inadequate to model the spectra. However, the low value of χ^2 ensure that this systematic uncertainty is low for most fits.

8.4 Temperature dependence of the parameters

We now focus of the 3 parameters of interest, $f_n(T)$, $k_n(T)$ and $\phi_n(T)$, that we study in the next sections.

8.4.1 Resonance frequency $f_n(T)$

As can be seen directly on the spectra, the resonance frequency $f_n(T)$ is shifting with temperature. We report this dependency in figure 8.13 and figure 8.14. For flexion, all modes behave exactly in the same way, with a softening of the cantilever when the temperature increases. This behaviour is due to the dependency on temperature of the Young's moduli of silicon and tantala. For torsion, the behaviour is more erratic, some mode sharing a common behaviour but not all. This might be partially due to systematic errors when tracking the peaks, with external noise biasing the fits by changing the shape of the spectra. However for mode 3, the reason is clearly different and not understood. Note that the common behaviour of modes in torsion is very close to that of the modes in flexion multiplied by a factor 1.2.

8.4.2 Stiffness $k_n(T)$ and effective masses

Instead of studying directly $k_n(T)$, let us define an effective mass of each mode by $m_n(T) = k_n(T)/[2\pi f_n(T)]^2$. If the measurement was performed at the extremity of the cantilever, this effective mass would be equal to $m_C/4$ (with m_C the cantilever mass, equation 3.21). However, the distance between the reference and probe laser beams is $d = 417\,\mathrm{m}$, shorter than the 741 m length of the cantilever. The illustration of figure 8.15 shows that the differential measurement thus senses only a fraction of the total deflection, and this fraction is changing when the laser spot is slowly drifting in time:

$$m_n(T) = \frac{k_n(T)}{[2\pi f_n(T)]^2} = \frac{m_C}{[\zeta_n(x_{\mathrm{prob}}) - \zeta_n(x_{\mathrm{prob}} - d)]^2} \tag{8.3}$$

where $\zeta_n(x)$ is the normal mode n in the Euler-Bernouilli framework. When we cross a pseudo node of one mode, the amplitude of the thermal noise vanishes, thus the stiffness deduced form the fit diverges, hence the effective mass diverges too. This is indeed what is observed on the data, as illustrated in figure 8.16. The benefit of this is that when such divergence occurs, we know exactly where we stand on the cantilever from the shape of the modes. We can then infer the laser spot position x_{prob} at several temperatures during the measurement, and extrapolate between those points to know at each temperature where we sit on the cantilever and what is the expected effective mass of each mode. This process leads to the measurement position plotted in figure 8.17, and to the curve for the expected effective mass for each mode in figure 8.16. There is one free parameter in this process, which is the cantilever mass m_C (which changes only the vertical position of the curves in those figures). We can adjust this parameter by a fitting process, and extract a guess for m_C for each mode. We end up with $m_C = 294 \pm 25\,\mathrm{ng}$, which corresponds to a tantala layer 300 nm thick. Imposing the mean value of the cantilever mass, we get the prediction of effective masses of the black dashed curves in figure 8.16, which match nicely the experimental data. The torsion mode effective masses are reported in figure 8.18. In absence of a detailed elasticity model comparable to the Euler Bernouilli approach, we will not analyse those data. Note that the lateral drift of the laser spots should also be taken into account in such analysis.

8.4.3 Damping coefficient $\phi_n(T)$

As shown in figure 8.19 to 8.22, $\phi_n(T)$ presents a maximum for each mode n as a function of temperature, and this maximum is increasing as a function of mode number n. The horizontal position of the maximum also increases with n. We have no specific model for the dependency, so we'll just use an ansatz with a generic function of f,

T with few ajustable parameters. We observe that the curves of ϕ_n vs $\log(T)$ seems hyperbolic, so we choose this generic shape:

$$\phi = \phi^{\max}[Ae^{a(T-T^{\max})-\sqrt{b+c(T-T^{\max})^2}} + (1-A)] \tag{8.4}$$

When we performed the fit for each mode, we saw that most parameters are quite independent of the mode number, or simple function of $T^{\max}$. We therefore limit our ansatz function to only two free parameters : $\phi^{\max}$ and $T^{\max}$:

$$\phi_n(T) = \phi_n^{\max}(0.6e^{0.2(T/T_n^{\max}-1)-0.8\sqrt{0.04+(T/T_n^{\max}-1)^2}} + 0.4) \tag{8.5}$$

As illustrated in figure 8.19 to 8.22, the fits match adequately the global behaviour of most modes.

In figure 8.23(a), we plot the values of $\phi_n^{\max}$ as a function of the resonance frequency f_n of the corresponding mode. For flexion and for torsion, the data gather along a line in this log-log scale, hinting at a power dependance for both:

$$\phi^{\max}(f) = \phi_0^{\max} f^{\alpha} \tag{8.6}$$

with $\alpha = 0.063 \pm 0.006$ for flexion and $\alpha = 0.053 \pm 0.006$ for torsion. This power law dependency and coefficient value are very similar to measurements on coated silica disk with the rings down method [48].The prefactors $\phi_0^{\max}$ differ only by 20% for both family of modes (dissipation being slightly larger for torsion): $\phi_0^{\max} = (2.85 \pm 0.22) \times 10^{-4}\,\mathrm{Hz}^{-}$ for flexion and $\phi_0^{\max} = (3.5 \pm 1.7) \times 10^{-4}\,\mathrm{Hz}^{-}$ for torsion.

In figure 8.23(b), we plot the values of the resonance frequency f_n as a function of $1/T_n^{\max}$ of the corresponding mode. For all modes, the data gather along a line in this lin-log scale, hinting at a shared Arrhenius law for both:

$$f_n = \frac{1}{2\pi\tau_0} e^{-\frac{E_a}{k_B T_n^{\max}}} \tag{8.7}$$

with $E_a = 53.5 \pm 2\mathrm{meV}$ and $\tau_0 = (1.2 \pm 0.6) \times 10^{-12}\,\mathrm{s}$. Uncertainty on τ_0 is large and actually correlated to the value of E_a. Those values compare nicely with reference [83] for other tantala coatings measured with a ring down method.

From this observations we can infer the expected value of dissipation for modes 1 and 10 in flexion (the fit of which are noisy), and 6 for torsion (which has a low snr for small T). Combining equations 8.5, 8.6 and 8.7, we have a generic extrapolation of dissipation at any frequency and temperature:

$$\phi(f,T) = \phi_0^{\max} f^{\alpha}(0.6e^{-0.2(1+\ln(2\pi f\tau_0)k_BT/E_a)-0.8\sqrt{0.04+(1+\ln(2\pi f\tau_0)k_BT/E_a)^2}} + 0.4) \tag{8.8}$$

8.4.4 Ring-down study

As mentioned in figure 8.8, some data sets are discarded because of large amplitude deflections, which are probably triggered by external random kicks or self-oscillations. Taking a closer look at those recordings, we find a significant fraction of them displaying a clear ring-down behaviour, as illustrated in a few example on figure 8.24. The envelope of the deflection around the first mode frequency f_1 can be fitted in its exponentially decaying part to extract a characteristic relaxation time τ_1, which is related to the dissipation by

$$\phi_1^{\text{ring-down}} = \frac{1}{\pi \tau_1 f_1} \tag{8.9}$$

We notice that the enveloppe sometimes display a strange beating phenomena, which we don't understand. However, the measured dissipation using this method are plotted in figures8.19 and 8.21, and compared to the dissipation measured through thermal noise. Although noisy, these datas are in good agreement and this result gives credit to the extrapolation of dissipation to mode 1.

8.4.5 Low frequency thermal noise

Let us have a final look at the thermal noise measurement at low frequency. As illustrated in figure8.25, noise measurement below a few kHz is hampered by external noise, mainly mechanical vibrations, which adds a large number of peaks on the spectrum. The fit of the resonance is spoiled by those peaks, and the value of k_1 or ϕ_1 not trustable, especially at low temperature. From the extrapolation of the behaviour of those parameters for higher order modes, we have however another way to estimate the thermal noise according to the Saulson model: the stiffness is set by equation 8.3, and we use the extrapolation of equation 8.8 for ϕ (either at all frequencies – $\phi(f)$, or to estimate the dissipation of mode 1 only and use the Saulson model with frequency independent dissipation – $\phi(f_1)$).

We see that the lowest part of the PSD, between the external disturbances peaks, indeed reaches the prediction of the Saulson model for those extrapolated values of the dissipation. The difference between $\phi(f)$ and $\phi(f_1)$ is weak (at most 25% at 100 Hz). Though the spectra are too noisy for a direct exploitation, they are however a good indication that dissipation behaves smoothly in this frequency range and can be extrapolated from higher order modes. Below 30 K, the PSD does not seem to reach the prediction of the model, however in this area the thermal noise is very low and other sources of noise are proportionally more important. Moreover, the heating of the cantilever by the lasers of the interferometer produces a few K rise that could explain part of the small mismatch.

8.5 Internal dissipation of tantala

8.5.1 Dilution factor D

Up to now, we have only been considering the global dissipation of the cantilever. We need to separate the contribution of each part of the composite cantilever: the silicon substrate on one hand, and the tantala coating on the other hand. This operation is done by considering the dilution factor D of the measurement: the total dissipation coefficient ϕ of the cantilever (i.e. ϕ_n for each mode) can be written [69]:

$$\phi = D\phi_c + (1 - D)\phi_s \tag{8.10}$$

where ϕ_c is the coating internal dissipation, and ϕ_s the substrate one. D can be computed in 2 different ways: it can be related to the elastic or to the kinetic energy of the elastic beam. The first approach leads to

$$D = \frac{E_c I_c}{E_c I_c + E_s I_s} \tag{8.11}$$

where $E_{c,s}$ is the Young's modulus of the coating (subscript $_c$) or substrate (subscript $_s$), $I_{c,s}$ the cross moment of inertia calculated with respect to the neutral line:

$$I_s = \frac{b h_s^3}{12} \tag{8.12}$$

$$I_c = \frac{b\left((h_c + h_s)^3 - h_s^3\right)}{12} \tag{8.13}$$

with h_s the thickness of the µcantilever and h_c the total coating thickness. Using the physical parameters summarised in table 8.1, we compute $D = 0.483 \pm 0.023$ from equation 8.11.

The second approach based on kinetic energies leads to

$$D = 1 - \frac{\rho_s h_s}{\rho_s h_s + \rho_c h_c}\left(\frac{f_s}{f_c}\right)^2 \tag{8.14}$$

with $\rho_{s,c}$ the material density, and f_s (respectively f_c) the resonance frequency of the mode before (respectively after) coating. In this formula, the experimental values of the resonance frequencies can be used instead of theoretical ones, leading to an independent estimation of D for each mode. As show in figure 8.26, this measurement is quite independent of the mode number, and in good agreement with the theoretical value from equation 8.11. The uncertainties on thickness and density of the substrate and coating lead to an uncertainty of 0.012 on D, which is comparable to the standard deviation around the mean on the 10 modes: 0.009.

Table 8.1 Sample size and material properties.

Property	Substrate (silicon)	Coating (tantala)	Note
Length (μm)	$L = 741 \pm 5$	$L = 741 \pm 5$	from SEM image
Width (μm)	$b = 90 \pm 1$	$b = 90 \pm 1$	from SEM image
Thickness (nm)	$h_s = 934 \pm 10$	$h_c = 300 \pm 10$	from SEM image and coating parameters
Young's modulus (GPa)	$E_s = 169$	$E_c = 121 \pm 2$	[124], [48]
Density (kg/m^3)	$\rho_s = 2340$	$\rho_c = 7470 \pm 90$	[102], [48]

Ideally, this dilution factor should be computed for every temperature T. However, the temperature dependency of the parameters in these formula are small: the resonance frequencies of the coated cantilever for example change by 0.7 % in a 140 K range, hence by $5 \times 10^{-5}\,\mathrm{K}^{-1}$. The substrate is made of silicon, whose tabulated temperature dependency is even weaker. We can therefore safely use room temperature measurement to compute D, and use the average value over the 10 modes $D = 0.50 \pm 0.02$. The accuracy around 4 % is mainly limited by our knowledge of the thickness and density the tantala coating.

8.5.2 Silicon substrate damping

In order to use equation 8.10 to compute the coating internal dissipation, once D is known, we need a measurement of the raw cantilever initial dissipation ϕ_s. This measurement is performed before coating, using the same protocol described in the previous parts for the coated sample. The analysis is not reported here in details, as the result is actually that for all temperature and modes, $\phi_s \approx 3 \times 10^{-6} \ll \phi_c$. We can therefore neglect the substrate contribution in equation 8.10, with an error smaller than 1%. Since $D = 0.5$, the coating dissipation is thus just twice the damping measured for the coated cantilever, with a slightly increased uncertainty due to the 4% one on D.

8.6 Conclusion: tantala internal dissipation

The final estimation of the tantala internal damping is reported in figure 8.27. All previous findings on the dissipation of the cantilever apply directly: power law frequency dependence, Arrhenius behavior, etc. Equation 8.8 can be applied as is, with the following parameters:

$$\alpha = 0.063 \pm 0.006 \tag{8.15}$$

$$\phi_0^{\max} = (5.7 \pm 0.4) \times 10^{-4}\,\mathrm{Hz}^{-\alpha} \tag{8.16}$$

$$E_a = 53.5 \pm 2\mathrm{meV} \tag{8.17}$$

$$\tau_0 = (1.2 \pm 0.6) \times 10^{-12}\,\mathrm{s} \tag{8.18}$$

Figure 8.1 SEM images of the raw cantilever (top view for top images, side view for bottom one). The dimensions of the cantilever are measured from these images as: length $741\,\mathrm{m}$, width $90\,\mathrm{m}$, thickness $934\,\mathrm{nm}$. The fabrication process by DRIE (deep reactive ion etching) is clearly visible by the characteristic shape of the cantilever on the side view.

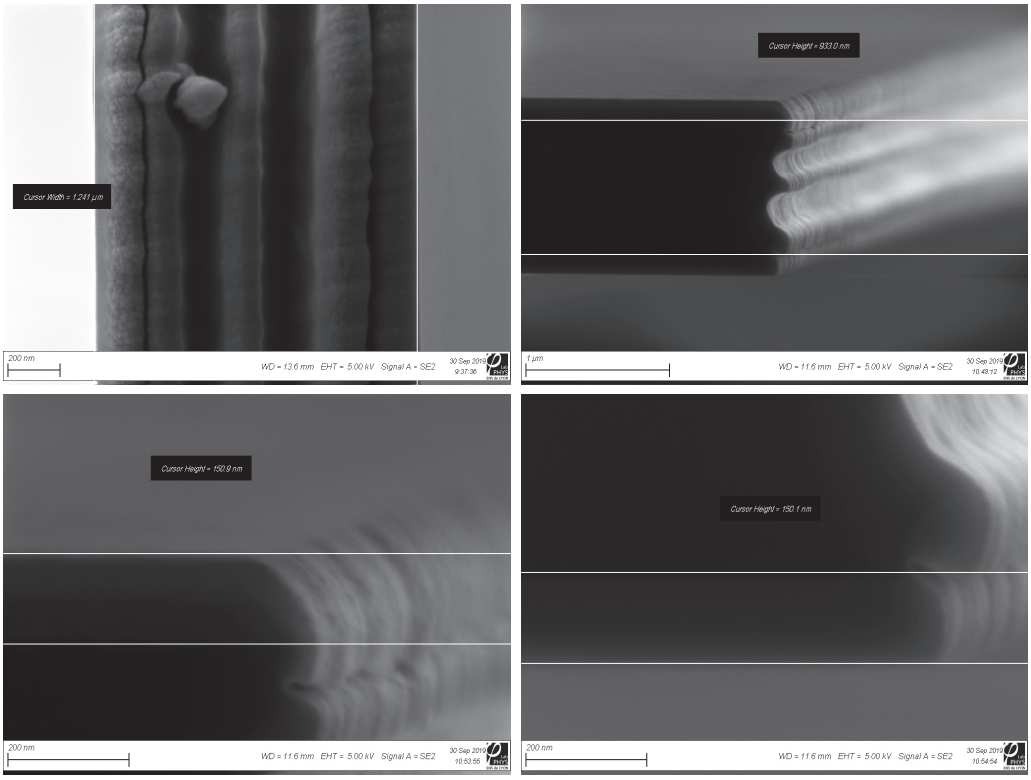

Figure 8.2 SEM images of the coated cantilever. The top-left image is a side view of the cantilever (rotated vertically to avoid charging artefacts with the insulating coating), while the other ones are images of the section of a cantilever that was cut in the middle of it length. The two bottom images are zoom on the top and bottom layers. The coating thickness is evaluated to $150\,\mathrm{nm} \pm 10\,\mathrm{nm}$ on each side.

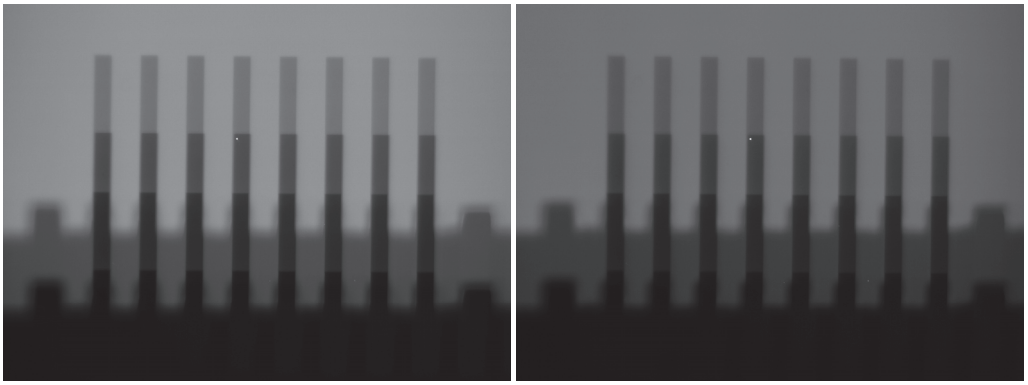

Figure 8.3 Picture of the laser spot position before each session: at $7\,\mathrm{K}$ (left) and $60\,\mathrm{K}$ (right).

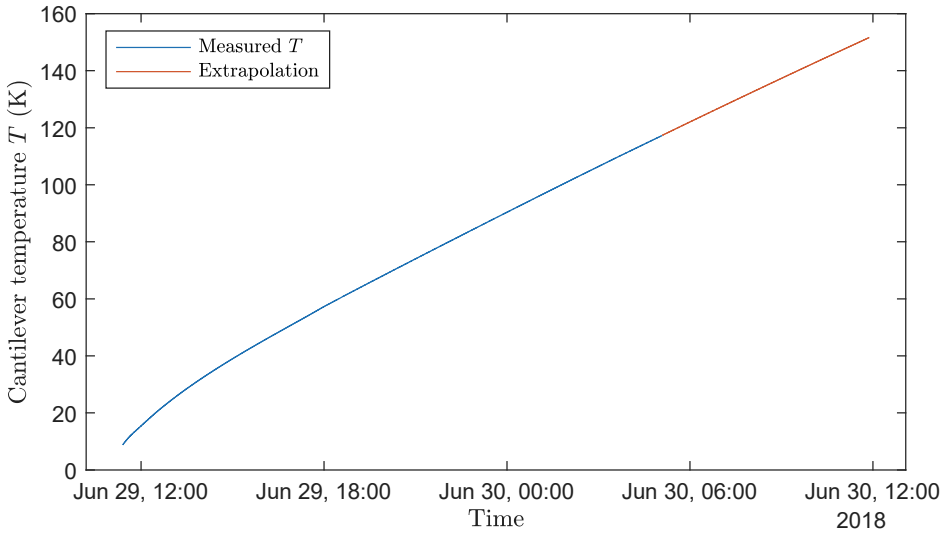

Figure 8.4 Temperature as a function of time. The last part of the curve is extrapolated from the lower temperature evolution.

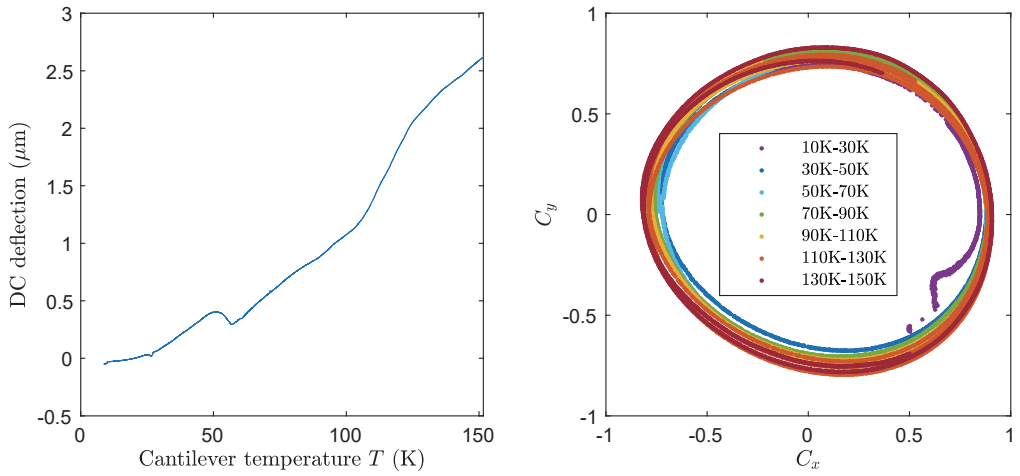

Figure 8.5 The long term drift of the interferometric measurement is limited to 3 m during the 140 K temperature ramp.

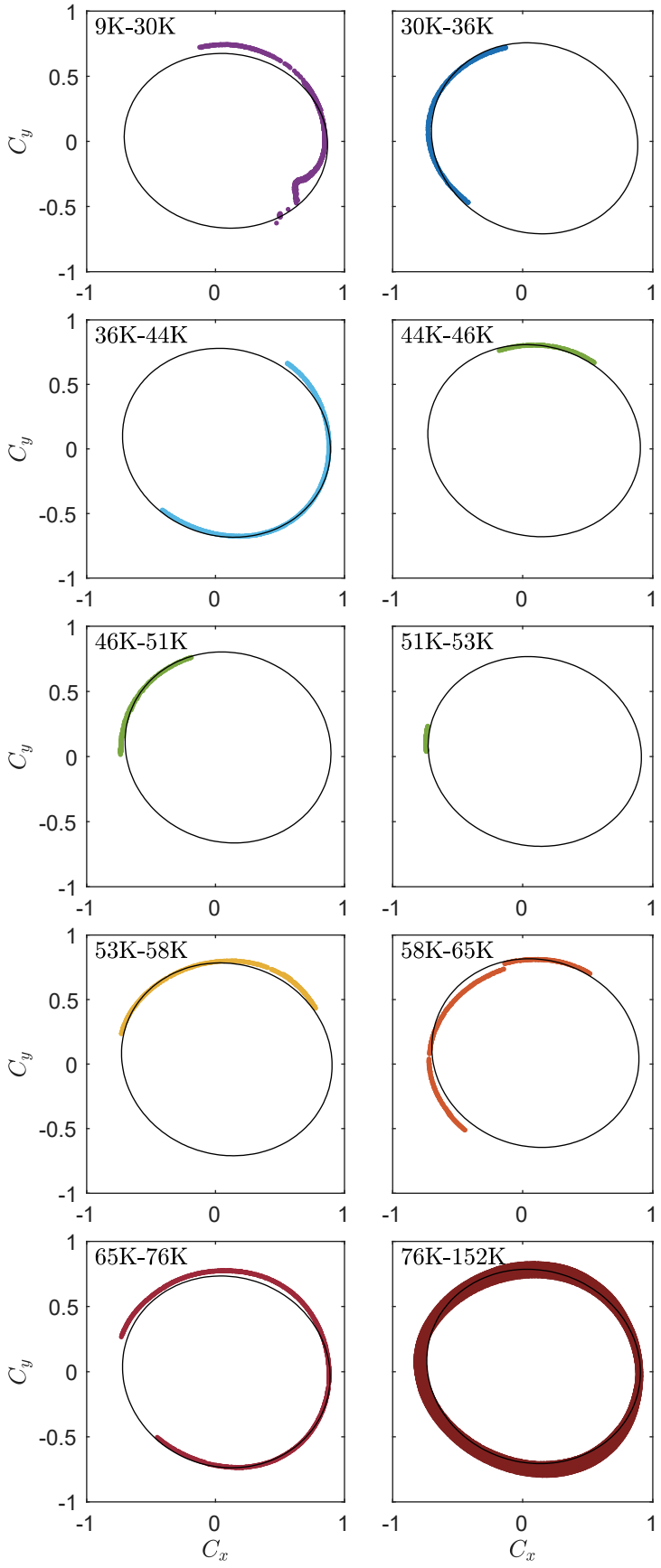

Figure 8.6 The 10 calibration ellipses of the interferometer that are used to measure deflection, superposed in their temperature ranges on the mean complex contrast of each data set.

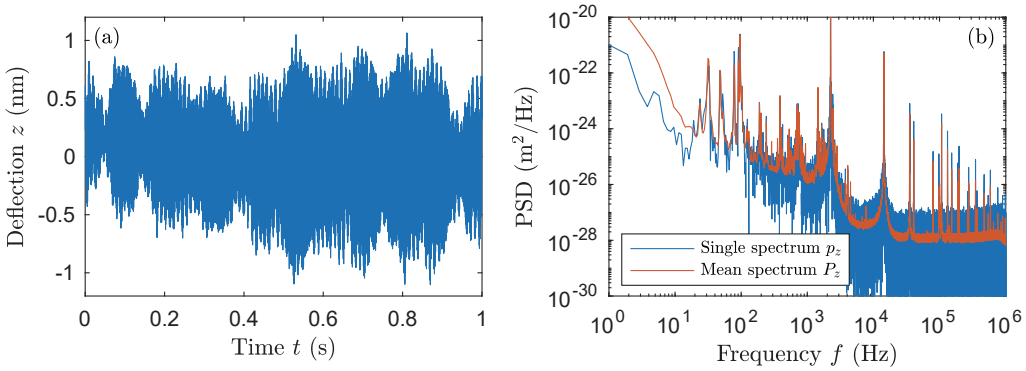

Figure 8.7 (a) Deflection versus time for a typical dataset, here at $T = 90\,\mathrm{K}$. (b) PSD (power spectrum density) of the deflection, for a single dataset, and mean over 100 realisations at the same temperature $T = 90 \pm 0.5\,\mathrm{K}$.

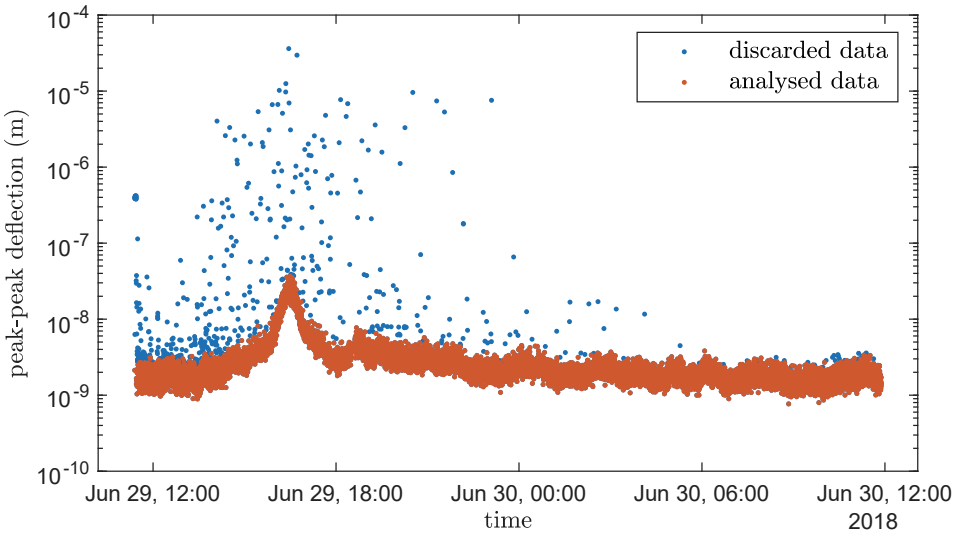

Figure 8.8 For each dataset, we compute the peak-peak amplitude of the deflection, and discard datasets with large oscillations (external kicks, self-oscillations, etc.) from the analysis.

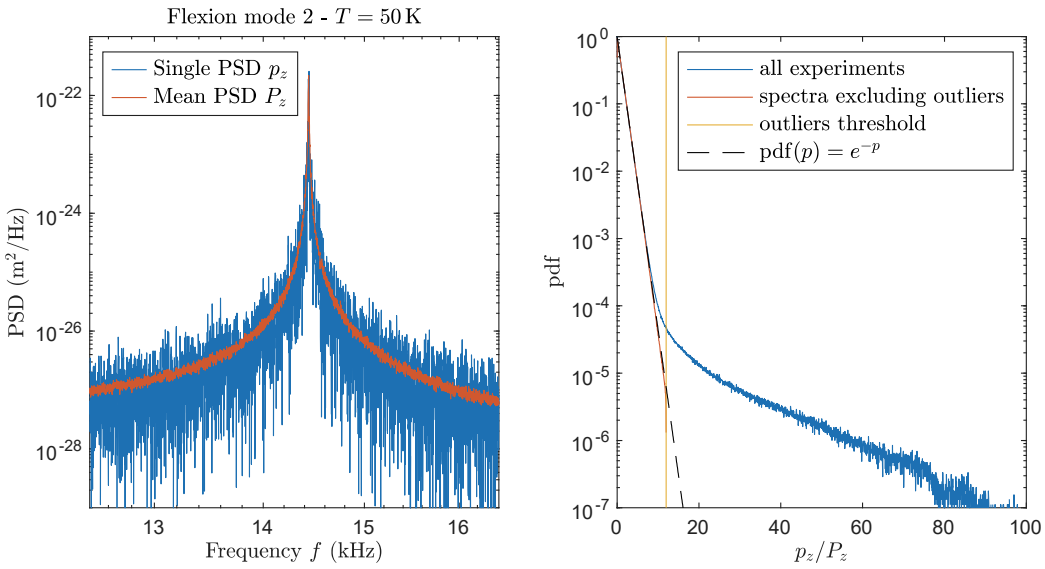

Figure 8.9 A single PSD p_z is noisy compared to the average one P_z (left, example for flexion mode 2 at $T = 50\,\mathrm{K}$). This noise is multiplicative, and follows an exponentially decaying distribution: $\mathrm{pdf}(p = p_z/P_z) = e^{-p}$. The side bump of the experimental distribution corresponds to outliers that are discarded from the analysis, using the criterium $p_z/P_z < 12$.

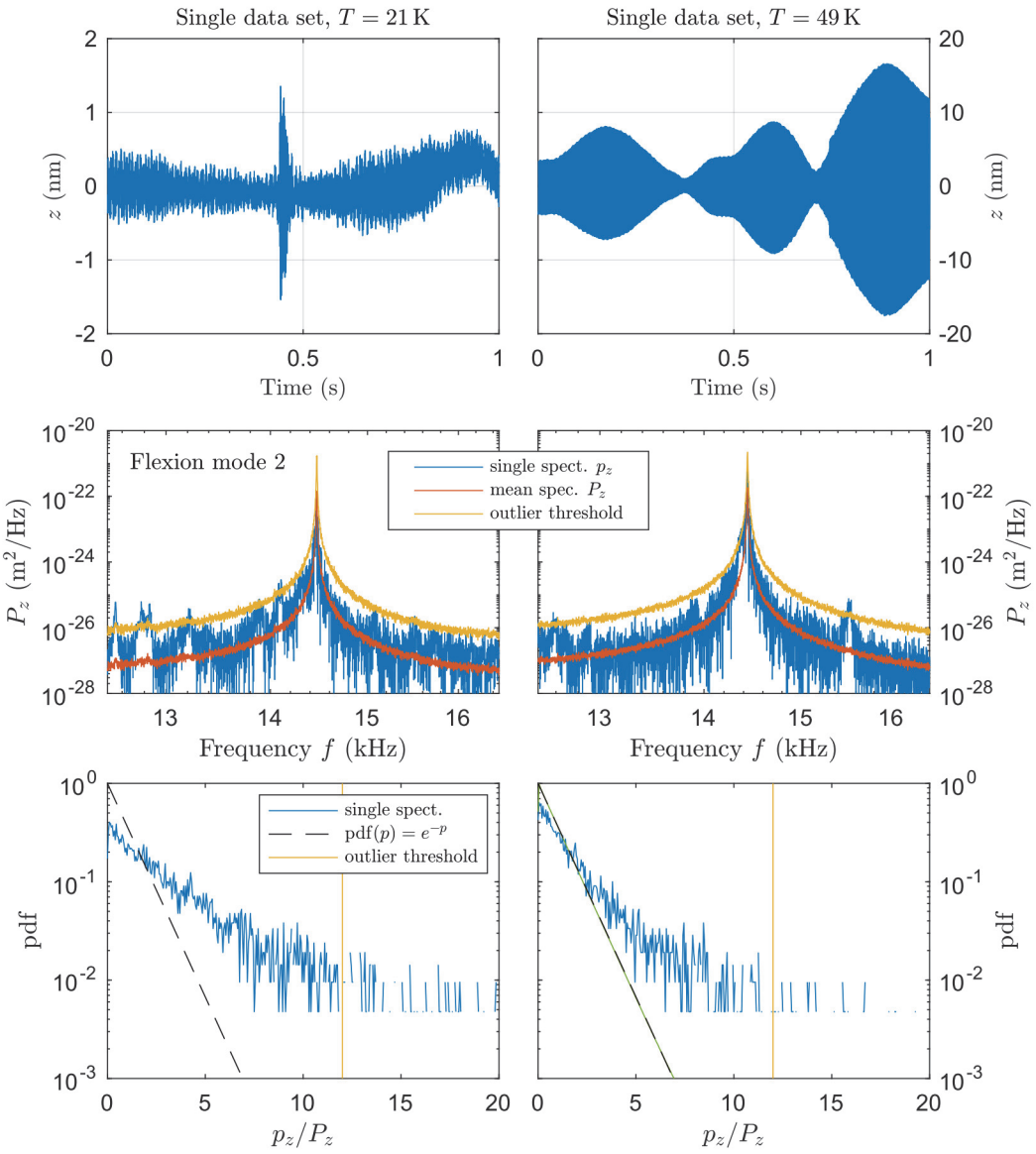

Figure 8.10 Examples of datasets presenting outliers in their spectrum with respect to the average. A single spectrum p_z is compared to the mean spectrum P_z at the same temperature (left: $T = 21\,\mathrm{K}$, right $T = 49\,\mathrm{K}$), and presents outliers: at some frequency, its value is larger than $12P_z$. The pdf of the ratio p_z/P_z is clearly not compatible with the expected exponentially decaying distribution, as far positive events are overrepresented. In the time signal, the origin of this behaviour is easy to identify: "external" kick for the left signal, and self-oscillations like motion for the right one.

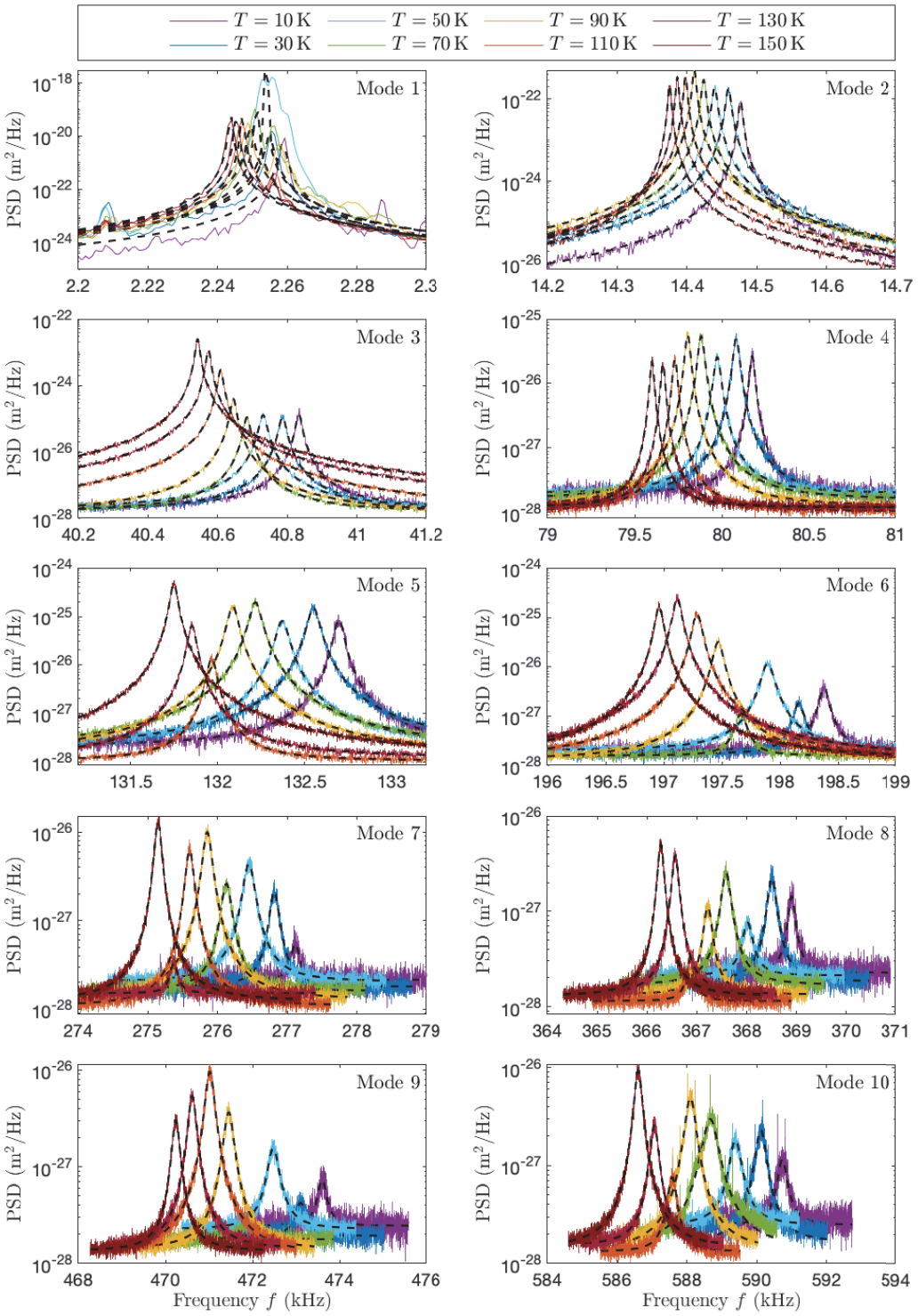

Figure 8.11 PSD of thermal noise for flexion modes 1 to 10, for temperatures between 10 K and 150 K, and superposed Saulson model fit.

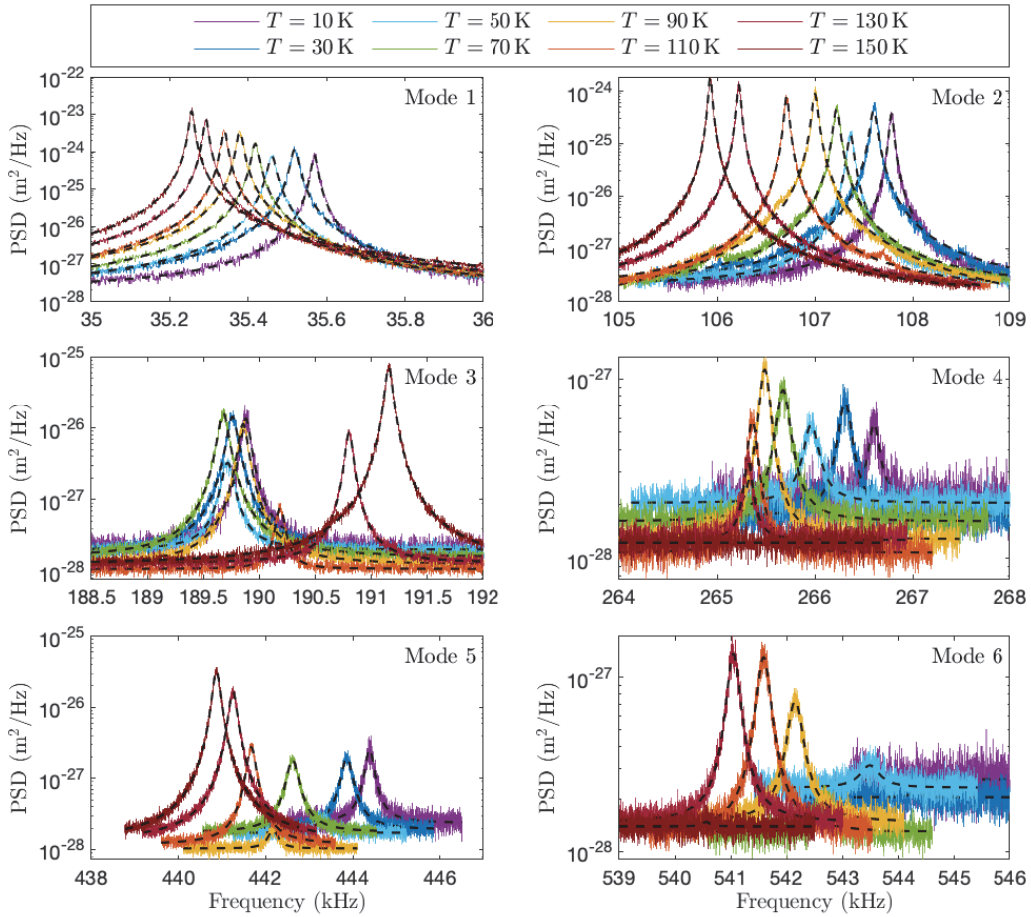

Figure 8.12 PSD of thermal noise for torsion modes 1 to 10, for temperatures between 10 K and 150 K, and superposed Saulson model fit.

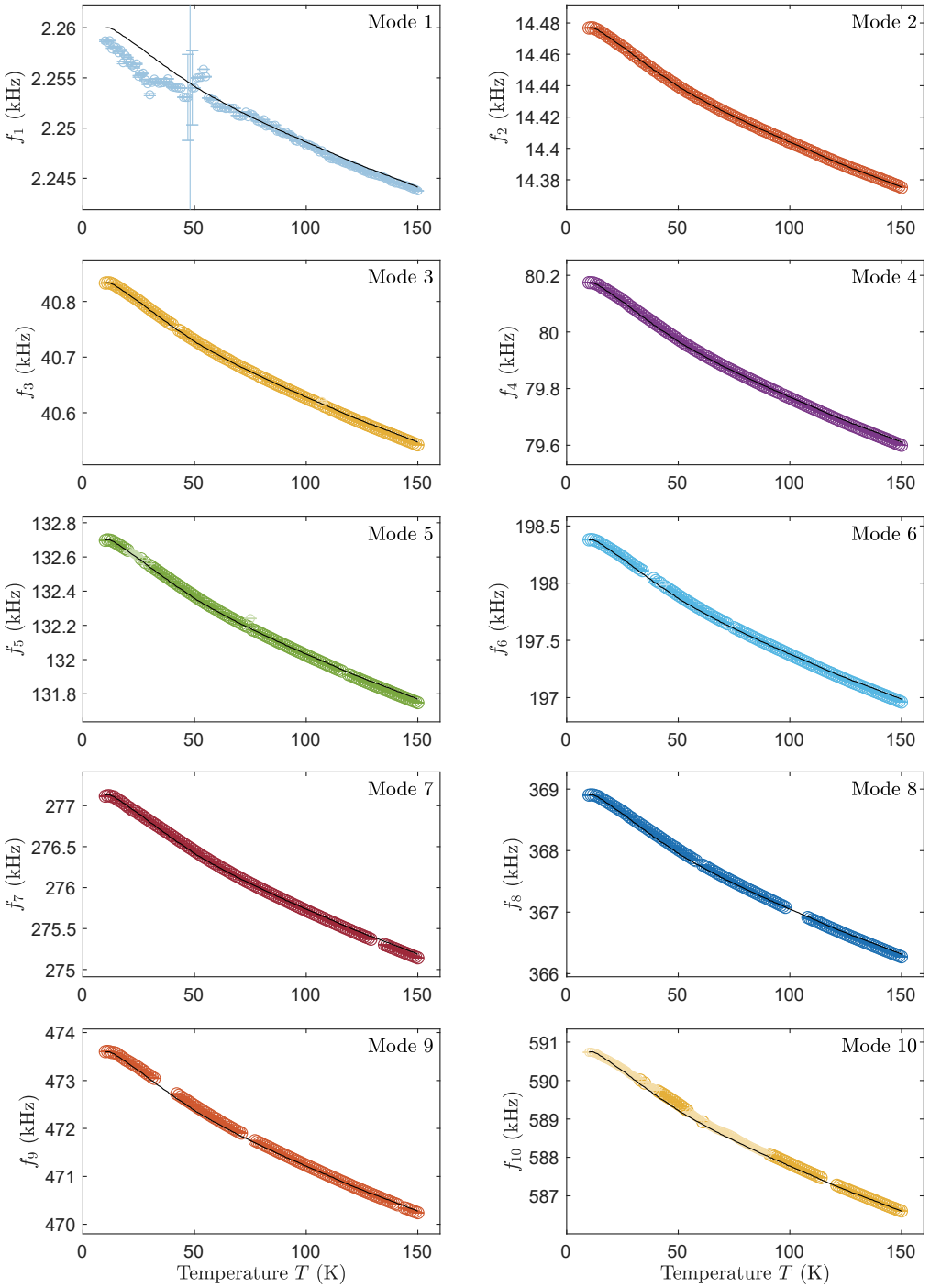

Figure 8.13 Resonance frequency of flexion modes 1 to 10 as a function of temperature. The continuous line is simply a projection of mode 2 temperature dependance at the other modes frequencies, showing that they all share the same behaviour. Fainter markers of small size correspond to fits where $\chi^2 > 1.25$. Most uncertainties are smaller than the marker size.

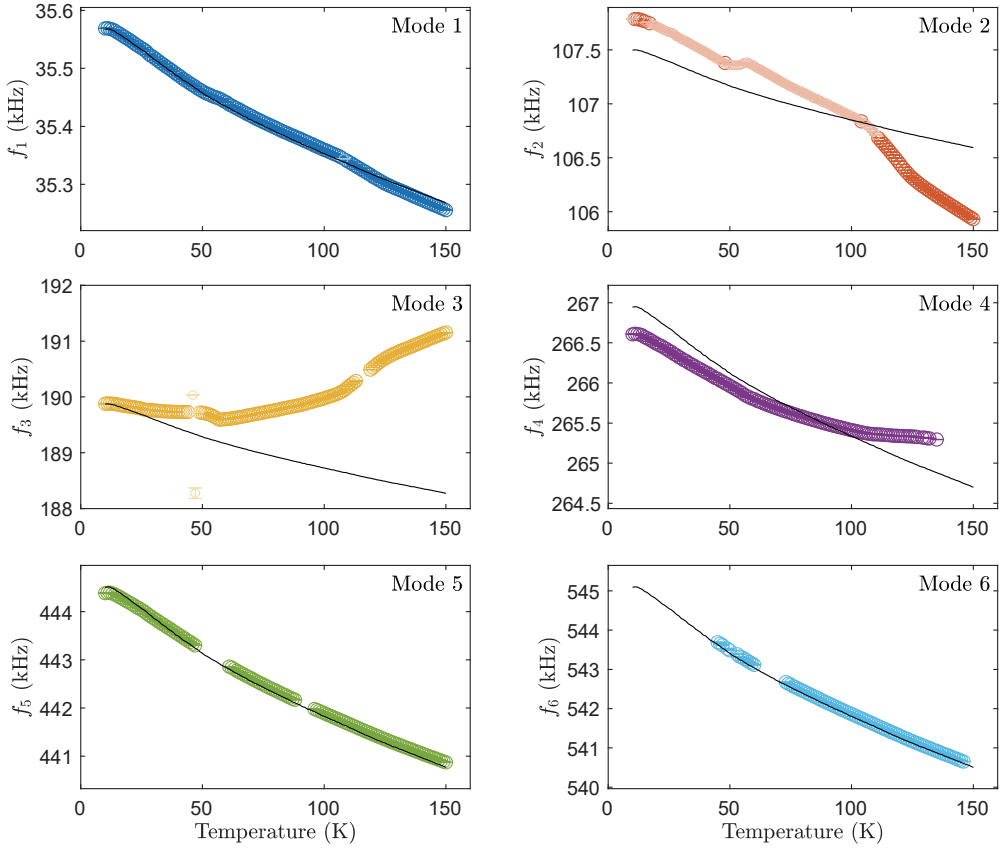

Figure 8.14 Resonance frequency of torsion modes 1 to 6 as a function of temperature. The continuous line is simply a projection of mode 1 temperature dependance at the other modes frequencies, showing that some share the same behaviour. Fainter markers of small size correspond to fits where $\chi^2 > 1.25$. Uncertainties are smaller than the marker size.

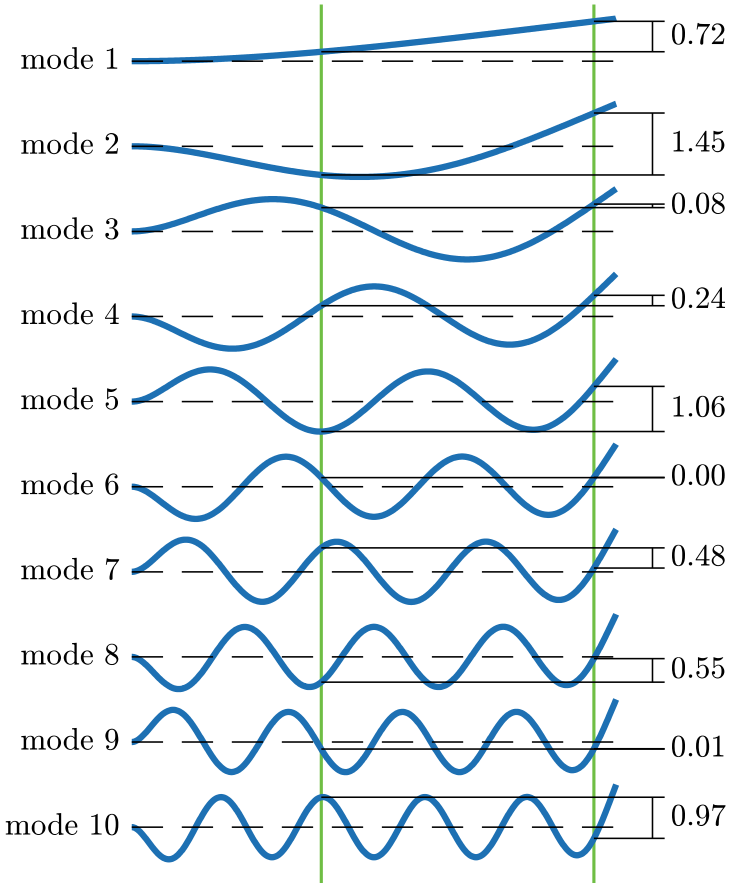

Figure 8.15 Example of the position of the laser beam with respect to flexion mode shapes when $x_{\text{prob}} = 707\,\text{m}$. The differential measurement senses a fraction of the actual deflection at the end of the cantilever, displayed on the right of each mode shape. For this particular sensing position for instance, the sensitivity to mode 3, 6 and 9 is very low. This corresponds to pseudo-nodes of the measurement for these modes.

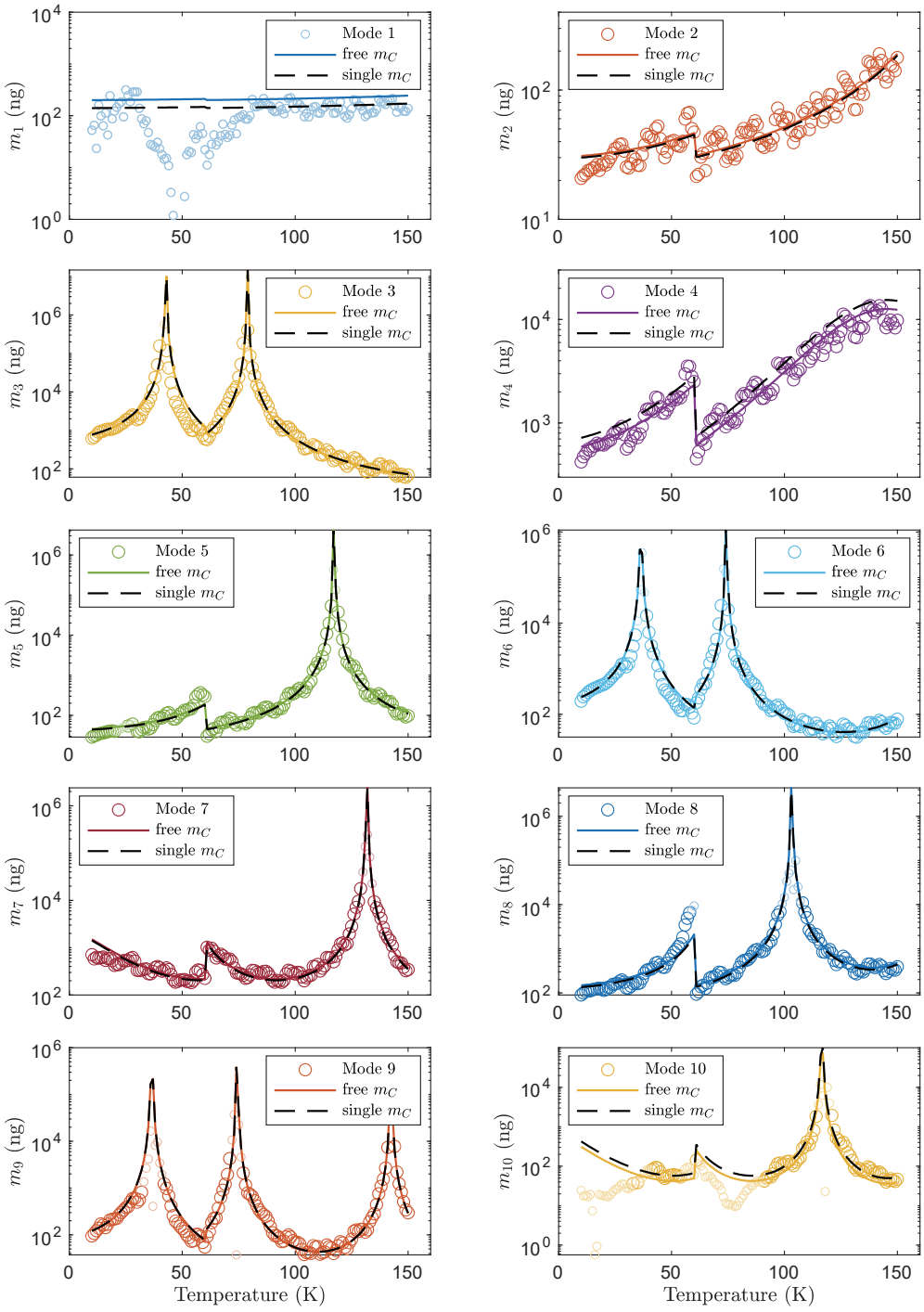

Figure 8.16 Effective masses m_n of flexion modes $n = 1$ to 10 versus temperature. Fainter markers of small size correspond to fits where $\chi^2 > 1.25$ or SNR < 1.1. A diverging m_n corresponds to pseudo nodes of mode n, and is used to infer the laser spots position at this specific temperature. From the extrapolation of position between those references, we get a continuous estimation of the effective masses, from which we infer the cantilever actual mass m_C.

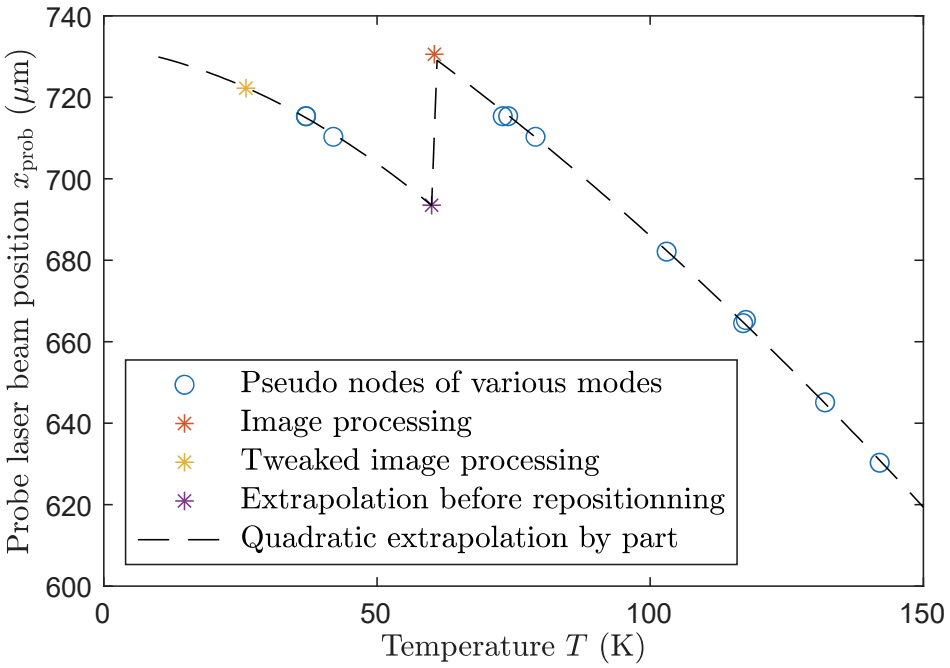

Figure 8.17 Position of the sensing laser spot on the cantilever as a function of temperature. Most experimental points correspond to pseudo nodes of the µcantilever modes measured in our experimental configuration (741 m long cantilever, reference laser position 417 m towards the base). We also include the points corresponding to image processing after each alignment. The dashed line is a polynomial extrapolation of the known points.

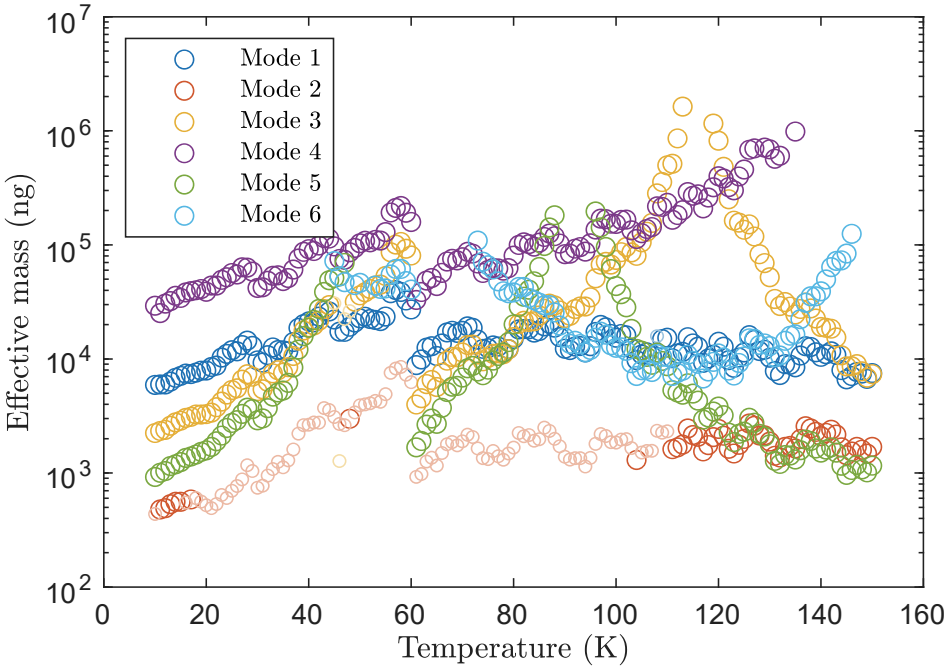

Figure 8.18 Effective masses of torsion modes versus temperature. Fainter markers of small size correspond to fits where $\chi^2 > 1.25$.

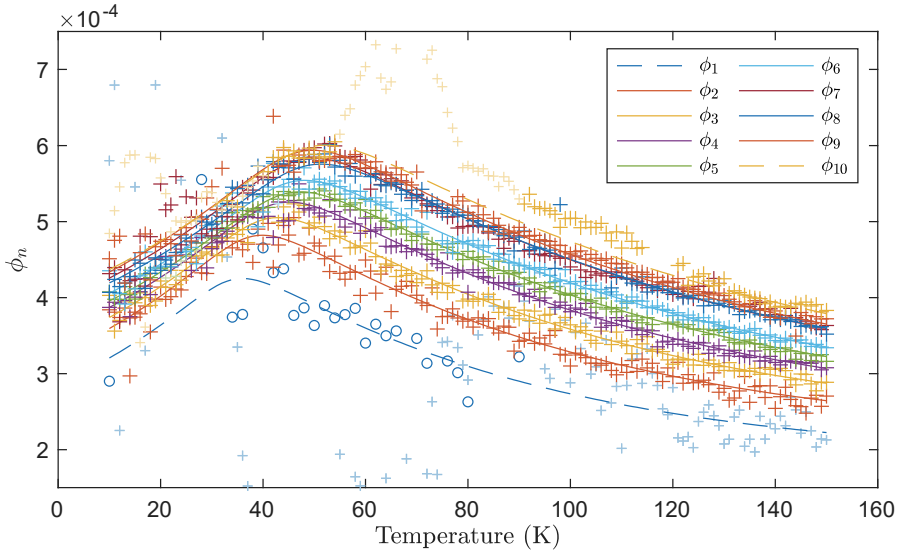

Figure 8.19 Dissipation ϕ_n for flexion modes $n = 1$ to 10. The continuous lines are fits of the data with the ansatz of equation 8.5, except for modes 1 and 10 where it is an extrapolation of the behaviour of other modes. Crosses are data obtained from fit of thermal noise spectra, while circles are data from the ring down study of mode 1. Fainter markers of small size correspond to fits where $\chi^2 > 1.25$.

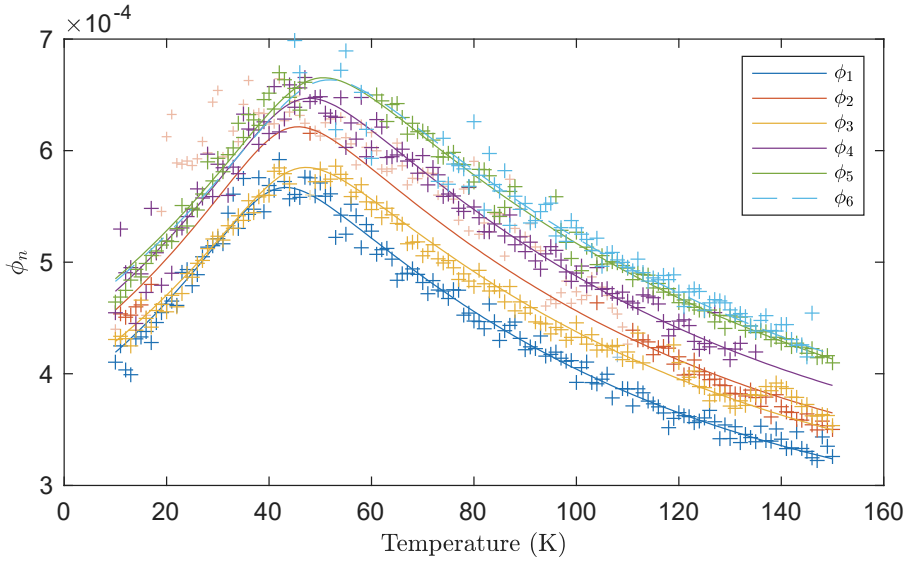

Figure 8.20 Dissipation ϕ_n for torsion modes $n = 1$ to 6. The continuous lines are fits of the data with the ansatz of equation 8.5, except for mode 6 where it is an extrapolation of the behaviour of other modes. Fainter markers of small size correspond to fits where $\chi^2 > 1.25$.

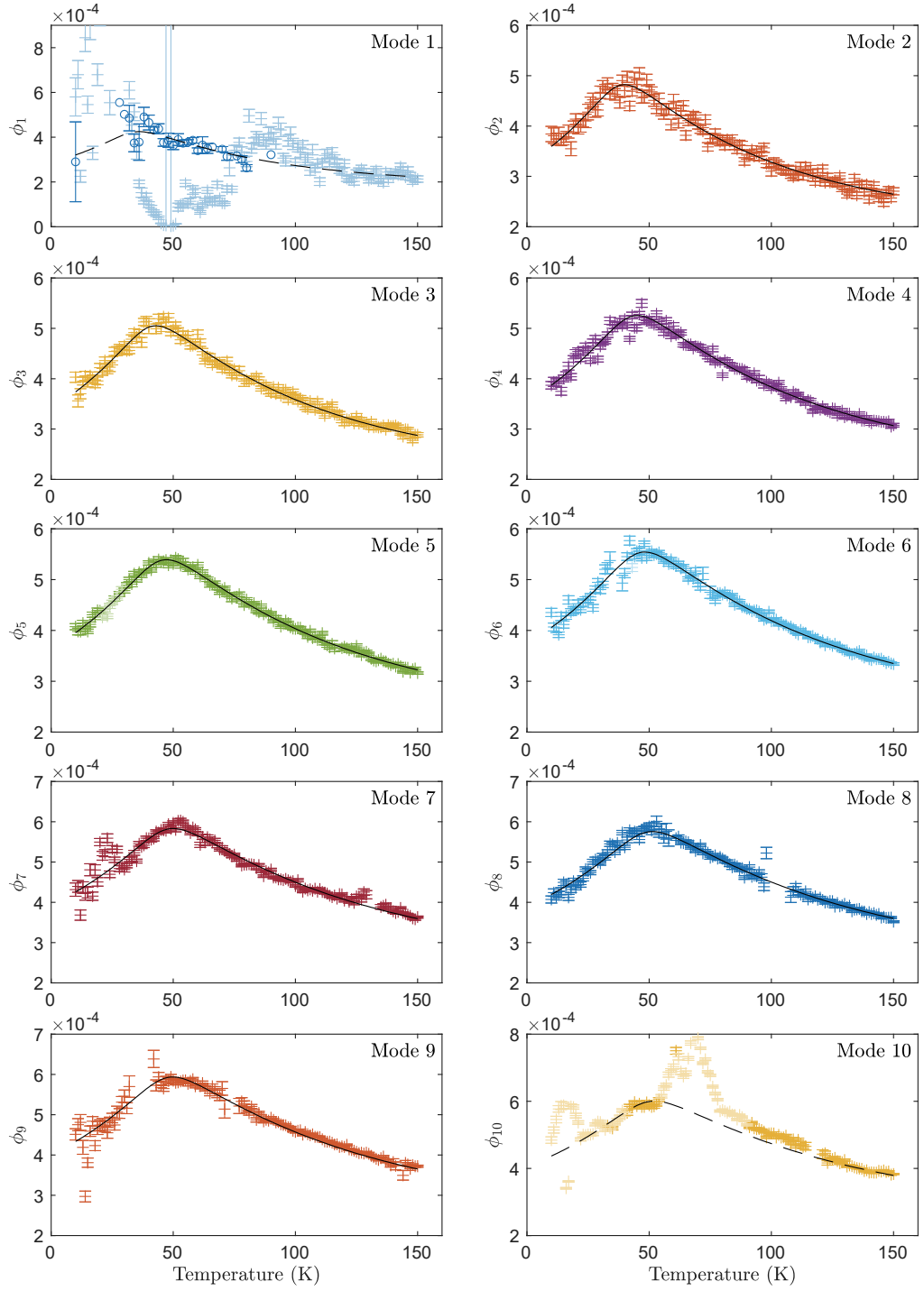

Figure 8.21 Dissipation ϕ_n for flexion modes $n = 1$ to 10 (split of all curves of figure 8.19). The continuous line is a fit of the data with the ansatz of eq. 8.5, except for modes 1 and 10 where it is an extrapolation of the behaviour of other modes. Crosses are data obtained from fit of thermal noise spectra, while circles are data from ring down studies of mode 1. Fainter coloured data correspond to fits where $\chi^2 > 1.25$.

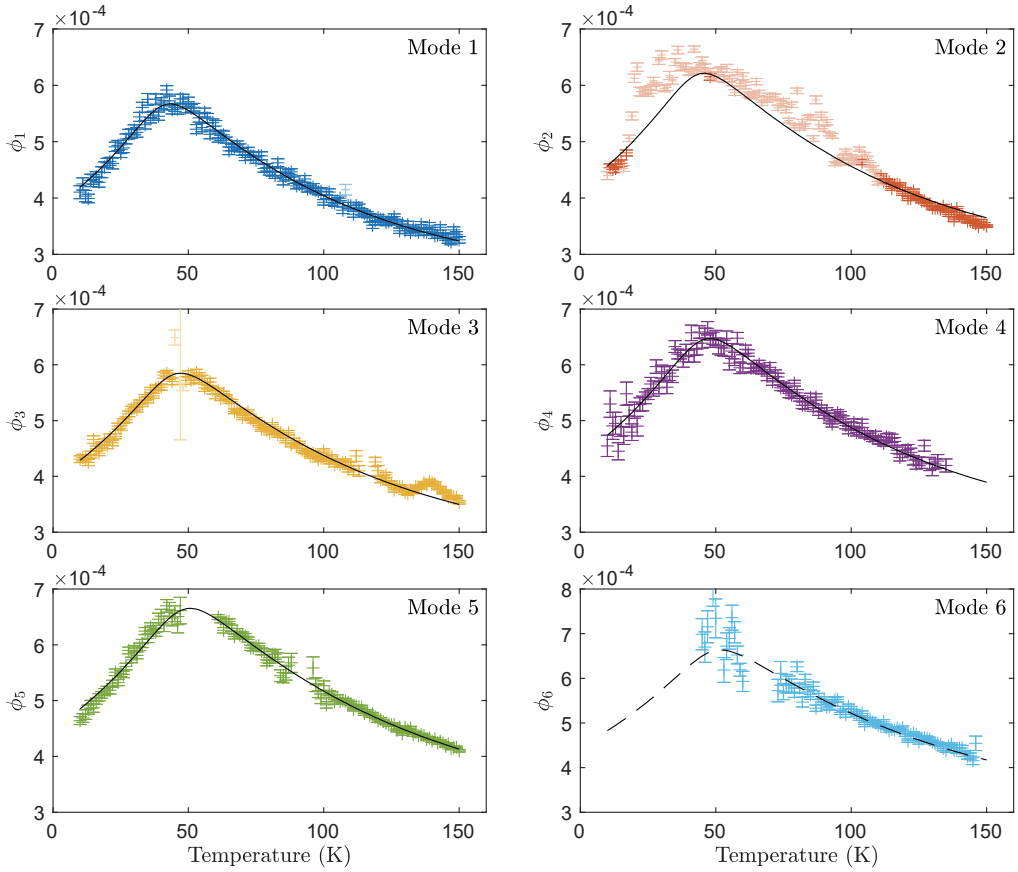

Figure 8.22 Dissipation ϕ_n for torsion modes $n = 1$ to 6 (split of all curves of figure 8.20). The continuous line is a fit of the data with the ansatz of eq. 8.5, except for mode 6 where it is an extrapolation of the behaviour of other modes. Fainter coloured data correspond to fits where $\chi^2 > 1.25$.

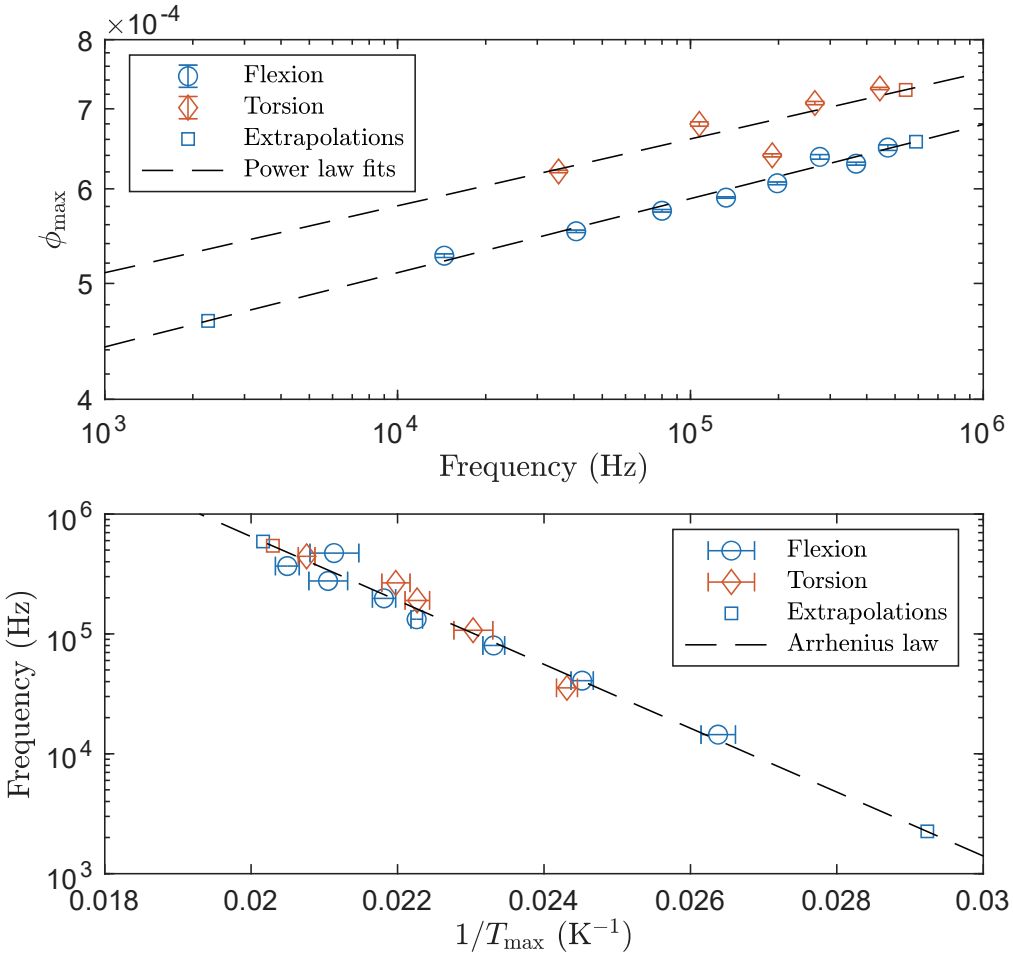

Figure 8.23 (top) $\phi_n^{\max}$ as a function of the resonance frequency f_n of the corresponding mode. In the log-log scale, data gathers along a line both for flexion and torsion. (bottom) f_n as a function of $1/T_n^{\max}$. In the lin-log scale, data gathers a line for both families of modes, hinting at an Arrhenius law. We can extrapolate from these fits the value of ϕ for the modes where data are noisy.

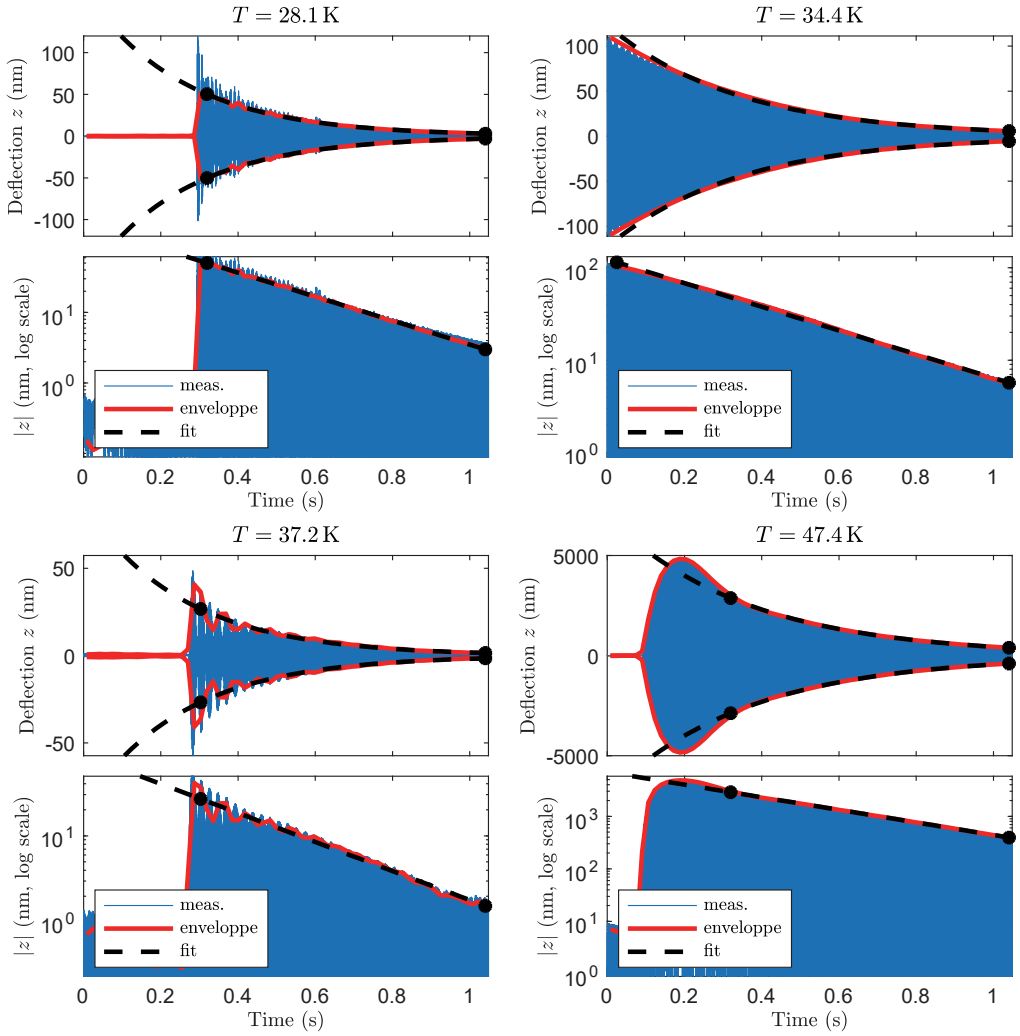

Figure 8.24 Time trace of deflection on a few datasets where ring-downs, triggered by an external noise or self-oscillations, are observed. The enveloppe is computed by the amplitude of the signal in a 244 Hz band around the resonance frequency f_1 of mode 1, and fitted with an exponential decay: Ae^{-t/τ_1}.

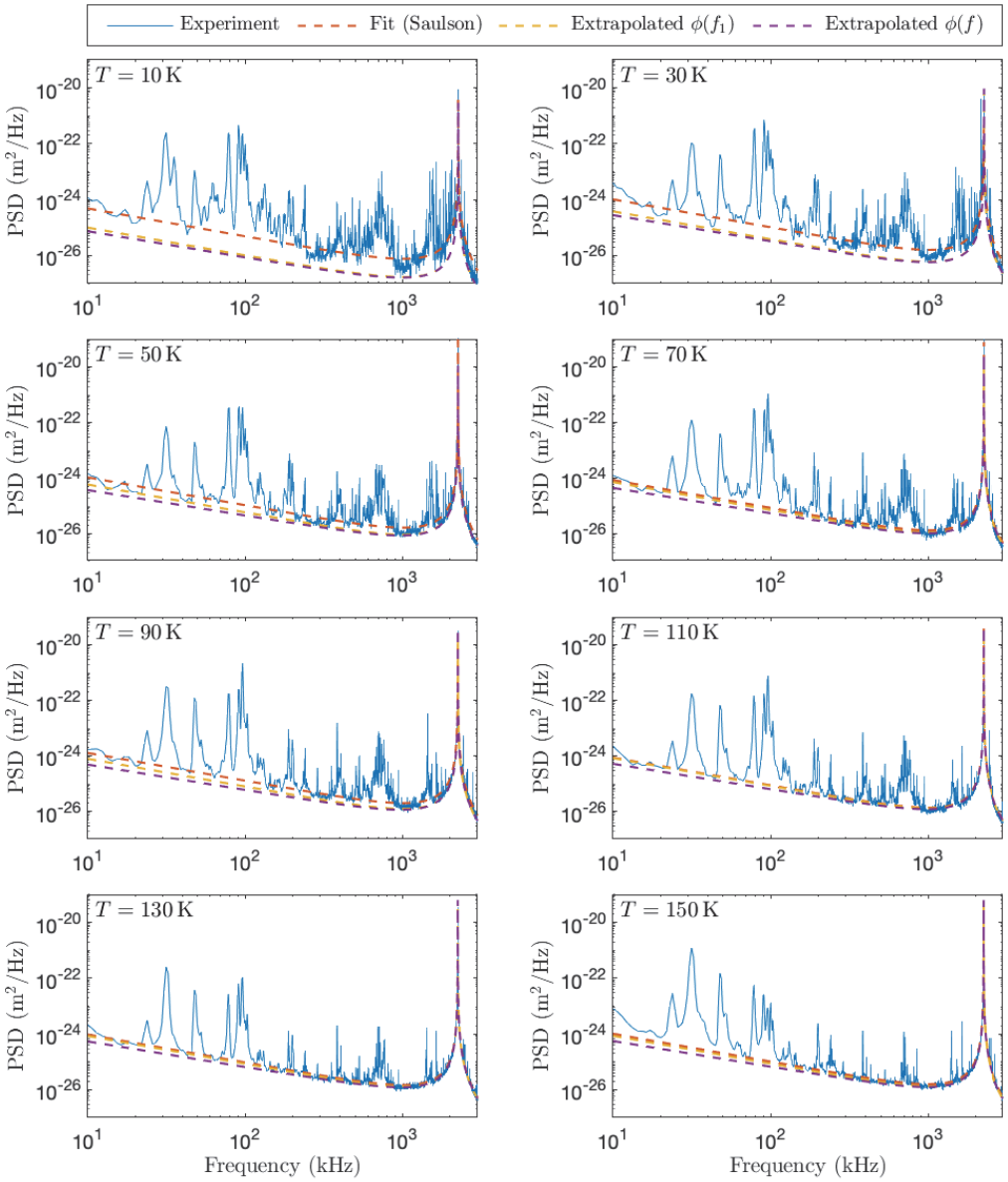

Figure 8.25 PSD of thermal noise for flexion mode 1 down to low frequencies, for temperature between 10 K and 150 K.

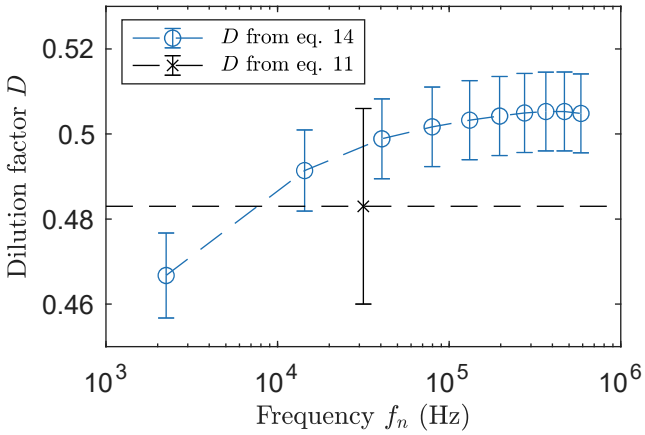

Figure 8.26 Dilution factor D computed from equation 8.14 and equation 8.11. The two methods lead to comparable estimations, with a dilution factor reasonably independent of the mode number.

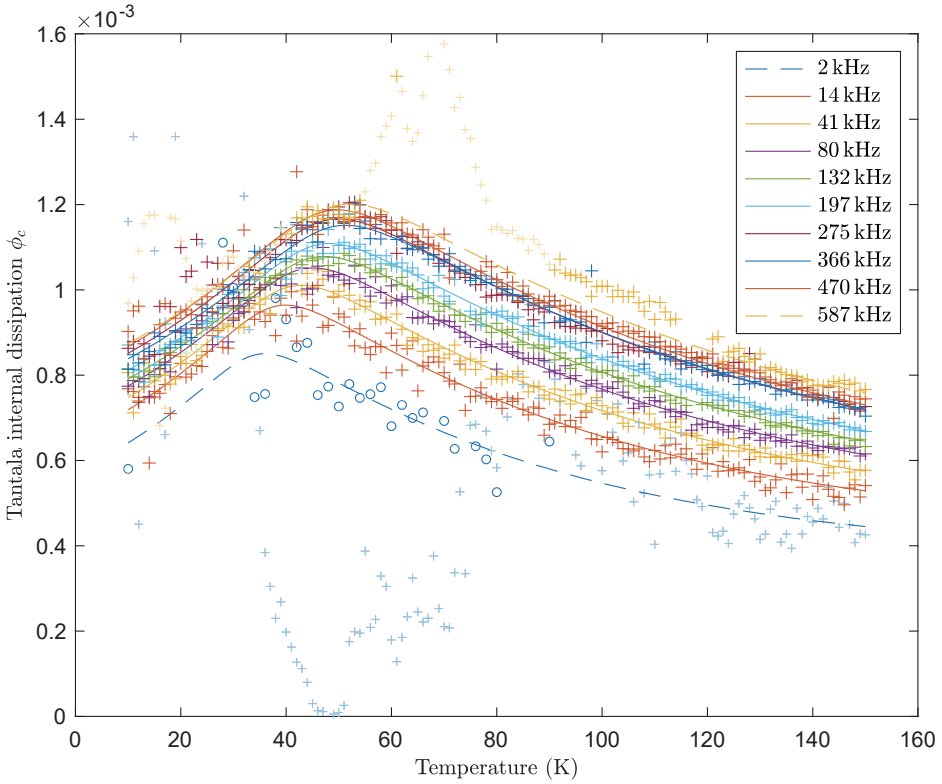

Figure 8.27 Internal dissipation ϕ_c of tantala computed from flexion modes $n = 1$ to 10 as a function of temperature. Fainter markers of small size correspond to fits where $\chi^2 > 1.25$. The continuous lines correspond to the model of equation 8.8 with the following parameters: $\alpha = 0.063$, $\phi_0^{\max} = 5.7 \times 10^{-4}\,\mathrm{Hz}^-$, $E_a = 53.5\,\mathrm{meV}$, $\tau_0 = 1.2 \times 10^{-12}\,\mathrm{s}$.

9 General conclusion

At the end of the year 2015, the first direct detection of a gravitational wave was realized, constituting one of the greatest achievement of experimental physics. This event marked the advent of gravitational wave astronomy. This detection was made possible only thanks to the continuous development and improvement of ground based, kilometer scale interferometric gravitational wave detectors.

Still, the challenge of improving the sensitivity gravitational wave detectors remains. A more sensitive detector can listen to a larger portion of the universe and detect gravitational wave events at a higher rate.

One of the main problematic in increasing this sensitivity is the thermal noise generated by the amorphous optical coating which is deposited on the mirrors of a gravitational wave detector to enhance their reflectivity. In accordance with the fluctuation-dissipation theorem, this noise is linked to the internal mechanical dissipation occuring in the coating's materials. To reduce this thermal noise, several detector projects plan to use mirrors cooled at cryogenic temperatures.

The understanding and the reduction of the internal dissipation of the optical coating used in gravitational wave detectors requires new experimental tools.

The work carried out during this thesis deals with the development of such a tool, called the CryoQPDI. It was done as a collaboration between the *Laboratoire des Matériaux Avancés*, which is responsible for the deposition of optical coatings on the large optics used in gravitational wave detectors, and the *Laboratoire de Physique de l'Ecole Normale Supérieure de Lyon*, which developed the quadrature phase differential interferometer (QPDI) concept the CryoQPDI is based on.

The CryoQPDI is a high resolution interferometer capable of measuring the Brownian motion of a μcantilever placed inside a cryostat. The thermal noise and the associated dissipation of a coated cantilever can be measured directly between 7 K and 300 K.

The direct measurement of the thermal agitation of a μcantilever at high resolution is challenging, and demand a carefull consideration of the instrument internal and external noise. The general design of the CryoQPDI presented in this manuscript, in particular the design of its interferometer, is therefore a quest for low noise. In its current state, the signal of the system is still affected by external noise peaks below

10 kHz at all temperature, and by sudden oscillations of the μcantilever encountered during cryogenic measurements. The laters are attributed to frictions caused by the cryostat structure's dilatation during warm up. Despite this noise, the system demonstrated its capability to provide meaningfull experimental results.

The main results obtained during the course of this thesis are listed hereafter.

- We demonstrated that a pulse tube based cryostat can be used with a quadrature phase differential interferometer to measure the thermal noise of a cryocooled μcantilever. This is possible because the typical acquisition time of an individual thermal noise spectrum is much smaller than the warm up time of the cryostat, so that the cantilever temperature does not need to be maintained constant during measurements. The vibrations coming from the pulse tube can thus be eliminated.
- We developed a special fixture to permit the deposition of an ion beam sputtered coatings on a μcantilever. This fixture, called the recto verso deposition system, allows the coating to be applied on both side of the cantilever during a single deposition run.
- Regarding the optical design of the CryoQPDI interferometer, the three major modifications made relative to the reference QPDI design are the development of the scanning objective, the use of a Semel-Savart plate as the interferometer birefringent beam splitter and the addition of a camera subsystem to image the sample.
- The scanning objective is the main interface between the sample and the main body of the interferometer. It provides both a small spot diameter and a long working distance, and also allows the alignment of the spot on a μcantilever. These conflicting requirements were met using an original combination of stock lenses together with a ray tracing software.
- We discovered that the crystal astigmatism generated by a birefringent material is the major source of contrast degradation in a QPDI. We showed that a Semel-Savart plate design can be used to compensate this crystal astigmatism, and obtained the highest contrast ever achieved with a QPDI using a birefringent beam splitter.
- The addition of a camera to the instrument optical scheme brings a considerable simplication of the alignment step which must be done before any measurement.
- We revisited the design of the intrument's photodetector. An excess of high frequency dark noise was found and correlated to the operational amplifier used in the photodetectors transimpedance amplifier. This finding led to a significant improvement of this noise, allowing a shot noise limited detection at all frequencies between DC and 1 MHz.
- Using the experimental tool developed during this thesis, we studied the internal dissipation of a tantala coated μcantilever between 10 K and 150 K. The dissipation

of the tantala coating present a weak maximum around 50 K, which a value and position which depend of the resonant frequency of the vibration mode considered. The mode loss angle maxima follow weak frequency dependance, and the temperature corresponding to these maxima obey an Arrhenius law with an activation energy of around 53 meV.

Directly measuring the thermal noise of a μcantilever is an originality compared to the methods previously employed to measure the mechanical dissipation of the optical coatings used in gravitational wave detectors, which are the ring down technique best represented by GeNS [22] and direct thermal noise measurements on macroscopic mirrors as performed by the MIT CTN [49]. The main advantages of the CryoQPDI concept compared to ring down measurements are threefold. First, the shape of a thermal noise spectra gives additional informations on the dissipation mechanism at play in the sample. This information is not accesible with a ring down method, as different dissipation mechanism gives the same exponential decay. Second, the method developed here offers a very high data throughput. All the vibration mode of the μcantilever are measured at the same time, and the duration of an experiment is not directly related to a mode time constant. The result presented in chapter 8 required a few days of measurement with the CryoQPDI, but would have required several weeks using a ringdown method. The third advantage inherent to the use of a micron-sized resonator is a high dilution factor. Here a single layer coating gave a dilution factor of 0.5, and dilution factors approaching unity can be expected with multilayer coatings. In ring down measurements where macrosopic resonators are used, the dilution factors are rather found around 1×10^{-2} to 1×10^{-3}. In our case, it was possible to ignore the dissipation of the substrate. Compared to the MIT CTN, the CryoQPDI is simpler to construct and to use, and offers a much greater bandwith allowing the study of a μcantilever's thermal noise spectrum around several of its vibration modes. The advantage regarding the dilution factor is also of relevance here.

While the experimental results obtained with the CryoQPDI are promising, reducing or eliminating the spurious noise present below 10 kHz would be very beneficial, as this noise prevent the exploitation of the signal in this frequency range, which also correspond to the range where gravitational wave detectors are limited by the coating Brownian noise. Despite important efforts, it was not possible to mitigate this noise during the course of this thesis. Even if they are of a lesser importance, a better control of the instrument would be gained after mitigating the sudden jumps of the signal encountered during cryogenic measurements.

The majority of the CryoQPDI construction was achieved during the thesis, even though further developments are always possible. In chapter 5, we mentionned that the imaging system should be completed to allow the simultaneous acquisition of the interferometer signal and imaging of the sample. This development would be especially beneficial for cryogenic measurement where the sample position drift with time.

The possibility of motorizing the scanning objective actuators was also mentionned. The presence of an operator is currently required during a cryogenic measurement only to realign the laser spots on the cantilever. With motorized actuators, this realignment could be automated, and the need for the presence of an operator could be avoided. This is of a special practical importance given the inherently long duration of a cryogenic measurement, which could then be done at night for example.

Nevertheless, the CryoQPDI can already be applied to the research for a low dissipation coating material. As we studied only a tantala monolayer, an immediate perspective is the study of other optical materials (including silica) as well a multilayer coatings (including bragg mirrors). Some other general questions in coating research is the influence of the substrate, the coating internal stress and the deposition energy.

A

Nominal properties of the Micromotive microcantilevers.

Table A.1 Nominal properties of the Micromotive μcantilevers.

Thickness (μm)	Length (μm)	K (N m^{-1})	f_1 (kHz)	$\sqrt{\langle z^2 \rangle}$ (nm)	N_{det}
1	500	0.030	5.50	0.37	8
	750	0.009	2.45	0.68	12
	1000	0.0038	1.38	1.04	16
5	500	3.80	27.5	0.033	4
	750	1.13	12.23	0.061	5
	1000	0.48	6.88	0.093	7

The nominal properties of the Micromotive μcantilevers are provided in table A.1 [33].

The manufacturer naming convention is as follow: in the sample name "OCTO750S", the term "OCTO" means a sample with 8 cantilevers, "750" is the μcantilevers length in μm, and the last letter "S" indicates a nominal thickness of 1 μm. A nominal thickness of 5 μm is denoted with the letter "D".

These cantilevers are made of silicon oriented along the (110) direction, with a Young's modulus of 169 GPa and a density of 2340 kg m^{-3}. K is the cantilever spring constant, f_1 is its fundamental resonant frequency, $\sqrt{\langle z^2 \rangle}$ is the cantilever thermal noise standard deviation at 300 K, and N_{det} is the number of detectable modes in a 1 MHz bandwidth (ignoring the measurement background noise). The nominal width of all the cantilevers is the same, at 90 μm.

B Statistics for the data analysis of thermal noise spectra

B.1 Uncertainty on thermal noise spectra

We consider a random variable F presenting a gaussian white noise, and want to assess the uncertainty of its power spectrum density PSD P_F. This PSD is computed as the mean value square modulus of the Fourier transform at each frequency:

$$P_F = \frac{1}{\Delta f}\langle|\tilde{F}|^2\rangle \tag{B.1}$$

with Δf the bin frequency width of the discrete Fourier transform. Without loss of generality and to simplify notations, we will set $\Delta f = 1$ and drop the bandwidth in next equations. In practice, the mean is evaluated by a finite average on N single realisations of the FFT $p_F = |\tilde{F}|^2$.

F being a gaussian random variable, its Fourier transform $\tilde{F}$ will also be a gaussian distributed random variable for both its real $x = \Re(\tilde{F})$ and imaginary part $y = \Im(\tilde{F})$:

$$\text{pdf}(x) = \frac{1}{\sigma\sqrt{2\pi}}e^{-\frac{x^2}{2\sigma^2}} \tag{B.2}$$

$$\text{pdf}(y) = \frac{1}{\sigma\sqrt{2\pi}}e^{-\frac{y^2}{2\sigma^2}} \tag{B.3}$$

with σ^2 the variance of the pdf (probability distribution function). We are however interested in the distribution of $p_F = |\tilde{F}|^2 = x^2 + y^2$. Let us change to polar coordinates $x + iy = re^{i\theta}$, we then have

$$dxdy = rdrd\theta \tag{B.4}$$

$$\text{pdf}(r)\text{pdf}(\theta)drd\theta = \text{pdf}(x)\text{pdf}(y)dxdy \tag{B.5}$$

$$\text{pdf}(r)\frac{1}{2\pi}drd\theta = \frac{1}{2\pi\sigma^2}e^{-\frac{x^2+y^2}{2\sigma^2}}rdrd\theta \tag{B.6}$$

$$\text{pdf}(r) = \frac{1}{\sigma^2}re^{-\frac{r^2}{2\sigma^2}} \tag{B.7}$$

from which we deduce

$$d(r^2) = 2rdr \tag{B.8}$$

$$\text{pdf}(r^2)d(r^2) = \text{pdf}(r)dr \tag{B.9}$$

$$\text{pdf}(r^2) = \frac{1}{2\sigma^2}e^{-\frac{r^2}{2\sigma^2}} \tag{B.10}$$

$$\text{pdf}(p_F) = \frac{1}{2\sigma^2}e^{-\frac{p_F}{2\sigma^2}} \tag{B.11}$$

By computing the mean value of p_F, we deduce:

$$P_F = \langle p_F \rangle \tag{B.12}$$

$$= \int_0^\infty p_F \text{pdf}(p_F) dp_F \tag{B.13}$$

$$= 2\sigma^2 \int_0^\infty p e^{-p} dp \tag{B.14}$$

$$= 2\sigma^2 \tag{B.15}$$

The probability distribution function of p_F/P_F is thus

$$\text{pdf}(p_F) = \frac{1}{P_F}e^{-\frac{p_F}{P_F}} \tag{B.16}$$

or equivalently, a single spectrum is the product of the average spectrum and a random number p distributed according to $\text{pdf}(p) = e^{-p}$ [90].

We have considered here a gaussian white noise, however the results can safely be extended to the thermal noise in position for example: indeed, those fluctuations are driven by the mechanical response $G(\omega)$ of the system to a gaussian white noise distributed force F, hence $P_z(\omega) = |G(\omega)|^2 P_F(\omega)$ will obey the same statistics at each frequency.

B.2 χ^2 values for all spectra fits

A general way to assess the validity of fits is to compute the distance between the experimental data and the fitting curve, and compare this value to the uncertainty on the experimental data. In our case, the spectra to fit are an average on individual spectra presenting a known dispersion (exponentially decaying distribution of multiplicative noise), so the uncertainty can be evaluated analytically: let $p_{z,n}$ be the n^{th} single spectrum, it can written as

$$p_{z,n} = p_n P_z \tag{B.17}$$

where P_z is the average spectrum, and p_n is a random number distributed according to $\text{pdf}(p) = e^{-p}$ (for each frequency bin). The experimental average is however limited to N single spectra :

$$P_{z,N} = \frac{1}{N}\sum_{1}^{N} p_{z,n} \tag{B.18}$$

$$= \frac{1}{N}\sum_{1}^{N} p_n P_z \tag{B.19}$$

$$= G_N P_z \tag{B.20}$$

The uncertainty on the average spectrum is thus a multiplicative factor G_N, corresponding to the average of the random variables p_n. The distribution of G_N can be computed analytically:

$$\text{pdf}(G_N) = \frac{N^{N+1}}{N!} G_N^{N-1} e^{-NG_N} \tag{B.21}$$

When $N \gg 1$, the distribution of G_N converges to a Gaussian of mean 1 and variance $1/N$ (mean and variance are exact results), hence:

$$P_{z,N} = P_z\left(1 \pm \frac{1}{\sqrt{N}}\right) \tag{B.22}$$

We can now compute the distance between the experimental data and the fitting curve with

$$\chi^2 = \frac{1}{\Delta f}\int_{\Delta f} df \frac{(P_{z,N}(f) - P_{\text{fit}}(f))^2}{\text{var}(P_{z,N}(f))} \tag{B.23}$$

$$= \frac{N}{\Delta f}\int_{\Delta f} df \left(1 - \frac{P_{\text{fit}}(f)}{P_{z,N}(f)}\right)^2 \tag{B.24}$$

with Δf the integration bandwidth around the resonance. For a perfect fit, χ^2 should be equal to 1, since the distance between the curve and the fit should statistically be equivalent to the uncertainty of each measurement. As a general rule, χ^2 smaller than 2 is a reasonable indication of a fit of good quality: the model is adequate to describe the experimental observations.

In figure B.1 and B.2, we plot the χ^2 for all fits of the spectra. Its value is very close to 1 for every temperature and resonances, except a few exception : mode 1 in flexion for all temperature (as already commented, noisy spectra), and some other modes in limited temperature ranges.

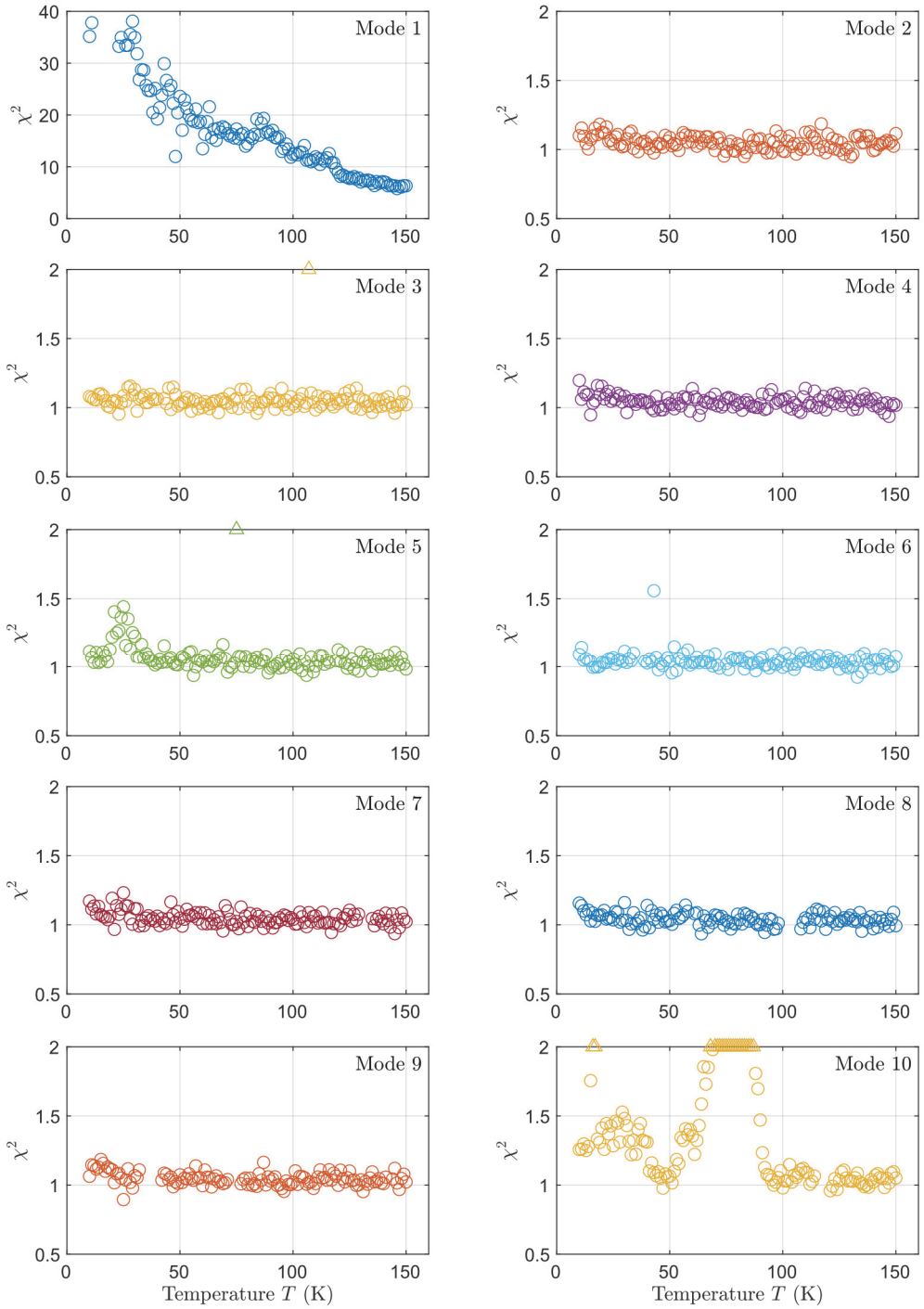

Figure B.1 χ^2 for all fits of the flexion spectra. Off axis values are plotted with triangles on the upper limit of the graphs. The value of χ^2 is very close to 1 (except for mode 1 and some temperature ranges of mode 10), demonstrating excellent quality of the fits.

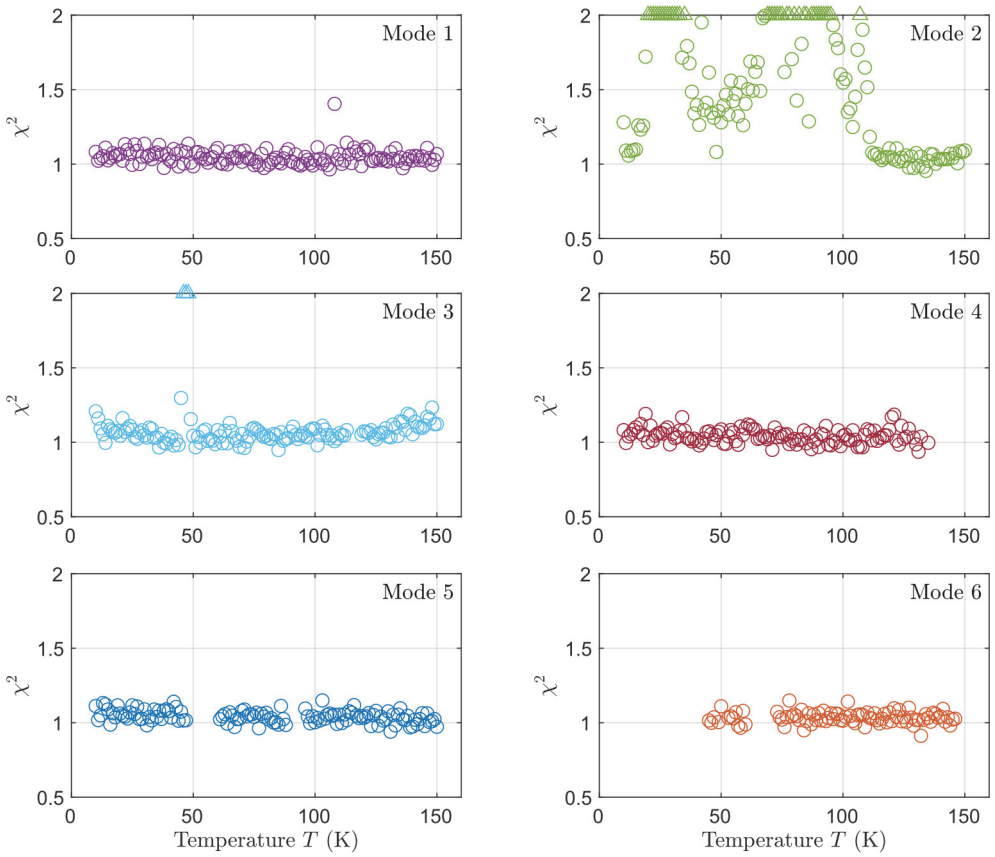

Figure B.2 χ^2 for all fits of the torsion spectra. Off axis values are plotted with triangles on the upper limit of the graphs. The value of χ^2 is very close to 1 (except for some temperature ranges of mode 2), demonstrating excellent quality of the fits.

Bibliography

[1] B. P. Abbott et al. “Observation of Gravitational Waves from a Binary Black Hole Merger”. In: *Phys. Rev. Lett.* 116 (6 Feb. 2016), p. 061102. DOI: 10.1103/PhysRevLett.116.061102.

[2] *AD8022 datasheet*. Rev. C. Analog Device. URL: https://www.analog.com/media/en/technical-documentation/data-sheets/AD8022.pdf.

[3] *AD8065/AD8066 datasheet*. Rev. L. Analog Device. URL: https://www.analog.com/media/en/technical-documentation/data-sheets/AD8065_8066.pdf.

[4] *AD8067 datasheet*. Rev. B. Analog Device. URL: https://www.analog.com/media/en/technical-documentation/data-sheets/AD8067.pdf.

[5] Felipe A. Aguilar Sandoval. “espectroscopia AFM de alta resolucion”. Spanish. PhD thesis. I dont know, 2097. URL: something.

[6] Mark Alexander and Derek F. Bowers. *SPICE-Compatible Op Amp Macro-Models*. AN-138. Analog Devices. 1990. URL: https://www.analog.com/media/en/technical-documentation/application-notes/AN-138.pdf.

[7] B. P. Abbott et all. In: 848.2 (Oct. 2017), p. L12. DOI: 10.3847/2041-8213/aa91c9. URL: https://doi.org/10.3847%2F2041-8213%2Faa91c9.

[8] *Analysis of the Sallen-Key Architecture*. SLOA024B. Revised September 2002. Texas Instrument. July 1999. URL: http://www.ti.com/lit/an/sloa024b/sloa024b.pdf.

[9] Laser Interferometer Space Antenna. *public website*. URL: https://www.elisascience.org/.

[10] John Ardizzoni. “A Practical Guide to High-Speed Printed-Circuit-Board Layout”. In: *Analog Dialogue* 39-9 (Sept. 2005). URL: https://www.analog.com/media/en/analog-dialogue/volume-39/number-3/articles/high-speed-printed-circuit-board-layout.pdf.

[11] Mauro Audi. *Ion pumps for UHV systems, synchrotrons & particle accelerators*. Agilent. URL: https://www.agilent.com/cs/library/technicaloverviews/public/Agilent_Ion_Pumps_for_UHV_systems_presentation.pdf.

[12] Bonnie Baker. *Operational amplifier macromodels: a comparison*. SBOA027. Burr-Brown/Texas Instrument. 1993. URL: http://www.ti.com/lit/an/sboa027/sboa027.pdf.

[13] L. Bellon et al. "Differential interferometry with a complex contrast". In: *Optics Communications* 207 (1-6 2002), pp. 49–56. DOI: https://doi.org/10.1016/S0030-4018(02)01475-X.

[14] Ludovic Bellon. "Exploring nano-mechanics through thermal fluctuations". Habilitation à diriger des recherches. Ecole normale supérieure de lyon - ENS LYON, 2010. URL: https://tel.archives-ouvertes.fr/tel-00541336.

[15] Max Born and Emil Wolf. *Principles of Optics*. 7th ed. Cambridge University Press, 2013. Chap. 15. ISBN: 9781139644181. DOI: https://doi.org/10.1017/CBO9781139644181.

[16] H Butt and M Jaschke. "Calculation of thermal noise in atomic force microscopy". In: *Nanotechnology* 6 (1 1995), pp. 1–7. DOI: https://doi.org/10.1088/0957-4484/6/1/001.

[17] Herbert B. Callen and Richard F. Greene. "On a Theorem of Irreversible Thermodynamics". In: *Physical Review* 86 (5 1952), pp. 702–710. DOI: https://doi.org/10.1103/PhysRev.86.702.

[18] Herbert B. Callen and Theodore A. Welton. "Irreversibility and Generalized Noise". In: *Physical Review* 83 (1 1951), pp. 34–40. DOI: https://doi.org/10.1103/PhysRev.83.34.

[19] Bruce Carter. "Understanding Op Amp Parameters". In: *Op Amps For Everyone, SLOD006B*. Ed. by Ron Mancini. Texas Instrument. Chap. 11. URL: https://web.mit.edu/6.101/www/reference/op_amps_everyone.pdf.

[20] G Carter. "Peening in ion-assited thin-film deposition: a generalized model". In: *Journal of Physics D: Applied Physics* 27 (1994), p. 1046. DOI: https://doi.org/10.1088/0022-3727/27/5/024.

[21] Sceram Advanced Ceramics. *Ceramic ball bearings*. French. URL: https://www.sceram.com/produits-standards/roulements-a-billes-ceramique/.

[22] E. Cesarini et al. "A "gentle" nodal suspension for measurements of the acoustic attenuation in materials". In: *Review of Scientific Instruments* 80 (2009), p. 053904.

[23] Mirza Čevro. "Ion-beam sputtering of $(Ta_2O_5)_x$–$(SiO_2)_{1-x}$ composite thin films". In: *Thin Solid Films* 245 (1–2 1995), pp. 91–103. DOI: https://doi.org/10.1016/0040-6090(94)06356-7.

[24] LIGO Scientific Collaboration and Virgo Collaboration. “Gwtc-1: A gravitational wave transient catalog of compact binary mergers observed by ligo and virgo during the first and second observing runs, vol. 9, p. 031040, Sep 2019.” In: *Phys. Rev. X* 9 (Sept. 2019), p. 031040. URL: https://arxiv.org/abs/1811.12907.

[25] The LIGO scientific collaboration. *public website*. URL: https://www.ligo.org/index.php.

[26] The Virgo Collaboration. *Advanced Virgo Technical Design Report*. 2012.

[27] The Virgo collaboration. *public website*. URL: http://public.virgo-gw.eu/language/en/.

[28] *Corning HPFS 7980 Fused Silica*. Corning. URL: https://www.corning.com/media/worldwide/csm/documents/5bf092438c5546dfa9b08e423348317b.pdf.

[29] Measurement Computing Corporation. *Data Acquisition Handbook*. Chap. 3. URL: https://www.mccdaq.com/pdfs/anpdf/Data-Acquisition-Handbook.pdf.

[30] Mervyn H Davis, Gary Proudfoot and Keith H. Bayliss. “Filamentless ion source for thin film processing and surface modification”. 5198718. URL: https://patents.google.com/patent/US5198718A/en?oq=5%2c198%2c718.

[31] Analog Device. *Analog Filter Wizard*. URL: https://www.analog.com/designtools/en/filterwizard/.

[32] Linear Technology/Analog Device. *LTSpice XVII*. URL: https://www.analog.com/en/design-center/design-tools-and-calculators/ltspice-simulator.html.

[33] *Duo-/Octosensis micro cantilever arrays*. Micromotive Mikrotechnik. URL: http://www.micromotive.de/en/Dokumente/DuoOctoDatasheet.pdf.

[34] Albert Einstein. “Investigation on the theory of the brownian movement (reprinted traduction)”. In: *Dover* 1 (1956), pp. 1–18. URL: https://web.archive.org/web/20180731002539/http://www.maths.usyd.edu.au/u/UG/SM/MATH3075/r/Einstein_1905.pdf.

[35] Albert Einstein. “Näherungsweise Integration der Feldgleichungen der Gravitation”. In: *Sitzungsberichte der Preußischen Akademie der Wissenschaften* (1916), pp. 688–696.

[36] Albert Einstein. “Über Gravitationswellen”. In: *Sitzungsberichte der Preußischen Akademie der Wissenschaften* (1918), pp. 154–167.

[37] Cosmic Explorer. *public website*. URL: https://cosmicexplorer.org/.

[38] R. Flaminio et al. “A study of coating mechanical and optical losses in view of reducing mirror thermal noise in gravitational wave detectors”. In: *Classical and Quantum Gravity* 27 (2010), p. 84030.

[39] M. Françon and S. Mallick. *Polarization Interferometers, Applications in microscopy and Macroscopy*. Wiley-Interscience, 1971. Chap. 1. ISBN: 0471274704.

[40] M. Françon and S. Mallick. *Polarization Interferometers, Applications in microscopy and Macroscopy*. Wiley-Interscience, 1971. Chap. 2. ISBN: 0471274704.

[41] M. Françon and S. Mallick. *Polarization Interferometers, Applications in microscopy and Macroscopy*. Wiley-Interscience, 1971. Chap. appendix A and B. ISBN: 0471274704.

[42] Maurice Françon. “Polarization Apparatus for Interference Microscopy and Macroscopy of Isotropic Transparent Objects”. In: *J. Opt. Soc. Am.* 47.6 (June 1957), pp. 528–535. DOI: https://doi.org/10.1364/JOSA.47.000528.

[43] *Frequency Response of Thin Film Chip Resistors*. 60107. revision 04-02-09. Vishay. 2009. URL: https://www.vishay.com/docs/60107/freqresp.pdf.

[44] A. Gerrard and J. M. Burch. *Introduction to Matrix Methods in Optics*. Dover Publications Inc., 1975. ISBN: 978-0486680446.

[45] Jerald G. Graeme. *Feedback plot define op amp AC performance*. SBOA015. Burr-Brown/Texas Instrument. 1991. URL: http://www.ti.com/lit/an/sboa015/sboa015.pdf.

[46] Jerald G. Graeme. *Op amp performance analysis*. SBOA054. Burr-Brown/Texas Instrument. 1993. URL: http://www.ti.com/lit/an/sboa054/sboa054.pdf.

[47] Jerald G. Graeme. *Photodiode Amplifiers – Op Amp Solutions*. McGraw-Hill Professional, 1995. ISBN: 978-0070242470.

[48] Massimo Granata et al. *Amorphous optical coatings of present gravitational-wave interferometers*. arXiv:1909.03737 - https://arxiv.org/abs/1909.03737. 2019. arXiv: 1909.03737.

[49] S. Gras et al. “Audio-band coating thermal noise measurement for Advanced LIGO with a multimode optical resonator”. In: *Physical Review D* 95.2 (Jan. 2017). ISSN: 2470-0029. DOI: 10.1103/physrevd.95.022001. URL: http://dx.doi.org/10.1103/PhysRevD.95.022001.

[50] Hamamatsu. *Opto-semiconductor handbook*. Chap. 02. URL: https://www.hamamatsu-news.de/hamamatsu_optosemiconductor_handbook/12/.

[51] Analog Device Hank Zumbahlen. *Linear Circuit Design Handbook*. Elsevier Newnes, 2008. Chap. 8. ISBN: 978-0-7506-8703-4.

[52] Gregory M Harry et al. “Thermal noise in interferometric gravitational wave detectors due to dielectric optical coatings”. In: *Classical and Quantum Gravity* 19.5 (Feb. 2002), pp. 897–917. doi: 10.1088/0264-9381/19/5/305. url: https://doi.org/10.1088%2F0264-9381%2F19%2F5%2F305.

[53] Peter L. M. Heydemann. “Determination and correction of quadrature fringe measurement errors in interferometers”. In: *Appl. Opt.* 20 (19 1981), pp. 3382–3384. doi: https://doi.org/10.1364/AO.20.003382.

[54] Philip C. D. Hobbs. *Building Electro-Optical Systems: Making it All Work*. John Wiley & Sons, 2008. Chap. 1. isbn: 9780470466339. doi: 10.1002/9780470466339.

[55] Philip C. D. Hobbs. *Building Electro-Optical Systems: Making it All Work*. John Wiley & Sons, 2008. Chap. 3. isbn: 9780470466339. doi: 10.1002/9780470466339.

[56] Philip C. D. Hobbs. *Building Electro-Optical Systems: Making it All Work*. John Wiley & Sons, 2008. Chap. 18. isbn: 9780470466339. doi: 10.1002/9780470466339.

[57] Paul Horowitz and Windfield Hill. *The Art of Electronics*. Cambridge University Press, 2015. Chap. 8. isbn: 978-0521809269.

[58] Paul Horowitz and Windfield Hill. *The Art of Electronics*. figure 8.127 B, page 584. Cambridge University Press, 2015. Chap. 8. isbn: 978-0521809269.

[59] Larry L. Howell, Spencer P. Magleby and Brian M. Olsen, eds. *Handbook of Compliant Mechanisms*. 1st ed. Springer-Verlag Berlin Heidelberg, 2013. Chap. 11. isbn: 9781118516485. url: https://onlinelibrary.wiley.com/doi/book/10.1002/9781118516485.

[60] J. B. Johnson. “Thermal agitation of electricity in conductors”. In: *Physical Review* 32 (1 1928), pp. 97–109. doi: https://doi.org/10.1103/PhysRev.32.97.

[61] Viktor Kanarov et al. “Charged particle source and operation thereof”. 7183716. url: https://patents.google.com/patent/US7183716B2/en?oq=7%2c183%2c716.

[62] Walt Kester. *Taking the Mystery out of the Infamous Formula, “SNR = 6.02N + 1.76dB,” and Why You Should Care*. MT-001. Rev. A. Analog Devices. 2008. url: https://www.analog.com/media/en/training-seminars/tutorials/MT-001.pdf0.

[63] Walt Kester. “Which ADC Architecture Is Right for Your Application?” In: *Analog Dialogue* 39-06 (June 2005). url: https://www.analog.com/en/analog-dialogue/articles/the-right-adc-architecture.html.

[64] H Kondo and T Mizoguchi. “Internal Stress in IBS Films”. In: *Materials Science and Engineering* (1988), pp. 519–522. doi: https://doi.org/10.1016/0025-5416(88)90220-0.

[65] Gabby Kroes, Lars Venema and Ramón Navarro. “Opto-mechanical design for transmission optics in cryogenic space instrumentation”. In: *International Conference on Space Optics — ICSO 2012*. Ed. by Bruno Cugny, Errico Armandillo and Nikos Karafolas. Vol. 10564. International Society for Optics and Photonics. SPIE, 2017, pp. 568–578. doi: 10.1117/12.2309211. url: https://doi.org/10.1117/12.2309211.

[66] Thomas Kugelstadt. “Active Filter Design Techniques”. In: *Op Amps For Everyone, SLOD006B*. Ed. by Ron Mancini. Texas Instrument. Chap. 16. url: https://web.mit.edu/6.101/www/reference/op_amps_everyone.pdf.

[67] Jie Li, Jingping Zhu and Xun Hou. “Field-compensated birefringent Fourier transform spectrometer”. In: *Optics Communications* 284.5 (2011), pp. 1127–1131. issn: 0030-4018. doi: https://doi.org/10.1016/j.optcom.2010.11.029.

[68] T Li et al. “Measurements of mechanical thermal noise and energy dissipation in optical dielectric coatings”. In: *Physical Review D* 89 (9 2014), p. 092004. doi: https://doi.org/10.1103/PhysRevD.89.092004.

[69] Tianjun Li et al. “Measurements of mechanical thermal noise and energy dissipation in optical dielectric coatings”. In: *Phys. Rev. D* 89 (9 May 2014), p. 092004. doi: 10.1103/PhysRevD.89.092004. url: http://link.aps.org/doi/10.1103/PhysRevD.89.092004.

[70] Richard G. Lyons. *Understanding Digital Signal Processing*. 3rd ed. Prentice Hall, 2010. Chap. 2. isbn: 978-0137027415.

[71] M.Semel. “Polarimetry and imagery through uniaxial crystals - Application to solar observations with high spatial resolution”. In: *Astron. Astrophys.* 1-2 (Aug. 1987), pp. 257–262. url: http://adsabs.harvard.edu/full/1987A%26A...178..257S.

[72] Jayanth Murthy Madapura. *Achieving higher ADC Resolution Using Oversampling*. AN1152. DS01152A. Microchip. 2008. url: https://www.microchip.com/wwwAppNotes/AppNotes.aspx?appnote=en533730.

[73] magnetsales.co.uk. *Alnico Grades*. url: https://web.archive.org/web/20171215153950/http://www.magnetsales.co.uk:80/products/alnico/.

[74] magnetsales.co.uk. *Application Guide*. url: https://web.archive.org/web/20171226101528/http://www.magnetsales.co.uk/home/application-guide/.

[75] Virendra N. Mahajan. *Aberration Theory Made Simple*. 2nd ed. Vol. TT93. SPIE Press Book, 2011. Chap. 1. isbn: 9780819488251. url: https://spie.org/publications/book/903924?SSO=1.

[76] Virendra N. Mahajan. *Aberration Theory Made Simple*. 2nd ed. Vol. TT93. SPIE Press Book, 2011. Chap. 8. ISBN: 9780819488251. URL: https://spie.org/publications/book/903924?SSO=1.

[77] Virendra N. Mahajan. *Aberration Theory Made Simple*. 2nd ed. Vol. TT93. SPIE Press Book, 2011. Chap. 7. ISBN: 9780819488251. URL: https://spie.org/publications/book/903924?SSO=1.

[78] Virendra N. Mahajan. *Aberration Theory Made Simple*. 2nd ed. Vol. TT93. SPIE Press Book, 2011. Chap. 8. ISBN: 9780819488251. URL: https://spie.org/publications/book/903924?SSO=1.

[79] Virendra N. Mahajan. *Aberration Theory Made Simple*. 2nd ed. Vol. TT93. SPIE Press Book, 2011. Chap. 2. ISBN: 9780819488251. URL: https://spie.org/publications/book/903924?SSO=1.

[80] Virendra N. Mahajan. *Aberration Theory Made Simple*. 2nd ed. Vol. TT93. SPIE Press Book, 2011. Chap. 3. ISBN: 9780819488251. URL: https://spie.org/publications/book/903924?SSO=1.

[81] Virendra N. Mahajan. *Aberration Theory Made Simple*. 2nd ed. Vol. TT93. SPIE Press Book, 2011. Chap. 8. ISBN: 9780819488251. URL: https://spie.org/publications/book/903924?SSO=1.

[82] Virendra N. Mahajan. "Strehl ratio of a Gaussian beam". In: *J. Opt. Soc. Am. A* 22.9 (Sept. 2005), pp. 1824–1833. DOI: https://doi.org/10.1364/JOSAA.22.001824.

[83] I W Martin et al. "Effect of heat treatment on mechanical dissipation in Ta2O5coatings". In: *Classical and Quantum Gravity* 27.22 (2010), p. 225020. DOI: 10.1088/0264-9381/27/22/225020. URL: https://doi.org/10.1088/0264-9381/27/22/225020.

[84] jensign.com by Michel I. Gallant. *Feedback Amplifier Stability Calculator*. URL: http://www.jensign.com/stability/calculator.html.

[85] jensign.com by Michel I. Gallant. *Transimpedance Amplifiers*. URL: http://www.jensign.com/transimpedance/index.html.

[86] Laurence W. Nagel and D.O. Pederson. *SPICE (Simulation Program with Integrated Circuit Emphasis)*. Tech. rep. UCB/ERL M382. EECS Department, University of California, Berkeley, Apr. 1973. URL: http://www2.eecs.berkeley.edu/Pubs/TechRpts/1973/22871.html.

[87] *NI PXI 5922 datasheet*. September 2018. National Instrument. URL: http://www.ni.com/pdf/manuals/374033b.pdf.

[88] *NI PXIe 6124 datasheet*. Dec08. National Instrument. URL: http://www.ni.com/pdf/manuals/372526b.pdf.

[89] NIST. *Material properties: OFHC Copper*. URL: https://trc.nist.gov/cryogenics/materials/OFHC%20Copper/OFHC_Copper_rev1.htm.

[90] Simon F. Nørrelykke and Henrik Flyvbjerg. "Power spectrum analysis with least-squares fitting: Amplitude bias and its elimination, with application to optical tweezers and atomic force microscope cantilevers". In: *Review of Scientific Instruments* 81.7 (2010), p. 075103. DOI: https://doi.org/10.1063/1.3455217.

[91] H. Nyquist. "Thermal agitation of electric charge in conductors". In: *Physical Review* 32 (1928), pp. 110–113. DOI: https://doi.org/10.1103/PhysRev.32.110.

[92] Pierdomenico Paolino. "Thermal noise and dissipation of a micro-cantilever". French. PhD thesis. Ecole normale supérieure de lyon - ENS LYON, 2008. URL: https://tel.archives-ouvertes.fr/tel-00423692.

[93] Pierdomenico Paolino, Felipe A. Aguilar Sandoval and Ludovic Bellon. "Quadrature phase interferometer for high resolution force spectroscopy". In: *Review of Scientific Instruments* 84 (9 2013), p. 095001. DOI: https://doi.org/10.1063/1.4819743.

[94] Newlight Photonics. *Birefringent Crystals*. URL: http://www.newlightphotonics.com/Birefringent-Crystals.

[95] Frank Pobell. *Matter and Methods at Low Temperatures*. 3rd ed. Springer-Verlag Berlin Heidelberg, 2007. Chap. 5. ISBN: 978-3-540-46360-3. URL: https://www.springer.com/gp/book/9783540463566.

[96] Frank Pobell. *Matter and Methods at Low Temperatures*. 3rd ed. Springer-Verlag Berlin Heidelberg, 2007. Chap. 4. ISBN: 978-3-540-46360-3. URL: https://www.springer.com/gp/book/9783540463566.

[97] *Precision Point: Cryogenic (4K...293K) material properties*. JPE. URL: https://www.janssenprecisionengineering.com/page/cryogenic-properties-of-materials/.

[98] *Principles of data acquisition and convertion*. SBAA051A. Revised April 2015. Texas Instrument. 1994. URL: http://www.ti.com/lit/an/sbaa051a/sbaa051a.pdf.

[99] The Einstein Telescope Project. *public website*. URL: http://www.et-gw.eu/.

[100] The LIGO-India project. *public website*. URL: http://www.ligo-india.in/.

[101] *PS1.0-6b TO datasheet*. version 15-01-13. First Sensor. URL: https://web.archive.org/web/20160706034927/http://www.first-sensor.com/cms/upload/datasheets/PS1.0-6b_TO_501429.pdf.

[102] John Rumble, ed. *CRC Handbook of Chemistry and Physics, 100th Edition*. CRC Press, Taylor and Francis Group, 2019.

[103] P Saulson. "Thermal noise in mechanical experiments". In: *Physical Review D* 42 (8 1990), pp. 2437–2445. DOI: https://doi.org/10.1103/PhysRevD.42.2437.

[104] C. Schönenberger and S. F. Alvarado. “A differential interferometer for force microscopy”. In: *Review of Scientific Instruments* 60.10 (1989), pp. 3131–3134. doi: https://doi.org/10.1063/1.1140543.

[105] Sidney A. Self. “Focusing of spherical Gaussian beams”. In: *Appl. Opt.* 22.5 (Mar. 1983), pp. 658–661. doi: https://doi.org/10.1364/AO.22.000658.

[106] Peter S. Shawhan. “Rapid alerts for following up gravitational wave event candidates”. In: *Proc. SPIE* 8448 (2012). For the proceedings of the SPIE Astronomical Instrumentation + Telescopes conference, Amsterdam, 2012, p. 844825. url: https://arxiv.org/abs/1206.6163.

[107] Maria C. Simon. “Ray tracing formulas for monoaxial optical components”. In: *Appl. Opt.* 22.2 (Jan. 1983), pp. 354–360. doi: https://doi.org/10.1364/AO.22.000354.

[108] Warren J. Smith. *Modern Optical Engineering*. 3rd ed. Vol. PM88. SPIE Press Book/McGraw-Hill, 2000. Chap. 3. isbn: 978-0819438386. url: https://spie.org/Publications/Book/387098.

[109] Warren J. Smith. *Modern Optical Engineering*. 3rd ed. Vol. PM88. SPIE Press Book/McGraw-Hill, 2000. Chap. 10. isbn: 978-0819438386. url: https://spie.org/Publications/Book/387098.

[110] Warren J. Smith. *Modern Optical Engineering*. 3rd ed. Vol. PM88. SPIE Press Book/McGraw-Hill, 2000. Chap. 12. isbn: 978-0819438386. url: https://spie.org/Publications/Book/387098.

[111] Warren J. Smith. *Practical Optical System Layout and Use of Stock Lenses*. McGraw-Hill, 1997. Chap. 2. isbn: 9780070592544. url: https://www.accessengineeringlibrary.com/content/book/9780070592544.

[112] Warren J. Smith. *Practical Optical System Layout and Use of Stock Lenses*. McGraw-Hill, 1997. Chap. 6. isbn: 9780070592544. url: https://www.accessengineeringlibrary.com/content/book/9780070592544.

[113] SVS-Vistek. *exo4000MU3 specifications*. url: https://www.svs-vistek.com/en/industrial-cameras/svs-camera-detail.php?id=exo4000MU3.

[114] Absolut System. *english website*. url: http://absolut-system.com/?lang=en.

[115] Thorlabs. *Camera Basics*. url: https://www.thorlabs.de/newgrouppage9.cfm?objectgroup_id=8962.

[116] Francisco E. Veiras, María T. Garea and Liliana I. Perez. “Wide angle conoscopic interference patterns in uniaxial crystals”. In: *Appl. Opt.* 51.15 (May 2012), pp. 3081–3090. doi: https://doi.org/10.1364/AO.51.003081.

[117] Gugliermo Ventura and Lara Risegari. *The Art of Cryogenics, Low-Temperature Experimental Techniques*. Elsevier, 2007. Chap. 1. ISBN: 978-0-08-044479-6. URL: https://www.elsevier.com/books/the-art-of-cryogenics/ventura/978-0-08-044479-6.

[118] Gugliermo Ventura and Lara Risegari. *The Art of Cryogenics, Low-Temperature Experimental Techniques*. Elsevier, 2007. Chap. 5. ISBN: 978-0-08-044479-6. URL: https://www.elsevier.com/books/the-art-of-cryogenics/ventura/978-0-08-044479-6.

[119] Akira E. Villar et al. "Measurement of thermal noise in multilayer coatings with optimized layer thickness". In: *Phys. Rev. D* 81 (12 June 2010), p. 122001. DOI: 10.1103/PhysRevD.81.122001. URL: https://link.aps.org/doi/10.1103/PhysRevD.81.122001.

[120] telescope-optics.net by Vladimir Sacek. *Telescope aberrations: types and causes*. URL: https://www.telescope-optics.net/aberrations.htm.

[121] Robert Alexander Wannamaker. "The Theory of Dithered Quantization". PhD thesis. University of Waterloo, 2003. URL: http://www.robertwannamaker.com/writings/rw_phd.pdf.

[122] David T Wei, Harold R. Kaufman and Cheng-Chung Lee. "Ion Beam Sputtering". In: *Thin Films for Optical Systems*. Ed. by François R Flory. CRC Press, 1995. Chap. 6, pp. 133–201.

[123] J. M. Weisberg, J. H. Taylor and L. A. Fowler. "Gravitational Waves from an Orbiting Pulsar". In: *Scientific American* 245 (1981), pp. 74–82.

[124] J. J. Wortman and R. A. Evans. "Young's Modulus, Shear Modulus, and Poisson's Ratio in Silicon and Germanium". In: *Journal of Applied Physics* 36.1 (1965), pp. 153–156. DOI: 10.1063/1.1713863. URL: http://link.aip.org/link/?JAP/36/153/1.

[125] Zemax. *OpticStudio*. We used an older version of the software, for which the information are no longer available online. URL: https://www.zemax.com/products/opticstudio.